Modeling the Dynamics of Cell Growth, Central Carbon Metabolism and Virus Production in Animal Cells

Dissertation
zur Erlangung des akademischen Grades

Doktoringenieur
(Dr.-Ing.)

von João Rodrigues Correia Ramos, M. Sc.

geb. am 18. März 1991 in Fogo, Kapverden

genehmigt durch die Fakultät für Verfahrens- und Systemtechnik der Otto-von-Guericke-Universität Magdeburg

Vorsitz
Prof. Dr.-Ing. Andreas Seidel-Morgenstern

Gutachter:

Prof. Dr. Ioscani Jimenez Del Val

Dr.-Ing Markus Rehberg

Prof. Dr.-Ing. Udo Reichl

Promotionskolloquium am 02. April 2025

“Mathematics is the language in which
God has written the universe.”

(Galileo Galilei)

Ramos, João Rodrigues Correia:
Modeling the Dynamics of Cell Growth, Central Carbon Metabolism and Virus Production in Animal Cells
PhD thesis, Max Planck Institute for Dynamics of Complex Technical Systems, 2025

Abstract

Cell culture processes are a well-established platform for the research and manufacture of therapeutic biologicals such as recombinant proteins and vaccines. Cell growth and production of these products requires optimal cultivation conditions (temperature, pH value, dissolved oxygen, etc.) and a well formulated medium (substrates or energy sources, amino acids, vitamins, and micro-nutrients). Growing cells can adjust the substrates usage and products release via reactions of the metabolic network (comprising transmembrane transporters and enzymes) to produce energy and precursors. Furthermore, it is also known that enzymes are controlled using sophisticated regulation mechanisms. Thus, increasing the cell growth and by-product yields requires the understanding of cellular metabolism, especially the central carbon metabolism where most of the energy and precursors are produced. Relatively few dynamic mathematical models have been developed that describe cell growth and the central carbon metabolism, especially for animal cell lines due to a lack of experimental data and complexity of this system. Most modeling approaches focus on cell growth and extracellular metabolites, while some include only parts of the central carbon metabolism (intracellular), limiting their applicability.

The overall focus of this work was the development of quantitative and dynamic mechanistic models that describe both cell growth and central carbon metabolism which are observed at different scales, i.e., the macroscopic scale (bioreactor) and microscopic scale (intracellular). For the macroscopic scale, a segregated cell growth model that describes substrates, by-products as well as cell number and cell volume was established. For the microscopic scale, a structured model of the central carbon metabolism was developed. Both models were coupled, allowing a direct connection between cell growth, substrates consumption, metabolic by-product release and the intracellular state. The central carbon metabolism describes the dynamics of key metabolites from glycolysis, the citric acid cycle, glutaminolysis, transamination, and the pentose phosphate pathway.

The first aim of this work was to establish a dynamic mathematical model for the human designer cell line AGE1.HN.AAT (provided by ProBioGen AG, Germany). The model comprises a set of 33 ordinary differential equations (ODEs) accounting for cell growth (concentration of viable cells, mean cell diameter, volume of viable cells), and the concentration of key substrates and metabolites both at the intracellular and extracellular level. It also describes the formation of the product alpha1-antitrypsin. Model validity was assessed using experimental data of four independent batch cultivations performed at different scales (0.5 and 2.5 L) in a chemically defined medium. Using the same set of parameters and specific initial conditions for each experiment, the model simulations captured the concentration dynamics in the four experiments well. Analysis of the simulated intracellular rates revealed at least two distinct cellular physiological states. The first cellular physiological state was characterized by a high glycolytic rate and high lactate production. Conversely, the second state was characterized by efficient ATP production, a low glycolytic rate, and reactions of the TCA cycle (tricarboxylic acid cycle) running in the reverse direction from alpha-ketoglutarate to citrate. The model was used to predict the impact of changes of media composition and maximum enzyme activity on the intracellular metabolism. Finally, based on the knowledge from this work, options for improving cell growth and measures towards the establishment of a more efficient metabolism were addressed.

The second aim of this work was the establishment of a dynamic mathematical model to describe cell growth, the central carbon metabolism and influenza A virus (IAV) production in suspension Madin-Darby canine kidney (MDCK) cells. This model structure was based on the previously established model for a human designer cell line (AGE1.HN.AAT, first aim of this work) and takes additional aspects related to IAV propagation into account. The model is composed of 35 ODEs that account for cell growth, the concentrations of key metabolites and virus production (virus titer). Most model parameters were estimated using experimental data from a mock-infected cell culture. Using the set of identified parameters and specific initial conditions for each experiment, model simulations accurately captured the overall dynamics of the mock-infected culture and could largely predict the dynamics of cultivations with infected cells. For the first 24 hours post infection (hpi), IAV infection appeared to have a negligible effect on the intracellular metabolism, with most of changes in metabolic rates occurring as a direct result of cell growth arrest, virus-induced apoptosis, cell damage and cell lysis.

A few notable exceptions were the dynamics of glutamate and ammonium release at later infection time points (>24 hpi). Based on the model simulations with a unique set of parameters largely capturing the dynamics of non-infected and infected cells, it was concluded that IAV infection has only a minor impact on central carbon and energy metabolism of MDCK suspension cells. Most metabolic changes could be directly explained by accounting for the cessation of cell growth during virus infection and the subsequent transition to apoptosis and cell death. Additional *in silico* studies were conducted to investigate the cause of the discrepancy between experimental data and model simulations for glutamate and ammonium during late infection phases. The results indicated that the discrepancy could be attributed to the degradation of amino acid by enzymes in the bioreactor induced by cell lysis in the late phase of infection.

Overall, this work showed that cell growth, intracellular metabolism, and extracellular by-product accumulation can be described closely with a relatively simple model (few parameters, <150), when the corresponding experimental data is available. Furthermore, model simulations enabled the identification of unique metabolic states and elucidated the transition between Warburg effect (inefficient glycolysis) and more efficient metabolism (low glycolysis, lactate consumption and active TCA). It was shown that such a model may be used for media design, which is highly desirable in a pharmaceutical industry setting, and provides a solid tool to identify changes in metabolism during virus infection.

This page was intentionally left blank for the online version.

Kurzfassung

Zellkulturverfahren sind eine gut etablierte Plattform für die Erforschung und Herstellung therapeutischer Arzneimittel, wie z.B. rekombinante Proteine und Impfstoffe. Das Zellwachstum und die Herstellung dieser Produkte erfordern optimale Kultivierungsbedingungen (Temperatur, pH-Wert, gelöster Sauerstoff, usw.) und ein gut formuliertes Medium (Substrate oder Energiequellen, Aminosäuren, Vitamine und Mikronährstoffe). Wachsende Zellen können von der Anpassung des Substratverbrauchs und der Produktfreisetzung durch Reaktionen ihres metabolischen Netzwerks (Kombination aller Transmembrantransporter und Enzyme) profitieren. Darüber hinaus werden diese Enzyme durch ausgeklügelte Regulationsmechanismen gesteuert. Die Steigerung des Zellwachstums und der Nebenproduktausbeute erfordert daher ein Verständnis des zellulären Stoffwechsels, insbesondere des zentralen Kohlenstoffstoffwechsels, in dem der größte Teil der Energie und der Vorläuferstoffe produziert wird. Aufgrund des Mangels an experimentellen Daten und der inhärenten Komplexität solcher Systeme wurden bisher nur wenige dynamische mathematische Modelle zur Beschreibung des Zellwachstums und des zentralen Kohlenstoffstoffwechsels entwickelt, insbesondere für tierische Zelllinien. Die meisten Modellierungsansätze konzentrieren sich auf das Zellwachstum und extrazelluläre Metabolite, während einige nur Teile des (intrazellulären) zentralen Kohlenstoffstoffwechsels berücksichtigen, was ihre Anwendbarkeit einschränkt.

Das Hauptziel dieser Arbeit war die Entwicklung quantitativer und dynamischer mechanistischer Modelle, die sowohl das Zellwachstum als auch den zentralen Kohlenstoffstoffwechsel beschreiben, die auf verschiedenen Skalen beobachtet werden, d. h. auf der makroskopischen Skala (Bioreaktor) und der mikroskopischen Skala (zelluläres Zytoplasma, intrazellulär). Für den makroskopischen Maßstab wurde ein segregiertes Zellwachstumsmodell erstellt, das Substrate, Nebenprodukte sowie Zellzahl und -volumen beschreibt. Für die mikroskopische Skala wurde ein strukturiertes Modell des zentralen Kohlenstoffstoffwechsels entwickelt. Beide Modelle wurden gekoppelt, so dass eine direkte Verbindung zwischen Zellwachstum, Substratverbrauch, Freisetzung von Stoffwechselnebenprodukten und dem intrazellulären Zustand hergestellt werden konnte. Der zentrale Kohlenstoffstoffwechsel beschreibt die wichtigsten Metaboliten aus

der Glykolyse, dem Zitronensäurezyklus, der Glutaminolyse, der Transaminierung und dem Pentosephosphatweg.

Das erste Ziel dieser Arbeit war die Entwicklung eines solchen dynamischen mathematischen Modells für die menschliche Designer-Zelllinie AGE1.HN.AAT (zur Verfügung gestellt von ProBioGen AG, Deutschland). Das Modell umfasst 33 gewöhnliche Differentialgleichungen, die das Zellwachstum (Konzentration lebensfähiger Zellen, mittlerer Zelldurchmesser, Volumen lebensfähiger Zellen) und die Konzentration von Schlüsselsubstraten und Metaboliten sowohl auf intrazellulärer als auch auf extrazellulärer Ebene berücksichtigen. Es beschreibt auch die Bildung des Produkts Alpha1-Antitrypsin. Die Gültigkeit des Modells wurde anhand experimenteller Daten von vier unabhängigen Batch-Kulturen in verschiedenen Größenordnungen (0.5 und 2.5 Liter) in einem chemisch definierten Medium bewertet. Unter Verwendung derselben Parameter und spezifischer Anfangsbedingungen für jedes Experiment konnten die Modellsimulationen die Gesamtdynamik aller Experimente gut wiedergeben. Die Analyse der simulierten intrazellulären Raten ergab mindestens zwei unterschiedliche zelluläre physiologische Zustände. Der erste Zustand war durch eine hohe glykolytische Rate und eine hohe Laktatproduktion gekennzeichnet. Im Gegensatz dazu war der zweite Zustand durch eine effiziente ATP-Produktion, eine niedrige glykolytische Rate und Reaktionen des TCA-Zyklus (Tricarbonsäurezyklus) gekennzeichnet, die in umgekehrter Richtung von Alpha-Ketoglutarat zu Citrat ablaufen. Das Modell wurde verwendet, um die Auswirkungen von Änderungen der Medienzusammensetzung und der maximalen Enzymaktivität auf den intrazellulären Stoffwechsel vorherzusagen. Schließlich wurden auf der Grundlage der Erkenntnisse aus dieser Arbeit Möglichkeiten zur Verbesserung des Zellwachstums und Maßnahmen zur Etablierung eines effizienteren Stoffwechsels erörtert.

Das zweite Ziel dieser Arbeit war die Erstellung eines dynamischen mathematischen Modells zur Beschreibung des Zellwachstums, des zentralen Kohlenstoffstoffwechsels und der Influenza-A-Virus (IAV)-Produktion in MDCK-Suspensionszellen. Diese Modellstruktur basiert auf dem zuvor erstellten Modell für eine menschliche Designer-Zelllinie (AGE1.HN.AAT, erstes Ziel dieser Arbeit) und berücksichtigt zusätzliche Aspekte im Zusammenhang mit der IAV-Vermehrung. Das Modell besteht aus 35 gewöhnlichen Difefrentialgleichungen, die das Zellwachstum, die Konzentrationen der wichtigsten

Metaboliten und die Virusproduktion (Virustiter) berücksichtigen. Die meisten Modellparameter wurden anhand von experimentellen Daten aus einer mock-infizierten (nicht infizierten) Zellkultur geschätzt. Unter Verwendung der ermittelten Parameter und der spezifischen Anfangsbedingungen für jedes Experiment konnten die Modellsimulationen die Gesamtdynamik der mock-infizierten Kultur genau erfassen und die Dynamik der Kulturen mit infizierten Zellen weitgehend vorhersagen. In den ersten 24 Stunden schien die IAV-Infektion nur eine vernachlässigbare Auswirkung auf den intrazellulären Stoffwechsel zu haben, wobei die meisten Änderungen der Stoffwechselraten als direkte Folge des Zellwachstumsstopps, der virusinduzierten Apoptose, der Zellschädigung und der Zelllyse auftraten. Einige bemerkenswerte Ausnahmen waren die Dynamik der Glutamat- und Ammoniumfreisetzung zu späteren Infektionszeitpunkten (>24 hpi). Auf der Grundlage der Modellsimulationen mit einzigartigen identifizierten Parametern, welche die Dynamik von nicht infizierten und infizierten Zellen weitgehend erfassen, wurde der Schluss gezogen, dass die IAV-Infektion nur einen geringen Einfluss auf den zentralen Kohlenstoff- und Energiestoffwechsel von MDCK-Suspensionszellen hat. Die meisten metabolischen Veränderungen ließen sich direkt erklären, wenn man die Einstellung des Zellwachstums während der Virusinfektion und den anschließenden Übergang zu Apoptose und Zelltod berücksichtigt. Zusätzliche In-silico-Studien wurden durchgeführt, um die Ursache für die Diskrepanz zwischen experimentellen Daten und Modellsimulationen für Glutamat und Ammonium während der späten Infektionsphasen zu untersuchen. Die Ergebnisse deuteten darauf hin, dass die Diskrepanz auf den Abbau von Aminosäuren durch Enzyme im Bioreaktor zurückzuführen sein könnte, der durch die Zelllyse in der späten Infektionsphase ausgelöst wird.

Insgesamt hat diese Arbeit gezeigt, dass Zellwachstum, intrazellulärer Stoffwechsel und extrazelluläre Nebenproduktakkumulation mit einem relativ einfachen Modell (wenige Parameter, <150) gut beschrieben werden können, wenn die entsprechenden experimentellen Daten verfügbar sind. Darüber hinaus ermöglichen Modellsimulationen die Identifizierung einzigartiger Stoffwechselzustände und klären den Übergang zwischen dem Warburg-Effekt (ineffiziente Glykolyse) und einem effizienteren Stoffwechsel (geringe Glykolyse, Laktatverbrauch und aktive TCA) auf. Ein solches Modell kann für die Entwicklung von Medien verwendet werden, was in der pharmazeutischen Industrie sehr

wünschenswert ist, und bietet ein solides Instrument zur Ermittlung von Veränderungen im Stoffwechsel während einer Virusinfektion.

This page was intentionally left blank for the online version.

Contents

This page was intentionally left blank for the online version.

List of abbreviations

3PG	3-Phosphoglycerate
A1AT	Alpha1-antitrypsin
AAT	Antitrypsin
αKG	a-Ketoglutarate
AA	Amino acid pool
AAex	Exchange between AA and aKG
AcCoA	Acetyl-CoA
Aco	Aconitase
ADK	Adenylate kinase
ADP	Adenosine diphosphate
AGE1.HN.AAT	Human designer cell developed by ProBioGen
AGE1.HN	Human designer cell developed by ProBioGen
Ala	Alanine
ALD	Aldolase
AlaTA	Alanine transaminase
AspTA	Aspartate transaminase
Asp	Aspartate
ATP	Adenosine triphosphate

ATPase	Adenyl pyrophosphatase
ATCC	American type culture collection
BPE	Bioprocess engineering group
CAC	Cis-aconitate
CHO	Chinese hamster ovary
Cit	Citrate
CL	Citrate lyase
CS	Citrate synthase
DNA	Deoxyribonucleic acid
DoE	Design of experiments
DT	Digital twin
EC	Energy charge
ECACC	European collection of cell cultures
cRNA	Complementary RNA (IAV)
ENO	Enolase
F16P	Fructose 1,6-bisphosphate
F6P	Fructose 6-phosphate
FAD	Flavin adenine dinucleotide
FADH2	Reduced flavin adenine dinucleotide

FIM	Fisher information matrix
FMA	Fumarase
Fum	Fumarate
G6P	Glucose 6-phosphate
G6PDH	Glucose 6-phosphate dehydrogenase
GAP	Glyceraldehyde 3-phosphate
GAPDH	Glyceraldehyde phosphate dehydrogenase
GDH	Glutamate dehydrogenase
GDP	Guanosine diphosphate
Glc	Intracellular glucose
Glc^x	Extracellular glucose
GLN	Intracellular glutamine
GLNase	Glutaminase
GLNT	Glutamine transporter
Gln^x	Extracellular glutamine
GLT	Glutamate transporter
Glu	Intracellular glutamate
GLUT	Glucose transporter
Glu^x	Extracellular glutamate

GLYS	Glycogen synthase
GMP	Guanosine monophosphate
GPI	Glucose-6-phosphate isomerase
GS	Glutamine synthase
GTP	Guanosine triphosphate
HA	Hemagglutinin (influenza virus membrane glycoprotein)
HK	Hexokinase
IAV	Influenza A virus
IBV	Influenza B virus
ICV	Influenza C virus
IDV	Influenza D virus
ICDH	Isocitrate dehydrogenase
ICIT	Isocitrate
IMP	Inosine monophosphate
KDH	α-Ketoglutarate dehydrogenase
Keto	Ketoglutarate
LAC	Intracellular lactate
Lac^x	Extracellular lactate
LDH	Lactate dehydrogenase

LOQ	Limit of quantification
M	Arbitrary metabolite
M1	Matrix protein 1 of influenza virus
M2	Matrix protein 2 of influenza virus
MAL	Malate
MDCK	Madin-Darby canine kidney cell line
MDH	Malate dehydrogenase
ME	Malic enzyme
ML	Machine learning
myc	Oncogene
mRNA	Messenger ribonucleic acid
MVDA	Multivariate data analysis
NA	Neuraminidase (IAV)
NAD	Nicotinamide adenine dinucleotide
NADH	Reduced nicotinamide adenine dinucleotide
NADP	Nicotinamide adenine dinucleotide phosphate
NADPH	Reduced nicotinamide adenine dinucleotide phosphate
NEP	Nuclear export protein (IAV)
NH4	Intracellular ammonium

$NH4^x$	Extracellular ammonium
NP	Nucleoprotein (IAV)
OAA	Oxaloacetate
ODE	Ordinary differential equations
p53	Tumor suppressor protein
PA	RNA-dependent RNA-polymerase subunit (IAV)
PB1	RNA-dependent RNA-polymerase subunit (IAV)
PB2	RNA-dependent RNA-polymerase subunit (IAV)
PC	Pyruvate carboxylase
PDH	Pyruvate dehydrogenase
PEP	Phosphoenolpyruvate
PEPCK	Phosphoenolpyruvate carboxykinase
PFK	Phosphofructokinase
PGK	Phosphoglycerate kinase
PK	Pyruvate kinase
PLS	Partial least square
PPP	Pentose phosphate pathway
Pyr	Intracellular pyruvate
Pyr^x	Extracellular pyruvate

PCA	Principal component analysis
R5P	Ribose 5-phosphate
RdRp	RNA-dependent RNA polymerase
RNA	Ribonucleic acid
RNP	Ribonucleoprotein
S	Arbitrary substrate
SDH	Succinate dehydrogenase
Suc	Succinate
SUCCoA	Succinyl-COA
TATK	Transaldolase and transketolase
TCA	Tricarboxylic acid cycle or Krebs cycle or citric acid cycle
TPI	Triosephosphate isomerase
UDPGlc	UDP N-acetylglucosamine
UT	Uridyl transferase
vRNA	Negative-sense RNA (IAV)
vRNP	Viral ribonucleoprotein (IAV)

List of symbols

Symbol	Unit	Description
Θ	-	Unit step function to avoid negative glucose concentrations
ε	-	Unit step function to allow cell growth arrest after infection
$\Phi_{1,..,3}$	-	Exponential step function
$\rho_{1,...,3}$	-	Constant to adjust the exponential step function
ω	-	Constant to adjust ammonium release from amino acid degradation
μ_{max}	1/min	Maximum cell-specific growth rate
μ	1/min	Cell-specific growth rate
α	-	Constant adjusting inhibition factor
β	1/min	Switch constant for cell death rate
$\overline{d}$	µm	Mean cell diameter
b_{NAD}	-	Adjustable parameter for influence of NAD/NADH
c	cells/mL or mmol/L	Concentration of an arbitrary state variable
$c_{k,f}$		Concentration of c in the feed stream
d_c	µm	Critical cell diameter
d_m	µm	Minimum cell diameter
E_{level}	-	Relative enzyme level
f	-	Growth inhibition factor

Symbol	Unit	Description
F_k	L	Volume of a feed stream
N^c	-	Number of cell classes
$v_e^{\max}$	L/cell/min	Cell number-specific activity of enzyme e
$v_{Glu_{trans}^x}$	mmol/L/µL/min	Cell volume-specific transport rate of Glu
$v_{HK}^{\max}$	mmol/cell/min	Cell number-specific maximum activity of HK
$v_{GPI}^{\max}$	mmol/cell/min	Cell number-specific maximum activity of GPI
$v_{G6PDH}^{\max}$	mmol/cell/min	Cell number-specific maximum activity of G6PDH
$v_{Lac_{trans}^x}$	mmol/L/µL/min	Cell volume-specific transport rate of Lac
$v_{\mathrm{Gln}_{trans}^x}$	mmol/L/µL/min	Cell volume-specific transport rate of Gln
$v_{\mathrm{NH4}_{trans}^x}$	mmol/L/µL/min	Cell volume-specific transport rate of NH4
$v_{dR5P}^{\max}$	mmol/cell/min	Cell number-specific maximum activity of R5P
$v_{UT}^{\max}$	mmol/cell/min	Cell number-specific maximum activity of UT
$v_{GLYS}^{\max}$	mmol/cell/min	Cell number-specific maximum activity of GLYS
$v_{PFK}^{\max}$	mmol/cell/min	Cell number-specific maximum activity of PFK
$v_{TATKF6P}^{\max}$	mmol/cell/min	Cell number-specific maximum activity of TATKF6P
$v_{TATK3PG}^{\max}$	mmol/cell/min	Cell number-specific maximum activity of TATK3GP

Symbol	Unit	Description
$v_{ALD}^{\max}$	mmol/cell/min	Cell number-specific maximum activity of ALD
$v_{Pyr_{trans}^{x}}$	mmol/L/µL/min	Cell volume-specific transport rate of Pyr
$v_{ENO}^{\max}$	mmol/cell/min	Cell number-specific maximum activity of ENO
$v_{PK}^{\max}$	mmol/cell/min	Cell number-specific maximum activity of PK
$v_{AlaTA}^{\max}$	mmol/cell/min	Cell number-specific maximum activity of AlaTA
$v_{AspTA}^{\max}$	mmol/cell/min	Cell number-specific maximum activity of AspTA
$v_{LDH}^{\max}$	mmol/cell/min	Cell number-specific maximum activity of LDH
$v_{ACO}^{\max}$	mmol/cell/min	Cell number-specific maximum activity of PDH
$v_{CL}^{\max}$	mmol/cell/min	Cell number-specific maximum activity of ACO
$v_{ICDH}^{\max}$	mmol/cell/min	Cell number-specific maximum activity of CL
$v_{GS}^{\max}$	mmol/cell/min	Cell number-specific maximum activity of ICDH
$v_{KDH}^{\max}$	mmol/cell/min	Cell number-specific maximum activity of GS
$v_{SDH}^{\max}$	mmol/cell/min	Cell number-specific maximum activity of SDH
$v_{FMA}^{\max}$	mmol/cell/min	Cell number-specific maximum activity of FMA
$v_{MDH}^{\max}$	mmol/cell/min	Cell number-specific maximum activity of MDH
$v_{ATPase}^{\max}$	mmol/cell/min	Cell number-specific maximum activity of ATPase
$v_{AAex}^{\max}$	mmol/cell/min	Cell number-specific maximum activity of AAex
$v_{cUGLC}^{\max}$	mmol/cell/min	Cell number-specific maximum activity of UGLC

Symbol	Unit	Description
$v_{CS}^{\max}$	mmol/cell/min	Cell number-specific maximum activity of CS
$v_{ME}^{\max}$	mmol/cell/min	Cell number-specific maximum activity of ME
$v_{PEPCK}^{\max}$	mmol/cell/min	Cell number-specific maximum activity of PECK
$v_{PC}^{\max}$	mmol/cell/min	Cell number-specific maximum activity of PC
$v_{GLDH}^{\max}$	mmol/cell/min	Cell number-specific maximum activity of GLDH
$v_{GLNase}^{\max}$	mmol/cell/min	Cell number-specific maximum activity of GLNase
$v_{d\mathrm{NH4}}$	mmol/cell/min	Cell number-specific maximum activity of NH4 degradation
k_{HK}^{m}	mmol/L	Affinity constant of HK
k_{GPI}^{m}	mmol/L	Affinity constant of GPI
k_{GPI}^{eq}	-	Equilibrium constant of GPI
k_{G6PDH}^{m}	mmol/L	Affinity constant of G6PDH
k_{UT}^{m}	mmol/L	Affinity constant of UT
$k_{TATKF6P}^{eq}$	-	Equilibrium constant of TATKF6P
$k_{TATK3PG}^{eq}$	-	Equilibrium constant of TATK3PG
k_{PFK}^{m}	mmol/L	Affinity constant of PFK
k_{F16P}	mmol/L	Affinity constant of ALD for F16P
k_{ENO}^{eq}	-	Equilibrium constant of ENO
$k_{PEP_{PK}}$	mmol/L	Affinity constant of PK for PEP

Symbol	Unit	Description
$k^{eq}_{ENO_{PEP}}$	-	Equilibrium constant of ENO for PEP
k^{m}_{PK}	mmol/L	Affinity constant of PK
k^{m}_{LDH}	mmol/L	Affinity constant of LDH
k^{iPYR}_{LDH}	$mmol^2/L^2$	Inhibition constant of LDH from Pyr
k^{m}_{Pyr}	mmol/L	Affinity constant of PDH to Pyr
$k_{Pyr_{PK}}$	mmol/L	Affinity constant of PK for Pyr
$k_{Pyr_{PDH}}$	mmol/L	Affinity constant of PDH for Pyr
k^{eq}_{ACO}	-	Equilibrium constant of ACO
k^{eq}_{ACO2}	-	Equilibrium constant of ACO
k^{m}_{Cit}	mmol/L	Affinity constant of CL for Cit
k^{CL}_{m}	mmol/L	Affinity constant of CL
k^{eq}_{ICDH}	-	Equilibrium constant of ICDH
k^{m}_{ICDH}	mmol/L	Affinity constant of ICDH
k^{eq}_{AAex}	-	Equilibrium constant of AAex
k^{eq}_{SDH}	mmol/L	Equilibrium constant of SDH
k^{m}_{MDH}	mmol/L	Affinity constant of MDH
k^{eq}_{FMA}	-	Equilibrium constant of FMA
k^{m}_{FMA}	mmol/L	Affinity constant of FMA

Symbol	Unit	Description
k^{m}_{MDH}	mmol/L	Affinity constant of MDH
k_{xATP}	cell/L/min	Specific ATP consumption related to growth
k_{mATP}	cell/L/min	Specific ATP consumption related to maintenance
NAD_{basal}	mmol/L	Adjustable parameter for influence of NAD/NADH
k^{m}_{cUGLC}	mmol/L	Affinity constant of a general enzyme to UDPGlc
κ^{m}_{CS}	mmol/L	Affinity constant of CS
k^{m}_{ME}	mmol/L	Affinity constant of ME
k^{i}_{ATP}	$mmol^2/L^2$	Inhibition constant of ME from ATP
k^{eq}_{UT}	mmol/L	Equilibrium constant of UT
k^{i}_{μ}	mmol/L	Inhibition constant of ALD
κ^{m}_{GS}	mmol/L	Affinity constant of GS
$k^{i}_{ATP_{ME}}$	$mmol^2/L^2$	Inhibition constant of ME from ATP
k^{i}_{μ}	mmol/L	Growth related inhibition constant of ALD
$k^{m}_{Glu_{GS}}$	mmol/L	Affinity constant of GS for Glu
k^{m}_{ICDH}	mmol/L	Affinity constant of ICDH

Symbol	Unit	Description
k^{m}_{OAA}	mmol/L	Affinity constant of CS for OAA
k^{m}_{AcCoA}	mmol/L	Affinity constant of CS for AcCoA
k^{m}_{SDH}	mmol/L	Affinity constant of SDH
k^{i}_{SDH}	mmol/L	Inhibition constant of SDH
k^{m}_{dR5P}	mmol/L	Affinity constant of a general enzyme to R5P
k^{m}_{PEPCK}	mmol/L	Affinity constant of PEPCK
k^{i}_{AcCoA}	mmol/L	Inhibition constant of PC
$k^{m}_{Pyr_{PC}}$	mmol/L	Affinity constant of PC for Pyr
k^{eq}_{ME}	-	Equilibrium constant of ME
k^{m}_{KDH}	mmol/L	Affinity constant of KDH
k^{m}_{AlaTA}	mmol/L	Affinity constant of AlaTA
$k^{eq}_{AspTA_{OAA}}$	mmol/L	Equilibrium constant of AspTA of OAA
$k^{eq}_{AspTA_{Glu}}$	mmol/L	Equilibrium constant of AspTA of Glu
k_{keto}	mmol/L	Equilibrium constant of AspTA to Keto
$k_{OAA_{AspTA}}$	mmol/L	Affinity constant of AspTA for OAA

Symbol	Unit	Description
$k_{Glu_{AspTA}}$	mmol/L	Affinity constant of AspTA for Glu
$k_{Keto_{AspTA}}$	mmol/L	Affinity constant of AspTA for Keto
$k_{Glu_{GLDH}}$	mmol/L	Affinity constant of LDH for Glu
k^{m}_{Glnase}	mmol/L	Affinity constant of GLNase
k^{eq}_{GLDH}	-	Equilibrium constant of GLDH
k^{i}_{GLDH}	mmol/L	Inhibition constant of GLDH
k^{eq}_{ALD}	-	Equilibrium constant of ALD
k^{a}_{PFK}	mmol/L	Activation constant of PFK
k^{i}_{G6P}	$mmol^2/L^2$	Inhibition constant of HK
k^{m}_{ATPase}	mmol/L	Affinity constant of ATPase
k_{3PG}	mmol/L	Affinity constant of ENO for 3PG
$k_{PEP_{ENO}}$	mmol/L	Affinity constant of ENO for PEP
$k^{eq}_{ENO_{3PG}}$	-	Equilibrium constant of ENO for 3PG
$k^{m}_{TATK3PG}$	mmol/L	Affinity constant of TATK3PG
$k^{m}_{TATKF6P}$	mmol/L	Affinity constant of TATKF6P

Symbol	Unit	Description
k^{m}_{GLDH}	mmol/L	Affinity constant of GLDH
$k^{m}_{ATP_{HK}}$	mmol/L	Affinity constant of HK for ATP
$k^{m}_{ATP_{ALD}}$	mmol/L	Affinity constant of ALD for ATP
$k^{m}_{3PG_{ALD}}$	mmol/L	Affinity constant of ALD for 3PG
k^{eq}_{ALD}	-	Affinity constant of ALD
$k^{m}_{ATP_{PC}}$	mmol/L	Affinity constant of PC for ATP
$k^{m}_{ATP_{PDH}}$	mmol/L	Affinity constant of PDH for ATP
$k_{Glu^{x}}$	mmol/L	Direct binding affinity constant for extracellular Glu
k_{Glu}	mmol/L	Direct binding affinity constant for Glu transporter
$k^{eq}_{Glu^{x}_{trans}}$	-	Direct biding equilibrium constant for Glu transporter
$k_{G\ln^{x}}$	mmol/L	Direct binding (simplified) affinity constant for extracellular Gln
$k^{m}_{Pyr^{x}_{trans}}$	mmol/L	Affinity constant of extracellular Pyr transporter
k_{pyr}	mmol/L	Inhibition constant of Pyr transporter
k^{m}_{AspTA}	mmol/L	Affinity constant of AspTA
$k^{m}_{ATP_{GS}}$	mmol/L	Affinity constant of GS for ATP

Symbol	Unit	Description
$k^{i}_{ATP_{Glnase}}$	$mmol^2/L^2$	Inhibition constant of GLNase from ATP
$k^{i}_{OAA_{SDH}}$	$mmol^2/L^2$	Inhibition constant of SDH from ATP
k^{m}_{GLYS}	mmol/L	Affinity constant of GLYS
$k^{m}_{ATP_{CL}}$	mmol/L	Affinity constant of CL for ATP
$k^{eq}_{Lac^{x}_{trans}}$	-	Equilibrium constant of transporter for Lac
$k^{m}_{mLac^{x}}$	mmol/L	Affinity constant of transporter to Lac^x
$k_{Lac_{trans}}$	mmol/L	Affinity constant of transporter for Lac
$k_{Lac^{x}_{trans}}$	mmol/L	Affinity constant of transporter for extracellular Lac
$k_{Pyr_{LDH}}$	mmol/L	Affinity constant of LDH for Pyr
$k_{Lac_{LDH}}$	mmol/L	Affinity constant of LDH for Lac
k^{iATP}_{LDH}	$mmol^2/L^2$	Inhibition constant of LDH from ATP
k_{cPyr}	$mmol^2/L^2$	Activation constant of LDH from Pyr
k^{a}_{PyrLDH}	-	Activation constant of LDH from Pyr
$k_{Glu_{LDH}}$	$mmol^2/L^2$	Inhibition constant of LDH from Glu
$k^{i}_{Glu_{LDH}}$	-	Inhibition constant of LDH from Glu
Symbol	**Unit**	**Description**

k_{LDH}^{eq}	-	Equilibrium constant of LDH
k_{dNH4}^{m}	mmol/L	Affinity constant of general enzyme for NH4
$k_{ATP_{dNH4}}^{a}$	mmol/L	activation constant of NH4 degradation from ATP
k_{NH4^x}	mmol/L	Direct binding affinity constant for NH_4 transporter
$k_{NH4_{trans}^x}^{eq}$	-	Direct biding equilibrium constant of NH_4 transporter
k_{NH4}	mmol/L	Direct binding affinity constant for NH_4 transporter
k_{AlaTA}^{m}	mmol/L	Affinity constant of AlaTA
$k_{Glu_{AlaTA}}^{i}$	$mmol^2/L^2$	Inhibition constant of AlaTA from Glu
$k_{Glc_{AlaTA}}^{i}$	mmol/L	Inhibition constant of AlaTA from Glc
$k_{ATP_{AlaTA}}^{i}$	mmol/L	Inhibition constant of AlaTA from ATP
$k_{Glc^x}^{m}$	mmol/L	Monod constant for extracellular Glc
$k_d^{\min}$	1/min	Basal cell death rate
$k_d^{\max}$	1/min	Maximum cell death rate
$k_d^{\min \inf}$	1/min	Basal cell death rate of infected cells
$k_d^{\max \inf}$	1/min	Maximum cell death rate of infected cells
k_{dGln^x}	1/min	Spontaneous glutamine degradation rate
m_{Glc^x}	mmol/L/µL/min	Maintenance related glucose consumption rate
$K_e^{\max}$	mmol/L/min	Cell volume-specific reaction rate of enzyme e
Symbol	**Unit**	**Description**

$K_{HK}^{\max}$	mmol/L/min	Cell volume-specific reaction rate of enzyme HK
$K_{GPI}^{\max}$	mmol/L/min	Cell volume-specific reaction rate of enzyme GPI
$K_{G6PDH}^{\max}$	mmol/L/min	Cell volume-specific reaction rate of enzyme G6PDH
$K_{dR5P}^{\max}$	mmol/L/min	Cell volume-specific reaction rate of general enzyme of R5P degradation
$K_{UT}^{\max}$	mmol/L/min	Cell volume-specific reaction rate of enzyme UT
$K_{GLYS}^{\max}$	mmol/L/min	Cell volume-specific reaction rate of enzyme GLYS
$K_{PFK}^{\max}$	mmol/L/min	Cell volume-specific reaction rate of enzyme PFK
$K_{TATKF6P}^{\max}$	mmol/L/min	Cell volume-specific reaction rate of transaldolase and transketolase for F6P
$K_{TATK3PG}^{\max}$	mmol/L/min	Cell volume-specific reaction rate of transaldolase and transketolase for 3PG
$K_{ALD}^{\max}$	mmol/L/min	Cell volume-specific reaction rate of enzyme ALD
$K_{ENO}^{\max}$	mmol/L/min	Cell volume-specific reaction rate of enzyme ENO
$K_{PK}^{\max}$	mmol/L/min	Cell volume-specific reaction rate of enzyme PK
$K_{LDH}^{\max}$	mmol/L/min	Cell volume-specific reaction rate of enzyme LDH
$K_{PDH}^{\max}$	mmol/L/min	Cell volume-specific reaction rate of enzyme PDH
$K_{d\mathrm{NH4}}^{\max}$	mmol/L/min	Cell volume-specific reaction rate of general enzyme for NH4 degradation
Symbol	**Unit**	**Description**

Symbol	Unit	Description
$K_{ACO}^{\max}$	mmol/L/min	Cell volume-specific reaction rate of enzyme ACO
$K_{CL}^{\max}$	mmol/L/min	Cell volume-specific reaction rate of enzyme CL
$K_{ICDH}^{\max}$	mmol/L/min	Cell volume-specific reaction rate of enzyme ICDH
$K_{GS}^{\max}$	mmol/L/min	Cell volume-specific reaction rate of enzyme GS
$K_{KDH}^{\max}$	mmol/L/min	Cell volume-specific reaction rate of enzyme KDH
$K_{SDH}^{\max}$	mmol/L/min	Cell volume-specific reaction rate of enzyme SDH
$K_{FMA}^{\max}$	mmol/L/min	Cell volume-specific reaction rate of enzyme FMA
$K_{MDH}^{\max}$	mmol/L/min	Cell volume-specific reaction rate of enzyme MDH
$K_{ATPase}^{\max}$	mmol/L/min	Cell volume-specific reaction rate of enzyme ATPase
$K_{AAex}^{\max}$	mmol/L/min	Cell volume-specific reaction rate of enzyme AAex
$K_{cUGLC}^{\max}$	mmol/L/min	Cell volume-specific reaction rate of enzyme UGLC
$K_{CS}^{\max}$	mmol/L/min	Cell volume-specific reaction rate of enzyme CS
$K_{ME}^{\max}$	mmol/L/min	Cell volume-specific reaction rate of enzyme ME
$K_{PEPCK}^{\max}$	mmol/L/min	Cell volume-specific reaction rate of enzyme PEPCK
$K_{PC}^{\max}$	mmol/L/min	Cell volume-specific reaction rate of enzyme PC

K_{AlaTA}^{max}	mmol/L/min	Cell volume-specific reaction rate of enzyme AlaTA
K_{AspTA}^{max}	mmol/L/min	Cell volume-specific reaction rate of enzyme AspTA
K_{GLDH}^{max}	mmol/L/min	Cell volume-specific reaction rate of enzyme GLDH
K_{GLNase}^{max}	mmol/L/min	Cell volume-specific reaction rate of enzyme GLNase
m_{Glc^x}	mmol/L/µL/min	Cell volume-specific uptake rate of Glc for maintenance
MOI	virions/cell	Multiplicity of infection
NAD_{basal}	-	Adjustable parameter for influence of NAD/NADH
$\mathcal{N}^c$	-	Number of cell classes
PPP_{basal}	mmol/L	Basal concentration of PPP metabolites
q_{AAT}	mg/cell	Cell specific product formation rate
r_i	mmol/L/min	Cell specific activity of enzyme i
r_{macro}	-	Formula for conversion of macroscopic scale rates to microscopic scale
r_{HK}	mmol/L/min	Cell volume-specific reaction rate of HK
r_{GPI}	mmol/L/min	Cell volume-specific reaction rate of GPI
r_{G6PDH}	mmol/L/min	Cell volume-specific reaction rate of G6PDH
Symbol	**Unit**	**Description**

r_{dR5P}	mmol/L/min	Cell volume-specific reaction rate of R5P degradation
r_{dNH4}	mmol/L/min	Cell volume-specific reaction rate of NH4 degradation
r_{UT}	mmol/L/min	Cell volume-specific reaction rate of UT
r_{GLYS}	mmol/L/min	Cell volume-specific reaction rate of GLYS
r_{PFK}	mmol/L/min	Cell volume-specific reaction rate of PFK
$r_{TATKF6P}$	mmol/L/min	Cell volume-specific reaction rate of TATKF6P
$r_{TATK3PG}$	mmol/L/min	Cell volume-specific reaction rate of TATK3PG
r_{ALD}	mmol/L/min	Cell volume-specific reaction rate of ALD
r_{ENO}	mmol/L/min	Cell volume-specific reaction rate of ENO
r_{PK}	mmol/L/min	Cell volume-specific reaction rate of PK
r_{LDH}	mmol/L/min	Cell volume-specific reaction rate of LDH
r_{PDH}	mmol/L/min	Cell volume-specific reaction rate of PDH
r_{ACO}	mmol/L/min	Cell volume-specific reaction rate of ACO
r_{CL}	mmol/L/min	Cell volume-specific reaction rate of CL
r_{ICDH}	mmol/L/min	Cell volume-specific reaction rate of ICDH
Symbol	**Unit**	**Description**

r_{GS}	mmol/L/min	Cell volume-specific reaction rate of GS
r_{KDH}	mmol/L/min	Cell volume-specific reaction rate of KDH
r_{SDH}	mmol/L/min	Cell volume-specific reaction rate of SDH
r_{FMA}	mmol/L/min	Cell volume-specific reaction rate of FMA
r_{MDH}	mmol/L/min	Cell volume-specific reaction rate of MDH
r_{ATPase}	mmol/L/min	Cell volume-specific reaction rate of ATPase
r_{AAex}	mmol/L/min	Cell volume-specific reaction rate of AAex
r_{cUGLC}	mmol/L/min	Cell volume-specific reaction rate of UGLC
r_{CS}	mmol/L/min	Cell volume-specific reaction rate of CS
r_{ME}	mmol/L/min	Cell volume-specific reaction rate of ME
r_{PEPCK}	mmol/L/min	Cell volume-specific reaction rate of PEPCK
r_{PC}	mmol/L/min	Cell volume-specific reaction rate of PC
r_{AlaTA}	mmol/L/min	Cell volume-specific reaction rate of AlaTA
r_{AspTA}	mmol/L/min	Cell volume-specific reaction rate of AspTA
r_{GLDH}	mmol/L/min	Cell volume-specific reaction rate of GLDH
Symbol	**Unit**	**Description**

r_{GLNase}	mmol/L/min	Cell volume-specific reaction rate of GLNase
$r_{Lac^x_{trans}}$	mmol/L/min	Medium volume-specific transport rate of Lac
$r_{NH4^x_{trans}}$	mmol/L/min	Medium volume-specific transport rate of NH4
$r_{Gln^x_{trans}}$	mmol/L/min	Medium volume-specific transport rate of Gln
$r_{Glu^x_{trans}}$	mmol/L/min	Medium volume-specific transport rate of Glu
$r_{Pyr^x_{trans}}$	mmol/L/min	Medium volume-specific transport rate of Pyr
r_{trans}	1/min	Specific transition rate
r_{m/Glc^x}	mmol/L/min	Medium volume-specific uptake rate of Glc for maintenance
r_{x/Glc^x}	mmol/L/min	Medium volume-specific uptake rate of Glc for growth
r_{GLUT}	mmol/L/min	Cell volume-specific transport rate of Glc
r_{xATP}	mmol/L/min	Cell volume-specific ATP consumption rate of cell growth
r_{mATP}	mmol/L/min	Cell volume-specific ATP consumption rate of cell maintenance
r_{ATPase}	mmol/L/min	Cell volume-specific rate of ATPase
r_{dATP}	mmol/L/min	Net ATP consumption rate
r_{CCM}	mmol/L/min	Net ATP production rate
Symbol	**Unit**	**Description**

r_{NADH}	mmol/L/min	Net ATP production from NADH
r_{FADH}	mmol/L/min	Net ATP production from FADH
r_{TCA}	mmol/L/min	Net ATP production from TCA
$r_{glycolysis}$	mmol/L/min	Net ATP production from glycolysis
r_{O2}	fmol/cell/min	Theoretical O2 consumption rate
$r_{k(c)}$	1/min or mmol/L/min	Rate of consumption/production of *c*
S_k	L	Sample volume
V	L	Reactor volume
V^c	µL/mL	Viable cell volume
V_s^c	L/cell	Cell-specific volume
V_w	-	Working volume
X_i	cells/mL	Number of viable cells of class i
X_v	cells/mL	Viable cell concentration
Y_{x/Glc^x}	mmol/L/cell	Cell growth-specific yield coefficient of Glc

1 Chapter Introduction

Cell culture processes were developed throughout the 20th century and are currently a well-established platform for the research and manufacture of therapeutic biologicals such as recombinant proteins, nucleic acids, live cells, and vaccines. These processes require cell lines with specific characteristics, which are generated through careful clone development, selection, and genetic engineering. Bacteria, yeast and animal cells, such as mammalian cells and insect cells, are commonly used in bioprocesses to produce therapeutic biologicals. These processes vary in scale and complexity, and are characterized by the coupling of upstream and downstream processes. The latter focuses on product recovery, purification, and subsequent product formulation. Upstream processes essentially rely on efficient cell growth in a defined environment and the production of products such as viruses, viral vectors, antibodies, and insulin, among others. Typically, in biopharmaceutical production, careful process optimization and design are required for both upstream and downstream processes to keep the cost per dose of the final product low. In addition, it is necessary to guarantee product quality, safety, and efficacy to conform to the guidelines of regulatory authorities. For process optimization, detailed knowledge about the impact of parameters such as temperature, pH value, dissolved oxygen, and carbon dioxide concentration on cell growth and product formation is required. The optimization of these parameters is crucial for each cell line as specific characteristics can be scale-dependent and vary for every cell line [1]. Optimization of basal medium and feed compositions are other important aspects. The formulated medium contains a supply of energy sources, amino acids, vitamins, and micro-nutrients which are required to grow and produce the product of interest. These substances are appropriately utilized by the cell via the reactions/transport to generate

energy, growth precursors, the desired product and other by-products. Specifically, the latter consists of enzymatic reactions that convert one metabolite to another and transmembrane transport. The enzymes and transmembrane transporters are proteins that intervene in all biological reactions and transport, respectively. These proteins are coded in genes that constitute the genome of each cell. Fig. 1.1 summarizes the different layers between the cell genome and metabolism. Gene transcription is the process of copying genes from DNA to mRNA. Translation is the usage of the information of mRNA to make proteins (enzymes and transporters). Substantial efforts have been made to annotate genomes of over 6000 organisms including the well-studied *Escherichia coli*, *Mus musculus*, *Pichia pastoris*, *Saccharomyces cerevisiae* and *Homo sapiens* [1]. These efforts eventually translate into detailed knowledge about the proteins and consequently the set of possible enzymes or transporters within a cell. The combined reactions/transport that can be utilized by a cell is defined as its genome-scale metabolic network (GEM).

The rate of energy and cell growth precursors formation in the metabolic network are determined by the resulting network property and are controlled using sophisticated regulation mechanisms. Substantial research efforts have been dedicated to understanding the fundamental principles of the underlying metabolic regulation mechanism of individual reactions *in vitro*. This includes studies covering multiple omics (genome (genomics), transcription (transcriptomics), protein (proteomics) and metabolites (metabolomics)). The study of genomics and metabolomics led to the uncovering of detailed enzyme kinetic mechanisms, including their dependency on the substrate, products and cofactors. However, *in vivo* mechanisms are largely hypothetical due to differential regulation in a more complex system where many principles such as allosteric effects, activation or inhibition may differ significantly. In order to improve our understanding of the cells, several mathematical approaches have been established, with varying degrees of complexity to describe biological data using enzyme kinetics [2]. The resulting increase in knowledge of cell metabolism played a crucial role in the development of genetic engineering and optimization of bioprocesses. In turn, advancements and refinements in bioprocess understanding have enabled the production of several highly valuable biological products at large scales. In addition to recombinant protein production, other critical biological products include inactivated

viruses and viral proteins used for vaccines. Vaccines play a vital role in public health, particularly during seasonal epidemics and global pandemics.

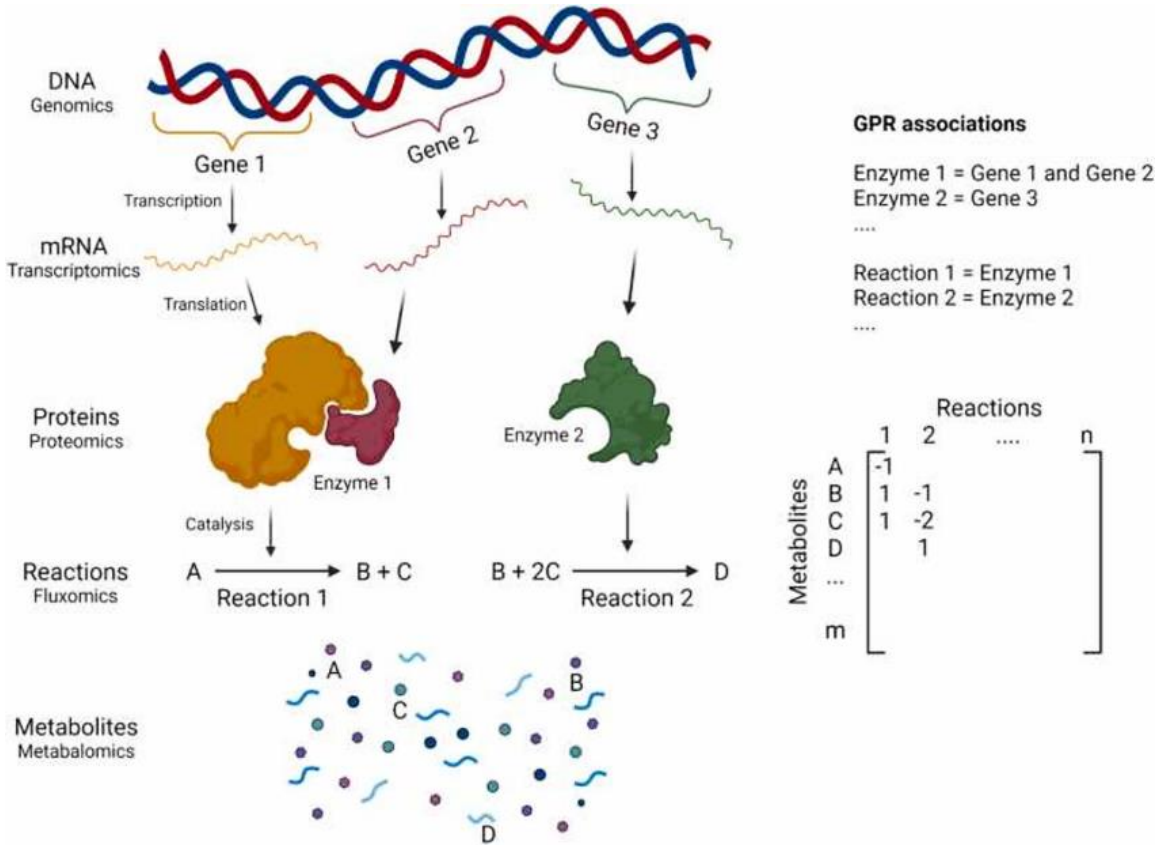

Figure 1.1.: Different layers of omics used for genome-scale model reconstruction. GPR is the Gene-Protein-Reaction association. Figure elements taken from Strain et al., 2023 [1] under CC4.0.

Seasonal influenza epidemics and global pandemics can have a significant economic impact on societies and result in a very high death toll. It is only due to the availability of vaccines and antivirals that more severe consequences can be averted, as seen in the recent COVID-19 outbreak. However, most influenza vaccines are still produced in embryonated hens' eggs. To overcome certain disadvantages of this production system and to meet rising demands, various cell culture-derived vaccine manufacturing processes have been established [3,4]. Typically, continuous cell lines are cultivated and infected with IAV near the end of the exponential cell growth phase with a low multiplicity of infection (moi). The virus replicates intracellularly after entering the cells, and the first

virions are released approximately 4–6 hours post infection (hpi). The virus yield in cell cultures is influenced by a variety of factors including the cell substrate used, the cell concentration at time of infection, moi, medium composition and pH value [3]. In comparison to other cell culture-based processes, most notably large-scale recombinant protein production with bioreactor harvests in the gram per liter range, typical virus yields are rather low. Due to the complexity of virus-host cell interaction, numerous explanations and hypotheses exist regarding these low cell-specific virus yields. These include the interferon-mediated antiviral response, a high rate of cell death as a result of virus-induced apoptosis and rapid cell degradation [5–14] as well as numerous host cell factors [15,16]. Recently, it was demonstrated that by combining model-based analysis with experimental data collected on genetically engineered cells, it is possible to investigate the effect of selected host cell factors on individual virus replication steps and to predict measures to increase virus yields [17]. So far, many studies performed to improve virus production processes focused on cell metabolism since the synthesis of viral components requires precursors and energy from the host cell. The majority of modeling approaches have focused on estimation of cellular resources required for virus production [18] or on metabolic flux analysis [19–21], and only few attempts have been made to incorporate aspects of virus replication. Quantitative changes in extracellular metabolite concentrations observed during the progression of infection for several viruses, including IAV, included changes in glucose consumption, lactate production and ammonium release, among other effects [22–26]. These changes have been primarily attributed to cell growth arrest, virus-induced apoptosis, breakdown of intracellular carbon and energy metabolism, and cell damage [22,26]. While some viruses appear to induce changes in aerobic glycolysis, many viruses also seem to stimulate fatty acid synthesis or influence amino acid metabolism, i.e. glutaminolysis – possible to meet specific virus replication requirements [27]. Nevertheless, the cumulative effect of these changes on virus yields is still poorly understood. Additionally, it is largely unclear whether the metabolic changes observed during virus production in cell culture are caused directly by virus-specific mechanisms or are influenced indirectly by the transition of infected cells to apoptosis and cell lysis. Even for cultivations infected with low moi of IAV, changes are observed as early as 6–8 hpi. These changes include a rapid decrease in viable cell concentration and a decrease in the average cell-specific volume, as well as changes in substrate consumption, metabolic by-product release, and in cell death rate. Quantitative studies

on the impact of virus infections on cell growth and metabolism require comprehensive sets of experimental data, ideally collected for both infected and mock-infected cells. This includes viable cell counts, cell size and viability, extracellular substrates and metabolic by-products, and, ideally, intracellular metabolite concentrations and enzyme activity measurements. The establishment of dynamic mechanistic models is crucial for evaluating such complex and high-dimensional data [28]. However large quantitative and dynamical models that describe both cell growth and intracellular metabolism are still largely missing. These limitations can be attributed to the complexity of eukaryotic cells, scarcity of experimental data, and computational limitations. A particular challenge is the complexity of the metabolism of animal cells, which arises from the multitude of regulatory mechanisms as well as the high number of substrates taken up and by-products released. The lack of experimental data can be attributed to the laborious process of data collection and the lack of uniform quantification methods established to measure intracellular metabolite concentrations and enzyme activities; quenching of metabolism and sampling are also challenging. Finally, the establishment of dynamic models can also be hampered by the availability of computational resources and limitations of algorithms required to estimate the large number of often poorly defined parameters.

The first aim of this project was the development of a mechanistic dynamic mathematical model that links cell growth, extra– and intracellular metabolism. This resulted in a set of 33 ODEs that combines a segregated cell growth model with a structured model of intracellular metabolism. It describes concomitantly viable cell concentration, mean cell diameter, viable cell volume, concentration of extracellular substrates, product of interest (alpha-1 antitrypsin) concentration, and intracellular concentrations of key metabolites from the central carbon metabolism. The model parameters were optimized using one batch experiment and the model was tested using three separate batch cultivations.

The second aim of this project was the extension of this mechanistic dynamic mathematical model to describe cell growth, extra– and intracellular metabolism in infected and non-infected cells. This resulted in a set of 35 ODEs that describes concomitantly viable cell concentration, mean cell diameter, viable cell volume, Influenza A virus (IAV) titer, concentration of extracellular substrates, and intracellular concentrations of key metabolites from the central carbon metabolism. The model

parameters were optimized using one shaker-flask cell growth experiment and the model was used to predict another shaker-flask experiment wherein the cells were infected.

Overall, this work will contribute to a better understanding of the complex interplay between cell growth, changes in cell size, virus production and metabolism and support the identification of parameters relevant for increasing cell-specific growth rate, recombinant protein production and viral productivity in mammalian cells.

2 Chapter
Background and theory

Bioprocess engineering uses organisms and biochemical systems to produce many biopharmaceuticals such as monoclonal antibodies, growth hormones, therapeutic enzymes among others. Animal cells play a crucial role as they are frequently used for production of biopharmaceuticals. Compared to other types of cells, animal cells have several advantages, such as the capacity to synthesize complex proteins and perform distinct modifications such as folding and glycosylation patterns. Furthermore, animal cells are amenable to genetic modification, which enhances their manufacturing capabilities. The cell lines used are continuous cell lines, obtained through several passages and immortalization of primary cells. Typically, primary cells are obtained from tissue samples and retain tissue-specific characteristics and have limited lifespan. The continuous cells are termed as adherent cell lines if they grow as monolayers attached to a surface or suspension cell lines if the growth in a liquid media.

In the context of bioprocesses and continuous animal cell lines, decades of research have revealed the sophisticated and diverse facets of metabolism. One of the hallmarks of continuously growing cells is the metabolization of glucose into large amounts of lactate under aerobic conditions, also known as the Warburg effect [29]. This is still used nowadays as a marker in cancer diagnosis. The Warburg effect is coupled with an impaired mitochondrial respiration, even though the latter would allow a more efficient energy production. Various metabolic factors have been identified as sources contributing to this phenomenon but no universal explanation has been found. This can be attributed to the overall complexity of animal cells. This arises from the multitude of regulatory mechanisms as well as the high number of enzymes and transporters that make up the cell metabolic network. Furthermore, metabolic characteristics have been found to

change according to the cell type, cell physiological state and cultivation conditions [29–31]. Study of animal cells is also significantly impacted by lack of experimental data. Data collection is a laborious process and there is a lack of uniform quantification methods established (for the determination of the concentration of the multitude of metabolites and enzyme activities). Overall, it is reasonable to affirm that research of animal cell growth and metabolism is imperative, with many questions still to be answered.

Several continuous cell lines such as CHO cells and MDCK cells are used and are widely investigated for production of biopharmaceuticals such as recombinant proteins and viruses for vaccines (e.g. IAV vaccines). The main advantage of these continuous cell lines over primary cells resided on their longer life span and their ability to divide indefinitely *in vitro* obtained via spontaneous or directed immortalization. The next sections summarize the characteristics of the two cell lines which were used in this work, along with an introduction to recombinant protein production and influenza virology. General concepts of cellular growth and metabolism, mathematical modeling and optimization of bioprocess are also briefly described.

2.1 AGE1.HN.AAT cell line

AGE1.HN.AAT is a human designer cell line established by the company ProBioGen (ProBioGen AG, Berlin, Germany). In this instance, primary cells from a tissue sample of a human brain were immortalized via the integration of genes from adenovirus into its genome [32,33]. More specifically the adenoviral E1 A and B genes of the human adenovirus type 5. Overall, these cells were designed to have an enhanced protein export, to be susceptible to a variety of viruses [34]. To produce recombinant protein, the gene encoding alpha1-antitrypsin (A1AT) was inserted into these cells. A1AT is a glycoprotein, also called alpha1-proteinase inhibitor, and is the most common protease inhibitor in human plasma [35]. This protein is mainly produced in the liver, and in minor quantities in by macrophages, intestinal and bronchial epithelial cells [36]. A1AT's main function is to inhibit the action of neutrophilic elastase (an enzyme that digests the elastin basement membrane, and other extracellular components) [35]. A deficiency of this protein can lead to lung emphysema and liver dysfunction [34,36]. Patients with this deficiency are mostly treated with A1AT obtained from human serum. This is expensive and there is a risk of infection, thus AGE1.HN.AAT cells have the potential to be an

alternative source for human A1AT [34]. The safety and compliance with the regulatory requirements for human therapeutic production of this cell line was also assured. For example, its development was performed under a dedicated cell culture suite and the development history recorded [37]. Besides they were adapted to grow in suspension using chemically defined medium [37]. The media used is compliant with regulatory guidance to minimize the risk of transmitting animal spongiform encephalopathy agents via human and veterinary medicinal products. One of the most important advantages of this cell line also is its ability to produce complex and human-like glycosylation patterns increasing the product efficacy and safety [38]. So far, several studies and metabolic characterizations have been performed for this cell line such as transition in apoptosis, metabolism under steady state and metabolism under limitations including cell growth optimizations [37,39–42].

2.2 Madin-Darby canine kidney cell line

MDCK cells were isolated in 1958 by S.H. Madin and N.B. Darby from the kidney epithelium of an adult cocker spaniel (*Canis lupus familiaris*). Initially, these cells contained a normal canine karyotype (2n= 78) [43], but over time, depending on the origin and number of passages, some may contain significantly higher chromosome numbers. Initially, MDCK cells were cultivated as adherent cells [44–47] and later adapted to grow in suspension. The cells were robust and able to grow rapidly and often used as a model to study epithelial phenotypes *in vitro* [48]. MDCK cells are susceptible to a wide range of viruses, of which influenza viruses (A, B and C) are the most relevant for human therapeutics [43]. As such nowadays they are widely used for research and virus propagation for vaccine production [49–51]. In the context of influenza virus vaccine production and research, two parental cell lines dominate the field (American Type Culture Collection (ATCC) and the European Collection of Cell Cultures (ECACC)). Several suspension cell lines have been developed from both ATCC and ECACC-derived cell lines [52–54], due to their potential of better scalability compared to the adherent counterpart. In particular, a MDCK suspension cell line used in this study, MDCK.SUS$_2$, has been extensively characterized and specific medium optimized to enable high cell density cultivations while minimizing cell aggregations [55,56].

2.3 Influenza virus

Influenza disease

Influenza or flu designates the contagious respiratory disease caused by influenza viruses [57]. Influenza viruses belong to the Orthomyxoviridae family and can be separated into four genera, based on the nucleoprotein: IAV, Influenza B viruses (IBV), Influenza C viruses (ICV) and Influenza D viruses (IDV) [58]. IAV particles are mostly spherical and their diameter ranges from 80-120 nm. The genome of IAV and IBV contain eight segments of negative-sense single stranded (-ss) viral RNA (vRNA), while ICV and IDV contain only seven segments [57].

Humans, other mammals, and birds are susceptible to infection with IAV, IBV and ICV, while IVD mostly infects cattle and are not known to infect humans [59]. In humans, these viruses mainly infect cells in the nose, throat, and bronchi (the upper respiratory system), leading to problems such as runny nose, sore throat, cough, fatigue, fever and headache. In some occasions influenza virus infection can also lead to gastrointestinal problems. Influenza infection may become severe because it may allow secondary opportunistic infections (bacterial or other viruses). Different subtypes of IAV and IBV cause seasonal flu epidemics in humans while ICV infections are less frequent and cause only mild illness. IAV research is of significant interest as IAV possesses a great potential to infect different hosts (avian and mammalian in this instance) [57]. Circulating and emerging IAV variants can lead to influenza epidemics and even global pandemics which can have significant economic impact on societies and result in a very high death toll. Due to its relevance this work mainly focuses on IAV.

Influenza A virus structure and intracellular replication

IAV contains eight segments of negative-sense single stranded vRNA, which encodes for at least 10 viral proteins (Fig. 2.1). The vRNA forms a complex with nuclear proteins (NP) and the RNA polymerase complex (PB1, PB2 and PA) denominated by viral ribonucleoproteins (vRNPs). The genome is enveloped by a membrane, containing a proton channel (matrix protein 2, M2) and a structural protein (matrix protein 1, M1) forming a capsid below this lipid membrane. The lipid membrane also contains two glycoproteins hemagglutinin (HA) and neuraminidase (NA).

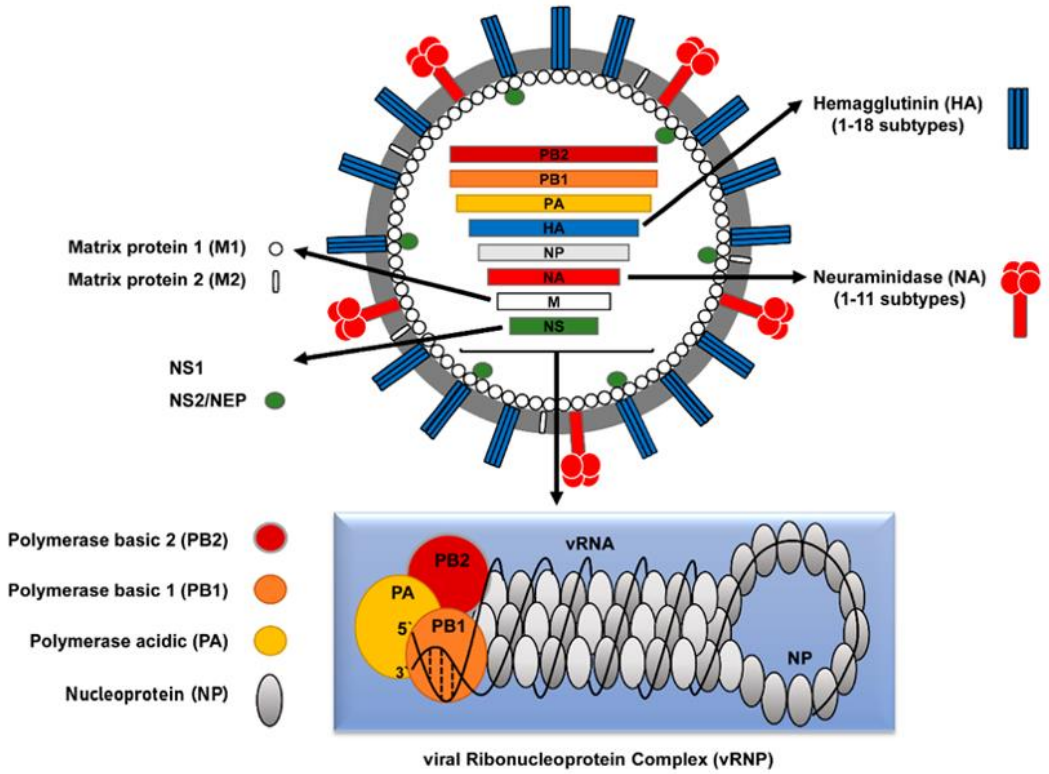

Figure 2.1.: Schematic structure of influenza A virus (IAV). The envelope of the IAV particle, formed from the host cell plasma membrane, contains trans-membrane proteins glycoproteins designated as hemagglutinin (HA) and neuraminidase (NA) and the proton channel matrix protein 2 (M2). The matrix protein 1 (M1) underlies the inner surface of the viral envelope and associates with nuclear export protein (NEP) and viral ribonucleoprotein complexes (vRNPs). The eight vRNPs comprise eight negative-strand RNA segments associated with the nucleoprotein (NP) and three RNA-dependent RNA-polymerase (RdRp) subunits (PA, PB1, PB2). Figure elements taken from Mostafa et al., 2018 [57] under CC4.0.

IAV attaches the host cell by binding to sialic acids on the host cell membrane, a step facilitated by the HA protein (Fig. 2.2). After the attachment, the virus is imported via endosomal trafficking (endocytosis). During the import, endosome acidification occurs, which leads to structural changes in the HA protein, leading to the fusion of the virus envelope with the membranes of the endosome. The viral genome is released and transported into the nucleus. In the next steps viral mRNAs are produced and translated

to produce viral proteins. The RdRp, NP and the RNA assemble to form a new viral genome. Finally, the viral genome is exported to the cell membrane where new virus particles are created and released via membrane budding.

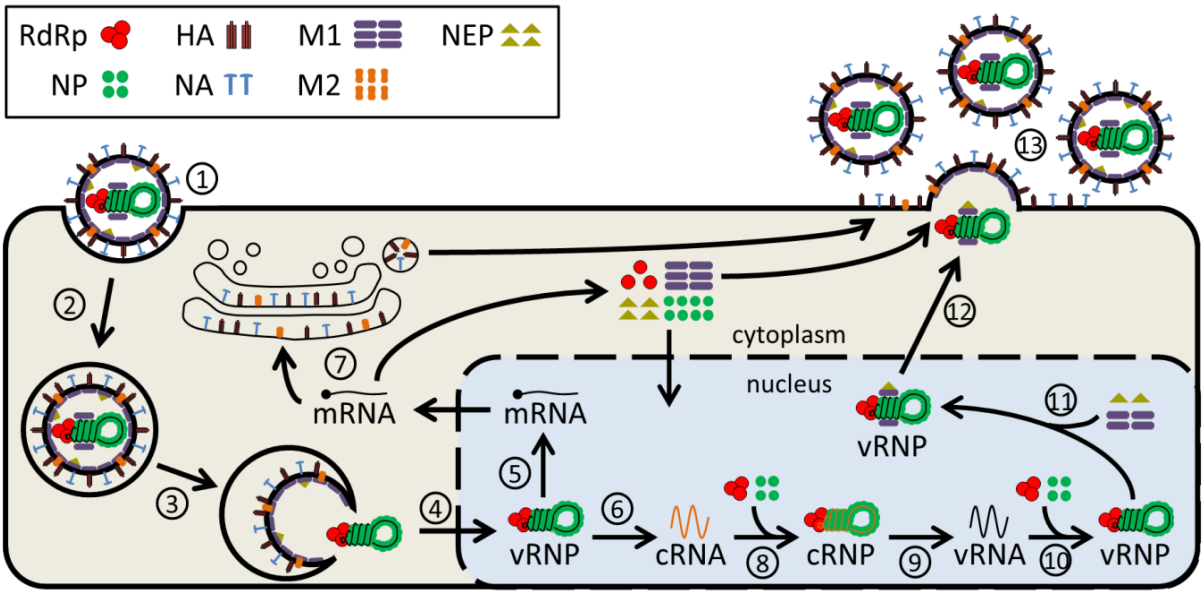

Figure 2.2.: Schematic depiction of influenza A virus infection. For simplification only one of the eight vRNPs is shown and non-structural proteins are omitted. The virus infection follows steps: (1) attachment, (2) endocytosis, (3) fusion, (4) nuclear import, (5) transcription, (6) synthesis of complementary RNA, (7) translation, (8) encapsulation of complementary RNA (cRNA), (9) negative-sense RNA (vRNA) synthesis, (10) viral RNA synthesis, (11) M1 and NEP assembly, (12) nuclear export, (13) virus assembly and budding. Figure elements taken from Heldt et al., 2013 [60] under CC4.0.

Influenza A virus evolution, epidemics, and pandemics

IAV subtypes are named according to the viral surface glycoproteins (HA and NA) and in total 18 HA and 11 NA genetically different have been identified. Over 131 subtypes of IVA (with unique combinations of HA and NA) have been identified in nature [61]. These subtypes likely emerged due to co-infection of two IAV subtypes and subsequent reassortment also referred to as antigenic shift. Theoretically the combination or

reassortment of known HA and NA suggests that 198 subtypes of IVA could exist, though some combinations could require direct human and livestock contact because aquatic birds are the main reservoir for IAV. Typically, IAV seldom crosses the species barrier from birds to humans or to other mammals. For this reason, most of the IAV subtypes were initially isolated from avian hosts [57]. Furthermore, only a limited number of IAV subtypes are usually circulating in humans such as H1N1, H2N2 and H3N2 and lead to seasonal epidemics or occasional pandemics (Fig. 2.3) [57]. New IAV can also emerge by antigenic drift or the accumulation of point mutations [57]. In addition the glycosylation of viral proteins contributes significantly to the complexity of IAV subtypes and should be considered during vaccine production [62]. Glycosylation complexity and glycosylation site are dependent on the host cell glycosylation machinery (endoplasmic reticulum and Golgi apparatus). As such, variations appear on HA and NA of IAV according to the host cell. The glycosylation patterns are important for the viral biological properties and immune response [63].

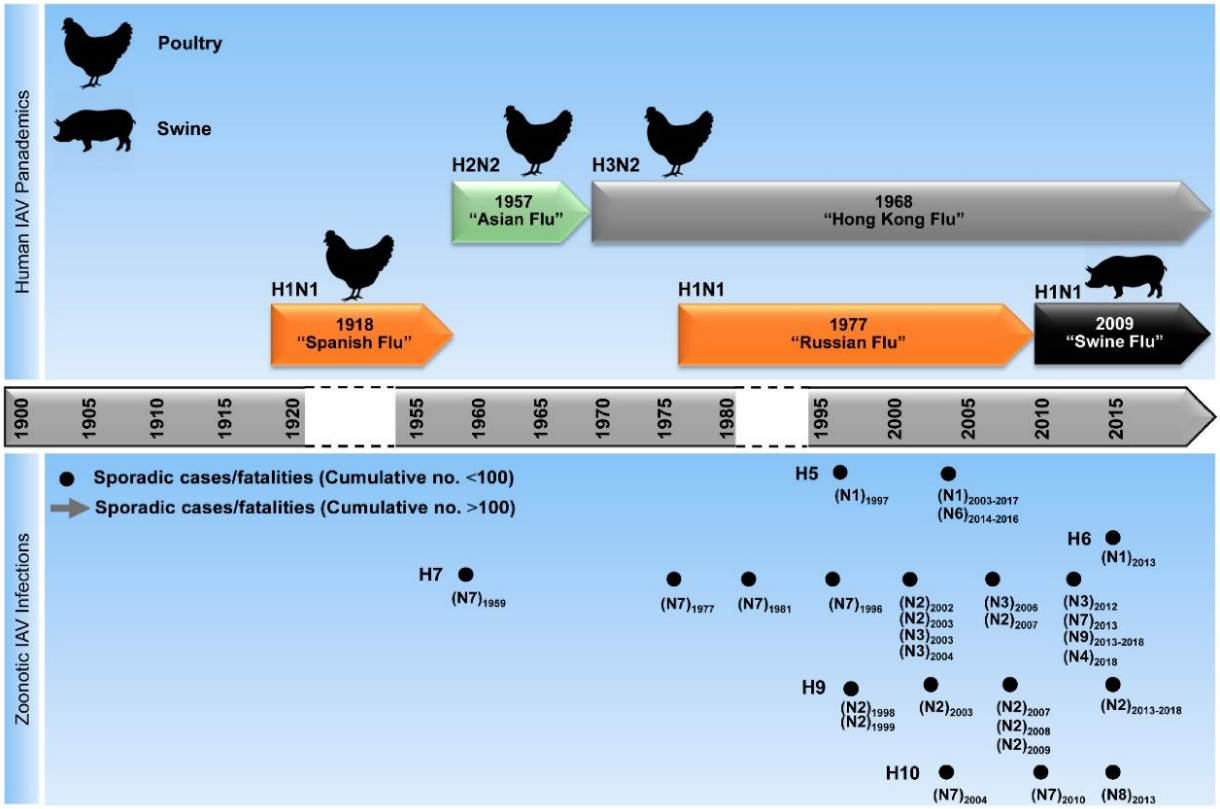

Figure 2.3.: Timeline of relevant influenza pandemics and epidemics caused by influenza A virus. The "Spanish Flu" of 1918-1957 was the most devastating influenza pandemic (likely caused by transmission of an H1N1-type IAV from poultry to humans). In 1957, the strain H2N2 led to the second influenza pandemic known as the "Asian Flu." In 1968, the third pandemic known as "Hong Kong Flu" was caused by the strain H3N2. In 1977 the H1N1 strain reemerged, resulting in the "Russian Flu". In 2009, a new H1N1 variant was transmitted from swine to humans leading to the first pandemic of the 21st century known as the "Swine Flu." In parallel, different avian influenza A virus strains (H5-, H6-, H7-, H9-, and H10-types) have occasionally crossed the host barriers causing mild to fatal infections in humans. Figure elements taken from Mostafa et al., 2018 [57] under CC4.0.

2.4 Cell growth and metabolism

The cell-based production of recombinant proteins requires cell lines with specific characteristics, which are generated through careful clone development and selection. Similarly, cell-based virus production for vaccines and viral vectors, requires specific cell lines susceptible and permissive for the selected virus. Several animal cells have been selected such as CHO cells, MDCK cells, BHK cells, HEK293 cells, HeLa cells, Vero cells or even insect cells such as SF9 cells (from *Spodoptera frugiperda*). The cultivation of

these cells in bioreactors is performed using different cell cultivation modes such as batch, semi-batch, fed-batch, continuous, etc. The cells require carefully formulated media with all the necessary nutrients to sustain cell growth (carbon source, amino acids, vitamins, minerals and occasionally growth factors). Growing cells undergo four different growth phases (section below) while adjusting substrates usage and metabolic by-product release via the reactions of its metabolic network. Typically, animal cell metabolic networks contain a large number of unique reactions and metabolites. For example, over 13000 reactions and 4000 metabolites have been identified for human cells [64] and over 6000 reactions and 4000 metabolites for CHO cells [65] (see section below).

2.4.1 Cell growth phases

Cell-based processes are typically operated at large scales and depend on achieving and maintaining high concentrations of viable cells. Typically, the cell cultivation starts with the inoculation after which the following cell growth phases are observed [68] (Fig. 2.4):

Lag phase: after inoculation, a lag phase where no apparent change in the population number is observed. This phase is shorter in suspension cells (few hours) compared to adherent cells (can take up to 24 h). This phase is attributed to a cell adaptation to a new environment and is in fact a dynamic, organized and evolvable process [66] that occurs before the cell growth phase.

Exponential cell growth: In this phase the number of cells increases in an exponential manner, concomitant with the increase of total cell dry weight and total cell volume. At a single cell level, there is an increase of single cell volume until it reaches a certain cell-specific volume, where the parental cell divides into two daughter cells, which continue the growth process. For this reason, at a population level, typically an increase of total cell volume and total cell dry weight is observed well before the actual increase in cell number [67,68]. During the exponential phase the relative number of cells in the S-phase of the cell cycle is high [69] and the cell-specific growth rate (μ) is close to the maximum cell growth rate (μ_{max}). This rate decreases because of several factors including substrates limitation, by-products inhibition and surface limitation. Due to these limitations, the cell growth rate decreases significantly and the cells enter a transition phase.

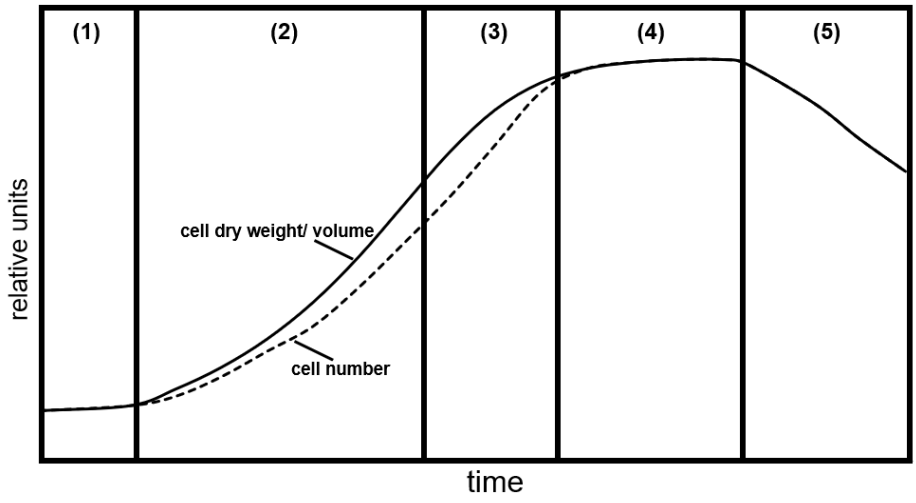

Figure 2.4.: Schematic depiction of cell growth phases. (1) lag phase, (2) exponential cell growth phase, (3) transition phase, (4) stationary phase and (5) cell lysis phase.

Transition phase: The cell growth rate decreases significantly in this phase due to nutrient limitations such as glucose and glutamine [70] and depletion of other medium components such as amino acids [71]. Furthermore, this decrease can also occur due to accumulation of by-products in the bioreactor. Lactate, which is produced from degradation of glucose, impairs growth as it reduces the pH [72]. Ammonium, which results from spontaneous decomposition of glutamine and metabolic usage of amino acids such as glutamine, impairs cell growth by interference with amino acid transport across cell membranes [73]. Following this phase typically, the cells enter a stationary phase.

Stationary phase: Additional substrate limitations and the accumulation of by-products lead the cells to enter a maintenance metabolism characterized by low substrate consumption. In this phase either full growth inhibition with no cell lysis occurs or the cell growth rate is equal to the cell lysis rate leading to a null apparent cell growth rate. If the bioreactor conditions are not renewed either substrates are depleted or the by-product concentrations reach toxic levels which lead to a rapid decrease in the cell viability.

Cell lysis phase: In this phase cell death rate increases followed cell lysis leading to the sharp decrease in cell numbers. The cell death occurs through various mechanisms

[74,75], including virus-induced apoptosis or extrinsic factors such as nutrient depletions and by-product toxicity.

2.4.2 Cell metabolism

In the context of cell-based processes, such as biopharmaceutical production, a cell's capacity for growth and the synthesis of the products of interest is fundamentally dependent on its intracellular metabolism. The latter includes the intricate system or reactions to convert substrates into cellular energy and necessary building blocks or precursors for cellular components (biomass) and the product of interest. These vital functions are orchestrated in the cell's complex metabolic network. This network is composed by the complete set of transmembrane transporters (for molecule transport) and enzymes (to catalyze reactions). Ultimately, the cell's metabolism is characterized by its utilization of this enzymatic network; consequently, detailed study of metabolism provides mechanist insights crucial for enhancing cell growth and eventually increasing the product yields through rational process design and optimization.

The metabolic network itself consists of several subsystems or pathways with numerous reactions. At least 150 unique pathways have been identified in human cell lines, comprising over 13000 unique reactions and over 4000 unique metabolites [64]. The core pathways in different cell lines are very much conserved and termed as the central carbon metabolism. The central carbon metabolism includes critical metabolic pathways that play a crucial role in the generation of energy, and the biosynthesis of various cellular compounds for cell growth and maintenance (Fig. 2.5). It includes glycolysis, pentose phosphate pathway, citric acid cycle, glutaminolysis, and oxidative phosphorylation. Each of these subsystems performs a unique function in the overall metabolic network and plays a critical role in the regulation of cellular energy production and growth. Their combined function accounts for most of the carbon metabolization. Their efficient operation is essential to the proper functioning of the cell. As such, understanding the complexities of central carbon metabolism is essential for the development and optimization of bioprocesses.

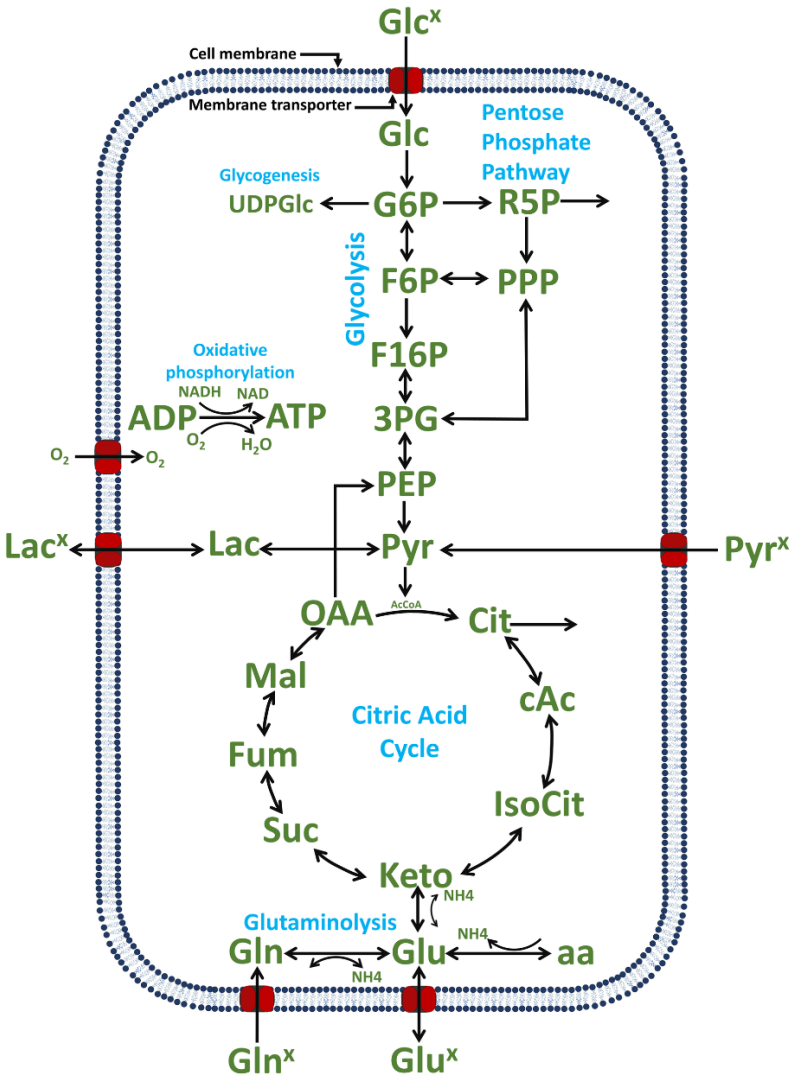

Figure 2.5.: Simplified metabolic network of the central carbon metabolism. In green: key metabolites. Arrows: reactions or transport, with the arrowhead indicating the reaction or transport direction (for simplification, reversible reactions have an arrow for both directions). Abbreviations of metabolites: 3PG: 3-phosphoglycerate, AcCoA: acetyl coenzyme A, ATP: adenosine tri-phosphate, cAc: cis-Aconitate, Cit: citrate, F16P: fructose 1,6-biphosphate, F6P: fructose-6-phosphate, Fum: fumarate, G6P: glucose-6-phosphate, Glc: glucose (intracellular), Glc^x: glucose (extracellular), Gln: glutamine (intracellular), Gln^x: glutamine (extracellular), Glu: glutamate (intracellular), Glu^x: glutamate (extracellular), IsoCit: iso-citrate, Keto: alpha-ketoglutarate, Lac^x: lactate (extracellular), Mal: malate, NH4: ammonium (intracellular), NH4^x: ammonium (extracellular), OAA: oxaloacetate, PEP: phosphoenolpyruvate, Pyr: pyruvate (intracellular), Pyr^x: pyruvate (extracellular), R5P: ribose-5-phosphate, SUC: succinate, UDPGlc: uridine diphosphate Glucose. Note that it is a simplified model as citric acid cycle and oxidative phosphorylation occur in the mitochondria, while the remaining reactions occur in cytosol.

Glycolysis

Glycolysis is an essential pathway of cellular metabolism, where glucose is converted to pyruvate. This process generates lactate, energy in the form of ATP and other precursors such as NADH in the cytoplasm.

Pentose phosphate pathway

The pentose phosphate pathway is an essential metabolic pathway that generates NADPH and sugars, which are essential for biosynthesis of nucleotides.

Citric acid cycle

The citric acid cycle, also known as the Krebs cycle or tricarboxylic acid cycle (TCA), is a central metabolic pathway that occurs in the mitochondria and produces energy in the form of GTP, ATP and precursors such as NADH and $FADH_2$.

Glutaminolysis

Glutaminolysis is a process in which glutamine is converted into other metabolic intermediates that enter TCA and glycolysis. Typically, glutamine metabolism plays a crucial role in metabolism of continuous cell lines, especially in cells with high energy demands.

Oxidative phosphorylation

Oxidative phosphorylation is the process by which ATP is generated from the oxidation of NADH and $FADH_2$, which are produced mainly in glycolysis and TCA cycle. This process is an essential source of energy for cells for cell growth and maintenance.

2.5 Recombinant protein production

Proteins play an essential role in virtually every function in a cell and have emerged as the therapeutic of choice as they can be engineered to target specific disease processes. Additionally, proteins are essential components of most vaccines, as they can be used to stimulate the immune system to build immunity against pathogens. However, isolating high quantities of desired proteins from natural sources is challenging, as such one of the main objectives in biotechnology is the production of soluble and functional recombinant

proteins [76]. Typically, this involves the isolation of a gene encoding the target protein and its introduction in host organisms capable of synthesizing that protein.

Escherichia coli is the most popular host for expression of recombinant proteins but as a prokaryotic system they are unable to produce complex proteins which may also need specific post translational modifications. The most widely recognized form of modification is glycosylation and can only be performed by eukaryotic cells. Therefore, eukaryotic cells such as mammalian cells, insect cells, yeast and microalgae are being used as viable alternatives for production of these complex proteins [76]. The most used mammalian cells are Chinese hamster ovary (CHO) cells, mouse myeloma (NS0), baby hamster kidney (BHK), human embryonic kidney (HEK-293), Madin-Darby canine kidney (MDCK) cells and human retina-derived (PERC6) cells [76]. In some case, the productivity of mammalian cells has reached the gram per liter range [77]. Several recombinant proteins that are commercially available are produced in mammalian cells such as hormones, growth factors, antibodies, enzymes, inhibitors etc. [78]. Other cell lines such as human cell lines are being investigated for recombinant protein production such as the AGE1.HN.AAT as source for human A1AT [34]. The most important advantage of human cell lines is their ability to produce complex and human-like glycosylation patterns, increasing the product efficacy and safety [38].

2.6 Vaccine production

A vaccine prevents disease spread and/or reduces their severity by creating immunity. It usually contains weakened or fragments of the disease-causing pathogens that stimulate the immune system to fight and create immunity against the pathogen (e.g., viruses and bacteria). As such, vaccines are one of the most significant medical advancements in human history, protecting against several illnesses thereby saving millions of lives annually. Vaccine manufacture is a sophisticated, multistep process including growth of pathogens, purification, and formulation. Steps in the manufacturing of influenza vaccines include growing the virus in a suitable host, such as embryonated eggs or cells (mammalian and insect), and then purifying the virus or its components. Viral vaccine typically consists of attenuated viral particles, dead viral particles, or viral proteins. These

components, especially viral proteins, are combined with adjuvants and other substances to enhance both the efficacy and durability. Ensuring the safety of these vaccines is paramount, while at the same time preserving their ability to activate the immune system and create immunity. Furthermore, to address the worldwide demand for vaccines, efficient and scalable manufacturing methods are necessary. Bioprocess engineering is essential to the manufacture of vaccines because it enables the optimization of production processes to boost efficiency, decrease costs, and assure quality consistency. The production of influenza vaccines is one of the most urgent aspects of vaccine manufacturing. Influenza viruses cause respiratory infection (flu). The latter is a significant threat to public health because it affects millions of people annually and may lead to hospitalization, severe illness, and death. Because the influenza virus constantly mutates, new vaccinations must be created annually to guarantee their effectiveness. Specifically, influenza vaccine productions are time constrained as there is a need for production before each flu season.

2.7 Mathematical modeling of bioprocess

The simulation of complex biological systems in bioprocesses is possible by mathematical models, which are powerful tools that are increasingly being used for process optimization. In most cases, the models that are developed consist of a set of ODE-based equations that either describe portions of or a whole biological system. The equations make it possible to simulate and predict the behavior of biological systems. Recently machine learning such as feed forward neural networks and hybrid methods that combine machine learning and first-principles equations are also being used to simulate and predict culture dynamics [79–81]. Overall, it is reasonable to affirm that the application of mathematical methods such as mathematical models in the field of bioprocess engineering has led to a considerable advance in the knowledge of bioprocesses. In addition, they enabled the identification of critical process and product quality parameters for optimization. However, limited availability of large amounts of experimental data and lack of fundamental knowledge due to the intrinsic complexity of biological systems have

historically been limiting factors. New essays for intracellular metabolite quantification (e.g. liquid chromatography-mass spectrometry (LC-MS), mass spectroscopy (MS) and nuclear magnetic resonance spectroscopy (NMR)) are offering unprecedented detailed intracellular data which will immensely facilitate model establishment for animal cells.

Models based on classification of bioprocesses: Mathematical models of cell cultivations can be classified as segregated vs. unsegregated [82,83], structured vs unstructured [82,83], deterministic vs stochastic (probabilistic) [84] and may comprise multiple scales (multi-scale model) [84]. A structured model refers explicitly and in detail to the cell population in terms of their intracellular contents, particularly it attempts to describe the intracellular dynamics of a large number of metabolites [82,84]. An example of these types of models are mechanistic models, which rely on the underlying biological mechanisms [82]. The unstructured models omit the intracellular description [82]. An example of these type of models are data driven models, in which the structure of the model is irrelevant and hidden [82]. Segregated models account for cell to cell heterogeneity in a population by explicitly considering cells in different stages of development, specifically cell age, size and metabolic state [82]. Unsegregated models do not account for cell heterogeneity as they only consider identical “average cells”, which can useful to describe overall trends and system responses [82]. The Stochastic models typically consider the behavior of individual cells or molecules, where their individual behavior results from randomness based on probability distribution functions [82]. In contrast, deterministic models describe the behavior of the entire population as continuous and predictable [82]. Moreover these models contain clear mathematical relationships of cause-and-effect and a set of initial conditions always produces the same simulation results.

2.7.1 Modeling methods

Biological data is complex and multidimensional, as such mathematical models are suitable approaches for their understanding and improvement. Modeling a bioprocess can make use of a wide variety of mathematical methodologies, including constraint-based modeling and dynamic models. Known mechanistic or kinetic descriptions of enzymes that are taking part in the bioreactions can be included in either method.

Machine learning methods are also increasingly being used in the context of bioprocesses. In addition, hybrid techniques, which blend known (parametric) models with unknown (non-parametric) models to provide a more accurate simulation of biological systems, are becoming increasingly popular. The latter includes for example the combination of dynamic metabolic models or constrained-based models with machine learning (ML) in the modeling framework [80].

Constraint-based models: Constraint-based models are a type of mathematical model that describe biological systems using constraints, such as the maximum–minimum reactions (substrate consumption or by-product formation), reactions stoichiometries and thermodynamic constraints (reaction reversibility). In such approaches the cellular behavior is assumed as being limited by the availability of resources. The standard constraint-based method used to compute fluxes at genome scale is flux balance analysis (FBA) [85]. A biological objective is assumed based on the idea that cellular behavior is regulated to achieve certain goals such as cell growth maximization. Constraint-based methods allow estimation of intra–extracellular flux distributions allowing the study of regulation of pathways in cellular metabolism to investigate certain objectives which are at least directionally correct. For example, a constraint-based model can be used to identify the limiting substrate for cell growth or for the product of interest formation, which can be useful even if the predicted limitation factor is not 100% accurate.

Data-driven models: Data-driven models describe statistical relationships between input controls and output in bioprocesses, essentially, they are models of correlations. These models can capture these correlations by employing advanced statistics and multivariate data analysis (MVDA), which includes methods such as principal component analysis (PCA) and partial least squares (PLS) [86]. In the realm of ML, artificial neural networks are employed as data-driven models, also known as black-box models. These models can achieve accurate experimental data fitting and without extensive knowledge of underlying biological mechanisms. This makes them easy to use and employ when there is lack of fundamental knowledge about the biological process. However, in general, like any data-driven approach it requires extensive data. Furthermore, data-driven models lack the extrapolation capabilities and have been shown to violate physical principles, in contrast with models based on fundamental knowledge (e.g. mechanistic models).

Dynamic models: Dynamic models typically consist of ODEs to compute the time-course behavior state variables. This mainly consists of cell and metabolite concentrations, and their mass balance can be written as:

$$\frac{d(c)}{dt} = \sum_{k=1}^{n} \frac{F_k}{V} c_{k,f} - c \sum_{k=1}^{n} \frac{S_k}{V} + \sum_{k=1}^{n} r_{k(c)} - \mu c \qquad 2.1$$

Where c is the concentration of a state variable, V is the reactor volume, F_k is the volume of a feed stream, $c_{k,f}$ is the concentration of c in the feed stream, S_k is the sample volume, $r_{k(c)}$ is the rate of consumption/production of c in the k^{th} reaction and μc is the growth rate dilution in case of intracellular metabolites. The $r_{k(c)}$ is governed by several reactions/transport kinetics, e.g. the Michaelis-Menten kinetic, described below. A dynamic model that includes kinetic descriptions is termed as a mechanistic model. These models rely on the accurate description of several underlying kinetic mechanisms to describe the observed cell growth and metabolism. *In vivo* mechanisms may differ from kinetics observed *in vitro*, and, depending on the complexity of the overall kinetics, several parameters need to be optimized. Due to these facts, accurate mechanistic modeling of cell metabolism is a challenging task.

Hybrid models: Data-driven models, such as ML (e.g. neural networks, discussed in the previous paragraph), have some limitations including data dependency, low extrapolation capabilities and potential violations of physical principles. To address these challenges, researchers have explored hybrid model structures that combine neural networks with prior fundamental knowledge (e.g. mechanistic information). Hybrid models require less training data, excel in extrapolation, and capture physically relevant behavior and are becoming widely applied [80,87–92]. Essentially a hybrid model structure consists in connecting outputs of neural networks with systems of equations. The equations can describe bioreactor material balance (e.g. system of ODEs) using the output of neural networks as inputs (kinetics of substrate consumption, by-product accumulation, cell growth and product formation) [81].

Kinetics of reactions catalyzed by enzymes: Unlike spontaneous reactions or reactions catalyzed by chemical compounds, most biological reactions are catalyzed by enzymes. A general simplification is depicted in Fig. 2.6, where S is the substrate, E is

the enzyme and *P* is the product. Typically, an enzyme-mediated reaction involves multiple steps, including substrate binding, enzyme conformational changes, substrate conversion, and product release, which can overall be represented by mass-action kinetic equations [68]. The order of such reactions depends on the number of substrates and products, resulting in numerous parameters. This multiplicity can make parameter identification and analysis cumbersome. Michaelis and Menten presented a pioneering simplification of reaction kinetic that links product formation to substrate conversion under specific assumptions. Cleland expanded on this by developing a comprehensive nomenclature and rate equations for various reaction types, considering the number of reactants/products (e.g. uni-uni, bi-uni, bi-bi,...) , reaction order (random or ordered), reversibility and enzyme isomerization (ping-pong, iso, …) [85,93,94]. Despite their utility, some of these kinetics were quite difficult to derive, and this motivated King and Altman to propose a simpler, graph-based method mainly relying on the reaction scheme [95]. A disadvantage of the latter is that it lacked the capacity to capture crucial regulatory mechanisms such as cooperativity and allosteric effects [68]. Enzyme cooperativity phenomenon gained importance after Hill discovered the sigmoidal oxygen binding curves in hemoglobin and proposed the hill kinetic [96]. This kinetic was a significant contribution that aided characterization of many enzymes such as the phosphofructokinase (PFK, a glycolytic enzyme). The role of the allosteric effect was especially recognized by Monod et al. which introduced the Monod-Wyman-Changeaux model to describe some glycolytic enzymes [97]. Essentially this kinetic postulated that the substrate affinity is influenced by both substrate and allosteric modulator concentrations.

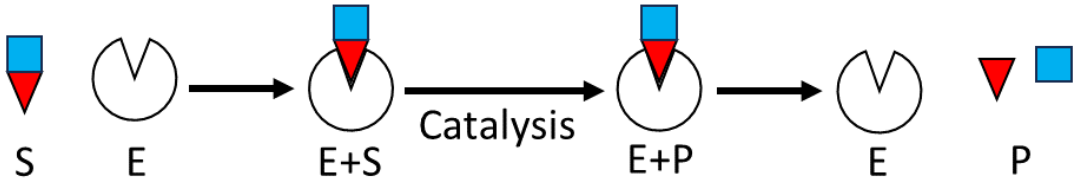

Figure 2.6.: Schematic representation of a reaction catalyzed by an enzyme. S is the substrate, E is the enzyme, P is the product, E+S is the enzyme-substrate complex and E+P is the enzyme-product complex

Overall, the complexity of enzyme kinetics reflects the diverse factors influencing the conversion of substrates to products. Furthermore, since the pioneering studies previously mentioned several enzyme kinetics, which dictate the rate of substrate conversion to the product have been proposed [2]. These kinetics have varying levels of complexity depending on the relevant factors considered such as allosteric effects, cooperation, reaction order and number of substrates/products. As such in this work, numerous enzyme kinetics with varying complexity were used such as mass-action, Michaelis-Menten, Monod, hill kinetic, Monod-Wyman-Changeaux, etc.

Estimation and identifiability of model parameters: Ideally a model is a mathematical description that can accurately simulate a determined biological process. To achieve this, the correct mathematical description (e.g., kinetic equations) must be identified and its related parameters optimized. As such parameter optimization is a crucial step in the development of mathematical models for biological systems. It consists of finding values for the model's parameters that allow the model simulation to accurately capture the dynamics in experimental data from a biological system. Often, this task can be very changeling due to sparse data availability and the inherent complexity of biological phenomena [68]. Due to their complexity (model structure), parameter estimation typically involves non-linear optimization methods to minimize a goodness-of-fit function (experimental data – simulation data). Several algorithms are available that are being successfully used to tackle nonlinear optimizations [98]. Identifiability, which refers to the ability of determining the unique parameter, is also a key concern during the development of mathematical models. Identifiability issues can be attributed to low-quality data, sparse data, or complex models with overparameterization. Several methods can be used to estimate the uncertainty of parameters (correlations and confidence intervals) such as the Fisher Information Matrix, bootstrap, and Bayesian approaches [99–101]. Identifiability issues become clear when several distinct sets of parameters yield similar goodness-of-fit resulting in large parameter uncertainties [68]. This tends to happen when different mechanisms in the model produce indistinguishable responses (i.e. depending on the parameters used, some mechanisms can compensate or eliminate the need for another). In a biological context, a plausible explanation for this effect is that metabolic networks are known to be robust against environmental fluctuations. Furthermore, it is known that the cell’s metabolic network possesses the “small world” property, meaning that metabolic conversions to form a specific metabolite is possible through many

alternative pathways. This suggests multiple combinations of reaction pathways can be used to produce a single metabolite. More specifically, if an enzyme is inhibited or “tuned off,” the cell metabolism can adapt and use alternative routes. This implies that the metabolic network is robust and redundant in order to maintain their functionality in face of variations. It is thus reasonable to assume that the hurdles of parameter identifiability of models describing such a system is further exacerbated by this metabolic network property. In conclusion, it is essential to understand and mitigate the challenges in biological model establishment, parameter optimization and identification is essential. In this work, mathematical models were established for different cell lines and bootstrap was used to obtain parameter confidence intervals. It also guaranteed that enough data points were used for accurate estimation of the parameters ($2r + 1$ of highly informative data points are enough to identify r unknown parameters [102]).

2.7.2 Cell growth models

Cell growth refers to the increase in cell number, cell mass or cell volume. Cell multiplication requires doubling of the genetic material and biosynthesis of macromolecules. This synthesis requires amino acids, energy and other precursors obtained through substrates catabolism, which simultaneously releases by-products. The rate of amino acid and substrate consumptions are directly linked to the cell growth rate. Several empirical mathematical formulations have been used to model cell growth concomitant with substrate consumption and by-product release. Modeling cell growth based on cell numbers is the simplest and ubiquitous approach due to data availability. It has been shown to be applicable to several cell types and growth conditions, such as CHO cells [46,103–105]. However, this approach of modeling cell number has some limitations because there is a delay between the increase in cell number and cell mass/volume. This translates into a clear disadvantage of modeling cell numbers as the average cell size changes drastically during exponential cell growth. Accounting for this is particularly important when analyzing intracellular phenomena, i.e. when a cell growth model is linked to intracellular metabolism. To overcome this issue some approaches focus on modeling cell growth through cell mass increase [84,106,107]. However, despite its inherent advantage to describe specific cells and their mass over time, validating such a model is difficult due to its complexity and lack of experimental data in some instances.

Another alternative, over modeling cell number only, is modeling cell volume. Experimental cell volume can be obtained using viable cell counters (Vi-Cell analyzers) which determines viable cell counts and cell diameters. The cell mean diameter is an average determined by taking stationary pictures of the cell broth sample. The total cell volume is obtained with the product of the mean cell volume and viable cell concentration. Modeling cell volume should allow more accurate predictions of concentrations than when considering cell numbers only (constant volume) [108]. Recently Rehberg et al. developed and validated a model describing cell volume and intracellular metabolism [109].

2.7.3 Metabolism models

Glycolysis: Since the pioneering work of Chance et al. [110], glycolysis has been in the focus of many mathematical models. The first models were developed for erythrocytes where enzyme kinetics were included (e.g.,[111,112]). Later other models were developed for mammalian cells (liver, muscle) to study glucose homeostasis and glycogenolysis [113]. Chloe et al. developed a model to describe glycolysis of HeLa cells, accounting for allosteric regulation by using the Monod-Wyman-Changeux kinetic derived from analysis of thousands of *in vitro* kinetic measurements [114]. Similar models were established for other cell lines [115,116]. More recently Rehberg et al. established and validated a structured model of glycolysis for MDCK cells, which considers the *in vitro* enzyme activities and performed model validation using pulse feed data [109].

Citric acid cycle: Since the pioneering model describing TCA and related metabolism in rat liver established by Garfinkel [117] that unraveled the citric acid cycle's control mechanisms, several model refinements followed [111,118–120]. Recently Bazil et al. established a model with 400 parameters to describe data from mitochondria [120]. However, in this instance discrepancies between *in vitro* and *in vivo* data pose validation challenges. As such Nazaret et al. [121] proposed some implications that enabled a successful prediction of steady state observed experimentally, demonstrating simpler models can capture key features. Similarly, Wu et al. established a simpler model describing mitochondrial metabolism in rat brain cells [120].

Central carbon metabolism: Both glycolysis and citric acid cycle are essential for energy and biomass precursors. Based on mathematical models established for each pathway individually, some approaches try to combine both in a single model. In E. coli, such models have been established and validated utilizing knockout mutants [122,123]. Similarly in yeast such a model has also been established and validated using data generated after glucose pulse feeds [124]. Such a detailed central carbon metabolism model exists for CHO cells [103,104,125,126], human-derived cell lines [127] and MDCK cells [68]. Overall, central carbon metabolism modeling and validation in animal cell lines is still scarce, largely due to a lack of intracellular data.

2.7.4 Modeling and optimization of bioprocess

The cell cultivation in bioreactors requires carefully formulated media with carbon source, amino acids, vitamins, minerals and occasionally growth factors. Physical process conditions such as pH, temperature, dissolved oxygen should also be optimum. While growing, cells adjust substrate usage and metabolic by-product release via the reactions of its metabolic network (discussed in the previous section). The metabolic network of animal cells consists in transmembrane transporters and enzymes that allow generation of energy, growth precursors, and the desired products. The rate of energy and product of interest formation are determined by the resulting network properties. The enzymes in the network are controlled using sophisticated regulation mechanisms. In case of viral vaccines production, the virus yield in cell cultures is essential to assure enough viral materials are produced. This yield is influenced by a variety of factors including the cell substrate used, the cell concentration at time of infection and moi [3]. For process optimization, detailed knowledge about the impact process parameters is required. As such, careful mathematical model formation for process simulation, optimization and design is required to increase cell growth yield of the product of interest.

In the past, the optimization of biological processes often relied on trial and error using a high number of experiments. With the additional use of mathematical methods, however, process design and optimization can be significantly accelerated [128,129]. Decision-making based on models is a more rational approach regarding critical factors and responses of the process under investigation. One option is the use of design of experiments (DoE) approaches, where experiments are planned in a statistically optimal

way to reduce the number of cultivations to be performed and to investigate the impact of parameters on product yield and product quality [130–132]. A drawback of these methods, however, is their inability to handle more complex systems dynamics, for example changes in critical cell properties or medium composition with process time, the release of inhibitory compounds into the cultivation broth, or the decrease in specific precursor concentrations required for product synthesis. Furthermore, conventional DoE approaches cannot explicitly consider the intracellular dynamics of animal cells, i.e. crucial aspects of the central energy and carbohydrate metabolism.

Another option for process optimization and design is the well-known constraint-based modeling. This approach relies mainly on the estimation of flux distributions of metabolic networks using a pseudo-steady state assumption [133–135]. As this approach deals with intracellular dynamics, it can support a typical DoE method. Examples are metabolic flux analysis (MFA) and flux balance analysis (FBA), which solve a linear system of equations to estimate the flux distribution in large-scale network models without taking into account any kinetic information [136–139]. For animal cells, various MFA models have been derived that rely on pseudo-steady state assumptions [140]. With these types of models, the response of a metabolic network can be used to assess possible steps towards achieving a significant increase in product yields. The models allow the detailed characterization of several biotechnological processes and the unraveling of cell line-specific properties [140–142].

Despite their widespread usage and simplicity, these models have limited applicability (due to their pseudo-steady state assumption) and usually include no information about the reactions kinetics involved [143].

For more realistic scenarios, dynamic models should be used to allow for the handling of complex and high-dimensional experimental data. Typically, this is achieved with the simulation of changes (such as metabolite concentration) over the time course using a set of ODEs with defined initial conditions and simplified, but biologically valid assumptions regarding cell growth, product formation, enzyme kinetics and virus production [144,145]. In particular, the formulated mathematical relationships should establish a direct link between experimental data and cellular behavior [146–148]. For example, such models could enable a detailed analysis of cell growth and in particular changes in the central carbon and energy metabolism during virus replication. Based on this, the understanding of the complex behavior of animal cells regarding growth and

product formation can be increased. A deeper understanding of the direct and indirect impact of virus replication on its host cells can also be obtained. In turn, possible bottlenecks may also be identified to take measures to increase cell-specific or overall virus yields. Linking such models with a more detailed description of protein glycosylation taking place in the endoplasmic reticulum and the Golgi apparatus, might even allow to uncover correlations of cultivation conditions with critical product quality attributes (i.e. antennary composition, sialylation or core fucosylation) [149–151]. Eventually, options for increasing cell concentrations and product yields can be evaluated [147], thus supporting processes intensification. Furthermore such models can also be combined with omics measurements [152] and hybrid approaches that complement what is mechanistically known [153] in order to confirm identified hypotheses.

Despite these benefits, few dynamic models have been established that describe both cell growth and intracellular metabolism of animal cells, while in E. Coli and yeast such models are validated and frequently used in metabolic redesign (as discussed in the previous section) [122,124,154]. Regarding studies to improve the yield of viruses for vaccine production, in case of cell culture-based influenza virus production it is well established and virus replication has been studied in detail. In addition, quantitative mathematical models have been derived that describe dynamics of viral replication at the intracellular [155,156] and the cell population level [60]. However, to better understand the complex interplay between the virus and its host cell, metabolism during virus replication should be considered and studied in more detail.

3 Chapter
Models and methods

3.1 Model definition

This section describes the development of two separate dynamic models, these models were published in [157,158] and parts of the method were used without quotation to facilitate reading. The first model was developed to describe batch cultivations of AGE1.HN.AAT suspension cells [157]. It consists of a set of 33 ODEs with 132 parameters which were fitted using 353 data points (one batch experiment). It describes cell growth (concentration of viable cells, mean cell diameters, volume of viable cells), concentration of alpha-1-antitrypsin and key metabolites in the central carbon metabolism concomitantly. The first model was extended into a second model to describe virus production in MDCK suspension cells in shaker flasks. The extended model introduced a more detailed description of intracellular lactate metabolism, the alpha-1-antitrypsin kinetics was disregarded and new kinetics to describe virus titer and virus-induced cell death were introduced. The extended model contains 35 ODEs with 143 parameters which were fitted using 360 data points (one experiment) [158]. The extended model describes the cell growth (concentration of viable cells, mean cell diameters, volume of viable cells), key central carbon metabolites and influenza A virus titer concomitantly.

3.1.1 AGE1.HN.AAT suspension cell model

This section introduces the dynamic model that describes both cell growth and metabolism developed for AGE1.HN.AAT cells by Ramos et al., 2020 [157]. This model couples a segregated growth model, which describes cell growth dynamics in batch

culture, with a structured model of the central carbon metabolism, which describes intracellular metabolite dynamics and connects extracellular product accumulation to the intracellular metabolic network. The segregated cell growth model was based on a model proposed for MDCK adherent cells [159], which considers different cell size classes. This enables the estimation of the mean cell diameter and consequently the cell volume. Modeling cell volume was essential for the coupling of the cell growth model with the structured model of the intracellular metabolism considering that volumetric maximum enzyme activities depend on the cell-specific volume (Eq. 3.1.10, i.e. enzyme concentration affected by changes in cell-specific volume). Further aspects regarding this modeling approach, including a discussion concerning the number of cell classes required in the segregated model, can be found elsewhere [109,159,160]. Five cell classes with linear increasing diameter were chosen to describe the experimental data collected for AGE1.HN.AAT cells. This was found as the minimum number of cell classes required to describe the experimental data and is in accordance with the number previously used for MDCK cells [159]. In contrast, however, various modifications of the model developed for adherently growing cells were required to describe growth and metabolism of AGE1.HN.AAT suspension cells. The most important change concerned the lack of a surface area limitation, which is only relevant for growth of contact-inhibited adherent cells. In addition, due to the rather long cultivation time, cell death was considered to handle the loss of cell viability typically observed after substrate depletion. The cell death phase is typically not relevant in industrial settings, however, for this cell line a rapid switch from exponential cell growth to cell death occurs (without a noticeable stationary phase). As such, modeling this phase allowed detailed analyses of the switch from exponential cell growth to cell death and its implication on the cell' metabolism. For the structured central carbon metabolism model, most assumptions regarding the set of reactions were made according to previous studies of metabolism of this cell line [37,161,162].

An overview of the structure of the metabolic network is shown in Fig. 3.1. Following in structure and basic assumptions the work for MDCK adherent cells [109,159,160,163] and others [126], reaction kinetics used were either simple or modified versions of first order kinetics, i.e. Michaelis-Menten or Hill kinetics. In addition, the model explicitly takes into account maximum enzyme activities measured experimentally [161] and the degradation of amino acids (r_{AAex}) was estimated as proposed for MDCK cells [160]. In

extension of the model proposed for MDCK cells [109,160], reactions that link the glycolytic pathway to the TCA cycle and vice versa were considered. Furthermore, various aspects of the intracellular metabolic network were considered in more detail. For instance, the ATP dynamic takes into account all reactions in which it is either directly consumed or produced, as well as other sources such as redox cofactors NADH (nicotinamide dinucleotide) and $FADH_2$ (flavin-adenine-dinucleotide) [164]. Furthermore, in contrast to the previous models, consumption rates of all extracellular substrates (glucose, glutamine, glutamate, lactate) were used as inputs for the intracellular metabolic network. The accumulations of extracellular by-products (lactate, ammonium and glutamate) were estimated directly from intracellular metabolic rates. Another aspect of metabolism considered is the transamination of oxaloacetate (OAA) to ketoglutarate. The latter was added since previous studies of AGE1.HN.AAT cells suggested that this pathway strongly influences ammonium release and OAA synthesis [162]. Finally, due to lack of data regarding the distribution of intracellular metabolites in the cytoplasm and the mitochondria, it is assumed that all intracellular metabolites are homogeneously distributed.

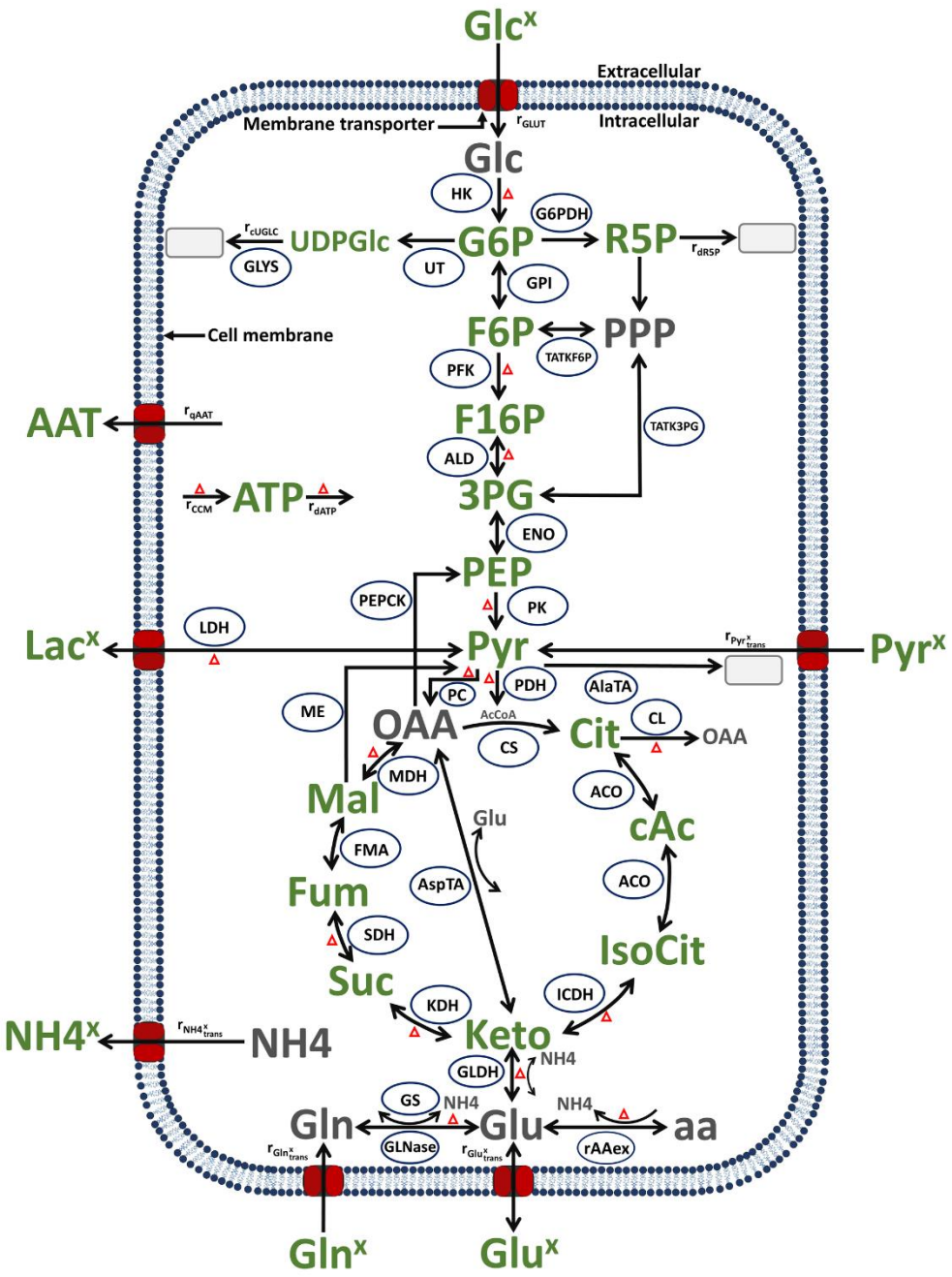

Figure 3.1.: Simplified model of the central carbon metabolism of AGE.HN.AAT suspension cells. In green: metabolites and product measured by Rath et al. [161]; in grey: metabolites not measured. Ellipsoids: enzymes considered in the model. Arrows: reactions or transport, with the arrowhead indicating the reaction or transport direction (for simplification, reversible reactions have an arrow for both directions). Grey rectangles: sinks or metabolites not accounted for in the model. Red triangles: all the reactions included in the energy balance. Abbreviations of

metabolites and product**:** 3PG: 3-Phosphoglycerat, AAT: Alpha1-antitrypsin, AcCoA: Acetyl coenzyme A, ATP: Adenosine tri-phosphate, cAc: cis-Aconitate, Cit: Citrate, F16P: Fructose 1,6-biphosphate, F6P: Fructose-6-phosphate, Fum: Fumarate, G6P: Glucose-6-phosphate, Glc: Glucose (intracellular), Glc^x : Glucose (extracellular), Gln: Glutamine (intracellular), Gln^x : Glutamine (extracellular), Glu: Glutamate (intracellular), Glu^x : Glutamate (extracellular), IsoCit: Iso-citrate, Keto: alpha-Ketoglutarate, Lac^x : Lactate (extracellular), Mal: Malate, NH4: Ammonium (intracellular), $NH4^x$: Ammonium (extracellular), OAA: Oxaloacetate, PEP: Phosphoenolpyruvate, Pyr: Pyruvate (intracellular), Pyr^x : Pyruvate (extracellular), R5P: Ribose-5-phosphate, SUC: Succinate, UDPGlc: Uridine diphosphate Glucose. Abbreviations of enzymes and transport rates: HK: Hexokinase, G6PDH: Glucose-6-phosphate dehydrogenase, r_{dATP}: Reaction rate for ribose-5-phosphate consumption, UT: Uridyl transferase, GLYS: Glycogen synthetase, r_{uGLC}: Reaction rate for other uridine diphosphate glucose consumption, GPI: Glucose-6-phosphate isomerase, TATKF6P: Transaldolase and transketolase, TATK3PG: Transaldolase and transketolase, PFK: Phosphofructokinase, ALD: Aldolase, r_{qAAT}: Reaction rate for product formation, ENO: Enolase, r_{CCM}: Reaction rate for overall ATP production, r_{dATP}: Reaction rate for overall ATP consumption, PK : Pyruvate kinase, PEPCK: Phosphoenolpyruvate-kinase, LDH: Lactate dehydrogenase, PC: Pyruvate carboxylase, PDH: Pyruvate dehydrogenase, AlaTA: Alanine transaminase, ME: Malic enzyme, CS : Citrate synthetase, CL: Citrate lyase, ACO: Aconitase, ICDH: Isocitrate dehydrogenase, KDH: Ketoglutarate dehydrogenase, AspTA: Aspartate transaminase, SDH: Succinate dehydrogenase, FMA: Fumarase, MDH: Malate dehydrogenase, GLDH: Glutamate dehydrogenase, GS: Glutamine synthetase, GLNase: Glutaminase, r_{AAex}: Amino acids degradation, r_{GLUT}: Reaction rate for extracellular glucose consumption, $r_{\mathrm{Pyr}^x_{trans}}$: Reaction rate for extracellular pyruvate consumption, $r_{\mathrm{NH4}^x_{trans}}$: Reaction rate for ammonium production from intracellular rates, $r_{\mathrm{Gln}^x_{trans}}$: Reaction rate for extracellular glutamine consumption, $r_{\mathrm{Glu}^x_{trans}}$: Reaction rate for extracellular glutamate consumption and/or production from intracellular rates. Figure taken from Ramos et al., 2020 [157].

In this modeling approach, the segregated cell growth model describes the macroscopic scale (dynamics of cells, product formation and extracellular metabolites) while the structured model describes the intracellular metabolism including glycolysis, TCA, transamination, and energy metabolism on the microscopic scale. Accordingly, the macroscopic scale needs to be linked with the intracellular scale and vice versa (Eq. 3.2.1) using r_{macro} (mmol min^{-1} L^{-1} for the volume referring to the bioreactor) and the corresponding intracellular rates r_i (mmol min^{-1} L^{-1} for the volume referring to the cells).

In the following section, the ODEs for the segregated cell growth model and the structured model for the central carbon metabolism of AGE1.HN.AAT cells are introduced.

Segregated cell growth model

The segregated cell growth model describes the dynamics of viable cells, substrates, product formation, and metabolic by-products on the macroscopic scale. It is assumed that cells transition from a first class (X_1 , cells with the smallest diameter) to the last class (X_5 , cells with the largest diameter) before dividing into two daughter cells (Eqs. 3.1.1–3.1.3).

$$\frac{dX_1}{dt} = r_{trans}(2\,\mathrm{X}_5 - X_1 f) - k_d X_1, \tag{3.1.1}$$

$$\frac{dX_2}{dt} = r_{trans}(X_1 f - X_2) - k_d X_2, \tag{3.1.2}$$

$$\frac{dX_i}{dt} = r_{trans}(X_{i-1} - X_i) - k_d X_i, \text{ for } \mathrm{i} = 3,...,\mathrm{N}^c. \tag{3.1.3}$$

As in Rehberg et al. [159], five cell classes were considered to describe changes in the mean cell diameter during the time course of cultivation. In these five cell classes ($N^c = 5$), the transition rate (r_{rans} , Eq. 3.1.4) controls the rate of cell division, the inhibition factor (f , Eq. 3.1.6) limits the amount of cells that undergo cell division, and a cell death rate (k_d , Eq. 3.1.7) accounts for cell death which occurs during the cultivation and specifically after substrate depletion.

The specific transition rate (r_{rans} , Eq. 3.1.4) is estimated based on a Michaelis-Menten kinetic (μ) using the extracellular glucose concentration Glc^x multiplied with a constant (δ).

$$r_{trans} = \mu\delta$$
$$with \begin{cases} \mu = \mu_{\max} \dfrac{[Glc^x]}{k^m_{Glc^x} + [Glc^x]} \\ \delta = \dfrac{1}{2^{1/N^c} - 1} \end{cases} \quad (3.1.4)$$

This constant (δ) depends on the number of different cell classes considered in the model (for a mathematical explanation [159]). The parameters $\mu_{\max}$, Glc^x and $k^m_{Glc^x}$ are the maximum cell-specific growth rate, the extracellular glucose concentration, and the Michaelis-Menten constant, respectively.

The viable cell concentration (X_v) is given by the sum of cells in each class.

$$X_v = \sum_{i=1}^{N^c} X_i \quad (3.1.5)$$

The inhibition factor (f) accounts for a growth inhibition of viable cells by a cell-specific concentration of extracellular glucose concentration (Glc^x).

$$f = 1 - e^{-\alpha \frac{Glc^x}{X_v}} \quad (3.1.6)$$

Note that this inhibition factor corresponds to the fraction of cells that start the division process (transition from the first cell class to the last cell class). Therefore, it has a maximum value of 1 (corresponding to 100% of the first cell class starting the division process) and a minimum of 0 (when 0% of the cells of the first cell class start the division process). To adjust the changes on the inhibition factor in all cultivations a scaling constant (α) is used. Note that the fraction of non-dividing cells from the first cell class was not considered in the growth-related glucose consumption (Eq. 3.1.13), but only in the maintenance related glucose consumption (Eq. 3.1.14).

In order to account for the loss of cell viability, especially after substrate depletion, the cell-specific death rate (k_d) considers a basal cell death rate ($k_d^{\min}$) during the exponential

cell growth phase (caused by cell damage, age, etc.) plus an additional term which approaches $k_d^{\max}$. The increase of $k_d^{\max}$ is inversely correlated with the effective cell growth rate (μf) and this correlation has been previously reported in the literature [165,166].

$$k_d = k_d^{\min} + k_d^{\max}\left(\frac{\beta}{\beta+\mu f}\right)^2 \tag{3.1.7}$$

The parameter β is a constant manually adjusted to fit the overall increase in k_d with cultivation time. This implies that the cell death is not explicitly assumed to depend on the accumulation of by-products such as ammonium or lactate as described in various other cell growth models. Implicitly, however, inhibition is accounted for as by-products accumulate while substrates such as glucose, glutamine and pyruvate are consumed and the substrate level (i.e. glucose concentration) directly influences the effective growth rate. If required, the corresponding term for by-product accumulation could be easily added to the k_d kinetic.

Considering the total number of cells of each class (X_i), the mean cell diameter ($\overline{d}$) is determined by Eq. 3.1.8.

$$\overline{d} = \sum_{i=1}^{N^c}\left(d_m + \frac{d_c - d_m}{N^c - 1}(i-1)\right)\frac{X_i}{X_v} \tag{3.1.8}$$

With equidistant cell diameters ranging from a minimum value (d_m), where cell division is initiated (if not inhibited), to a critical value (d_c) where it divides into two daughter cells. (I.e., the first cell class (X_1) has the lowest diameter (d_m) and the last cell class (X_5) has the largest diameter (d_c). The estimated mean cell diameter in the model is fitted to the mean cell diameter calculated from the experimental data collected by Rath et al. [39,161]. Note that both d_c and d_m were manually adjusted for each experiment to minimize the difference between the experimental and simulated viable cell volume.

Based on the mean diameter (d_c) it is possible to calculate the viable cell volume (V^c, µL) and the cell-specific cell volume (V_s^c, L/cell) using Eqs. 3.1.9 and 3.1.10, respectively.

$$V^c = \pi \frac{\overline{d}^3}{6} X_v 10^{-9} \tag{3.1.9}$$

$$V_s^c = \frac{V^c}{X_v} 10^{-6} \tag{3.1.10}$$

$$r_{macro} = r_i \frac{V_s^c X_v}{V_w} \tag{3.1.11}$$

With cell-specific cell volume (V_s^c, L/cell, Eq. 3.1.10), the viable cell concentration (V^c, cells per mL, Eq. 3.1.5) and the conversion factor to the reference working volume of 1 mL (V_w, 10^{-3}) to convert viable cell volume per mL to viable cell volume per L.

The cell-specific enzyme activities were expressed per cell (v_e, mmol/cell/min), and because the average cell volume changes during cultivation, the maximum volumetric enzyme activities change as well (Eq. 3.1.12).

$$K_e^{\max} = \frac{v_e E_{level}}{V_c^s} \tag{3.1.12}$$

Where $K_e^{\max}$ denotes the maximum volumetric enzyme activity of an enzyme e (mmol/L/min) and is dependent on its related cell-specific enzyme activity (v_e, mmol/cell/min), cell enzyme level (E_{level}, constant) and the cell-specific volume (V_s^c, L/cell). The enzyme level (E_{level}) is a term that was previously proposed for MDCK cells [109] and corresponds to the experiment-specific relative enzyme level of the cell population, which indicates that total enzyme content varies between experiments.

Cells consume substrates and release metabolic by-products over the time course of cultivation, i.e. glucose, glutamine, and glutamate as well as lactate and ammonium. Regarding glucose consumption, growth (r_{x/Glc^x}) and maintenance (r_{m/Glc^x}) rates are considered as described in [159].

$$r_{x/\mathrm{Glc}^x} = \mu\left(X_1 f + \sum_{i=2}^{N^c} X_i \right) Y_{x/Glc^x} \tag{3.1.13}$$

Where the cell growth-specific yield is Y_{x/Glc^x}. And for maintenance

$$r_{m/Glc^x} = m_{Glc^x} V^c \Theta\left[Glc^x \right] \tag{3.1.14}$$

Where m_{Glc^x} is a constant and Θ is a step function, which is one for $Glc^x > 0$ and zero otherwise. This yields the following ODE that describes the dynamics of extracellular glucose uptake.

$$\frac{d[Glc^x]}{dt} = -r_{X/Glc^x} - r_{m/Glc^x} \tag{3.1.15}$$

In contrast to glucose, for other extracellular metabolites such as glutamine and pyruvate, a simpler approach to describe their consumption was used since cell growth was assumed to be independent of their presence in the medium. For this reason, the dynamics of the remaining extracellular substrates and the metabolic by-products were described by Michaelis-Menten-like kinetics. This application is similar to the approach previously used for this cell line [161] and other authors [116,167–170]. Furthermore, it is assumed that the intracellular concentration of certain amino acids, such as glutamate and glutamine, has an impact on their consumption rate as their intracellular concentration has been shown to impact transporter capacity [171]. Note that, ammonium accumulation was simulated accounting for the spontaneous degradation of extracellular glutamine, as reported in [172], and all other intracellular reactions where it is either consumed or produced. These reactions include two enzyme-catalyzed reactions (glutaminase, glutamine synthetase) and amino acid catabolism (r_{AAex}), which were

lumped in one reaction ($r_{\mathrm{NH4}^x_{trans}}$). Since the intracellular ammonium concentration could not be quantified, it is assumed that ammonium does not accumulate intracellularly. Finally, product formation is assumed to be growth-related and a mass action kinetic was used. Refer to the supplement for each kinetic (Eqs. in Appendix A).

$$\frac{d[Gln^x]}{dt} = -r_{Gln^x{}_{trans}} - r_{dGln^x} \tag{3.1.16}$$

$$\frac{d[Glu^x]}{dt} = -r_{Glu_{trans}} \frac{V_s^c X_v}{V_w} \tag{3.1.17}$$

$$\frac{d[\mathrm{NH4}^x]}{dt} = r_{dGln^x} + r_{\mathrm{NH4}^x_{trans}} \tag{3.1.18}$$

$$\frac{d[Lac^x]}{dt} = r_{LDH} \frac{V_s^c X_v}{V_w} - r_{Lac^x{}_{trans}} \tag{3.1.19}$$

$$\frac{d[Pyr^x]}{dt} = -r_{Pyr^x{}_{Trans}} \tag{3.1.20}$$

$$\frac{d[AAT]}{dt} = r_{qAAT} \tag{3.1.21}$$

Structured model of the central carbon metabolism

The structured model for central carbon metabolism includes reactions from glycolysis, citric acid cycle, glutaminolysis, transamination, and the pentose phosphate pathway. To cover changes in extra– and intracellular metabolites concentrations this model requires several growth-related variables such as mean cell volume and glucose uptake rate, so it was linked to the segregated cell growth model.

Glycolysis

The following set of equations (Eqs. 3.1.22–3.1.30) was used to describe the dynamics of intracellular metabolites involved in the glycolytic pathway. In each ODE, changes in the intracellular metabolite concentrations were obtained considering consumption or production in different reactions or transport. Refer to the Appendix A for individual

reactions kinetics. Note that the term $\mu f[C]$ expresses the dilution of each intracellular metabolite (C) by changes in the cell volume caused by the effective growth rate (μf).

$$\frac{d[Glc]}{dt} = r_{\mathrm{GLUT}} - r_{HK} - \mu f[Glc] \tag{3.1.22}$$

$$\frac{d[G6P]}{dt} = r_{HK} - r_{GPI} - r_{G6PDH} - r_{UT} - \mu f[\mathrm{G\,6\,P}] \tag{3.1.23}$$

$$\frac{d[\mathrm{F\,6}P]}{dt} = r_{GPI} - r_{PFK} + r_{TATKF6P} - \mu f[\mathrm{F\,6\,P}] \tag{3.1.24}$$

$$\frac{d[R5P]}{dt} = r_{G6PDH} - r_{TATKF6P} - r_{TATK3PG} - r_{dR5P} - \mu f[\mathrm{R\,5\,P}] \tag{3.1.25}$$

$$\frac{d[UDPGlc]}{dt} = r_{UT} - r_{cUGlC} - r_{GLYS} - \mu f[\mathrm{UDPGlc}] \tag{3.1.26}$$

$$\frac{d[F16P]}{dt} = r_{PFK} - r_{ALD} - \mu f[\mathrm{F\,16\,P}] \tag{3.1.27}$$

$$\frac{d[\mathrm{3\,PG}]}{dt} = 2r_{ALD} - r_{ENO} + r_{TATK3PG} - \mu f[3PG] \tag{3.1.28}$$

$$\frac{d[PEP]}{dt} = r_{ENO} - r_{PK} - r_{PEPCK} - \mu f[\mathrm{PEP}] \tag{3.1.29}$$

$$\frac{d[Pyr]}{dt} = r_{PK} - r_{LDH} - r_{PDH} + r_{ME} - r_{PC} + r_{Pyr^{x}{}_{Trans}} \frac{V_w}{\left(V_s^c X_v\right)} + r_{Lac^{x}{}_{trans}} \frac{V_w}{\left(V_s^c X_v\right)} - r_{AlaTA} - \mu f[\mathrm{Pyr}] \tag{3.1.30}$$

Citric acid cycle, glutaminolysis and transamination

Glycolysis was linked to the TCA cycle through different enzymes like pyruvate dehydrogenase (PDH), phosphoenolpyruvate carboxylase (PEPCK), pyruvate carboxylase (PC), and malic enzyme (ME). The following set of equations (Eqs. 3.1.31–3.1.41) introduces the ODEs used to describe the dynamics of the different metabolites

of this pathway. The dilution of each intracellular metabolite due to changes in the cell volume caused by cell growth was considered by using the term $\mu f[C]$. For individual enzyme kinetics, refer to Appendix A.

$$\frac{d[AcCoA]}{dt} = r_{PDH} - r_{CS} - \mu f[AcCoA] \tag{3.1.31}$$

$$\frac{d[Cit]}{dt} = r_{CS} - r_{ACO} - r_{CL} - \mu f[Cit] \tag{3.1.32}$$

$$\frac{d[cAc]}{dt} = r_{ACO} - r_{ACO2} - \mu f[cAc] \tag{3.1.33}$$

$$\frac{d[Isocit]}{dt} = r_{ACO2} - r_{ICDH} - \mu f[Isocit] \tag{3.1.34}$$

$$\frac{d[Gln]}{dt} = r_{Gln^x{}_{trans}} \frac{V_w}{\left(V_s^c X_v\right)} - r_{Glnase} + r_{GS} - \mu f[Gln] \tag{3.1.35}$$

$$\frac{d[Glu]}{dt} = r_{GLU_{trans}} + r_{Glnase} + r_{AAex} - r_{GS} - r_{GLDH} + r_{AspTA} - \mu f[\mathrm{Glu}] \tag{3.1.36}$$

$$\frac{d[\mathrm{Keto}]}{dt} = r_{ICDH} - r_{KDH} + r_{GLDH} - r_{AspTA} - \mu f[\mathrm{Keto}] \tag{3.1.37}$$

$$\frac{d[\mathrm{Suc}]}{dt} = r_{KDH} - r_{SDH} - \mu f[\mathrm{Suc}] \tag{3.1.38}$$

$$\frac{d[\mathrm{Fum}]}{dt} = r_{SDH} - r_{FMA} - \mu f[\mathrm{Fum}] \tag{3.1.39}$$

$$\frac{d[\mathrm{Mal}]}{dt} = r_{FMA} - r_{MDH} - r_{ME} - \mu f[\mathrm{Mal}] \tag{3.1.40}$$

$$\frac{d[\mathrm{OAA}]}{dt} = r_{MDH} + r_{AspTA} + r_{CL} + r_{PC} - r_{PEPCK} - r_{CS} - \mu f[\mathrm{OAA}] \tag{3.1.41}$$

Energy metabolism

ATP is either generated directly in some reactions or produced from several precursors such as NADH and $FADH_2$ through oxidative phosphorylation. On the other hand, ATP is consumed for cell growth, maintenance metabolism, various other reactions of glycolysis and the TCA cycle, and in several futile cycles. Here, ATP production and its usage were lumped in the rates (r_{CCM}) and (r_{dATP}), respectively. Furthermore, it was assumed that energy precursors do not accumulate, rather they are used directly in the oxidative phosphorylation (electron transport) pathway, and that 2.5 ATP are produced from NADH and 1.5 ATP from $FADH_2$ as reported in [164,173]. For simplification and lack of experimental data for many cofactors, their regulation or their homeostasis-driven regulation are not considered which evidently could place limitations on the model predictions. The following ODE (Eq. 3.1.42) was used. The dilution of ATP due to changes in the cell volume, caused by cell growth, was considered by using the term $\mu f[C]$. Kinetic equations for each reaction/transport are provided in Appendix A.

$$\frac{d[\mathrm{ATP}]}{dt} = r_{CCM} - r_{dATP} - \mu f[\mathrm{ATP}] \tag{3.1.42}$$

3.1.2 MDCK suspension cell model

This section introduces the dynamic model that describes both cell growth, virus production and metabolism developed for MDCK suspension cells by Ramos et al., 2022 [158]. The model established for this study follows, in structure and basic assumptions, a model established previously for a human derived cell line AGE1.HN.AAT suspension cells [157]. This model describes cell growth, virus production and metabolism by coupling model variables from a segregated growth model (for the macroscopic scale) with a structured model of the central carbon metabolism (for the microscopic scale). Compared to the previous approach [157], various modifications were made to cover the virus infection phase. This includes a description of virus production (the concentration of all virus particles in the supernatant) as well as changes in cell growth and the death of infected cells that are not related to the substrate availability. Further modifications,

described in more detail below, refer to the introduction of new states in the structured part of the model dealing with the central metabolism. This includes new state variables for the intracellular concentration of lactate and ammonium, a rate to describe the consumption of pyruvate, the transport of ammonium and lactate, and some reactions/transport kinetics modified to fit the experimental data sets obtained for shake flask cultivations (compared to stirred tank bioreactors described before [55]). Finally, equations related to alpha-1-antitrypsin production were removed. An overview of this model is shown in Fig. 3.2.

Following the previous model, the macroscopic scale are linked with the intracellular scale and vice versa (Eq. 3.2.1) using r_{macro} (mmol min^{-1} L^{-1} for the volume referring to the bioreactor) and the corresponding intracellular rates r_i (mmol min^{-1} L^{-1} for the volume referring to the cells). The cell-specific enzyme activities were expressed per cell (v_e, mmol/cell/min), and because the average cell volume changes during cultivation, the maximum volumetric enzyme activities change as well (introduced previously in Eq. 3.1.12).

In the following section, the ODEs for the segregated cell growth model, virus titer and the structured model for the central carbon metabolism of MDCK suspension cells are introduced.

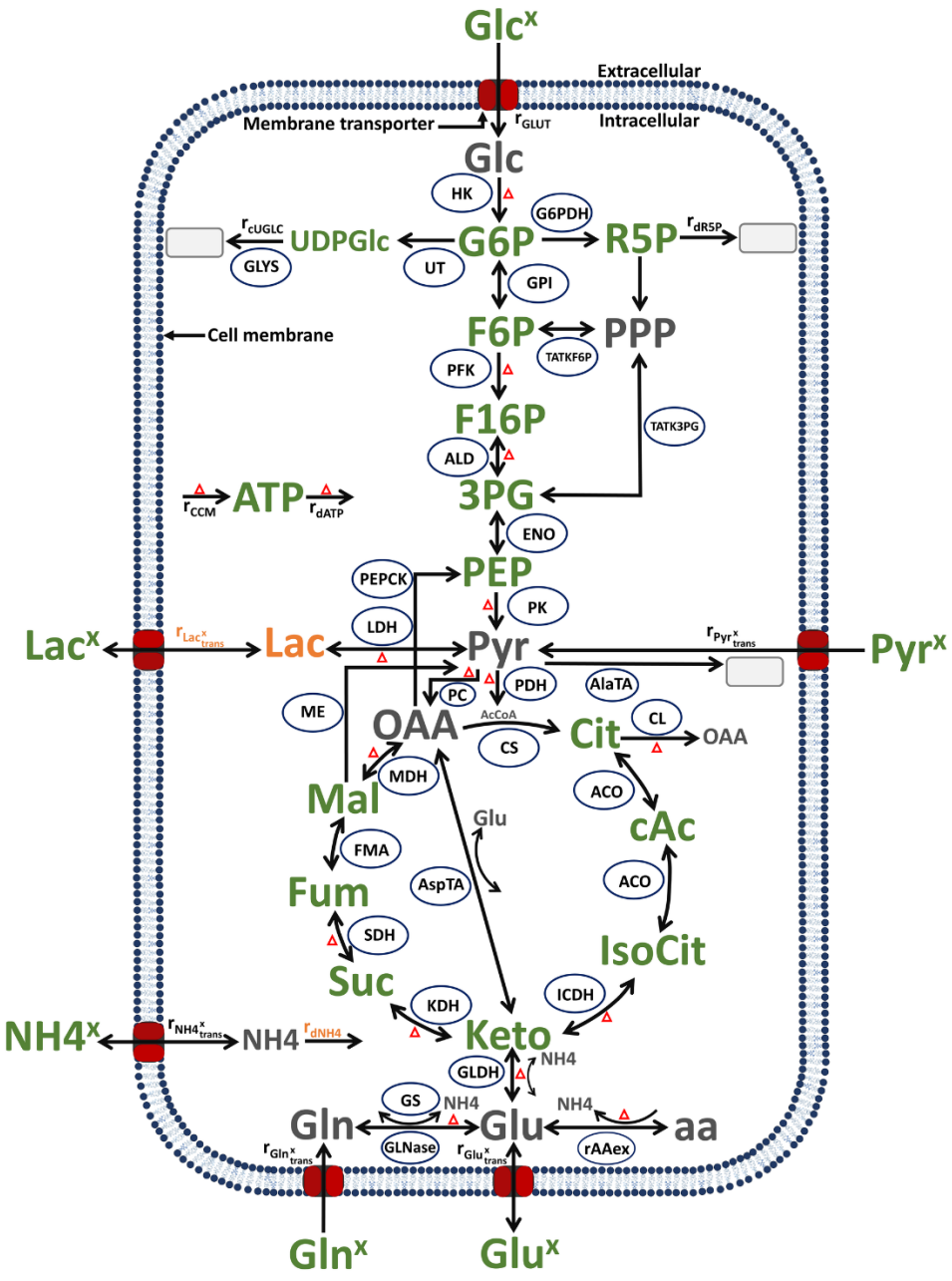

Figure 3.2.: Simplified model of the central carbon of MDCK suspension cells, modified from [157] **(changes to the previous model in orange).** In green: metabolites and product measured experimentally; in grey: metabolites not measured. Ellipsoids: enzymes considered in the model. Arrows: reactions or transport, with the arrowhead indicating the reaction or transport direction (for simplification, reversible reactions have an arrow for both directions). Grey rectangles: sinks or metabolites not accounted for in the model. Red triangles: all the reactions

included in the energy balance. Abbreviations of metabolites and product**:** 3PG: 3-phosphoglycerate, AcCoA: acetyl coenzyme A, ATP: adenosine tri-phosphate, cAc: cis-Aconitate, Cit: citrate, F16P: fructose 1,6-biphosphate, F6P: fructose-6-phosphate, Fum: fumarate, G6P: glucose-6-phosphate, Glc: glucose (intracellular), Glc^x: glucose (extracellular), Gln: glutamine (intracellular), Gln^x: glutamine (extracellular), Glu: glutamate (intracellular), Glu^x: glutamate (extracellular), IsoCit: iso-citrate, Keto: alpha-ketoglutarate, Lac^x: lactate (extracellular), Mal: malate, NH4: ammonium (intracellular), $NH4^x$: ammonium (extracellular), OAA: oxaloacetate, PEP: phosphoenolpyruvate, Pyr: pyruvate (intracellular), Pyr^x: pyruvate (extracellular), R5P: ribose-5-phosphate, SUC: succinate, UDPGlc: uridine diphosphate Glucose. Abbreviations of enzymes and transport rates: HK: Hexokinase, G6PDH: Glucose-6-phosphate dehydrogenase, r_{dATP}: Reaction rate for ribose-5-phosphate consumption, UT: Uridyl transferase, GLYS: Glycogen synthetase, r_{uGLC}: Reaction rate for other uridine diphosphate glucose consumption, GPI: Glucose-6-phosphate isomerase, TATKF6P: Transaldolase and transketolase, TATK3PG: Transaldolase and transketolase, PFK: Phosphofructokinase, ALD: Aldolase, r_{qAAT}: Reaction rate for product formation, ENO: Enolase, r_{CCM}: Reaction rate for overall ATP production, r_{dATP}: Reaction rate for overall ATP consumption, PK : Pyruvate kinase, PEPCK: Phosphoenolpyruvate-kinase, LDH: Lactate dehydrogenase, PC: Pyruvate carboxylase, PDH: Pyruvate dehydrogenase, AlaTA: Alanine transaminase, ME: Malic enzyme, CS : Citrate synthetase, CL: Citrate lyase, ACO: Aconitase, ICDH: Isocitrate dehydrogenase, KDH: Ketoglutarate dehydrogenase, AspTA: Aspartate transaminase, SDH: Succinate dehydrogenase, FMA: Fumarase, MDH: Malate dehydrogenase, GLDH: Glutamate dehydrogenase, GS: Glutamine synthetase, GLNase: Glutaminase, r_{AAex}: Amino acids degradation, r_{GLUT}: Reaction rate for extracellular glucose consumption, $r_{\mathrm{Pyr}^x_{trans}}$: Reaction rate for extracellular pyruvate consumption, $r_{\mathrm{NH4}^x_{trans}}$: Reaction rate for ammonium production from intracellular rates, $r_{\mathrm{Gln}^x_{trans}}$: Reaction rate for extracellular glutamine consumption, $r_{\mathrm{Glu}^x_{trans}}$: Reaction rate for extracellular glutamate consumption and/or production from intracellular rates. Figure taken from Ramos et al., 2022 [158].

Segregated cell growth and infection model

The segregated cell growth and infection model describes the dynamics of cells, substrates, metabolic by-products, and virus particles on the macroscopic scale.

The specific transition rate (r_{trans} , Eq. 3.1.43), between the cell classes is described by a Monod equation (μ) using the extracellular glucose concentration (Glc^x) multiplied with a constant (δ) that depends on the number of cell classes considered in the model (for a mathematical explanation, see [159]). The transition rate is not equal for infected and mock-infected cells; to use the same model variable for both, two step-functions are used. The first step function (ε) is 0 for mock-infected cells and 1 for infected cells.

$$r_{trans} = \mu\,\delta\left(1-\Phi_1\varepsilon\right)$$
$$with\begin{cases}\mu = \mu_{\max}\dfrac{[Glc^x]}{k^m_{Glc^x}+[Glc^x]}\\ \delta = \dfrac{1}{2^{1/N^c}-1}\end{cases} \qquad (3.1.43)$$

The parameter $\mu_{\max}$ is the maximum cell-specific growth rate and $k^m_{Glc^x}$ is the Monod constant. A time-dependent sigmoidal step function (Φ_1 and Φ_2) was used to take into account the decrease in μ and the increase in the death rate (k_d , Eq. 3.1.46), respectively, after virus infection. This function was previously used to describe the transition of viable cells to apoptosis for IAV infected cells [156], and the smoothness of the transition depends on a constant (ρ_1 , manually adjusted).

$$\Phi_1 = \frac{1}{1+e^{(\rho_1-\mathrm{hpi})}} \qquad (3.1.44)$$

The viable cell growth inhibition factor f (Eq. 2.1.45) corresponds to a limitation in the number of cells that start cell division and is related to extracellular glucose concentration (Glc^x). It has a maximum value of 1 (corresponding to 100% of the first cell class can start the division process) and a minimum of 0 (0% of the cells of the first cell class can start the division process). A scaling constant (α) was used to adjust the changes in the inhibition factor. Here, due to the arrest observed in total cell number after infection it was

assumed that infected cells do not divide anymore by using the step function (ε) introduced above.

$$f = \left(1 - e^{-\alpha \frac{Glc^x}{X_v}}\right)(1-\varepsilon) \tag{3.1.45}$$

Overall, the inhibition factor f (Eq. 3.1.45) is effectively zero after virus infection and the growth rate decreases with a smooth step such as function (Φ_1) leading also to a smooth decrease in the transition rate (r_{trans}, Eq. 3.1.43). This implies that even after a synchronous infection, some cells of the classes ($X_2 - X_4$, Eqs. 3.1.47–3.1.49) finish the division process leading to a small but noticeable increase in the cell concentration shortly after the infection step. More importantly, however, this also has an impact on the dynamics of the mean cell diameters and consequently the cell-specific volume and maximum enzyme activities.

During the cell growth phase, cell death after substrate depletion is described by the rate k_d (Eq. 3.1.46) as introduced before by Ramos et al. [157]. It considers a basal cell death rate ($k_d^{\min}$) related to cell age, mechanical damage, etc. and an additional term ($k_d^{\max}$), which is inversely correlated with the effective cell growth rate. The parameter β is an adjustable constant for which effective growth rate and death rate are equal.

$$k_d = \left(k_d^{\min} + k_d^{\max}\left(\frac{\beta}{\beta + \mu f}\right)^2\right)(1-\varepsilon) + \left(k_{d\,\mathrm{inf}}^{\min} + k_{d\,\mathrm{inf}}^{\max}\Phi_2\right)\varepsilon \tag{3.1.46}$$

Mechanisms of cell death are obviously not the same for infected and mock-infected cells. In particular, infected cells mainly die due to virus-induced apoptosis. Accordingly, death rate (k_d) in these two scenarios also makes use of the step function (ε) introduced previously, and a smooth step-like function (Φ_2). The latter is similar to the previously introduced step function (Φ_1, Eq. 3.1.44), where the constant parameter ρ_1 was replaced with a different value (ρ_2, manually adjusted). More specifically, for infected cells, it is assumed that a basal cell death rate ($k_{d\,\mathrm{inf}}^{\min}$) applies and, in addition, a term ($k_{d\,\mathrm{inf}}^{\max}$) is added,

which is a time-related increase in the cell death rate caused by using the time step function (Φ_2). The time-related increase in the cell death rate is closely related to the transition to an apoptotic state typically observed for infected cells, as described by Rüdiger et al. [156].

The segregated cell growth model approach allows the consideration of several classes of cells. Similar to previous approaches [157,159], five classes ($N^c = 5$) were used to describe changes in the mean cell diameter of MDCK cells. Analyses and discussions regarding the choice of five cell classes can be found in appendix C and further discussions elsewhere in [109,157,159,160].

Because a segregated cell growth model enables the estimation of the mean cell diameter, it also allows the estimation of the total viable cell volume. Estimating the cell volume was critical for determining the cell-specific volume, which impacts the maximum volumetric enzyme activities (discussed in the previous section, Eq. 3.1.12). The model describes the cell transition between each cell class using a transition rate (r_{trans}, Eq. 3.1.43), starting with the class (X_1) which contains the smallest cells and ending with the class (X_5) containing the largest cells. The latter divide and produce two cells of the first class (Eqs. 3.1.47–3.1.49).

$$\frac{dX_1}{dt} = r_{trans}(2\,X_5 - X_1 f) - k_d X_1, \tag{3.1.47}$$

$$\frac{dX_2}{dt} = r_{trans}(X_1 f - X_2) - k_d X_2, \tag{3.1.48}$$

$$\frac{dX_i}{dt} = r_{trans}(X_{i-1} - X_i) - k_d X_i, \text{ for } \mathrm{i} = 3,...,\mathrm{N}^c. \tag{3.1.49}$$

Given the different cell classes introduced, the viable cell concentration (X_v) was calculated as the sum of cells in each class (Eq. 3.1.50).

$$X_v = \sum_{i=1}^{N^c} X_i \tag{3.1.50}$$

The mean cell diameter ($\overline{d}$) was estimated using Eq. 3.1.51, in which the number of cells of each class (X_1) and their respective diameters are considered. Here, the diameter of cells in each class are equidistant ranging from a minimum value (d_m, for the smallest cells found in the first class X_1) to a critical diameter value (d_c, for the largest cells found in class X_{N^c}). Note that both d_c and d_m were manually adjusted for each experiment.

$$\overline{d} = \sum_{i=1}^{N^c} \left(d_m + \frac{d_c - d_m}{N^c - 1}(i-1) \right) \frac{X_i}{X_v} \tag{3.1.51}$$

Using the mean diameter ($\overline{d}$), the viable cell volume (V^c, µL) and the cell-specific volume (V_s^c, L/cell) were calculated using Eqs. 3.1.52 and 3.1.53, respectively.

$$V^c = \pi \frac{\overline{d}^3}{6} X_v 10^{-9} \tag{3.1.52}$$

$$V_s^c = \frac{V^c}{X_v} 10^{-6} \tag{3.1.53}$$

Substrates and dynamics of released metabolic by-products are also part of the macroscopic model. These include extracellular glucose, glutamine, glutamate, lactate and ammonium. The glucose dynamics was described using cell growth-related and maintenance terms. The remaining extracellular metabolites were described using a Michaelis-Menten-like kinetics or more complex equations in accordance with previous studies describing their transport through the cell membrane [116,157,161,167–170]. In particular, these metabolites were produced and/or consumed independently from the cell growth rate and cell growth occurs even after depletion in some cases. The spontaneous degradation of extracellular glutamine to ammonium was also taken into account, as reported in [172]. Eqs. 3.1.54–3.1.59 introduce the ODEs associated with the extracellular

metabolites and the transport kinetics in these ODEs, chosen based on previous literature [109,157,159,160,174]. Kinetic equations for each reaction/transport are provided in Appendix B.

$$\frac{d[Glc^x]}{dt} = -r_{X/Glc^x} - r_{m/Glc^x} \tag{3.1.54}$$

$$\frac{d[Gln^x]}{dt} = -r_{Gln^x{}_{trans}} - r_{dGln^x} \tag{3.1.55}$$

$$\frac{d[Glu^x]}{dt} = -r_{Glu_{trans}} \frac{V_s^c X_v}{V_w} \tag{3.1.56}$$

$$\frac{d[\mathrm{NH4}^x]}{dt} = r_{dGln^x} - r_{\mathrm{NH4}^x_{trans}} \frac{V_s^c X_v}{V_w} \tag{3.1.57}$$

$$\frac{d\left[Lac^x\right]}{dt} = r_{Lac^x_{trans}} \frac{V_s^c X_v}{V_w} \tag{3.1.58}$$

$$\frac{d[Pyr^x]}{dt} = -r_{Pyr^x{}_{Trans}} \tag{3.1.59}$$

A state variable was required to describe the virus dynamics. As the maximum number of virions produced per cell, the CSVY ($v_p = 11989$), corresponds to only 0.55% of the mean cell volume, no attempts were made to describe the virus particle increase by substrate- or precursor-based kinetics. Instead, the concentration of all virions (V_t) released from infected cells was considered using Eq. 3.1.60), where v_p is the virus production rate and Φ_3 is a smooth step function to account for the time delay between virus infection and virus release (eclipse phase). This step function is similar to the previously introduced step function (Φ_1, Eq. 3.1.44), where the constant parameter ρ_1 was replaced with a different value (ρ_3, manually adjusted).

$$\frac{d[V_t]}{dt} = X_v \cdot v_p \Phi_3 \tag{3.1.60}$$

Structured Model of the Central Carbon Metabolism

The structured model for central carbon metabolism describes the microscopic scale, and comprises reactions from glycolysis, citric acid cycle, glutaminolysis, transamination, and the pentose phosphate pathway. The model was coupled with the structured cell growth model using growth-related variables such as the cell-specific volume, and uptake or release rates of the extracellular substrates and metabolic by-products, respectively. This coupling was accomplished by converting the model variables between the different scales using (Eq. 3.2.1, discussed in the section below). This implied using substrate consumption rates as input and metabolic by-products accumulation rates as the outputs of the intracellular metabolic network, effectively allowing the description of dynamics of metabolites both at the extra- and the intracellular level. In this model extension, to describe the dynamics of metabolic product accumulation on the extracellular level intracellular concentrations of lactate and ammonium were considered (Eqs. 3.1.70 and 3.1.77). In addition, kinetics related to PEP, 3-phosphoglycerate, Lac^x, Glu^x, $NH4^x$, Cit and Keto, were updated from the model described in the previous section by Ramos et al. [157]. There may be some differences in central carbon metabolism of MDCK suspension cells compared to AGE1.HN.AAT suspension cells or that metabolism of suspension cells. These differences may, however, be due to cultivations performed in shaker flasks (MDCK cells) and stirred tank reactors (AGE1.HN.AAT cells). Specifically, the main changes concern few enzymes or transporter kinetics such as enolase (ENO), aldolase (ALD), pyruvate kinase (PK), PC, glutaminase (Glnase), ammonium transporter ($NH4^x_{trans}$), citrate lyase (CL) and aspartate transaminase (AspTA) according to the literature [174]. The equations of ODEs for the structured intracellular metabolism states are provided below and individual enzyme/transporter kinetics are provided in Appendix B.

Glycolysis

Glycolysis and pentose phosphate pathways were described using the ODEs in Eqs. 3.1.61–3.1.70 in accordance with the structure and basic assumptions for modeling MDCK cells [109] and other animal cell lines [157]. For each intracellular metabolite (C), the consumption or production by individual enzymes was considered. The enzyme and transport kinetics in these ODEs, chosen based on previous literature [109,157,159,160,174]. Additionally, the transport of glucose (r_{GLUT}), pyruvate) ($r_{Pyr^x_{trans}}$) and lactate ($r_{Lac_{trans}}$) were considered, linking the extra- and intracellular forms of these metabolites. The dilution of each intracellular metabolite due to changes in the cell volume caused by cell growth was considered by using the term $\mu f[C]$. Kinetic equations for each reaction/transport are provided in Appendix B.

$$\frac{d[Glc]}{dt} = r_{\mathrm{GLUT}} - r_{HK} - \mu f[Glc] \tag{3.1.61}$$

$$\frac{d[G6P]}{dt} = r_{HK} - r_{GPI} - r_{G6PDH} - r_{UT} - \mu f[\mathrm{G\,6\,P}] \tag{3.1.62}$$

$$\frac{d[\mathrm{F\,6}P]}{dt} = r_{GPI} - r_{PFK} + r_{TATKF6P} - \mu f[\mathrm{F\,6\,P}] \tag{3.1.63}$$

$$\frac{d[R5P]}{dt} = r_{G6PDH} - r_{TATKF6P} - r_{TATK3PG} - r_{dR5P} - \mu f[\mathrm{R\,5\,P}] \tag{3.1.64}$$

$$\frac{d[UDPGlc]}{dt} = r_{UT} - r_{cUGlC} - r_{GLYS} - \mu f[\mathrm{UDPGlc}] \tag{3.1.65}$$

$$\frac{d[F16P]}{dt} = r_{PFK} - r_{ALD} - \mu f[\mathrm{F16\,P}] \tag{3.1.66}$$

$$\frac{d[\mathrm{3\,PG}]}{dt} = 2r_{ALD} - r_{ENO} + r_{TATK3PG} - \mu f[3PG] \tag{3.1.67}$$

$$\frac{d[PEP]}{dt} = r_{ENO} - r_{PK} - r_{PEPCK} - \mu f[\mathrm{PEP}] \tag{3.1.68}$$

$$\frac{d[Pyr]}{dt} = r_{PK} - r_{LDH} - r_{PDH} + r_{ME} - r_{PC} + r_{Pyr^x{}_{Trans}} \frac{V_w}{\left(V_s^c X_v\right)} - r_{AlaTA} - \mu f[\mathrm{Pyr}] \tag{3.1.69}$$

$$\frac{[Lac]}{dt} = r_{LDH} - r_{Lac_{trans}} - \mu f[Lac] \tag{3.1.70}$$

Citric acid cycle, glutaminolysis and transamination

Following the structure and basic assumptions from previous work [157], Eqs. 3.1.71–3.1.82 were used to describe citric acid cycle (TCA), glutaminolysis and transamination. For each ODE, the individual enzyme and transport kinetics, chosen based on previous literature [109,157,159,160,174]. Additionally, the transport of glutamine ($r_{\mathrm{Gln}^x_{trans}}$), glutamate ($r_{GLU_{trans}}$) and ammonium ($r_{\mathrm{NH4}^x_{trans}}$) were considered, linking the extra- and intracellular forms of these metabolites. The dilution of each intracellular metabolite due to changes in the cell volume caused by cell growth was considered by using the term $\mu f[C]$. Kinetic equations for each reaction/transport are provided in Appendix B.

$$\frac{d[AcCoA]}{dt} = r_{PDH} - r_{CS} - \mu f[AcCoA] \tag{3.1.71}$$

$$\frac{d[Cit]}{dt} = r_{CS} - r_{ACO} - r_{CL} - \mu f[Cit] \tag{3.1.72}$$

$$\frac{d[cAc]}{dt} = r_{ACO} - r_{ACO2} - \mu f[cAc] \tag{3.1.73}$$

$$\frac{d[Isocit]}{dt} = r_{ACO2} - r_{ICDH} - \mu f[Isocit] \tag{3.1.74}$$

$$\frac{d[Gln]}{dt} = r_{Gln^x{}_{trans}} \frac{V_w}{\left(V_s^c X_v\right)} - r_{Glnase} + r_{GS} - \mu f[Gln] \tag{3.1.75}$$

$$\frac{d[Glu]}{dt} = r_{GLU_{trans}} + r_{Glnase} + r_{AAex} - r_{GS} - r_{GLDH} + r_{AspTA} - \mu f[\mathrm{Glu}] \tag{3.1.76}$$

$$\frac{d[NH4]}{dt} = r_{\mathrm{NH4}^x{}_{trans}} + (1+\omega) r_{AAex} + r_{GLNase} + r_{GL\mathrm{DH}} - r_{d\mathrm{NH4}} - r_{GS} - \mu f[NH4] \tag{3.1.77}$$

$$\frac{d[\mathrm{Keto}]}{dt} = r_{ICDH} - r_{KDH} + r_{GLDH} - r_{AspTA} - \mu f[\mathrm{Keto}] \tag{3.1.78}$$

$$\frac{d[\mathrm{Suc}]}{dt} = r_{KDH} - r_{SDH} - \mu f[\mathrm{Suc}] \tag{3.1.79}$$

$$\frac{d[\mathrm{Fum}]}{dt} = r_{SDH} - r_{FMA} - \mu f[\mathrm{Fum}] \tag{3.1.80}$$

$$\frac{d[\mathrm{Mal}]}{dt} = r_{FMA} - r_{MDH} - r_{ME} - \mu f[\mathrm{Mal}] \tag{3.1.81}$$

$$\frac{d[\mathrm{OAA}]}{dt} = r_{MDH} + r_{AspTA} + r_{CL} + r_{PC} - r_{PEPCK} - r_{CS} - \mu f[\mathrm{OAA}] \tag{3.1.82}$$

Energy metabolism

Following the structure and basic assumptions from previous work [157], Eq. 3.1.83 was used to describe ATP dynamics. ATP production was lumped into one rate (r_{CCM}), where 2.5 ATP are produced from NADH and 1.5 ATP from $FADH_2$ as reported in [164,173]. ATP usage was lumped into a degradation term (r_{dATP}), which contains the terms for the estimated consumption for cell growth and maintenance. It was assumed that energy precursors do not accumulate but are used directly in the oxidative phosphorylation

(electron transport) pathway. Furthermore, due to the lack of experimental data, the impact of cofactors on enzyme regulation and homeostasis was not considered. The dilution of ATP due to changes in the cell volume caused by cell growth was considered by using the term $\mu f[C]$. Kinetic equations for each reaction/transport are provided in Appendix B.

$$\frac{d[\mathrm{ATP}]}{dt} = r_{CCM} - r_{dATP} - \mu f[\mathrm{ATP}] \tag{3.1.83}$$

3.2 Coupling the cell growth and metabolism model

Coupling the segregated cell growth model and the structured model for the central carbon metabolism for AGE1.HN.AAT and MDCK (Fig. 3.3) requires the following considerations: Using the same model variables at the macro- and microscopic scale considered in this approach demands a conversion function, which provides a link between rates on the macroscopic scale (r_{macro}, mmol/min/L referring to the working volume of the shaker) and the corresponding rates at the microscopic scale r_i (mmol/min/L refers to the volume of cells). Where V_s^c is cell-specific volume (L/cell) and X_v is the total viable cell concentration (cells/mL). To convert the viable cell volume per mL to the viable cell volume per L, a conversion factor (V_w, 10^{-3}) was used.

$$r_{macro} = r_i \frac{V_s^c X_v}{V_w} \tag{3.2.1}$$

Cell enzyme activities were expressed per cell (v_e, mmol/cell/min), and because the average cell volume changes during cultivation, the maximum volumetric enzyme activities change as well (Eq. 3.2.2).

$$K_e^{\max} = \frac{v_e E_{level}}{V_c^s} \tag{3.2.2}$$

Where $K_e^{\max}$ denotes the maximum volumetric enzyme activities (mmol/L/min) and are dependent on their related cell-specific enzyme activity (v_e, mmol/cell/min), the enzyme level (E_{level}, constant) and the cell-specific volume (V_c^s, L/cell). The enzyme level (E_{level}) is a term that was previously proposed for MDCK cells [109] and corresponds to the experiment-specific relative enzyme level of the cell population, which indicates that total enzyme content varies between experiments. In this instance, since the experiments were conducted using the same pre-culture, the enzyme level was set to one for both cultivations.

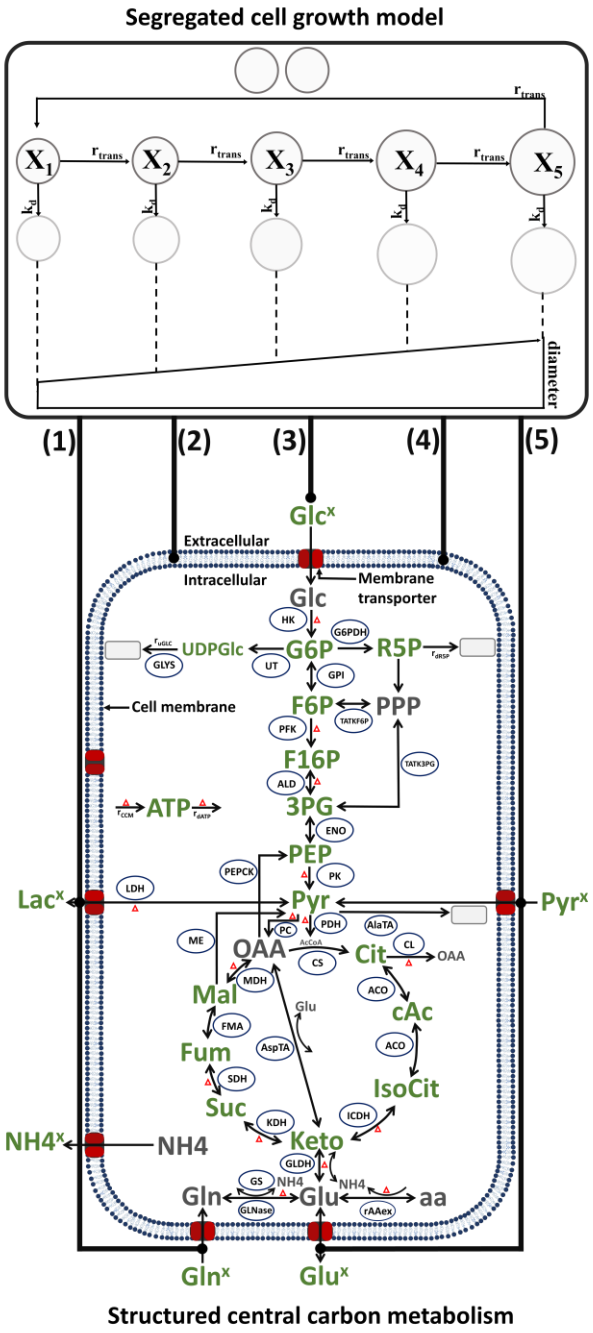

Figure 3.3.: Scheme of coupling of the segregated cell growth and the structured central carbon metabolism model. Connected parameters: **(1)** Time-dependent extracellular metabolite productions/consumptions rate (Gln^x, Lac^x, $NH4^x$), predicted directly from intracellular rates; **(2)** Cell-specific volume, and the cell-volume-specific maximum enzyme activity; **(3)** Time-dependent main substrate uptake rate (Glc^x); **(4)** Growth rate, to account for dilution of intracellular metabolites pools during cell growth;

(5) Time-dependent extracellular metabolite productions/consumptions (Glu^x, Pyr^x). k_d is the cell death rate, r_{trans} is the transition rate, Glc^x: glucose (extracellular), Gln^x: glutamine (extracellular), Glu^x: glutamate (extracellular), Lac^x: lactate (extracellular), $NH4^x$: ammonium (extracellular), Pyr^x: pyruvate.

3.3 Parameter estimation and model simulation

3.3.1 AGE1.HN.AAT suspension cell model

Parameter fitting and visualization of the results was carried out in MATLAB (Version R2012b, The Mathworks, Inc.). For handling of the model and the data, the Systems Biology Toolbox 2 developed by Schmidt and Jirstrand [175] was used. Integration of ODEs was performed with CVODE from SUNDIALS [176]; the enhanced scatter search (eSS) algorithm was used for stochastic global optimization [177,178]. For the implementation of the bootstrap method, *in silico* data were generated through Monte-Carlo sampling using the average of the experimental data and their corresponding standard deviation. In the next step, parameters were fitted using these newly generated data sets.

In the first step, parameters from the segregated cell growth model (Eqs. 3.1.1–3.1.21) were fitted using one of the available experimental data sets. For optimization the initial values of the parameters were estimated from the experimental data (i.e. cell-specific growth rate) or taken from the literature [109,160]. Next, variables from this model (growth related glucose consumption rate, maintenance related glucose consumption rate, cell-specific volume, cell growth rate) were used as input for the structured central carbon metabolism model and the parameters of this model were fitted using one of the available experimental data sets. In this step, dynamics of some extracellular metabolites (extracellular glutamine, extracellular pyruvate, extracellular lactate, extracellular glutamate) were also considered since these were predicted directly from the intracellular ODEs. Overall, 132 parameters were fitted using around 353 data points and the minimization applied Eq. 3.2.3,

$$\min_{p} \sum_{e=1}^{T^e} \sum_{n=1}^{T^n} \sum_{i=1}^{T^i} \left(\frac{prediction_{eni} - data_{eni}}{\eta} \right)^2 \tag{3.2.3}$$

Where p is the parameter set, $e = 1, ..., T^e$ the number of experiments, $n = 1, ..., T^n$ is number of states and $i = 1, ..., T^i$ the time, while η is the weighting to the maximum for state n in the experiment e. Due to the complexity of the developed model and the limited number of experimental data sets to test the model predictability, parameter overfitting (fitting of the noise in the data set) cannot be ruled out in this instance. Nevertheless, parameter fitting of over 2500 data sets generated *in silico* using Monte-Carlo sampling (as described above) resulted in reasonably small confidence intervals (Tables B1.1 and B1.2 in Appendix B1). Due to the model complexity and data variability, only one data set is used for parameter estimation. Accordingly, the parameter overfitting cannot be discarded but it can be presumably limited if the same parameter set is also able to describe independent experiments.

The established model was used with different initial conditions, and the same parameter set to simulate different batch cultivations. Note that the initial conditions for the state variables of the segregated cell growth model were adjusted manually within the error of the experimental data at the start of the cultivation. The initial conditions of the structured intracellular model states were obtained from the simulation of a pre-culture from late exponential growth phase. To simulate the preculture growth until the exponential growth phase (for around 75 h), the known concentrations of all compounds in the medium is used as initial conditions. Regarding the initial conditions for the intracellular states the initial values were based on the first sampling time point (in cases where no data was available, we use reasonable low initial concentrations from previous studies of our group and general literature). Thereafter, the estimated basal cell death rate ($k_d^{\min}$) was increased by a factor of 300 for 7 min cultivation time to take into account the drop in intracellular metabolite concentrations resulting from sampling, centrifugation and re-suspension of cells before measurements were performed. Note that sampling, centrifugation, and resuspension of cells lasted around 7 min in this case and thus it was assumed that the cells metabolic activity would persist. A list of all initial values is provided in Tables B1.3 and B1.4 in Appendix B1.

3.3.2 MDCK suspension cell model

The model was implemented using the Systems Biology Toolbox 2 [175] in MATLAB (Version R2012b, the Mathworks, Inc.). Model simulations were carried out using MATLAB executable (mex) of the model, which speeds up the execution time significantly. For the integration of ODEs, the CVODE from SUNDIALS was used [176]. For the parameter optimization, a covariance matrix adaptation evolution (CMA-ES) algorithm was used that enables stochastic and derivative free global optimization [179,180]. The CMA-ES was used as it performed better than methods used in a similar study [157]. For the implementation of the bootstrap method, *in silico* data were generated through Monte-Carlo sampling using the average of the experimental data and their corresponding standard deviation. In the next step, parameters were fitted using these newly generated data sets.

In a first step, parameters related to cell growth and extracellular glucose dynamics (Eqs. 3.1.43 and 3.1.45–3.1.54) were fitted using the experimental data from the mock-infected culture. Next, parameters for the infected culture were fitted (Eqs. 3.1.44 and 3.1.60; step functions Φ_1, Φ_2, Φ_3) to describe virus dynamics and the transition from exponential cell growth phase to cell death after virus infection, respectively. Finally, the parameters related to the dynamics of the remaining extracellular (Eqs. 3.1.55–3.1.59) and intracellular metabolites were fitted (Eqs. 3.1.61–3.1.83). During optimization, the initial values for the parameters were either taken from the literature [45,52,58] or estimated from experimental data (i.e., the cell-specific growth rate). Note that, apart from the description of virus dynamics, cell growth and cell death, the same kinetics (transport kinetics, intracellular reactions kinetics) and the same set of parameters were used for both the infected and mock-infected cells. Overall, 143 parameters were fitted using 360 data points applying Eq. 3.2.3. Bootstrap parameter fitting of over 2500 data sets generated *in silico* using Monte-Carlo sampling (as described above) was performed. The parameter bounds using these parameter sets can be found in Tables B2.1 and B2.2 in Appendix B2.

Note that the initial values for the state variables of the cells and extracellular metabolite concentrations were adjusted manually within the error range of the first experimental data point. The same principle was used for the state variable that describes the virus

particle concentration. Initial conditions for the concentration of intracellular metabolites were obtained via simulation of a pre-culture coming from late exponential growth phase (85 h). For the simulation of the pre-culture, the initial concentration of state variables related to extracellular metabolites were based on the known medium composition. For the state variables regarding intracellular metabolites, the concentration of the first sampling time point was used (in case these data were not available, a low concentration was assumed taking into account values from previous studies [109,157,159,160]). A list of all initial values is given in Tables B2.3 and B2.4 in Appendix B2.

4 Chapter
Results and discussion

The next two sections describe the results and discussions regarding simulations of the two separate dynamic models of two suspension cells. These modeling results were published in [157,158] and parts of the discussion were used without quotation to facilitate reading. The first model was developed to describe batch cultivations of AGE1.HN.AAT suspension cells, covering cell growth, A1AT production and key metabolites in central carbon metabolism [157]. The procedures and analytics used to collect the experimental data used for AGE1.HN.AAT suspension cells were described in detail elsewhere [157,161,181]. A model extension was performed to describe MDCK suspension cell shaker flask cultivations. The extended model describes cell growth, IAV production and key metabolites in central carbon metabolism [158]. The procedures and analytics to collect the experimental data of MDCK suspension cells were described in detail elsewhere [56,158].

4.1 AGE1.HN.AAT suspension cell model

4.1.1 Cell growth

Model simulations against experimental data (viable cells, the mean cell diameter, and the total cell volume) for four AGE1.HN.AAT cultivations at 0.5–2.5 L scale performed by Rath et al. [39,161] are shown in Fig. 4.1. Each simulation is based on specific initial conditions and using one set of parameters (Table 3 in Appendix B1.3). Note that the simulations also cover both the exponential cell growth phase and cell death phase which

is often neglected in animal cell models (e.g. the previous studies dealing with the same cell line [39]).

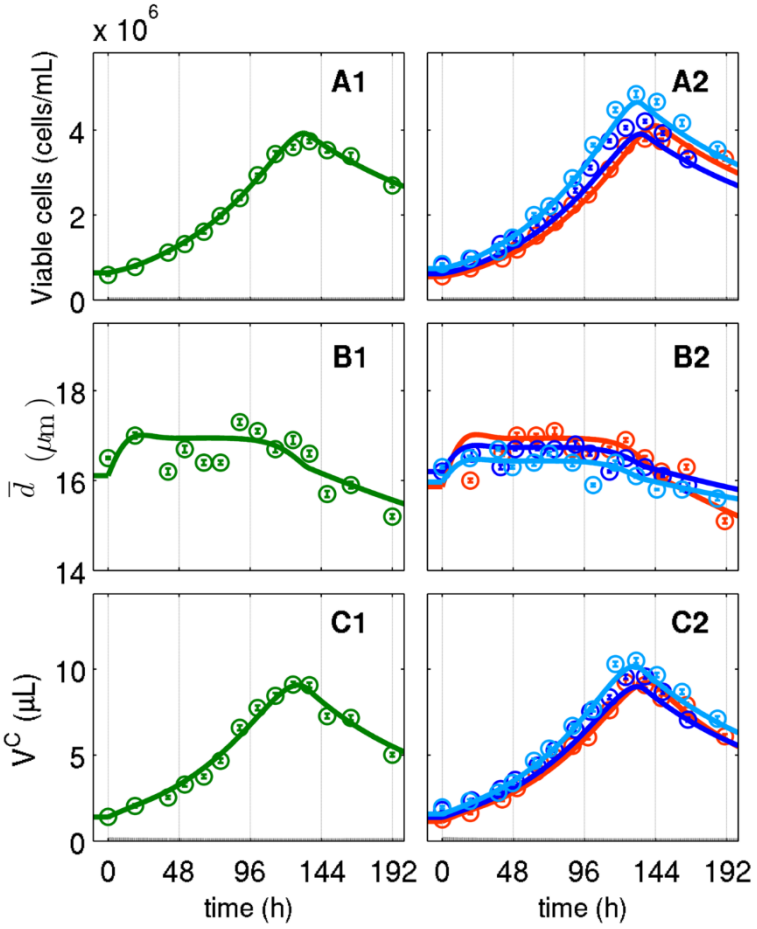

Figure 4.1.: Suspension AGE1.HN.AAT cell growth in a chemically defined medium for four small-scale cultivations. Viable cell concentration (A1–2), mean cell diameter (B1–2) and viable cell volume (C1–2). Data and error bar represent mean and standard deviation of technical triplicates for four independent experiments (0.5 L ○, ○ and 2.5 L ○, ○ stirred tank bioreactors); lines: model simulations. Experimental data used for parameter estimation (A1, B1, C1). Figure taken from Ramos et al., 2020 [157].

After inoculation with about 6×10^5 cells/mL, all cultivations started with exponential cell growth until maximum cell concentration ranging from 3.8–4.6×10^6 cells/mL at about 130 h were achieved. Following a similar trend as cell concentration, the viable cell volume (V^c) increased from about 1.3 µL to a maximum in the range of 9–10.2 µL, before the

onset of cell death. Initially, cell diameters ranged from 15.8–16.2 µm (Fig. 4.1B). After about 18 h, a mean cell diameter of 16.5–17.0 µm was achieved, which decreased after about 110 h to a minimum of 15.1–15.8 µm. Although the experimental data is rather noisy, the same trend (higher mean cell diameter which decreases at later growth cell growth phase) is observed for all cultivations, as it is typically observed for suspension cell line cultivations. Specifically, these variations of cell volume and diameters are similar to the previously established segregated cell growth model by Rehberg et al. [159] for adherent MDCK cells, though to a lesser degree. The model simulations describe these changes in cell concentration and mean cell diameter and viable cell volume (Fig. 4.1A–C). Modeling the cell volume is important because there is usually a delay between the increase in viable cell concentration compared to the viable cell volume during cell growth [182] which impacts the intracellular metabolism. In this instance, the model simulations cover changes of the mean cell diameter of about 10% during the cultivation of AGE1.HN.AAT cells. Modeling such minor changes in diameter is relevant since the consideration of this effect results in up to 30% variation of the mean cell-specific volume (Eqs. 3.1.18–3.1.19, V_c^s in Fig. 4.7). Furthermore, since the volumetric maximum enzyme activity is expressed per cell-specific volume (Eq. 2.1.85), this would lead to up to 15% change in the volumetric maximum enzyme activities. As such the volumetric maximum enzyme activity was not constant due to changes in the mean cell diameter over time (Fig. 4.1B), which is used to calculate the cell-specific volume (Eq. 3.1.19). In other words, a smaller cell-specific volume leads to a higher volumetric maximum enzyme activity and *vice versa*. This correlated well with experimental observations for this cell line by Rath et al. [161], where the overall volumetric enzyme activity of AGE1.HN.AAT cells was higher during the stationary growth phase (on average smaller cells) compared to the exponential phase (on average larger cells). Increased cell diameters and consequently lower volumetric enzyme activities were also found during the exponential growth phase of adherent MDCK cells [109,159,160]. The differences observed in changes in maximum enzyme activity from exponential phase to stationary phase could of course also be due to changes in transcriptomics which could not be measured in the scope of this study.

Overall, the segregated growth model used in this study described well the growth of AGE1.HN.AAT suspension cells. Taking explicitly into account changes in the mean cell diameter enabled the estimation of cell-specific volume which facilitated the establishment of the structured intracellular model.

4.1.2 Extracellular substrates and metabolic by-products

Model simulations of extracellular substrates and metabolic by-products dynamics for four cultivations at 0.5–2.5 L scale are shown in Fig. 4.2. Extracellular glucose, which was considered as the main substrate for cell growth, was consumed rapidly until about 130 h (Fig. 4.2A). Shortly before its complete depletion, the cell death increased significantly (Fig. 4.1A). Lactate accumulated in the bioreactor until about 130 h when glucose was depleted (Fig. 4.2D). During this phase, glucose was converted mostly to pyruvate and during this process ATP other energy precursors were produced. Pyruvate was used to produce lactate in a reversible reaction catalyzed by lactate dehydrogenase (LDH), one of the fastest and highly regulated enzymes in glycolysis. In this study, two, ad hoc, kinetics for LDH were used to account for the LDH reversibility allowing the model to capture the switch between lactate production (first 130 h of cultivation) and consumption (after 130 h) (Eq. A.1.23 in Appendix, Fig. 4.7). This added complexity was necessary since the intracellular lactate concentration was not considered in the model. One of these kinetics is a Michaelis-Menten with a non-competitive inhibition by ATP and pyruvate, previously used in [183,184] to model LDH activity. ATP concentration influences the LDH rate since lactate conversion to pyruvate can regenerate NADH from NAD^+ and NADH can be converted to ATP. It is likely that for this reason after glucose depletion, cells partially consumed the extracellular lactate. This likely allowed model simulation to capture the increase of ATP concentration observed after glucose and glutamine and pyruvate were depleted (further discussed in the preceding section on energy metabolism and product formation). Lactate consumption by cells has also been observed in other cell lines under different cultivation conditions, and might be controlled by signaling cascades [47,126,185–190]. As an example, for the parental cell line AGE1.HN lactate production has been correlated with PDK4 gene inhibition [191], and in other continuous cell lines its consumption correlated with lactic acidosis [186].

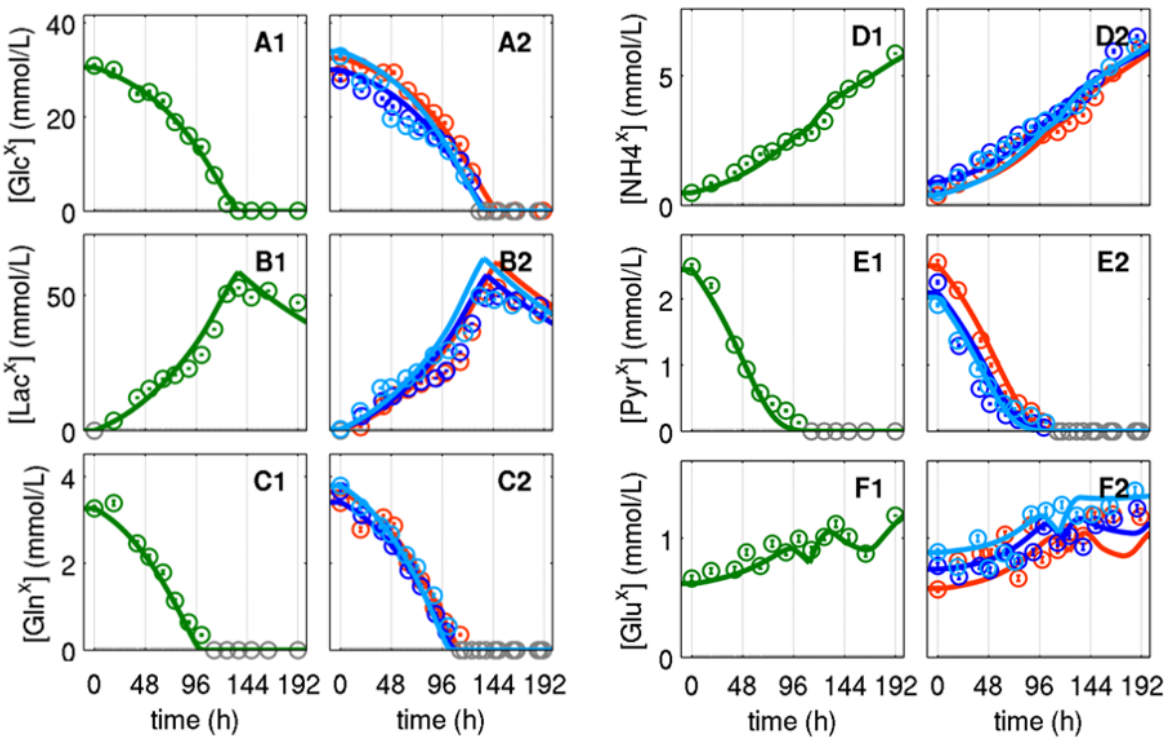

Figure 4.2.: Experimental data and model simulations of key metabolites of glycolysis for suspension AGE1.HN.AAT cell growth a chemically defined medium. Glucose-6-phosphate (A1–4), uracil diphosphate-glucose, uridine diphosphate glucose (B1–4), fructose-6-phosphate (C1–4), fructose-1,6-biphosphate (D1–4), 3-phosphoglycerate (E1_4), phosphoenolpyruvate (F1–4) and intracellular pyruvate (G1–4). Data and error bar represent mean and standard deviation of technical triplicates for four independent experiments (0.5 L ○, ○ and 2.5 L ○, ○ stirred tank bioreactors); lines: model simulations. Experimental data used for parameter estimation (A1, B1, C1, D1, F1, G1). The grey lines indicate the limit of quantification for each metabolite and the grey data points are under the limit of quantification. Figure modified from Ramos et al., 2020 [157].

Extracellular glutamine and pyruvate (Figs. 4.2C and 4.2E, respectively) were consumed rapidly and were depleted before glucose depletion and subsequent cell death at about 100-115 h. Ammonium (Fig. 4.2D) accumulated over the complete cultivation period, with a partial increase of the accumulation rate after glutamine depletion. Glutamate (Fig. 4.2F) mostly accumulated in the media, while there are short instances where it was consumed. Interestingly, even after glutamine depletion, glutamate still accumulated. This

phenomenon is not uncommon in cell cultivations as glutamate is a non-essential amino acid and it can also be produced from catabolism of other amino acids such as glutamine, lysine and proline [192,193]. Although extracellular amino acids were not quantified in these experiments, previous batch cultivations with a similar medium composition performed for this cell line show that most amino acids are not depleted at the end of the exponential cell growth phase [162]. It is thus plausible to assume that even when TCA and glycolysis were shutdown, amino acid catabolism persisted, leading to the continuous accumulation of glutamate observed. This is further reinforced by the fact that ammonium, which is released mainly from amino acid catabolism, also accumulated in the same timely manner (Fig. 4.2D). Therefore, assuming that glutamate is mainly produced from amino acid catabolism, it is likely that the glutamate excretion by cells is related to its intracellular excess. This is predicted in the model simulations, where the amino acid degradation rate (Fig. 4.7), which correlates with glutamate production, was predicted to remain high over the late cultivation period. This might be biologically relevant as one of the mechanisms that the cells use to keep intracellular amino acid homeostasis is the control of amino acid entry or exit through their corresponding transporters [194].

Overall, the model simulations captured well the dynamics of all extracellular substrates and metabolic by-products. In particular, the segregated cell growth model correctly estimated the consumption rates of the substrates glucose, glutamine, and pyruvate. With these consumption rates as an input for the structured intracellular model of metabolism, the model also correctly estimated the release rates of the metabolic by-products lactate, ammonium, and glutamate.

4.1.3 Central carbon metabolism

Model simulations of key metabolites from glycolysis, TCA, and energy metabolism of four cultivations at 0.5–2.5 L scale performed by Rath et al. [39,161] are discussed in this section. Note that the limit of quantification of a metabolite is influenced by the viable cell volume per milliliter (if the volume of sample is constant, a higher cell volume per sample decreases the limit of quantification and vise-versa).

Glycolysis: Regarding the upper glycolytic pathway, two interesting dynamics can be observed (Fig. 4.3). The first was a slow accumulation of glucose-6-phosphate **(**G6P) and

fructose-6-phosphate (F6P) until about 96 h followed by their decrease until depletion. The second was a peak-like accumulation of fructose-1,6-biphosphate (F16P) between 96 and 130 h. Most of the remaining metabolites (3-phosphoglycerate (3GP), uridine diphosphate glucose (UDPGlc) and phosphoenolpyruvate (PEP)) show a relatively stable concentration until the extracellular glucose was depleted at about 130 h (Fig. 4.2A). Intracellular pyruvate formed an initial peak at about 20 h and decreased over the cultivation time, this is likely due to the overflow of initial pyruvate in the medium and its rapid production from glucose, which is abundant at the start of the cultivation. This high glycolytic activity (i.e. glucose was not limiting) is supported by the fact that most glycolytic metabolite concentrations remained about constant or even increased until around 96 h. Furthermore, at approximately 130 h, glucose was depleted, as were all glycolysis metabolites.

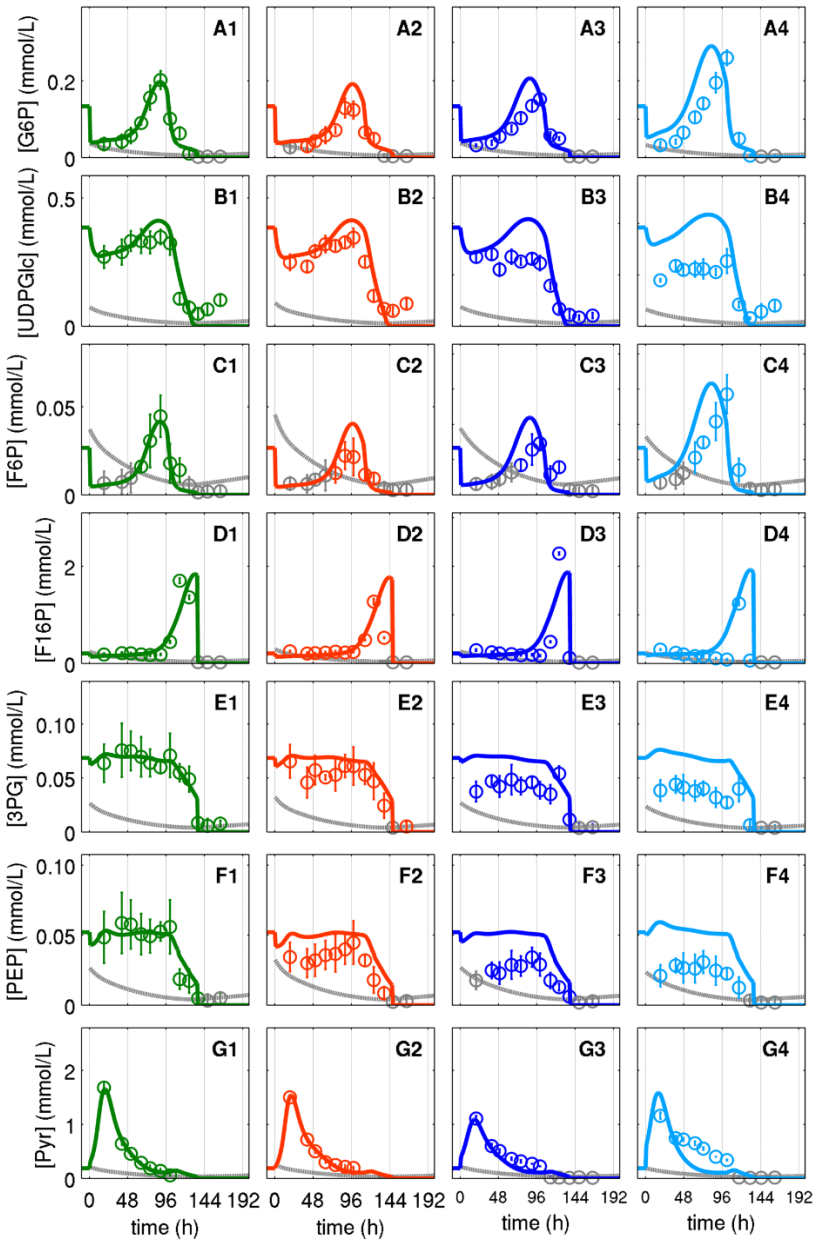

Figure 4.3.: Model simulations against experimental data of key metabolites of glycolysis for suspension AGE1.HN.AAT cell growth a chemically defined medium. Glucose-6-phosphate (A1–4), uracil diphosphate-glucose, uridine diphosphate glucose (B1-4), fructose-6-phosphate (C1-4), fructose-1,6-biphosphate (D1–4), 3-phosphoglycerate (E1–4), phosphoenolpyruvate (F1–4) and intracellular pyruvate (G1–4). Data and error bar represent mean and standard deviation of technical triplicates for four independent experiments (0.5 L ○, ○ and 2.5 L ○, ○ stirred tank bioreactors); lines: model simulations. Experimental data used for

parameter estimation (A1, B1, C1, D1, F1, G1). The grey lines indicate the limit of quantification for each metabolite and the grey data points are under the limit of quantification. Figure taken from Ramos et al., 2020 [157].

In all four experiments, experimental data showed similar dynamics for the key metabolites of glycolysis and the model simulations capture these dynamics well, based on one parameter set. Some discrepancies between model simulations and experimental data can, however, be observed, i.e. for PEP and 3PG. This implies that mechanisms for some enzyme directly linked to these metabolites, for instance ENO or PK kinetics, might need further improvements. Since simulations with the unique set parameter generally led to a better fit of data from cultivations at 2.5 L when compared to 0.5 L, it is also likely that fixed kinetics and their related parameters for some enzymes do not account for minor differences between cultivations performed at different scales. Nevertheless, these results also indicate that reasonable assumptions were made for the most critical enzymes in glycolysis, i.e. hexokinase (HK), PFK, and LDH [195]. PFK has been described as closely linked to oscillations frequently found in glycolytic rates [196,197], and it is one of the highly regulated enzymes of this pathway with allosteric regulation by energy precursors such as ATP, ADP, and cAMP [196–199]. For this particular case, a kinetic similar to the Hill kinetic that has been applied for allosteric enzymes was used here [198]. With this kinetic for PFK (Eq. A.1.15 in the Appendix A), the glycolytic rates are negatively correlated with the intracellular ATP concentration when glucose was present in the medium (0–130 h). During model development it was found that another critical enzyme was ALD. Without a proper selection of its kinetic (Eq. A.1.21 in the Appendix A), it was not possible to simulate the peak-like behavior observed for F16P. It was found that the dynamic of F16P is negatively correlated with the cell-specific growth rate (Eq. A.1.21 in the Appendix A). Regulation of this enzyme has been previously reported to correlate with changes in cell proliferation, mainly through its localization inside or outside of the nucleus depending on the cell growth stage [200], which can be taken into account indirectly via the cell growth rate.

Taken together, the model simulation approximates well the dynamics of most of the glycolytic metabolites. These results indicate that reasonable and biologically relevant assumptions were made for the kinetics and parameters of most of the critical enzymes in glycolysis.

TCA: The concentration of most metabolites from the TCA cycle remained high until around 130 h when glucose was depleted, apart from succinate (Fig. 4.4). Succinate has the highest concentration compared to other TCA intermediates and it exceeds even alpha-ketoglutarate by a factor of ten. Although alpha-ketoglutarate is produced from more than one source, contrary to succinate, the concentration of the metabolites can only be related to their related Michaelis-Menten affinity constants. It is also clear that alpha-ketoglutarate dynamics differed at the beginning of the cultivations even in the same scale. Citrate concentration shows a relatively high concentration before glucose depletion while cis-aconitate concentration was near the limit of quantification. This suggests an equilibrium of aconitate (ACO) in favor of citrate production since iso-citrate concentration was around 100-fold lower. Similarly, the fact that fumarate concentration remained low, and at a level similar to iso-citrate, suggests that it was rapidly converted to malate by fumarase (FMA), a reversible reaction and one of fastest enzymes in the TCA cycle.

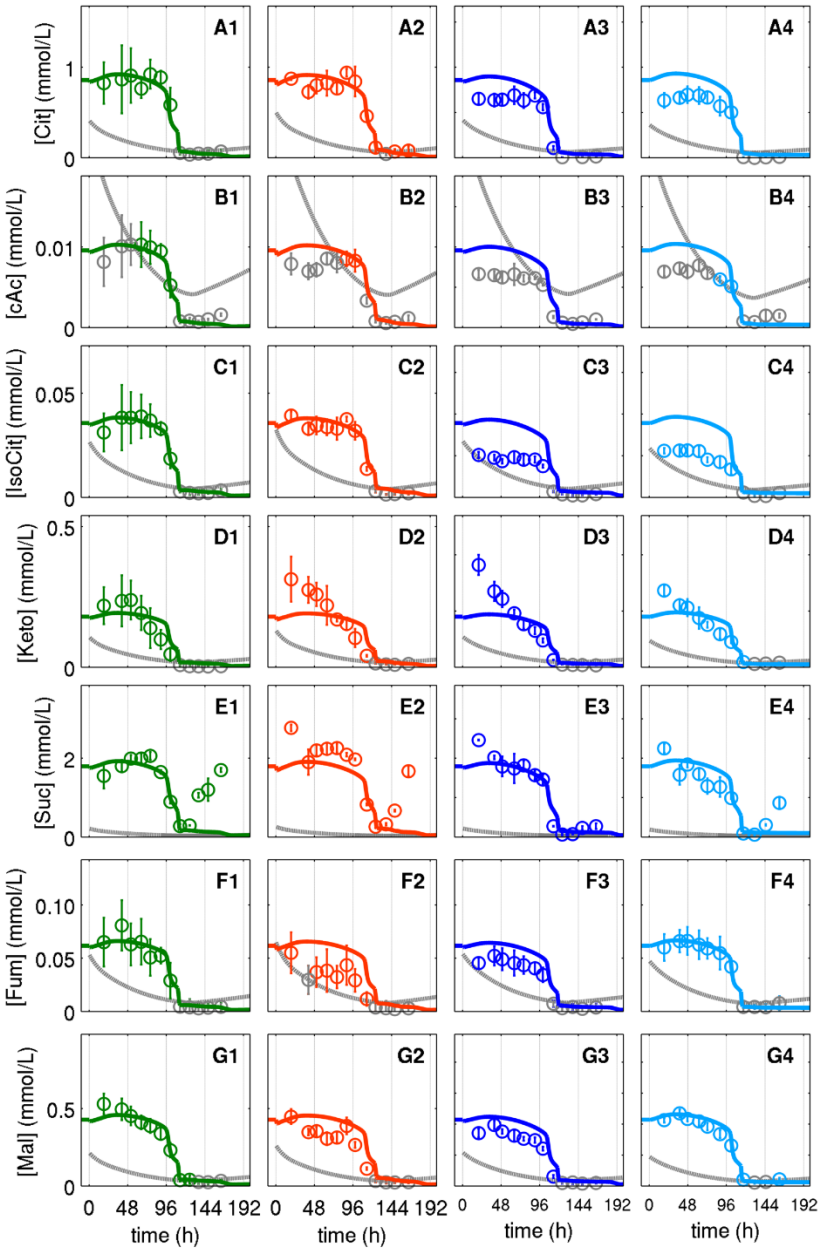

Figure 4.4.: Model simulations against experimental data of key metabolites of TCA cycle for suspension AGE1.HN.AAT cell growth a chemically defined medium. Citrate (A1–4), cis–aconitate (B1–4), iso-citrate (C1–4), alpha-ketoglutarate (D1–4), succinate (E1–4), fumarate (F1–4) and malate (G1–4). Data and error bar represent mean and standard deviation of technical triplicates for four independent experiments (0.5 L ○, ○ and 2.5 L ○, ○ stirred tank bioreactors); lines: model simulations. Experimental data used for parameter estimation (A1, B1, C1, D1, F1,

G1). The grey lines indicate the limit of quantification for each metabolite and the grey data points are under the limit of quantification. Figure taken from Ramos et al., 2020 [157].

Overall, despite some discrepancies for succinate at the end of the cultivations and alpha-ketoglutarate at the start of the cultivations, the overall dynamics of the metabolites in TCA were captured well by the model simulation. This suggests that biologically valid and appropriate kinetics and parameters assumptions were made for most of the enzymes in this pathway.

Analysis of the glycolytic and TCA cycle metabolic rates: Given the correct descriptions of dynamics of most metabolites in glycolysis and TCA cycles, the rates estimated for the enzymes in these pathways can be analyzed in detail against previous knowledge or lack thereof. The model simulations showed that the input from glycolysis into the TCA was relatively low, similar to studies on animal cells [191,201–203]. Typically, in cancer-derived cell lines, the metabolism is reprogrammed to some extent resulting in a weaker connectivity between glycolysis and TCA through the pyruvate dehydrogenase (PDH). This was likely also the case for AGE1.HN.AAT cells since this enzyme has the lowest maximum activity compared to other enzymes of the TCA [181]. The highest metabolic rate input from glycolysis into the TCA in the model simulations was through PC that converts pyruvate to OAA (Figs. 4.6 and 4.7). PC has also been found to significantly contribute to TCA carbon supply according to ^{13}C labeling experiments in CHO cells [204]. The low activity of PDH and OAA production through PC resulted in a partly reversed TCA to account for the supply of metabolites such as citrate, cis-aconitate and isocitrate (further discussed below, and shown in Fig. 4.8). This truncation of TCA has also been reported for other cancer cell lines, as it allows generation of citrate and iso-citrate, which are important for lipid production [205]. For example, in melanoma cells, using ^{13}C labeling it was found that the precursors for lipid production are generated mainly from these reverse reactions in the TCA cycle, and that the main source of these precursors is glutamine and not pyruvate [206]. Unsurprisingly, it is known that glutamine is the main metabolite fueling the TCA since it is converted to alpha-ketoglutarate, a TCA intermediate [207]. In this modeling approach, alpha-ketoglutarate production from transamination, where both OAA and glutamate are consumed, was also considered. Previous studies with AGE1.HN.AAT cells [162] had also elaborated on the importance of the transamination reactions in these cells. In this

model, glutamate is produced from the degradation of amino acids which results in production of ammonium. Furthermore, glutamate can also be produced from alpha-ketoglutarate through the enzyme glutamate dehydrogenase (GLDH), which consumes ammonium during this process. This reaction is known to play an important role in the ammonium detoxification (rate shown below in Fig. 4.7). In the model simulations glutamate was produced through GLDH and amino acid degradation and glutamate was then converted to ketoglutarate by aspartate transaminase with OAA consumption. This is a strong indication that transamination and part of the TCA are used mainly for energy production while the other part of TCA provides intermediates for lipid biosynthesis through citrate [208]. However, to better support this theory, the model should be further extended to include lipid synthesis and degradation of other amino acids. This could also potentially benefit the analysis of the relevance of these findings, especially regarding the anaplerotic reaction (glycolysis-TCA cycle connection through PC) addressed previously.

Energy metabolism and product formation: ATP concentrations increased while glucose and glutamine (Figs. 4.2A and 4.2C) were available in the medium (Fig. 4.5). Shortly before the depletion of glucose at about 130 h, a rapid decrease in ATP concentrations occurs on all cultivations. Soon after increasing again (around 140 h) and remaining high until the end of cultivation. A1AT was produced and exported to the medium while the cells were growing (until about 130 h) and remained constant until the end of cultivation. This clearly shows that the production of this protein is growth-related and therefore a simple growth related kinetic was sufficient to describe its dynamic (Eq. A.1.8 in Appendix A).

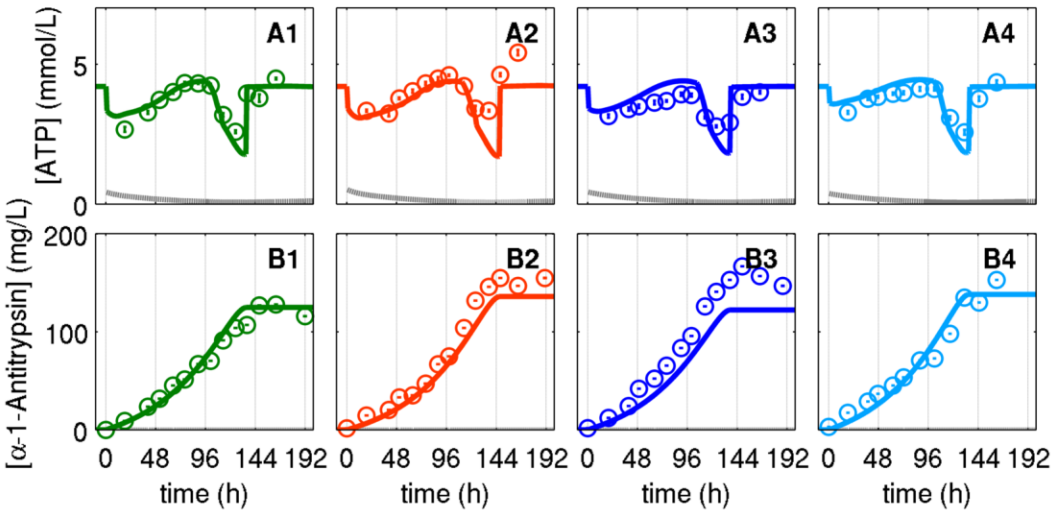

Figure 4.5.: Model simulations against experimental data ATP and alpha1-antitrypsin (A1AT) of suspension AGE1.HN.AAT cell growth a chemically defined medium. ATP (A1–4) and alpha1-antitrypsin (B1–4). Data and error bar represent mean and standard deviation of technical triplicates for four independent experiments (0.5 L ○, ○ and 2.5 L ○, ○ stirred tank bioreactors); lines: model simulations. Experimental data used for parameter estimation (A1, B1). The grey lines indicate the limit of quantification for ATP. Figure taken from Ramos et al., 2020 [157].

Model simulations capture relatively well the dynamics of ATP and A1AT in all four batch cultivations. This indicates that a simple product formation kinetic is sufficient to describe its dynamic. For ATP, it indicates that a correct balance between its consumption (Eq. A.1.49 in Appendix A) and production (Eq. A.1.45 in Appendix A) was achieved. ATP is mainly produced in glycolysis (Eq. A.1.43 in Appendix A) and oxidative phosphorylation (Eq. A.1.44 in Appendix A). According to model simulations, at least 50% of the total ATP was produced in glycolysis (Fig. 4.7) while glucose is present in the medium (until about 130 h). This is in agreement with previous studies reporting a range between 1–64% [209]. Additionally, this finding supports the theory that glycolysis could sustain growth demand of AGE1.HN.AAT cells as previously suggested in [191], i.e. that the glycolytic ATP production rate is higher than the simulated ATP consumption for growth (Eq. A.1.46 in Appendix A and Fig. 4.7). The model simulations also suggests that the rapid decrease in ATP observed is mainly due to the depletion of glucose and the subsequent decrease in ATP production in glycolysis ($r_{glycolysis}$ in Fig. 4.7 below). Shortly after, the increase in

ATP concentration again was captured due to an estimated increase in oxidation of NADH when lactate consumption occurs (r_{NADH} Fig. 4.7 below). The increase in oxidative phosphorylation also leads to higher estimated theoretical oxygen consumption at the end of the cultivation period (Eq. A.1.52 in Appendix A and r_{O2} in Fig. 4.7 below). In this phase, since cells are not growing, ATP was mainly used for maintenance and consumed in other futile cycles (Eq. A.1.47–A.1.48 respectively in Appendix A). Overall, the theoretical oxygen consumption for AGE1.HN.AAT was about 22–106 fmol/cell/h (r_{O2} in Fig. 4.7 below), which is in a similar range reported for other continuous cell lines of 7–97 fmol/cell/h [210,211]. Interestingly, a much lower oxygen consumption rate was found for the early exponential growth phase compared to stationary phase (Fig. 4.7 below) supporting the theory that while there is no limitation of glucose, cells do not use the oxidative phosphorylation pathway at its full potential. A lower oxygen uptake during cell growth phase without glucose limitation and a higher oxygen uptake near glucose limitation (1–1.5 mM) has been previously reported for other cells such as the murine hybridoma cells [212]. This confirms again that cells can switch to a more efficient metabolism as glucose limitation starts by decreasing the glycolytic activity, consuming lactate and activating the oxidative phosphorylation pathway.

Overall, the model simulations captured very well the dynamics of ATP and product of interest (A1AT) and the estimated theoretical oxygen production rates are well within the range observed for other continuous cell lines. These findings indicate that valid and biological assumptions were made regarding the kinetics of energy and product formation and their related parameters.

4.1.4 Analysis of simulated metabolic rates

In the following, the simulated metabolic rates over time, which are variables in the model, are presented (Figs. 4.6 and 4.7). Given the accuracy of the developed model to describe cell growth, extracellular and intracellular metabolites dynamics, these metabolic rates were used for further analysis, e.g. identification cellular physiological states (Fig. 4.8). Furthermore, the established model was also used for *in silico* studies in the next section.

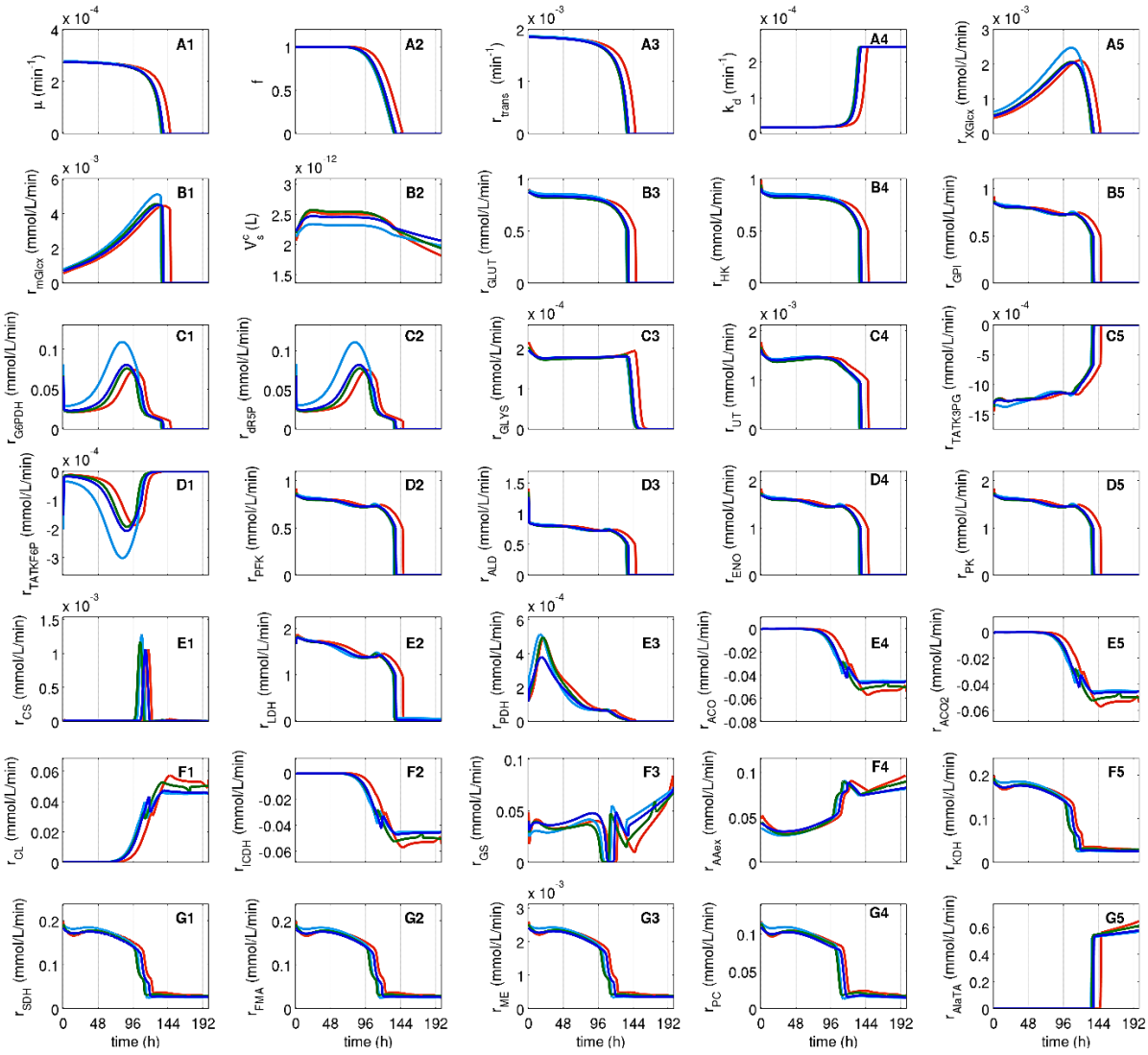

Figure 4.6.: Metabolic rates from cell growth and central carbon metabolism obtained from model simulations of four independent experiments (0.5 L ○, ○ and 2.5 L ○, ○ stirred tank bioreactors). (A1) growth rate, inhibition factor (A2), transition rate (A3), cell death rate (A4), glucose consumption rate for growth (A5), glucose consumption for maintenance (B1) , cell-specific volume (B2), glucose transporter rate (B3), HK rate (B4), GPI rate (B5) , G6PDH rate (C1), general R5P consumption rate (C2), GLYS rate(C3), UT rate (C4), TATK3PG rate (C5) , TATKF6P rate (D1), PFK rate (D2), ALD rate (D3), ENO rate (D4), PK rate (D5), CS rate (E1), LDH rate (E2), PDH rate (E3), ACO rate (E4), ACO rate (E5), CL rate (F1), ICDH rate (F2), GS rate (F3), AAex rate (F4), KDH rate (F5), SDH rate (G1), FMA rate (G2), ME rate (G3), PC rate (G4) and AlaTA rate (G5). Figure taken from Ramos et al., 2020 [157].

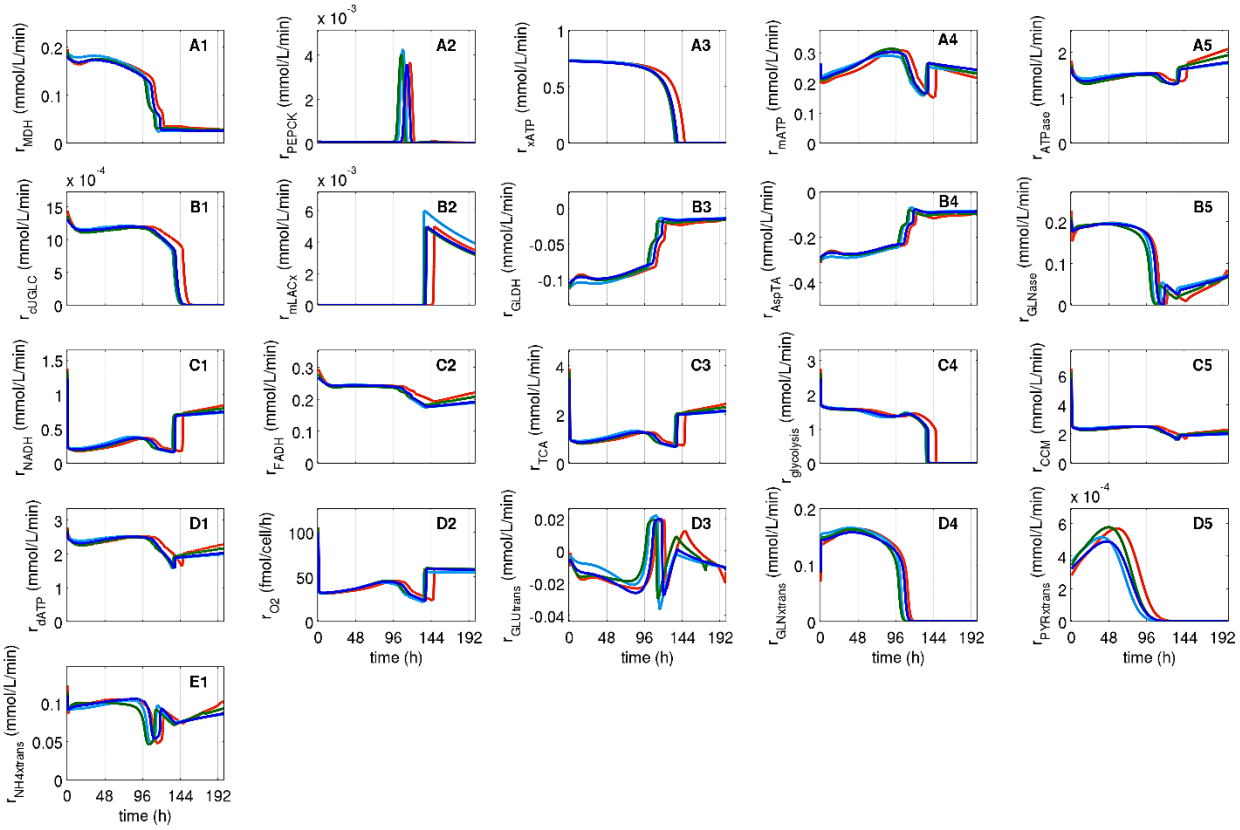

Figure 4.7.: Metabolic rates from central carbon metabolism obtained from model simulations of four independent experiments (0.5 L ○, ○ and 2.5 L ○, ○ stirred tank bioreactors). (MDH rate (A1), PEPCK rate (A2), ATP consumption for growth (A3), ATP consumption for maintenance (A4), ATPase rate (A5), general consumption rate for UDPGlc (B1), lactate consumption rate (B2), GLDH rate (B3), AspTA rate (B4), GLNase rate (B5), NADH oxidative phosphorylation rate (C1), FADH oxidative phosphorylation rate (C2), TCA net ATP production rate (C3), glycolytic ATP net production rate (C4), net production of ATP (C5), net consumption of ATP (D1), theoretical oxygen consumption rate (D2), Glu transporter rate (D3), Gln transporter rate (D4), Pyr transporter rate (D5) and NH4 transporter rate (E1). Figure taken from Ramos et al., 2020 [157].

Identification of dominant reactions: Based on the analysis of experimental data, and the corresponding simulated metabolic rates, two distinct cellular physiological states were identified which are shown in Fig. 4.8.

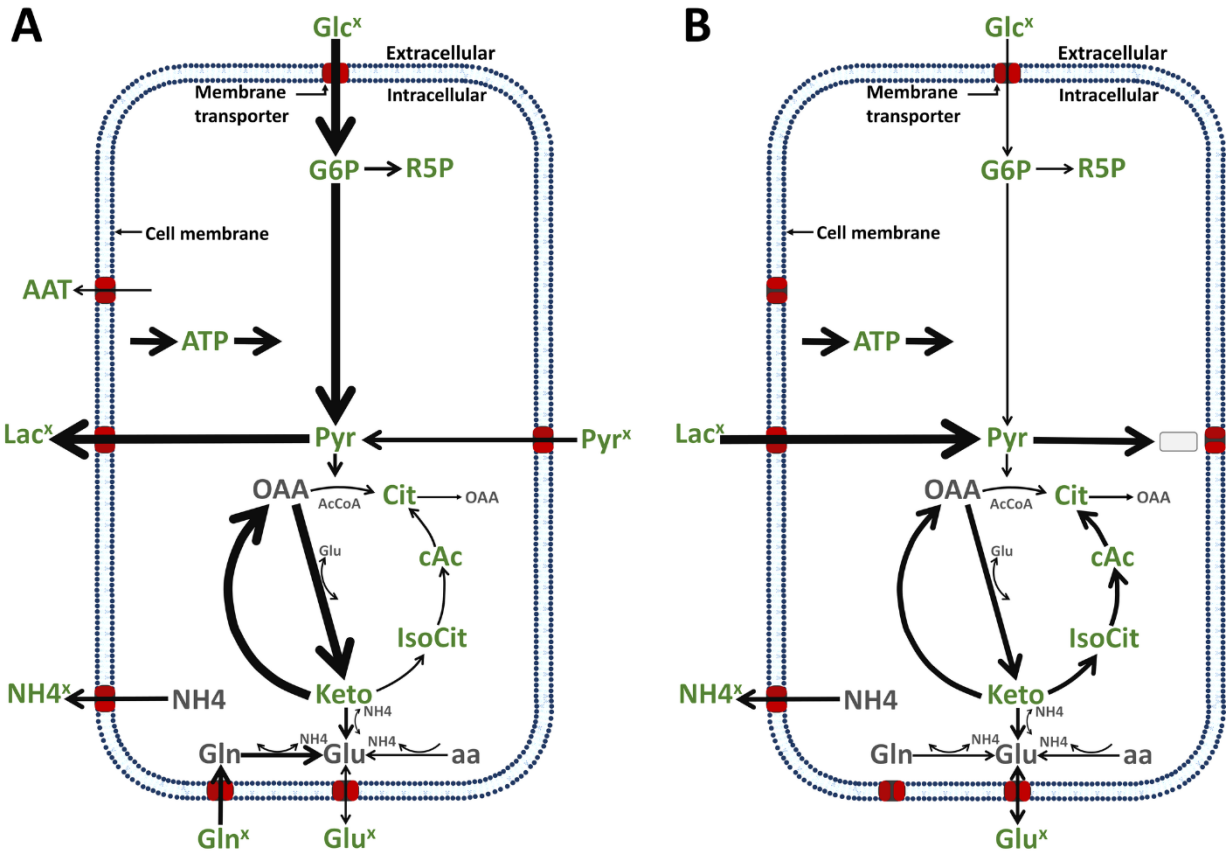

Figure 4.8.: The two main cellular physiological states identified for AGE1.HN.AAT cell growth. (A) Cellular physiological state characterized by a high glycolytic rate and a truncated TCA with lactate production and pyruvate uptake. (B) Cellular physiological state characterized by a low glycolytic rate, reactions of the TCA cycle running from alpha-ketoglutarate to oxaloacetate**,** amino acid catabolism, ammonium production, and lactate consumption. The grey box is a metabolic sync. Figure adapted from Ramos et al., 2020 [157].

In the first cellular physiological state (Fig. 4.8A) has high glycolytic rates and wherein most of the glucose was converted to pyruvate, and subsequently pyruvate was converted to lactate. Glucose entering the cells did not accumulate as its simulated intracellular concentration was always below the limit of detection. I.e., glucose was

converted rapidly to G6P and, almost as fast, G6P converted to other intermediates and subsequently to pyruvate. This is in line with the well-known phenomena in cancer-derived cell lines termed as the Warburg effect where glucose is rapidly and almost entirely converted to lactate (1 Glc : 2 Lac), even under aerobic conditions [213,214]. Here, the experimental data suggests a ratio of 1–1.9 (maximum glucose and lactate concentration in Figs. 4.2A and 4.2B). Furthermore, it is reported that 0–40% of G6P generated through HK is channeled to the pentose phosphate pathway by glucose-6-phosphate dehydrogenase (G6PDH) [215–217]. For the cultivations considered, the simulated ratio was less than 10% (Fig. 4.6). This ratio correlates well with findings from metabolic flux analysis performed for this cell line by Niklas et al [218] using ^{13}C labeling. Finally, as discussed in the previous section, during this cellular physiological state (beginning of cultivation until about 130 h) model simulations suggested that at least 50% of the ATP was produced from glycolysis and a lower oxygen consumption rate is predicted compared to stationary phase ($r_{glycolysis}$ Fig. 4.7).

The second cellular physiological state (Fig. 4.8B) is characterized by the consumption of lactate and the degradation of amino acids to fuel a truncated TCA cycle. This resulted in ammonium secretion even when glutamine was depleted, in line with the experimental data. Since glycolysis also provided OAA for transamination (when the glucose concentration was low), both glycolytic and TCA rates decreased. Accordingly, glutamate consumption in transamination was also lower and glutamate accumulated intra- and extracellularly. At this stage, more OAA was produced from citrate degradation by the CL indicating that a reverse TCA is required to provide enough OAA to keep transamination active and, therefore, reactions that provide energy precursors. Since transamination shortens the TCA cycle, a more efficient way of producing ATP during limitations can be assumed. Transamination is one option for cells to deal with the weak link of glycolysis to the TCA through PDH to keep ATP production high when needed, in particular, an increase in PDH activity would not help when glucose is depleted. Furthermore, this hypothesis is supported by the fact that a higher PDH activity could lead to OAA depletion because it is needed for citrate synthesis (from Acetyl-CoA and OAA), which would shut down the TCA\transamination. Finally, as discussed earlier, during this phase ATP was produced mainly from oxidative phosphorylation and a higher theoretical oxygen

consumption rate is predicted compared to the first metabolic phase, suggesting that this cellular physiological state is indeed more efficient (r_{O2} Fig. 4.7).

In summary, at least two distinct cellular physiological states were identified through the analysis of the simulated metabolic rates. The main hypothesis derived from the first identified cellular physiological states is that the Warburg effect contributes to a significant amount of ATP production in glycolysis. The main hypothesis derived from the second identified cellular physiological states is that the transamination is a solution to deal with the weak link of glycolysis with TCA through PDH. A compelling argument for this was that according to the model simulations using pyruvate as a substrate, PC produced enough OAA, which was used with glutamate to generate ketoglutarate via transamination, leading to a truncated TCA. In turn, this led to ketoglutarate being used as the precursor for the second half of the TCA where energy precursors were produced in substantial amounts.

4.1.5 *In silico* studies

In the following, the newly established model was used to perform *in silico* predictions to address open questions regarding the metabolism of AGE1.HN.AAT cells and options to improve process performance.

The first open question relates to the high glutamine synthetase (GS) activity observed experimentally in AGE1.HN.AAT cells, on whether this could cause ATP dissipation since glutaminase (GLNase) is also expressed in higher levels in these cells [161]. Regarding the ATP dissipation theory, it is worth mentioning that GS synthesized glutamine from glutamate, consumes ATP and ammonium, and thus can theoretically in fact ‘’dissipate’’ ATP. Since the GS activity was explicitly considered in the ODEs for glutamine and ATP, the GS maximum activity levels could be investigated *in silico* using the established model.

The second open question relates to the concentration of pyruvate in the basal medium, as during media optimization [219], it was found that an increase of initial pyruvate concentration resulted in a negative impact on cell growth and it was then postulated that it was because of energy spilling and that it did not increase TCA rates. As the intracellular

metabolism is complex and the high dimensional experimental data may difficult to interpret, the established mathematical model is a great tool that can aid this endeavor, i.e. assess possible impacts of changing in initial concentration of pyruvate and analyze its impact on intracellular metabolism and gain insights on the cause(s) of the negative impact observed experimentally by increasing pyruvate.

Two *in silico* studies were performed and to analyze the results five key reactions of animal cell metabolism were selected as markers for the intracellular cellular physiological state: (1) r_{LDH} (lactate production), (2) r_{PFK} (glycolytic activity), (3) r_{FMA} (TCA activity), (4) r_{CCM} (ATP production), and (5) $r_{\mathrm{NH4}^{x}_{trans}}$ (ammonium production). Furthermore, the analysis was limited to the exponential cell growth phase, which is the most relevant for cell expansion and product formation in AGE1.HN.AAT cells.

In the first study, the model was used to assess the impact of changes in enzymatic reaction rate of GS. More specifically this study based on the increase or decrease of the GS maximum activity, which is equivalent to this enzyme's gene overexpression and knockout, respectively. The results of this *in silico* study are presented in Fig. 4.9. In this scenario, changes in the GS activity had almost no impact on both lactate production (Fig. 4.9A**)** and glycolytic rate **(**Fig. 4.9B). TCA activity was slightly higher for a lower GS activity (Fig. 4.9C), and the same trend applied to the ATP production rate (Fig. 4.9D). On the other hand, higher GS activity did seem to lead to less ATP net production rate. Finally, the largest impact was on ammonium production as expected, i.e. the ammonium production rate is inversely correlated with the GS maximum activity (Fig. 4.9E). Taken together, the results of this *in silico* study shows that changes in high GS activity does lead to ATP dissipation, and strongly impacts the accumulation of ammonium.

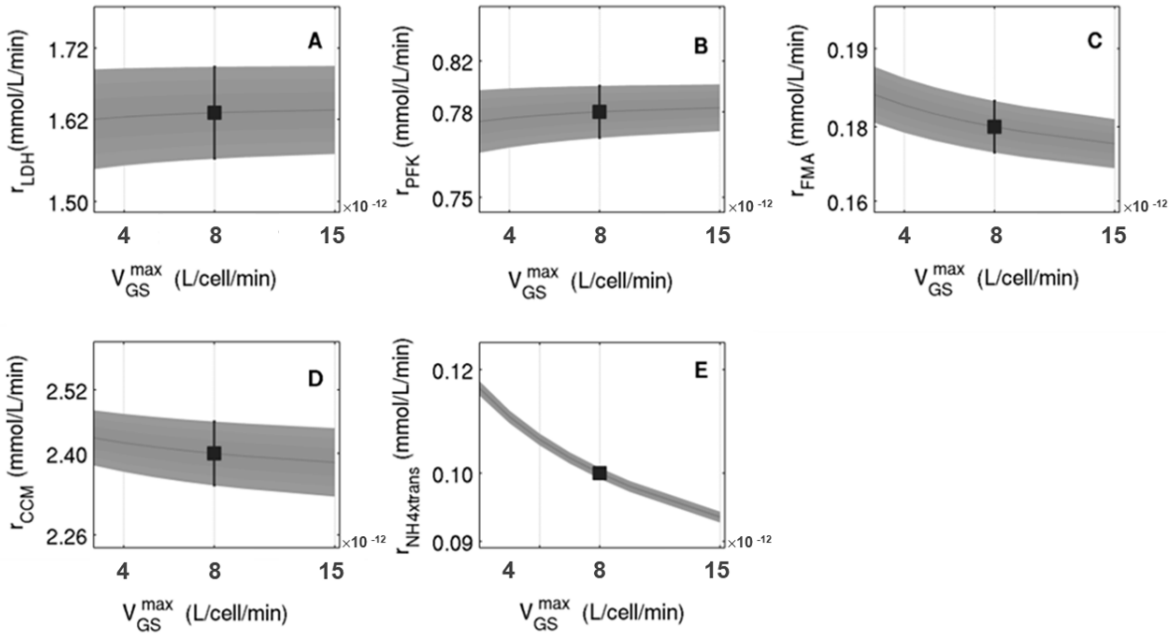

Figure 4.9.: Predicted impact of changes in the maximum activity of glutamine synthetase (GS) on selected key reactions of animal cell metabolism. (A) lactate production (r_{LDH}), (B) glycolytic activity (r_{PFK}), (C) TCA activity (r_{FMA}), (D) ATP production (r_{CCM}) and (E) ammonium production ($r_{NH4^{x}_{trans}}$). The black dots represent the mean rate and standard deviation during the simulation of the four batch experiments. Grey fill: mean and standard deviation of *in silico* simulations. Figure adapted from Ramos et al., 2020 [157].

In the second *in silico* study, the impact of changing the initial concentrations of pyruvate in the medium was investigated and the results are presented in 4.10. In this scenario, changes of initial pyruvate concentration in the medium did not have a significant impact on lactate production rate (Fig. 4.10A). This is the tendency of glycolytic rates with an increase of initial pyruvate concentration (Fig. 4.10B). Changes in the initial pyruvate concentration also had an impact on both TCA cycle rate and ammonia production rate (Figs. 4.10C and 4.10E). A negative correlation between the initial concentration of pyruvate and the production of ammonium was predicted. This *in silico* prediction might be biologically relevant as it has been previously reported that high pyruvate concentration in the media resulted in lower ammonia production in different cell lines such as MDCK, CHO-K1 and BHK21 [189]. On the other hand, contrary to what was

initially postulated [219] for the AGE1.HN.AAT cells, a positive correlation between the initial concentration of pyruvate and TCA cycle rate is predicted. This result is not surprising since this dynamic modeling approach differs from the constraint-based method which deals better with the mass balance. Nevertheless, it is also clear that even doubling the initial pyruvate only led to a very minor increase on net ATP production (Fig. 4.10D), because of the tendency of decrease in glycolytic rates and lactate production. This result might be biologically significant as it has been shown for CHO cells that the addition of pyruvate resulted in an increase in TCA cycle activity [220]. These results pointes that the negative impact of initial pyruvate in cell growth might be related to tendency to decrease glycolytic rates and consequently lactate production. The latter might have interfered with NAD/NADH balance, thus even an increase in TCA cycle activity is not enough to offset this. This conclusion is slightly different from what was previously postulated as the source of the negative impact on cell growth regarding the intracellular metabolism of AGE1.HN.AAT cells. Nevertheless, these findings are supported by what was previously reported for other cell lines. Overall, these results highlight the potential for usage of this model for further *in silico* investigations.

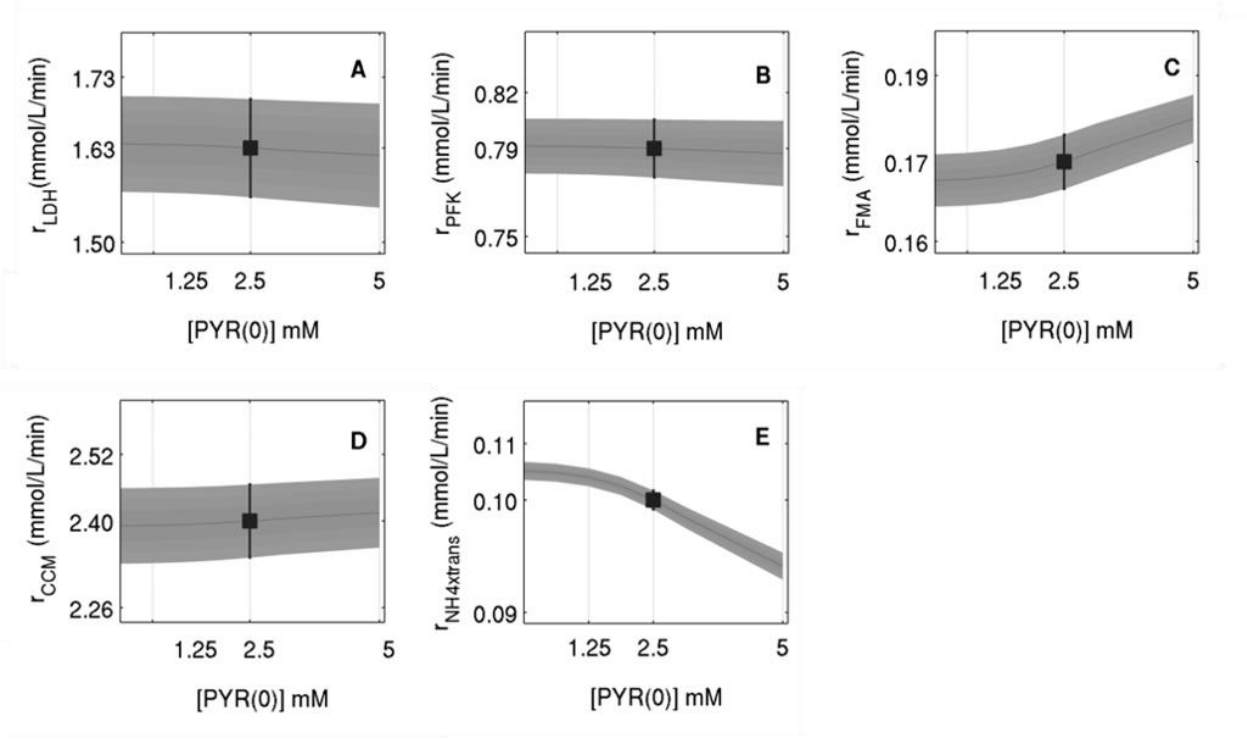

Figure 4.10.: Predicted impact of changes in initial extracellular pyruvate concentration ([PYR(0)]) on selected key reactions of animal cell metabolism. (A) lactate production (r_{LDH}), (B) glycolytic activity (r_{PFK}), (C) TCA activity (r_{FMA}), (D) ATP production (r_{CCM}) and (E) ammonium production ($r_{NH4^{x}_{trans}}$). The black dots represent the mean rate and standard deviation during the simulation of the four batch experiments. Grey fill: mean and standard deviation of *in silico* simulations. Figure adapted from Ramos et al., 2020 [157].

4.1.6 Summary

Overall, reasonable predictions of the dynamics of cell growth and key metabolites of four cultivations with a unique set of parameters were made. This is especially relevant as it includes the cell death phase, which is often neglected. This model also covers cultivations at two different scales (0.5 and 2.5 L). This strongly suggests reasonable and biologically relevant assumptions were made for the cell growth and enzyme kinetics. The analysis of the established model allowed the identification of two distinct cellular physiological states. One state was characterized by a high glycolytic rate and high lactate production, whereas the other was characterized by efficient ATP production, a

low glycolytic rate, and truncated TCA cycle (running in the reverse direction from alpha-ketoglutarate to citrate). Furthermore, the established model was used for *in silico* studies such as predicting the impact of changes of medium composition and maximum enzyme activity on the intracellular metabolism mimicking gene overexpression and knockout. It was found that an increase GS activity (its gene overexpression) would lead to ATP dissipation and decrease metabolic efficiency, while increasing pyruvate in the medium would likely changes the glycolytic rates and NAD/NADH balance thus leading to lower cellular health which was observed experimentally. Such knowledge shows potential for this model to be used to improve cell growth and to find measures towards the establishment of more efficient metabolism (e.g. gene expression and media/feed design).

4.2 MDCK suspension cell model

4.2.1 Cell growth and virus production

Model simulations against experimental data (viable cells, the mean cell diameter, and the total cell volume) for two MDCK cultivations are shown in Fig. 4.11. The first cultivation, Cultivation 1, is a standard cell growth cultivation (mock-infected cultivation, without virus infection). The second cultivation, Cultivation 2, is a cultivation where cells were infected during the exponential cell growth phase (at around 48 h).

After inoculation with 7.60×10^5 cells/mL, cell concentrations increased exponentially in both shake flask cultivations (Fig. 4.11), reaching a maximum observable cell growth rate of 0.0025 h^{-1} (Fig. 4.11 (A1–2). The first cultivation (Cultivation 1, mock-infected) reached a maximum cell concentration of 9.47×10^6 cells/mL at around 130 h before cells began to die due to substrate depletion. The second cultivation (Cultivation 2, infected) reached a cell concentration of 2.10×10^6 cells/mL at around 48 h and was infected with IAV at moi = 10 (infectivity based on $TCID_{50}$ assay). As soon as 3 hpi, the cell concentrations and mean diameter of cells and consequently viable cell volume sharply started to decrease. In comparison, the mean cell diameters of Cultivation 1 decreased only gradually (from 14 µm reached at around 22 h post inoculation to 11 µm end of cultivation, Fig. 4.11B). Similar findings for changes in the mean cell diameter of mock-infected cultures have been reported for adherent MDCK cells [157] and other suspension cell lines [157], though to a lesser degree for the latter. Overall, the model simulations accurately reproduced the dynamics of cell concentrations, mean cell diameters and viable cell volumes for both mock-infected and infected cells. The model simulations for both cultivations cover changes in the mean cell diameter of about 20%, which resulted in up to 50% variation in the mean cell-specific volume (V_s^c, Eq. 3.1.10) and up to a 40% variation in volumetric enzyme activities ($K_e^{\max}$, Eq. 3.1.12). These changes are consistent with previous findings for lower volumetric enzyme activities during exponential cell growth (on average larger cells) compared to later cultivation phases (on average smaller cells) for adherent MDCK cells [109,221] and other suspension cell lines [161]. The differences observed in changes in maximum enzyme activity from exponential

phase to stationary phase could also be due to changes in transcriptomics which were not measured in the scope of these experiments.

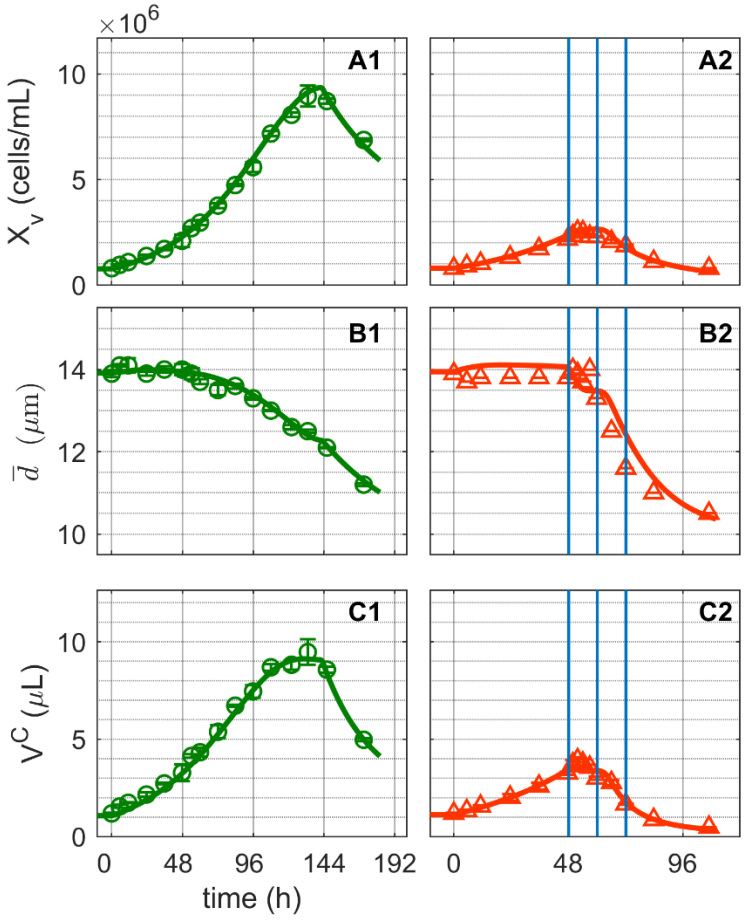

Figure 4.11.: Dynamics in cell growth of mock-infected and infected MDCK suspension cells. (A1–2) Viable cell concentration, (B1–2) mean cell diameter and (C1–2) total volume of viable cells. Data and error bars represent the mean and standard deviation of technical triplicates for two independent experiments (mock-infected Θ and infected Δ). Lines: model simulations. Vertical blue lines correspond to 0, 12 and 24 h post infection. Experimental data used for parameter estimation: A1, B1, C1. Figure taken from Ramos et al., 2022 [158].

Staining of infected cells with a monoclonal antibody directed against the IAV nucleoprotein (NP) showed that all cells in Cultivation 2 were infected simultaneously, which was expected due to the high multiplicity of infection used (moi = 10, Fig. 4.12A). Initially, the viral ribonucleoproteins (vRNP) accumulated in the cell nucleus after infection

(Fig. 4.12B). Shortly after (1.8 hpi), the percentage of vRNP dropped to about 30% (Fig. 4.12B), indicating the export of viral genomes to the cytoplasm for budding and virus release. In the supernatant of Cultivation 2, the first virions could be quantified at around 6 hpi (by the HA assay) and a maximum of 10.24 $\log_{10}$(virions/mL) was observed at 24 hpi (Fig. 4.12C). The percentage of apoptotic cells started to increase at around 12 hpi (Fig. 4.12D). The model simulations accurately describe the increase in number of infected cells and increase in the total number of virions, while the vRNP was not included in the model.

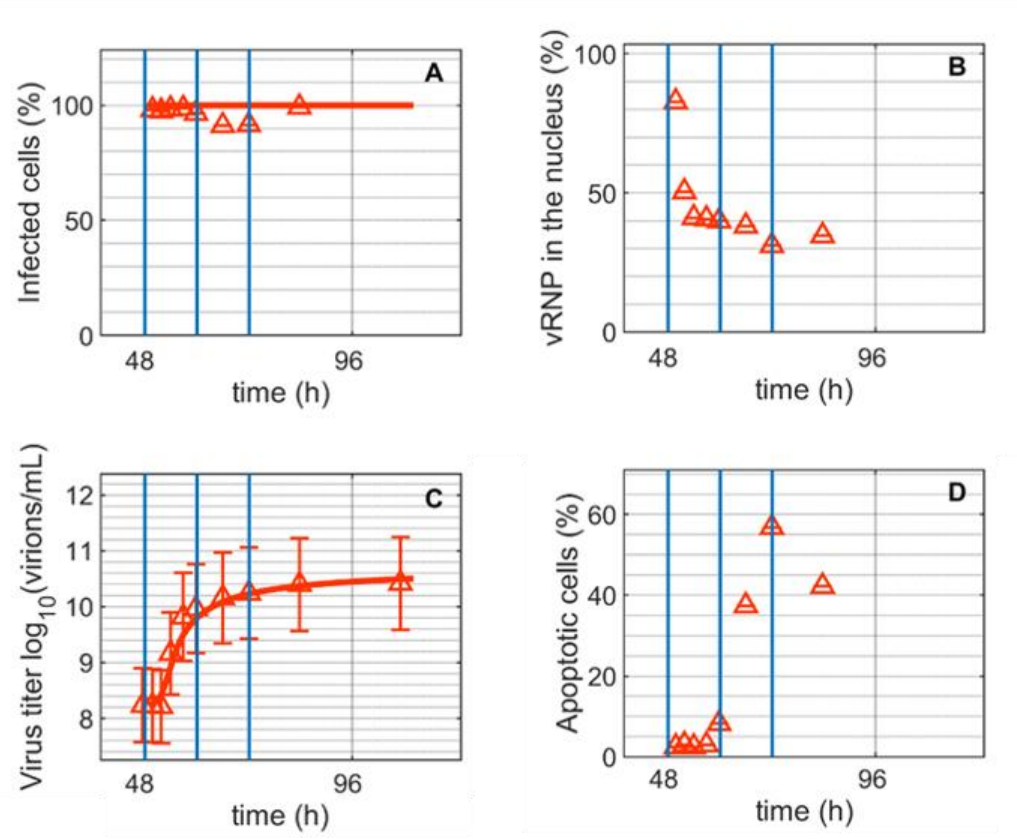

Figure 4.12.: Dynamics of influenza A virus replication in MDCK suspension cells after synchronous infection at 48 h post inoculation. (A) Percentage of infected cells, (B) percentage of viral ribonucleoproteins (vRNP) in the cell nucleus, (C) virus titer, and (D) percentage of apoptotic cells. Vertical blue lines correspond to 0, 12 and 24 h post infection, respectively. Data and error bars represent the mean and standard deviation of technical triplicates for one experiment (infected Δ). Figure adapted from Ramos et al., 2022 [158].

4.2.2 Extracellular substrates and metabolic by-products

The main substrates and metabolic by-products considered were glucose, lactate, glutamine, ammonium pyruvate and glutamate (Fig. 4.13). Extracellular glucose (Fig. 4.13 (A1)) was rapidly consumed until depletion approximately 144 h after Cultivation 1 (mock-infected) was inoculated. Glutamine and pyruvate were consumed even faster and were depleted at around 100 h (Fig. 4.13 (C1, E1)). Similar to other suspension cell lines, the onset of the cell death phase of the mock-infected cells (Cultivation 1) occurred concomitant to glucose depletion (Fig. 4.11 (A1)), confirming its critical role as a key substrate. For Cultivation 2, which was infected at around 48 h post inoculation, the cells initially consumed glucose, glutamine and pyruvate at a similar rate as cells in Cultivation 1, but their consumptions ceased as virus replication progressed and subsequently cell death occurred (Figs. 4.13 (A2) and 4.11 (A2). Mock-infected cells consumed glutamine and pyruvate from the extracellular environment until their depletion at around 100–110 h (Fig. 4.13 (C1, E1)). However, both metabolites were not depleted when the cells were infected at 48 hours post inoculation since cell growth was halted and cells started to die as virus replication progressed (Figs. 4.13 (C2, E2) and 4.11 (A2)). Similar to the previously established model [157], transport of these metabolites into the intracellular environment was not considered to be growth-related, as both substrates were depleted before the end of the exponential cell growth phase (Figs. 4.11 (A1) and 4.13 (C1, E1)). Their consumption kinetics might be governed by homeostasis or involve other mechanisms unrelated to cell growth [194]. In this instance, their mechanism of transport was described using Michaelis–Menten kinetics or direct binding equation [174] (Eqs. A.2.3 and A.2.8 in Appendix A). The model simulations using the same set of parameters for both cultivations allowed an accurate description of the dynamics of these extracellular metabolites (glucose, pyruvate and glutamine). Notably, not only during the first 24 hpi, but also during later phases of infection.

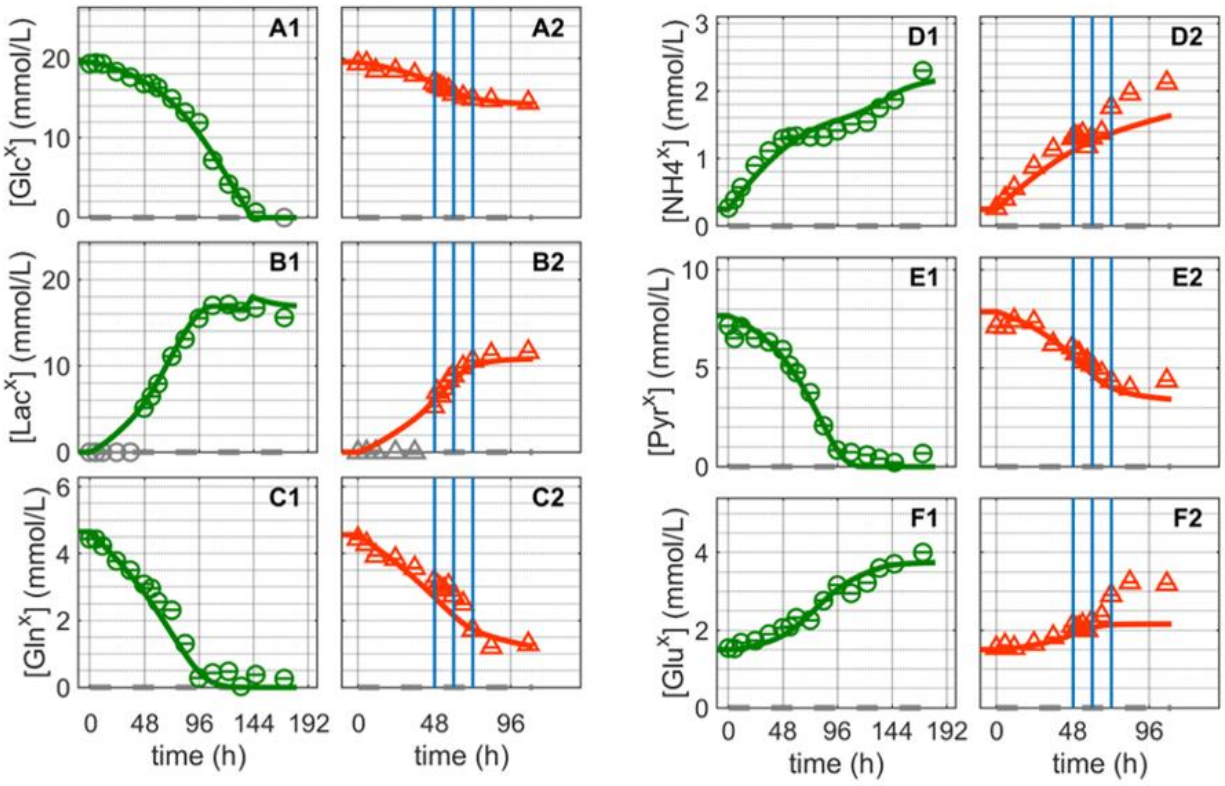

Figure 4.13.: Dynamics in extracellular substrates and metabolic by-products of mock-infected and infected MDCK suspension cells. (A1–2) Glucose, (B1–2) lactate, (C1–2) glutamine, (D–2) ammonium, (E1–2) pyruvate, and (F1–2) glutamate. Data and error bars represent the mean and standard deviation of technical triplicates for two independent experiments (mock-infected Θ and infected Δ). Lines: model simulations. Vertical blue lines correspond to 0, 12 and 24 h post infection, respectively. The grey dashed lines indicate the limit of quantification for each metabolite and grey data points are under the limit of quantification. Experimental data used for parameter estimation: A1, B1, C1, D1, E1 and F1. Figure adapted from Ramos et al., 2022 [158].

The concentration of extracellular lactate increased in the bioreactor while glucose was available and was consumed in both cultivations (Fig. 4.13B). As previously reported for MDCK cells [68,163], the stoichiometric ratio of lactate to glucose was approximately 1:1 for both cultivations. Typically, in continuous cell lines, a large portion of the glucose consumed is converted by glycolytic enzymes to pyruvate, which in turn is converted to lactate to regenerate NAD^+ to maintain a high ATP generation rate [222,223]. The previous model developed for AGE1.HNAAT used lumped reaction to describe

extracellular lactate production directly from intracellular pyruvate [157]. However, to better describe the extracellular lactate dynamics, in this model extension the intracellular lactate state was considered in more detail. In particular, it was assumed that intracellular lactate is produced via LDH in a reversible reaction (Eqs. 3.1.70 and A.2.23 in Appendix A), and a transport equation was added to connect intracellular lactate to its extracellular form (Eq. A.2.7 in Appendix A). LDH is known to be a highly regulated enzyme with a very fast turnover. Additionally, depending on the metabolic state of the cell, it can favor either lactate production or lactate consumption. Different theories exist regarding the control of the switch between lactate production and consumption [47,126,185–188,190,224]. Here, a reversible hill kinetic with two modifiers for LDH (Eq. A.2.23 in Appendix A) and a reversible hill equation ($r_{Lac^x_{trans}}$, Eq. A.2.7 in Appendix A) to connect intracellular lactate with its extracellular equivalent were sufficient to account for this inherent complexity as it allowed the correct prediction of this switch. This switch allows a minor lactate consumption after glucose depletion (Fig. 4.13 (B1) and $r_{Lac^x_{trans}}$ in Fig. 4.18 introduced below). As a result, model simulations accurately reproduced the lactate dynamics in mock-infected (Cultivation 1) and infected cells (Cultivation 2) (Fig. 4.13).

Ammonium and glutamate accumulated until the end of cultivation in Cultivation 1, even after the depletion of glutamine (Fig. 4.13 (D1, F1)). Glutamate is a non-essential amino acid produced from glutamine as their primary source and other amino acids, e.g., via proline and lysine catabolism [192]. Similarly, the production of ammonium is closely linked to the metabolism of various amino acids. Apart from glutamine and glutamate, no additional amino acids were quantified in this study, but it has been found that the majority of amino acids are not depleted at the end of the exponential growth phase of MDCK suspension cell cultivations using the same medium [56]. Therefore, and as reported previously for other suspension cell lines [157,193], an intracellular accumulation of glutamate and ammonium appears to occur even during late stages of cultivation, followed by their release into the supernatant. Accordingly, model simulations are also in good agreement with the experimental data in the mock-infected cells cultivation (Fig. 4.13 (D1, F1)) since it also predicted their intracellular excess. For Cultivation 2 (infected), however, significant discrepancies between model predictions and experimental data are observed (Fig. 4.13 (D2, F2)). Starting about 12 hpi, ammonium and glutamate

concentrations are clearly underestimated. Assuming that assumptions in the model about glutamate and ammonium metabolism are justified as it describes well these metabolites in cells that were not infect, and during the early infection phase, it must be concluded that virus infection either results in drastic changes in cellular metabolism during the late phase of IAV infection or there are other sources in which virus-induced cell death and cell lysis play a significant role. In particular, either enzymes released into the extracellular environment following cell lysis retain a high level of activity or both metabolites leak into the supernatant due to cell lysis. The latter, however, was safely excluded as *in silico* model simulations clearly demonstrated that the complete release of intracellular glutamate and ammonium into the supernatant would not result in more than a 1.5% increase in their extracellular concentrations (an increase of about 0.025 mmol/L for glutamate and 0.009 mmol/L for ammonium, respectively; see Section 3.1 of supplementary studies in Appendix C). On the other hand, it could not be ruled out that enzymes released into the extracellular environment because of cell lysis could retain a significant activity level. According to results obtained from *in silico* model simulations, taking the amino acid degradation/conversion enzymes rate based on viable cell volume (microscale) and converting it to the bioreactor volume scale (macroscale) would be enough to explain the increase in extracellular ammonium and glutamate concentrations (see Section 3.2 of supplementary studies in Appendix C). Similar mechanisms might also apply for other metabolites including lactate and pyruvate. In any case, these events take place in a time window where most virus particles have been released into the supernatant and the number of productive cells is declining rapidly. These findings are more or less irrelevant for virus production process optimization, but are relevant for cultivation processes where high cell densities are achieved (e.g. Fed-batch) and cell lysis clearly occurs at a much higher rate.

4.2.3 Central carbon metabolism

Model simulations of key metabolites from glycolysis, TCA, and energy metabolism of two shaker flask cultivations of MDCK cells are discussed in the preceding section. Note that the limit of quantification refers to the intracellular concentrations and not to the extracellular concentrations (in the sample). As the sample volume was constant, the limit of quantification is inversely proportional to the viable cell volume per milliliter; an increase

in the number of cells per sample reduces the concentration of intracellular metabolite required to reach the limit of quantification and vice versa.

Glycolysis: Similar dynamics were observed for most glycolytic metabolites for both cultivations (Fig. 4.14). A short, more or less peak-like initial accumulation of metabolites followed by a gradual decrease over the cultivation time. The dynamics of ribose-5-phosphate (R5P) and UDPGlc are very similar, with a relatively stable initial concentration followed by rapid depletion over time (Fig. 4.14). G6P and F6P exhibited similar dynamics prior to their depletion, and the same was true for 3GP and PEP. On the other hand, the dynamics of F16P is unique as it remains mostly under the limit of quantification. In Cultivation 1, the glycolytic metabolites were depleted concomitant with glucose depletion at around 144 h (Figs. 4.13 (A1) and 4.14). In Cultivation 2, the concentrations of these metabolites decreased significantly shortly after virus infection. Model simulations of glycolytic metabolites concentration closely capture their dynamics in mock-infected cells. This indicates that reasonable assumptions were made about kinetics for enzymes from glycolysis and pentose phosphate pathway, particularly regarding the enzymes involved in feedback control, namely HK, PFK and LDH [195–197]. Model predictions of glycolytic metabolite concentrations in infected cells are also in agreement with the experimental data, especially for the first 24 hpi (before onset of cell lysis and degradation). However, the model slightly underestimated the concentrations of G6P and F6P, though their concentrations started to drop below the limit of detection around 12 hpi. Additionally, the model did not predict the peak-like dynamic of F16P after virus infection, though this point may be considered an outlier since it is a single measurement. Given the precision with which the dynamics of most metabolites were described, model assumptions regarding the kinetics and control of glycolysis appear to be sufficiently justified. Note that the same kinetics and set of parameters was used for simulation of non-infected cells and prediction of infected cells. Thus, these results suggest that virus infection had a relatively minor impact on glycolysis, especially during the first 24 hpi when virus-induced apoptosis and cell lysis are more or less negligible. This is consistent with the fact that the total virus particle volume (of 12,000 virions/cell in this instance) accounts for around 0.55% of the volume of a single cell (V/V total volume of virus produced in a cell per average volume of a cell). This implies that in theory a single cell can produce many more virions. Even considering that some of the viral components (protein, RNA) synthesized in infected cells are not used for progeny virus production, i.e. are produced in excess, the overall burden

of virus replication on cellular metabolism can be considered low. This further cements that the changes in metabolism observed during virus replication are an indirect product of the latter.

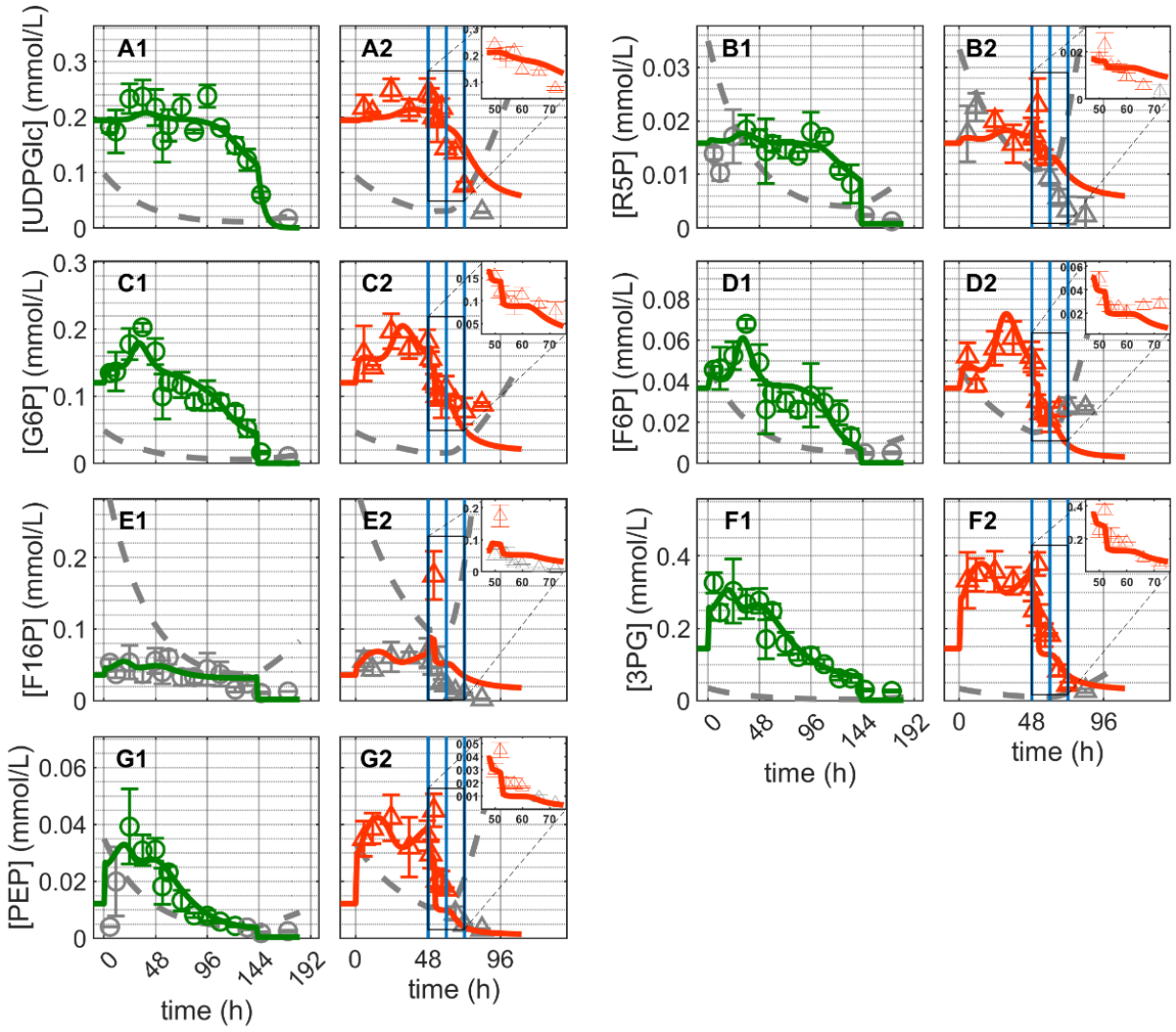

Figure 4.14.: Dynamics of metabolites in glycolysis and pentose phosphate pathway of mock-infected and infected MDCK suspension cells (top right insert: 48–72 h of infected cultivation). (A1–2) Uridine diphosphate glucose, (B1–2) ribose–5-phosphate, (C1–2) glucose-6-phosphate, (D1–2) fructose-6-phosphate, (E1–2) fructose-1,6-biphosphate, (F1–2) 3-phosphoglycerate and (G1–2) phosphoenolpyruvate. Data and error bars represent the mean and standard deviation of technical triplicates for two independent experiments (mock-infected Θ and infected Δ). Lines: model simulations. Vertical blue lines correspond to (0, 12 and 24 h post

infection, respectively). The grey lines indicate the limit of quantification for each metabolite and the grey data points are under the limit of quantification. Experimental data used for parameter estimation: A1, B1, C1, D1, E1, F1 and G1. Figure taken from Ramos et al., 2022 [158].

TCA: The concentration of most TCA cycle metabolites showed an initial peak-like behavior and then decreased until about 144 h, and remained practically constant after and until the end of Cultivation 1 (Fig. 4.15). The exception was succinate (Suc), which did not exhibit the initial peak-like accumulation and as its concentration remained almost constant initially (Fig. 4.15 (E1)). The concentration of citrate (Cit) remained approximately 100-fold that of cis-aconitate (cAc) and iso-citrate suggesting their isomerization by the enzyme ACO favored citrate production (Fig. 4.15 (A1, B1, C1)). The remaining TCA cycle intermediates, such as alpha-ketoglutarate (Keto), fumarate (Fum) and malate (Mal) showed similar dynamics and their concentrations exceeded their limit of quantification (Fig. 4.15 (D1, F1, G1)). The model simulation captures reasonably well the dynamics of these metabolites in Cultivation 1. This implies that reasonable assumptions were made about reaction kinetics of the TCA cycle, glutaminolysis and transamination. In particular, for example, by accounting for the inhibitory effect of oxaloacetate on succinate dehydrogenase [225,226] (Eq. A.2.41), the model simulation was able to capture the increase in Suc concentration near the end of Cultivation 1.

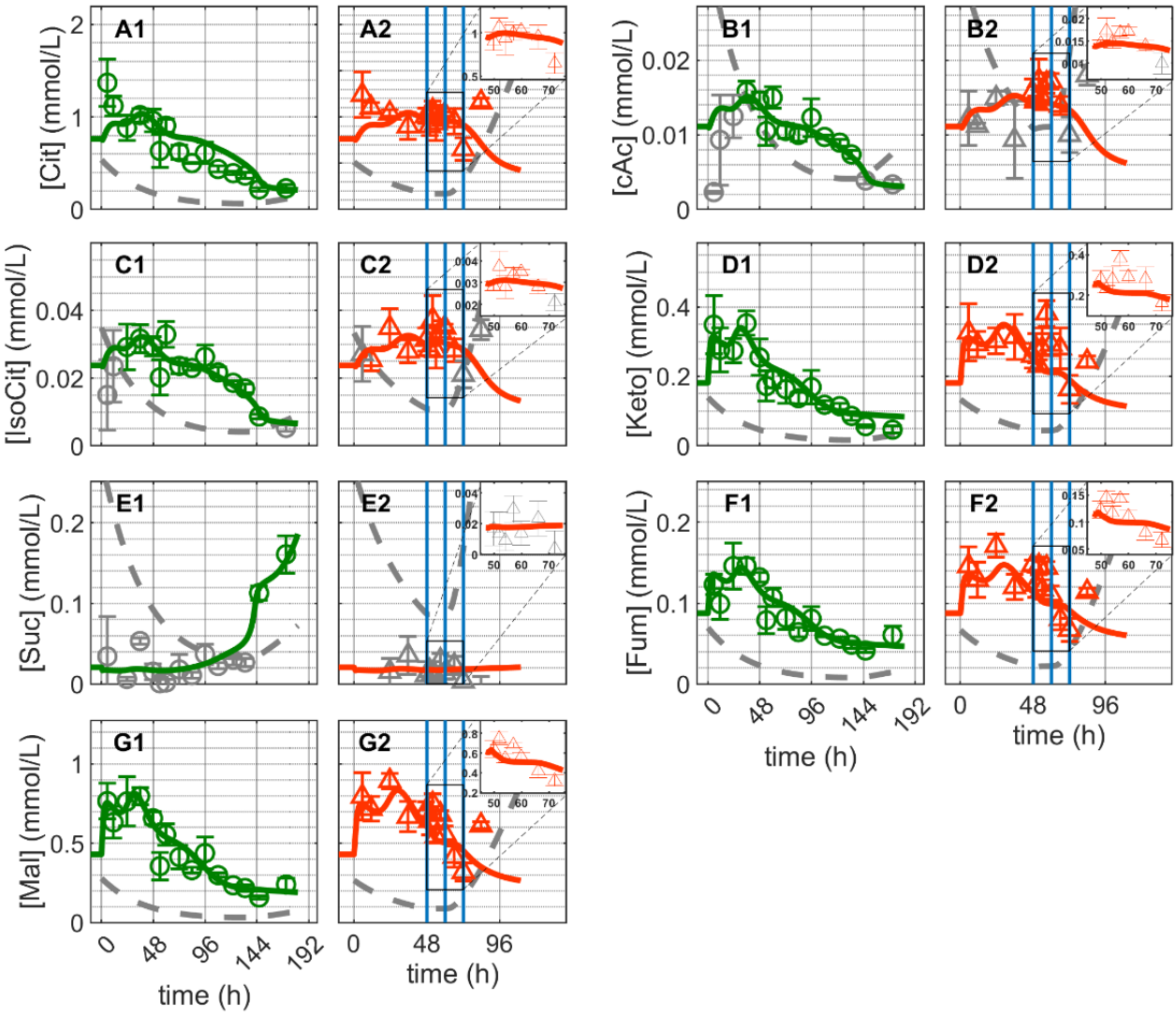

Figure 4.15.: Dynamics of metabolites in TCA cycle in mock-infected and infected MDCK suspension cells (top right insert: 48–72 h of infected cultivation). (A1–2) Citrate, (B1–2) cis-aconitate, (C1–2) iso-citrate, (D1–2) alpha-ketoglutarate, (E1–2) succinate, (F1–2) fumarate and (G1–2) malate. Data and error bars represent the mean and standard deviation of technical triplicates for two independent experiments (mock-infected Θ and infected Δ). Lines: model simulations. Vertical blue lines correspond to (0, 12 and 24 h post infection, respectively). The grey lines indicate the limit of quantification for each metabolite and the grey data points are under the limit of quantification. Experimental data used for parameter estimation: A1, B1, C1, D1, E1, F1 and G1. Figure taken from Ramos et al., 2022 [158].

For Cultivation 2 (infected approximately 48 h post inoculation), concentrations of Cit, cAc and iso-citrate decreased immediately after infection and increased again around 24 hpi (Fig. 4.15 (A2, B2, C2)). Contrary to mock-infected cells in Cultivation 1, the concentration of Suc remained below the limit of quantification after infection. Additionally, the concentrations of Keto, Fum and Mal increased rapidly immediately after infection (on average about 20%), decreased between 12–24 hpi and subsequently increased again with the onset of cell lysis and degradation (Fig. 4.15 (D2, F2, G2)). Using the same set of parameters estimated for mock-infected cells, the model predicts the dynamics of these metabolites reasonably well for about 24 hpi. The discrepancies between model predictions and the peak-like increase in Keto, Fum and Mal immediately after infection are difficult to interpret. Metabolic changes at early infection stages might be related to virus-induced cessation of cell growth [22], and/or early virus protein production [27], which in turn can lead to changes in the control of enzymes [26,27,171,227–230]. In this case, the noticeable accumulation of some metabolites of TCA cycle is either a side effect of virus infection or due to specific changes in related enzymes induced by early infection events. However, in any scenario, because of the characteristics of the metabolic network established (in particular its structural robustness and small-world property considering only a low number of reactions linking intracellular metabolites) [231], the dynamics of the reactions involved would allow a fast transition towards its inherent “normal behavior” (homeostasis on equilibrium point) where model assumptions are valid again. Nonetheless, the observed differences between model prediction and experimental data are generally small in the first 24 hpi, implying that virus replication only had a minor impact on the TCA cycle and its closely related metabolic pathways. The discrepancies that begin at around 24 hpi are most likely due to virus-induced apoptosis, which results in the disintegration of mitochondrial membranes and cell lysis. In addition to this, the discrepancies due to the increase in the concentrations of certain metabolites of the TCA cycle starting about 24 hpi may indicate a partial shutdown of the central carbon and energy metabolism. In any case, limitations concerning certain model assumptions and enzyme kinetics cannot be completely ruled out.

Energy metabolism: ATP concentration (Fig. 4.16) in mock-infected cells (Cultivation 1) remained high throughout the exponential cell growth phase (Fig. 4.16 (A1)) and decreased shortly after glutamine and pyruvate depletion at approximately 100 h post inoculation. The model simulation accurately reproduces the dynamics of ATP, implying

that a good balance between its consumption and production was made (Eqs. A.2.46, A.2.48 and A.2.50 in Appendix A). ATP and its precursors are generated in glycolysis, TCA cycle, oxidative phosphorylation and other related metabolic pathways (Eqs. A.2.44, A.2.45 and A.2.51–A.2.52). According to model simulations, while glucose is present in the medium (until about 144 h), glycolysis ($r_{glycolysis}$, Eq. A.2.44 in Appendix A) accounts for approximately 20% of the total ATP production ($r_{glycolysis}$ in Fig. 4.20). This is well within the range of 1–64% previously reported for other animal cell lines [209]. Additionally, the estimated theoretical oxygen consumption ranged from 62–113 fmol/cell/h (r_{o2} in Fig. 4.20), which is comparable to the consumptions reported for other continuous cell lines of 7–97 fmol/cell/h [210,211].

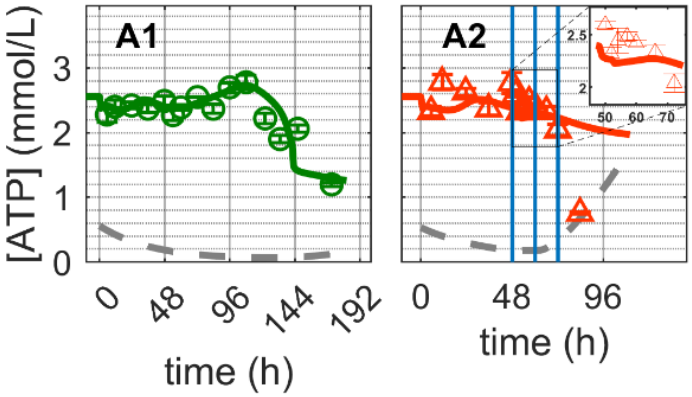

Figure 4.16.: Dynamics of ATP in mock-infected and infected MDCK suspension cells (top right insert: 48–72 h of infected cultivation). (A1–2) Adenosine triphosphate. Data and error bars represent the mean and standard deviation of technical triplicates for two independent experiments (mock-infected Θ and infected Δ). Lines: model simulations. Vertical blue lines correspond to (0, 12 and 24 h post infection, respectively). The grey lines indicate the limit of quantification for each metabolite and the grey data points are under the limit of quantification. Experimental data used for parameter estimation: A1. Figure taken from Ramos et al., 2022 [158].

For Cultivation 2, ATP concentrations remained high initially during the exponential cell growth phase and during the first 24 hpi, and subsequently decreased rapidly approaching the limit of quantification as virus infection progressed (Fig. 4.16 (A2)). Model simulations using the same kinetics and set of parameters estimated for mock-infected cells resulted in a reasonable prediction of ATP concentration dynamics during the first

24 hpi. As specific mechanisms for the shutdown of metabolic pathways associated with apoptosis and cell deterioration have not been implemented (only cell death has been considered so far), the model significantly overestimates the concentration of ATP at later time points. In fact, the sharp decrease in ATP concentration starting at 24 hpi also supports the hypothesis of at least a partial metabolic shutdown. In this case, ATP was predominately produced via the TCA cycle (r_{TCA}, Eq. (A.2.45 in Appendix A), contributing approximately 80% of total ATP (r_{TCA}, Fig. 4.20); therefore, failing to account for a partial shutdown or truncation of TCA previously identified in the model simulations could lead to the overproduction of ATP observed. However, generally, and as for glycolysis and TCA cycle, model assumptions for ATP generation and consumption seem to be sufficiently justified. In particular, since model parameters estimated for mock-infected cells enabled a good prediction of the dynamics in IAV infected cells as long as the shutdown of intracellular pathways does not play a significant role, i.e., for the first 12–24 h after virus entry, onset of intracellular virus replication and virus release.

4.2.4 Analysis of simulated metabolic rates

Given the overall accuracy of the developed model to describe cell growth, extracellular and intracellular metabolites dynamics, these metabolic rates were used for further analysis. These metabolic rates were used for a detailed analysis of cellular physiological state changes of infected compared to mock-infected cells. The simulated metabolic rates, which are state variables in the model, are presented (Figs. 4.17–4.20). Furthermore, the established model was also used for *in silico* studies in the supplementary studies (Appendix C).

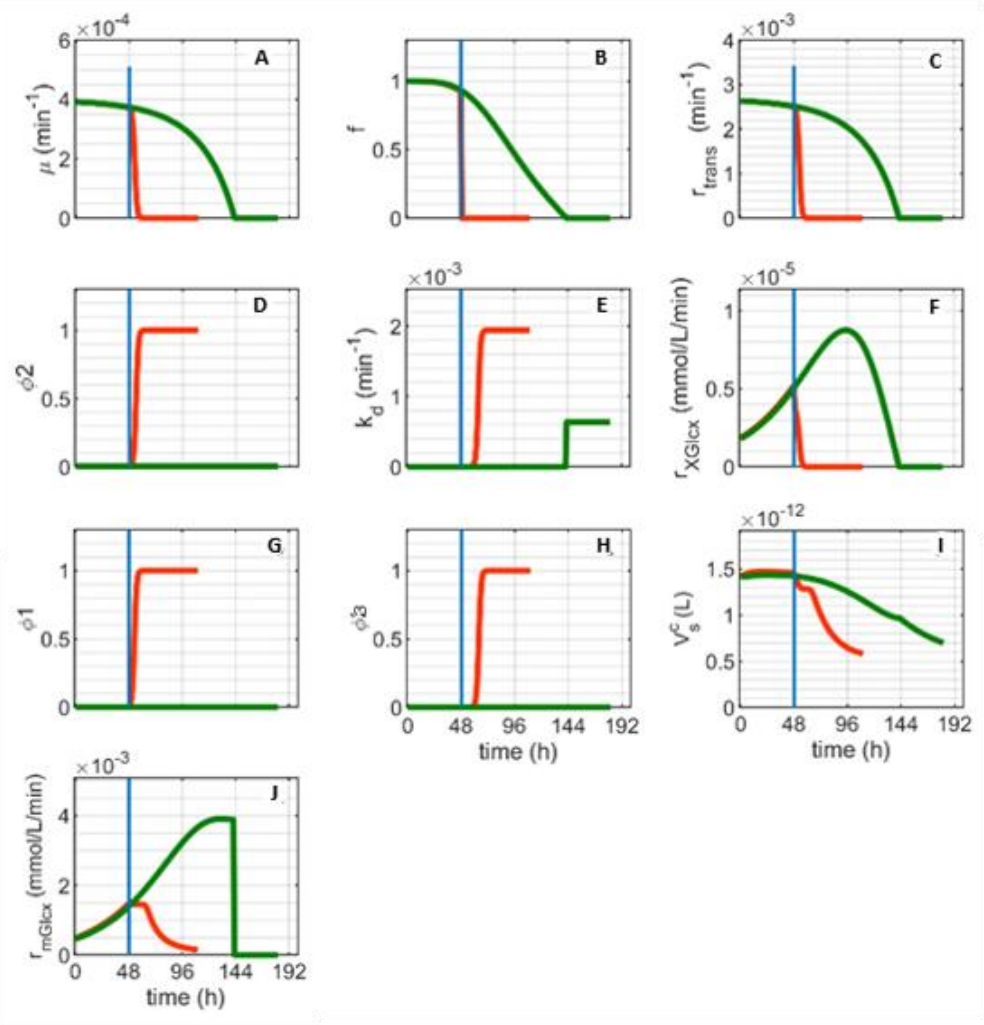

Figure 4.17.: Metabolic rates from cell growth obtained from model simulation of MDCK suspension cells (mock-infected –, infected –). (A) Growth rate, (B) inhibition factor, (C) transition rate, (D) step function Φ_2, (E) cell death rate, (F) growth related glucose consumption rate, (G) step function Φ_1, (H) step function Φ_3, (I) cell-specific volume and (J) maintenance-related glucose consumption. Vertical blue line represents 0 h post infection for Cultivation 2. Figure adapted from Ramos et al., 2022 [158].

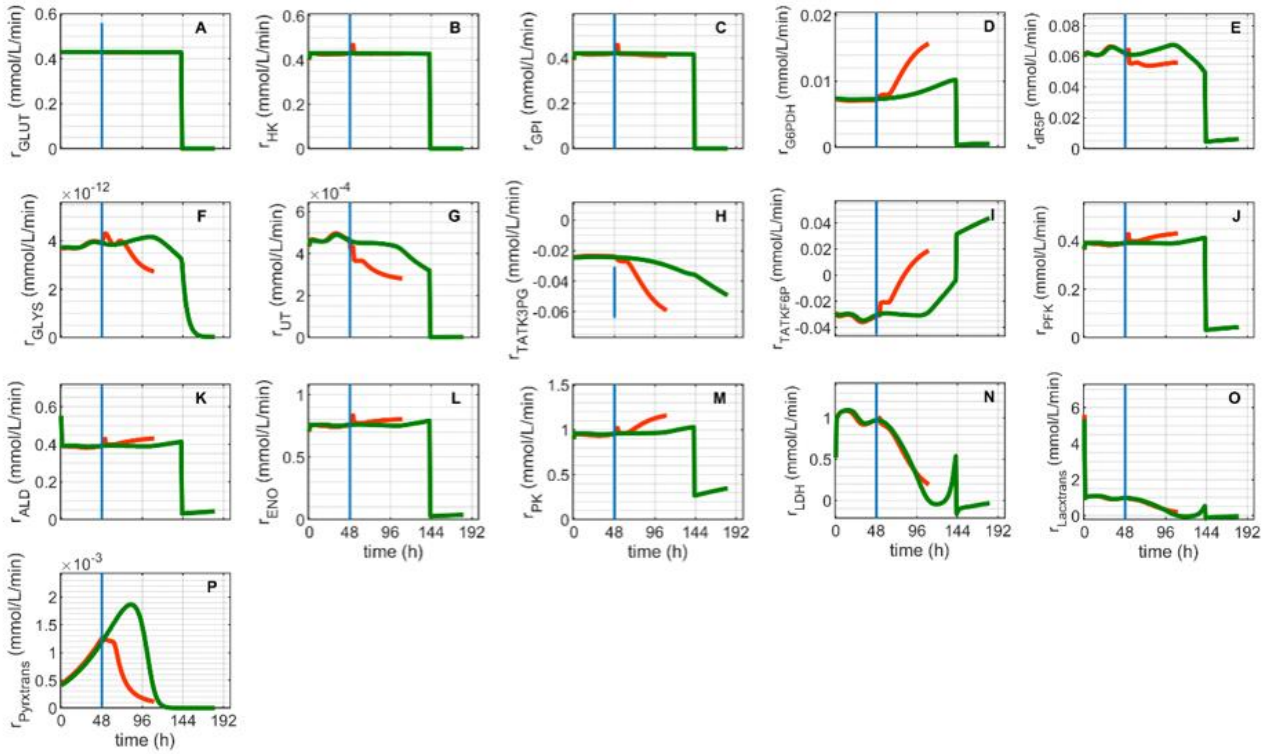

Figure 4.18.: Metabolic rates from glycolysis obtained from model simulation of MDCK suspension cells (mock-infected —, infected —). (A) Glucose transporter rate, (B) hexokinase rate, (C) glucose-6-phosphate isomerase rate, (D) glucose-6-phosphate dehydrogenase rate, (E) ribose-5-phosphate consumption rate, (F) glycogen synthetase rate, (G) uridyl transferase rate, (H) transaldolase and transketolase rate, (I) transaldolase and transketolase rate, (J) phosphofructokinase rate, (K) aldolase rate, (L) enolase rate, (M) pyruvate kinase rate, (N) lactate dehydrogenase rate, (O) extracellular lactate production/ consumption rate and (P) extracellular pyruvate consumption rate. Vertical blue line represents 0 h post infection for Cultivation 2. Figure adapted from Ramos et al., 2022 [158].

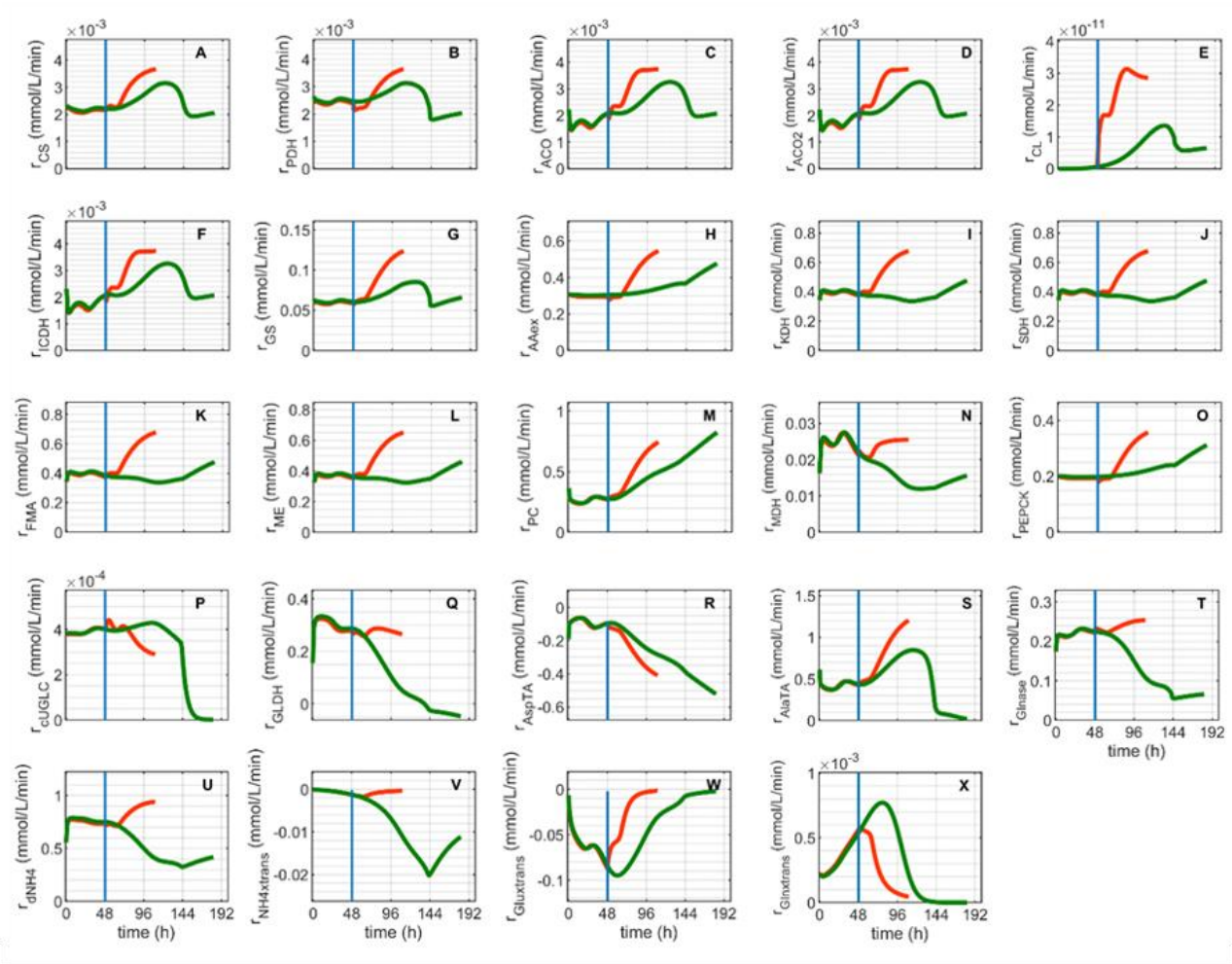

Figure 4.19.: Metabolic rates from TCA obtained from model simulation of MDCK suspension cells (mock-infected —, infected —). (A) Citrate synthetase rate, (B) : pyruvate dehydrogenase rate, (C) aconitase rate, (D) aconitase rate, (E) citrate lyase rate, (F) isocitrate dehydrogenase rate, (G) glutamine synthetase rate, (H) amino acids degradation rate, (I) ketoglutarate dehydrogenase rate, (J) succinate dehydrogenase rate, (K) fumarase rate, (L) malic enzyme rate, (M) pyruvate carboxylase rate, (N) malate dehydrogenase rate, (O) phosphoenolpyruvate-kinase rate, (P) uridine diphosphate glucose consumption rate, (Q) glutamate dehydrogenase rate, (R) aspartate transaminase rate, (S) alanine transaminase rate, (T) glutaminase rate, (U) ammonium consumption rate, (V) extracellular ammonium production rate, (W) extracellular glutamate production rate and (X) extracellular glutamine consumption rate. Vertical blue line represents 0 h post infection for Cultivation 2. Figure taken from Ramos et al., 2022 [158].

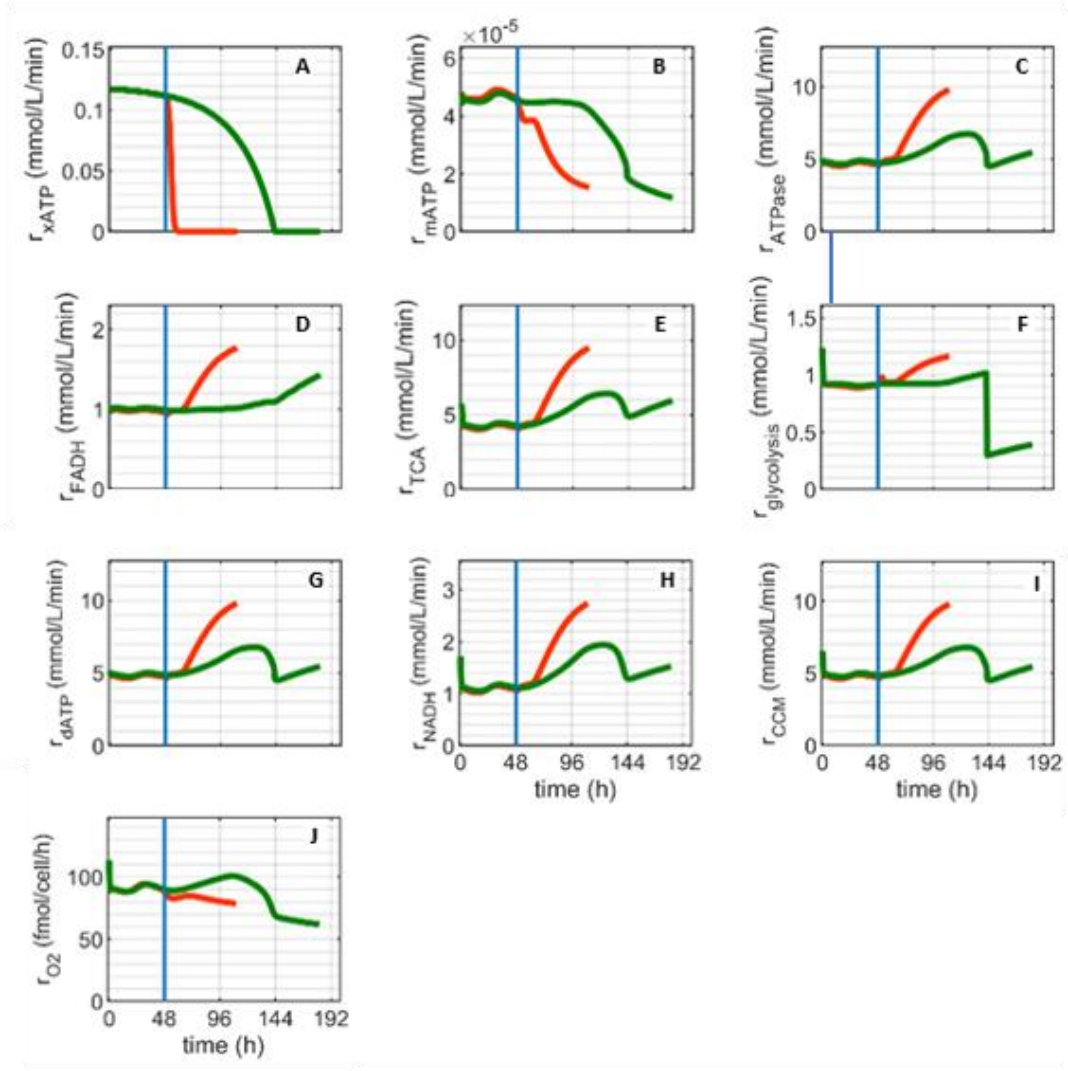

Figure 4.20.: Metabolic rates from TCA obtained from model simulation of MDCK suspension cells (mock-infected —, infected —). (A) ATP consumption for growth, (B) ATP consumption for maintenance, (C) ATPase rate, (D) FADH oxidative phosphorylation rate, (E) TCA net ATP production rate, (F) glycolytic net ATP production rate, (G) net consumption of ATP, (H) NADH oxidative phosphorylation rate, (I) net production of ATP and (J) theoretical oxygen consumption rate. Vertical blue line represents 0 h post infection for Cultivation 2. Figure adapted from Ramos et al., 2022 [158].

Based on these metabolic rates shown in Figs. 4.17–4.20, the aggregated metabolic rates were calculated in different cultivation phases (exponential cell growth phase, cell death phase and virus infection phase). A brief analysis of cellular metabolic states on infected

and mock-infected cells based on these aggregated model simulations is shown for selected reactions of glycolysis and pentose phosphate pathway (Fig. 4.21), and for TCA cycle, glutaminolysis and transamination (Fig. 4.22).

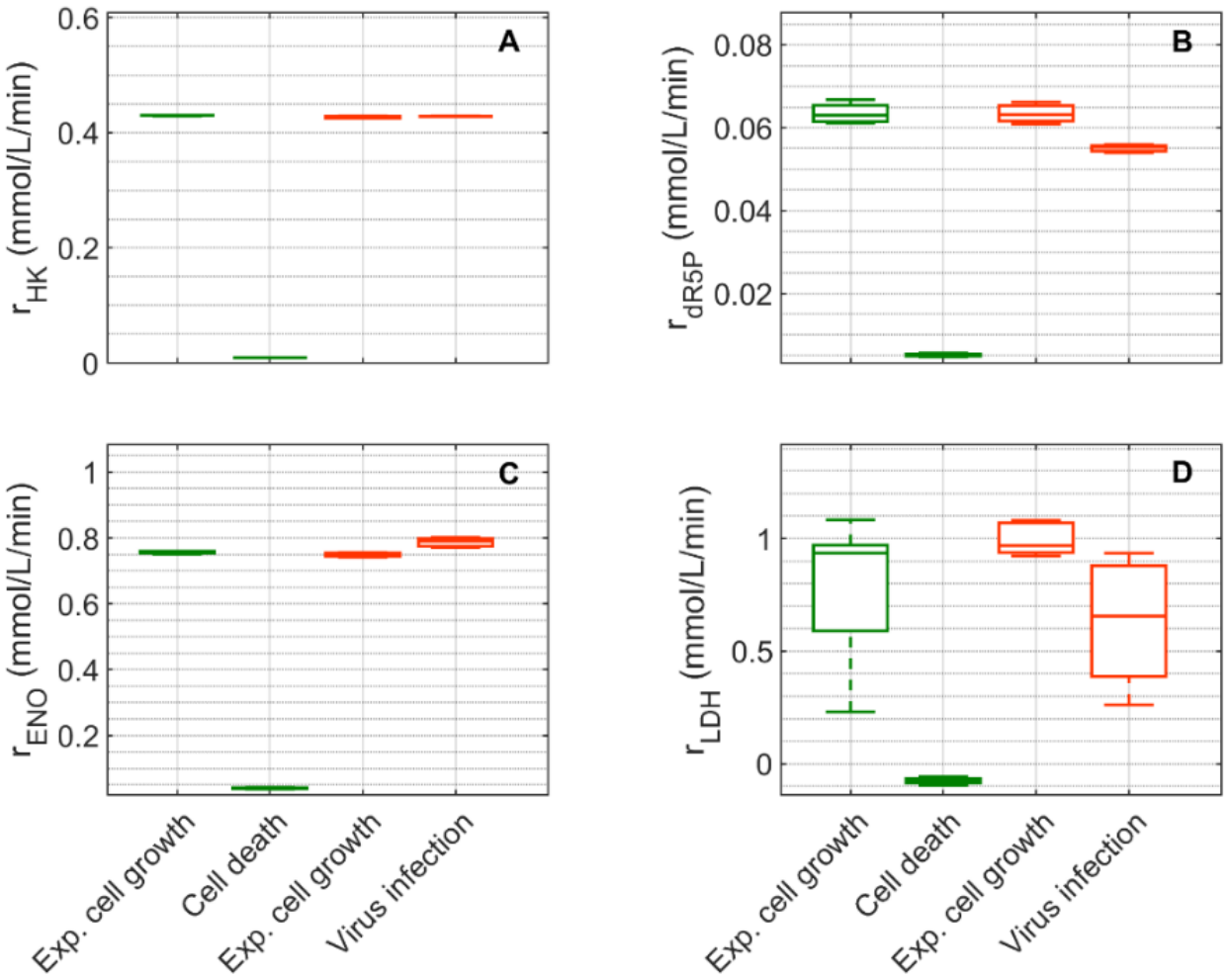

Figure 4.21.: Box-and-whisker plot for selected intracellular rates of glycolysis and pentose phosphate pathway estimated from model simulations for mock-infected and infected MDCK suspension cells. (A) Hexokinase, (B) ribose-5-phosphate, (C) enolase, and (D) lactate dehydrogenase. Calculated from model simulations of the exponential growth phase of Cultivation 1 (␣, 6–108 h), the death phase of Cultivation 1 (␣, 146–169 h), the exponential growth phase of Cultivation 2 (␣, 6–48 h) and the virus replication phase of Cultivation 2 (␣, 49.9–107 h). The bar represents the median, the box is the first and third quartile, and the whisker the minimum and maximum of the rates from the model simulations of the corresponding cultivation phase. Figure taken from Ramos et al., 2022 [158].

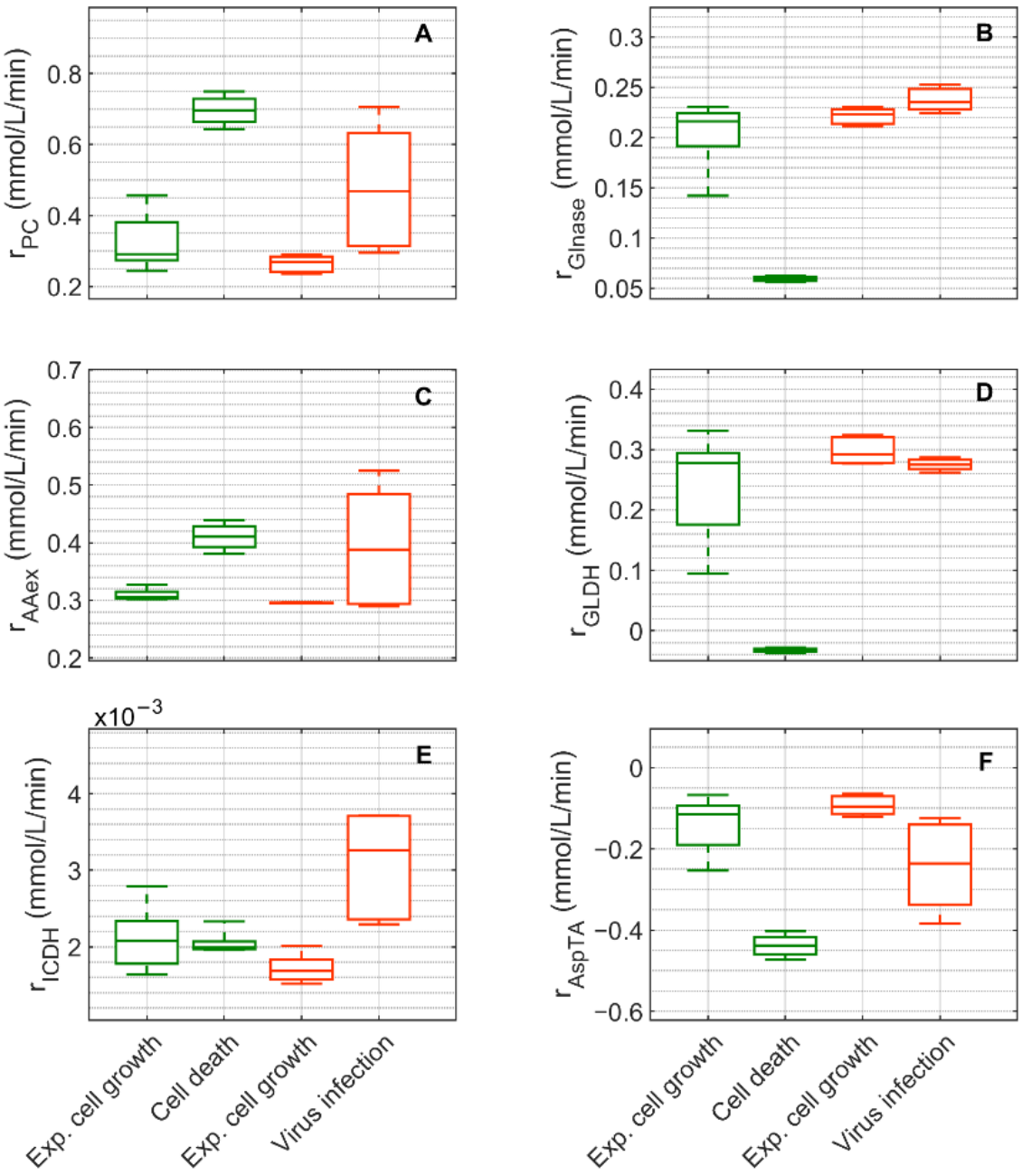

Figure 4.22.: Box-and-whisker plot for selected intracellular rates of citric acid cycle, glutaminolysis and transamination estimated from model simulations for mock-infected and infected MDCK suspension cells. (A) pyruvate carboxylase, (B) glutaminase, (C) amino acid degradation, (D) glutamate dehydrogenase, (E) isocitrate dehydrogenase and (F) aspartate transaminase. Calculated from model simulations of the exponential growth phase of Cultivation

1 (␣, 6–108 h), the death phase of Cultivation 1 (␣, 146–169 h), the exponential growth phase of Cultivation 2 (␣, 6–48 h) and the virus replication phase of Cultivation 2 (␣, 49.9–107 h). The bar represents the median, the box is the first and third quartile, and the whisker the minimum and maximum of the rates from the model simulations of the corresponding cultivation phase. Figure taken from Ramos et al., 2022 [158].

Analysis of the metabolic behavior based on selected rates: Extracellular glucose (Fig. 4.13A) was transported into the intracellular environment and rapidly converted to G6P through the HK during the exponential cell growth phase in both cultivations (Fig. 4.21A). After glucose was depleted in Cultivation 1 (mock-infected cells) at approximately 144 h and the cell entered death, the estimated HK rate decreased to zero. Cells of Cultivation 2 (infected at around 48 h) still consumed glucose at a similar rate after infection (Fig. 4.21A). Approximately 14–16% of the intracellular glucose (after conversion by HK, percentage of r_{dR5P} divided by the HK rate, Fig. 4.21B) was further processed to R5P via glucose-6-phosphate dehydrogenase or via transaldolase and transketolase during the exponential cell growth phase of both cultivations (6–108 h mock-infected, 6–48 h infected). This is well within the previously reported range of 0–40% for glucose conversion to R5P [215–217]. In the established model, the usage of R5P in other reactions was lumped in a general consumption rate (r_{dR5P}, Eq. A.2.18 in Appendix A), and its rate is also zero after glucose depletion in mock-infected cells (Fig. 4.21B). This rate slightly decreased after viral infection (Fig. 4.21B), but does not reach zero. The upper glycolytic metabolites that are not channeled to R5P reach enolase (r_{ENO}, Fig. 4.21C), which has a dynamic behavior similar to HK in both cultivations. Apart from lactate dehydrogenase (r_{LDH}, Fig. 4.21D), all rates addressed thus far have a relatively small standard deviation. Cells in Cultivation 1 had a high and positive LDH rate during exponential cell growth, indicating lactate was produced from pyruvate. When glucose was depleted and the start of the cell death phase, the LDH rate became negative, indicating lactate was consumed and converted to pyruvate. Similarly, in Cultivation 2, a high LDH rate was observed during the exponential cell growth phase of (Fig. 4.21D). After virus infection, however, these cells still had glucose and kept consuming it (Fig. 4.13 (A2)). Due to glucose consumption, glycolysis remained active (see HK and ENO, Figs. 4.21A and 4.21C), which led to a relatively high lactate production rate (Fig. 4.21D).

This high LDH rate after infection allowed a very good prediction of the extracellular lactate accumulation in the bioreactor observed after infection (Fig. 4.13 (B2)). Pyruvate that was produced in glycolysis was used by other enzymes including PDH (r_{PDH}, Fig. 4.19), transaminase (r_{AlaTA}, Fig. 4.19), and pyruvate carboxylase (PC, Fig. 4.22A). As previously reported for other cell lines [204,224], conversion of pyruvate to OAA via PC resulted in a significant carbon supply to the TCA cycle from glycolysis. In fact, a relatively high PC rate was estimated during both cultivations' exponential cell growth phases, which increased significantly not only during the cell death phase (Cultivation 1), but also after virus infection (Cultivation 2). Another important carbon source of precursors for the TCA cycle of animal cells is glutamine, which following its conversion to glutamate via GLNase may enter the TCA cycle. For mock-infected cells, the GLNase rate was relatively high during exponential cell growth phase, but decreases after substrate depletion and subsequent cell death (r_{GLNase}, Fig. 4.22B). However, GLNase activity was not zero during this phase since glutamine synthetase (r_{GS}, in Fig. 4.19) was still active. For Cultivation 2, a similar rate was estimated during the exponential cell growth phase and after viral infection (Fig. 4.22B) since the cells were infected before depletion of extracellular glutamine (Fig. 4.13 (C2)). Another possible source of glutamate in the model is the lumped amino acid degradation rate (r_{AAex}, Fig. 4.22C). For both cultivations, the estimated amino degradation rate was high during the exponential cell growth phase and further increased during the cell death phase (Cultivation 1) and after virus infection (Cultivation 2). During the exponential phase of both cultivations, the resulting glutamate was converted to Keto via glutamate dehydrogenase (GLDH, r_{GLDH} in Fig. 4.22D). However, a stark difference was observed between these cultivations during the cell death phase (Cultivation 1) and after virus infection (Cultivation 2). The GLDH rate was estimated to be negative for Cultivation 1, indicating that glutamate was produced from Keto. As a result, glutamate accumulated intracellularly and was exported to the supernatant during this phase, leading to good agreement between model simulations and experimental data (Fig. 4.13 (F1)). On the other hand, the GLDH rate was estimated to remain high after virus infection in Cultivation 2. This prevented the accumulation of glutamate on the intracellular level, and likely contributed to the discrepancy between experimental data and model simulations after virus infection (Fig. 4.13 (F2)). But this

discrepancy could also be assumed to be due to leakage of enzymes in the supernatant after cell lysis (see Section 3.2 of supplementary studies in Appendix C). Interestingly, in all scenarios, Keto was mostly produced from glutamate since the isocitrate dehydrogenase rates estimated were low (Fig. 4.22E). The fact that the aspartate transaminase rate (r_{AspTA}) was estimated to be negative in all scenarios (Fig. 4.22F) implies that the TCA cycle was truncated and only half of the TCA cycle was active in addition to the transamination reactions for energy production, as previously reported [157] and as discussed previously. The other half of the TCA cycle, as usual, provided intermediates for biosynthesis through citrate [208], and as discussed previously.

4.2.5 Summary

Overall, reasonable simulations and predictions of the dynamics of key metabolites in mock-infected and infected cells, respectively, was achieved. This is especially relevant for the period relevant for IAV replication and release (first 24 hpi). It is also pertinent that it was achieved using a single set of parameters and that only kinetics for transition to cell growth arrest and cell death after virus infection were implemented for infected cells. This strongly suggests that the description of metabolic changes in IAV-infected cells, compared to mock-infect cells, primarily only requires a reasonable description of cell growth arrest and transition to cell death, rather than changes of specific enzyme kinetics or parameters. The fact that prediction of metabolite dynamics in infected cells did not require a new set of parameters (compared to mock-infected cells), suggests that IAV-specific mechanisms affecting the host cell's central metabolic pathways do not play a significant role. However, there have been studies that have shown metabolic differences during infection that are host cell-dependent [23–26] and even between virus subtypes such as influenza A virus subtypes [22]. at. Finally, the *in silico* study performed here shows that cell lysis can have a significant impact on extracellular metabolites concentrations at late infection phase due to enzymes that are released into supernatant remaining active. Cell lysis is extremely important in cultivations where high cell densities are attained and high cell lysis are typically observed such as fed-batch.

5 Chapter Conclusions

In the first step of this thesis, a quantitative and dynamic mechanistic model that describes cell growth, central carbon metabolism and product formation was established. The model combines a segregated cell growth model coupled with a structured intracellular model of metabolism to describe growth and metabolism of AGE1.HN.AAT suspension cells. This model covers the cell growth (exponential cell growth and cell death phase) and product formation (A1AT). It also considers glycolysis, TCA, pentose phosphate pathway, and transamination. An important aspect of this approach is that substrate consumption rates were used as input to the intracellular model and the intracellular rates were used as outputs to simulate the extracellular by-products accumulation. The performance of this model was assessed using experimental data (extracellular and intracellular metabolite concentrations, enzyme activities) collected for four batch experiments. Using specific initial conditions and the same set of parameters, the model described extracellular dynamics for growth and death phases well. By considering changes in cell volume, dynamics of intracellular concentrations metabolites and the recombinant protein were also fitted well. Due to good agreement of model simulations with experimental data, valid and relevant biological simulations were made regarding cell growth and enzyme kinetics. As such the established model was further used to perform *in silico* studies and analysis of the cellular metabolic state through the simulated metabolic rates.

Based on simulated rates of key enzymes of the metabolic network, at least two distinct cellular physiological states were observed. The first cellular physiological state was characterized by a high glycolytic rate and a high lactate production rate. The second cellular physiological state was characterized by efficient ATP production, a low glycolytic rate, and (partially) reverse or truncated TCA cycle reactions. Furthermore, it was found

that the main link between glycolysis and TCA occurred through PC, and discussed the importance of transamination on a truncated TCA.

In silico studies were used to assess AGE1.HN.AAT metabolism, to study possible targets for cell line optimization and changes in medium composition. Changes in GS activity was found to have only a minor impact on metabolism as previously suggested by another study. Sources of the negative impact on cell growth and metabolism from increased pyruvate concentration in the medium were corroborated with *in silico* simulations.

Taken together, with some simplifications and a few basic biological assumptions, it is possible to establish a rather complex dynamic model that not only describes cell growth and product formation in animal cell culture but also links extracellular metabolite dynamics with main intracellular pathways. Furthermore, it was shown that such a model could serve as a basis to address questions related to cell line engineering, medium design, and as a tool for rational process design.

The second goal of this thesis was the extension of the previous model to describe MDCK suspension cell growth, metabolism and virus production. The model covers cell growth (exponential cell growth and cell death phase) and the virus production phase. Like the first model it also considers glycolysis, TCA, pentose phosphate pathway, and transamination. Likewise, substrate consumption rates were used as input to the intracellular model and the intracellular rates were used as outputs to simulate extracellular by-product accumulation. Based on one set of parameters estimated using experimental data from a mock-infected (non-infected) cell culture, the model accurately simulated the dynamics of mock-infected cells and generally correctly predicted the dynamics of virus-infected cells for up to 60 hpi. Given the good agreement of model simulation with experimental data, valid and relevant biological simulations were made regarding cell growth, virus production and enzyme kinetics. As such the established model was further used to perform *in silico* studies and compare mock-infected and infected cell metabolism by analyzing the simulated metabolic rates. The only difference between mock-infected cells and infected cells was the inclusion of mechanisms to allow transition into the cell growth arrest. This implies that mock-infected and infected cells do not differ much in their metabolism for the initial period of virus replication and virus release for high moi scenarios. It also clearly suggests that most differences in

metabolism observed in the metabolic rates after infection are directly related to cessation of cell growth and the subsequent transition to apoptosis and cell death. For the final stage of virus production, which is of minor relevance in IAV vaccine manufacturing, a straightforward interpretation of some of the results is difficult. This concerns, in particular, the relatively high accumulation of glutamate and ammonium in the supernatant. *In silico* study showed that a release of metabolites from lysing cells (by far) cannot explain their concentration increase in the bioreactor at the late infection phase. A second *in silico* study showed that to explain this increase, a conversion of extracellular amino acids by enzymes released from the cells must be assumed.

Taken together, it is possible to establish a complex dynamic model that describes cell growth and virus production and links extracellular metabolite dynamics with intracellular pathways metabolism. Furthermore, it was shown that such a model could serve to improve our understanding of the complex interplay between cell growth, virus production and metabolism and support the identification of parameters relevant for increasing specific viral productivity of MDCK suspension cells.

6 Chapter Outlook

The main goals of this thesis were successfully achieved: developing dynamic models describing cell growth, cell volume, extracellular substrates and metabolic by-products linked with description of key intracellular metabolite dynamics. The established models consistently explain experimental data from several bioreactor experiments. These models could be potentially used for media/feeds design and show promising results that support previous research outcomes and can be used for *in silico* studies of metabolic phenomena. Model development/ validation is an iterative cycle given that they can be extended and new data sets are always generated that can be used to optimize model parameters. As such in this outlook I propose future approaches to experimental designs and model extensions and model development techniques. These suggestions could greatly benefit the endeavor of developing similar or more complex models that can lead to exciting discoveries regarding cell metabolism.

Perturbation experiments: Model validation could be performed for the established models. This implies testing if the kinetics used for reactions and transmembrane transports still hold in a short time frame experiment, e.g. 1 hour. The perturbation experiments can consist in at least one cycle of starvation and one cycle of feed with one of the main substrates such as glucose or glutamine. At least 3 data points per metabolite should be measured in each cycle.

Model extension: Data collection on a large scale at both bioreactor and intracellular level is very laborious and fitting such a large model is already challenging. Nevertheless, the current methods for metabolite quantification will evolve and allow quantification of

many metabolites more efficiently and may allow some level of automation. Furthermore, more powerful computers and more capable algorithms will become available. At that point, with data (e.g. for amino acids, lipids and other organic compounds at bioreactor and/or intracellular level), model extension could be performed. Having other relevant pathways included such as amino acid degradation and lipid production will greatly improve the utility of such models, especially for usage in the pharmaceutical industry. The current model could also benefit from inclusion of growth-related intracellular metabolites usage as part of the metabolites are directly used for protein production and glycosylation rather than being processed in the central carbon metabolism. More specifically, if the cell composition is determined experimentally, these rates (usage of amino acids such as Glu and Gln for proteins and Glc for glycosylation) can be added to these models as follows,

$$-\mu\tau[c] \qquad (6.0.1),$$

where μ is the cell growth rate, c is an arbitrary state variable (intracellular metabolite, in this instance) and τ is the normalized quantity of c in the cell dry composition.

Virus infection experiments: Transferring such models to other cell lines to study metabolism of infected and non-infected cells would be an exciting endeavor. The main hypothesis derived here was that, if the cell growth arrest and transition into apoptosis (cell death) is captured in infect cells, no change is required to any kinetics or their related parameters used to simulate non-infected cells. As such, it would be beneficial to have future studies with other IAV subtypes or with other influenza virus strains relevant for vaccine production to establish a broader database for simulation studies and to contribute to a better understanding of the complex interactions of viruses with their host cells.

Incorporation in the era of industry 4.0: Industry 4.0 refers to the fourth industrial revolution, where advanced technologies (e.g. artificial intelligence and robotics) are integrated into traditional processes. One of the hallmarks is the establishment of digital twins (DTs, an identical virtual system that considers the physical and biological aspects of process and interacts with the real process [232]) for real time process monitoring and simulation. The goal is to allow smarter decision makings, more flexible and efficient

bioprocesses. Large scale dynamic models, as established in this thesis, can be trained on complex and high-dimensional experimental data and can be used for cell culture state simulations and predictions. DTs containing such a model at its core would be beneficial for real time model predictions for monitoring cell culture evolution or even for real decision making such as cell culture feed.

List of figures

List of tables

List of publications

Parts of the following publications were included in this work.

Journal articles

Ramos JRC, Bissinger T, Genzel Y, Reichl U. **2022**. Impact of influenza A virus infection on growth and metabolism of suspension MDCK cells using a dynamic model. Metabolites.12: 239. https://doi.org/10.3390/metabo12030239

Ramos JRC, Rath AG, Genzel Y, Sandig V, Reichl U. **2020**. A dynamic model linking cell growth to intracellular metabolism and extracellular by-product accumulation. Biotechnol Bioeng. 117: 1533–1553. https://doi.org/10.1002/bit.27288

Talks

Ramos JRC, Bissinger T, Genzel Y, Reichl U. A dynamic model for cell growth, metabolism and virus production of MDCK suspension cells. 2020, Society of Mathematical Biology Annual Meeting, Virtual Meeting

Posters

Ramos JRC, Bissinger T, Genzel Y, Reichl U. A Dynamic Model for Cell Growth, Metabolism & Virus Production of MDCK Suspension Cells. 2019, YCOPE 2019, Magdeburg, Germany.

Bissinger T, **Ramos JRC**, Ringeisen J., Genzel Y, Reichl U. Dynamics of intracellular metabolite pools in MDCK suspension cells during cell growth and influenza virus infection. 2018, Cell Culture Engineering XVI, Tampa, Florida, USA.

Bissinger T, **Ramos JRC**, Ringeisen J., Genzel Y, Reichl U. Intracellular Metabolic Pool Dynamics in MDCK Suspension Cells during Growth and Influenza Virus Infection. 2017, 25th ESACT Meeting, Lausanne, Switzerland.

Ramos JRC, Rath AG, Genzel Y, Rose T, Sandig V, Reichl U.A Dynamic Model of Growth and Metabolism of AGE1.HN Suspension Cells. 2016, 6th IFAC Conference on Foundations of Systems Biology in Engineering, Magdeburg, Germany.

Bibliography

1. Strain, B.; Morrissey, J.; Antonakoudis, A.; Kontoravdi, C. Genome-scale models as a vehicle for knowledge transfer from microbial to mammalian cell systems. *Comput. Struct. Biotechnol. J.* **2023**, *21*, 1543–1549, doi:10.1016/j.csbj.2023.02.011.

2. Johnson, K.A. A century of enzyme kinetic analysis, 1913 to 2013. *FEBS Lett.* **2013**, *587*, 2753–2766, doi:10.1016/j.febslet.2013.07.012.

3. Genzel, Y.; Rödig, J.; Rapp, E.; Reichl, U. Vaccine Production: Upstream Processing with Adherent or Suspension Cell Lines. In *Animal Cell Biotechnology*; Pörtner, R., Ed.; Methods in Molecular Biology; Humana Press: Totowa, NJ, 2014; Vol. 1104, pp. 371–393 ISBN 978-1-62703-732-7.

4. Genzel, Y.; Reichl, U. Continuous cell lines as a production system for influenza vaccines. *Expert Rev. Vaccines* **2009**, *8*, 1681–1692, doi:10.1586/erv.09.128.

5. Genzel, Y.; Schulze-Horsel, J.; Möhler, L.; Sidorenko, Y.; Reichl, U. Influenza Vaccines – Challenges in Mammalian Cell Culture Technology. In *Cell Technology for Cell Products*; Springer Netherlands: Dordrecht, 2007; pp. 503–508.

6. Lowy, R.J. Influenza virus induction of apoptosis by intrinsic and extrinsic mechanisms. *Int. Rev. Immunol.* **2003**, *22*, 425–449, doi:10.1080/08830180305216.

7. Santos, L.A.; Solá, S.; Rodrigues, C.M.P.; Rebelo-de-Andrade, H. Distinct kinetics and pathways of apoptosis in influenza A and B virus infection. *Virus Res.* **2015**, doi:10.1016/j.virusres.2015.05.008.

8. Ludwig, S.; Pleschka, S.; Planz, O.; Wolff, T. Ringing the alarm bells: signalling and apoptosis in influenza virus infected cells. *Cell. Microbiol.* **2006**, *8*, 375–386, doi:10.1111/j.1462-5822.2005.00678.x.

9. de Vries, W.; Haasnoot, J.; van der Velden, J.; van Montfort, T.; Zorgdrager, F.; Paxton, W.; Cornelissen, M.; van Kuppeveld, F.; de Haan, P.; Berkhout, B. Increased virus replication in mammalian cells by blocking intracellular innate defense responses. *Gene Ther.* **2008**, *15*, 545–552, doi:10.1038/gt.2008.12.

10. Young, D.F.; Andrejeva, L.; Livingstone, A.; Goodbourn, S.; Lamb, R.A.; Collins, P.L.; Elliott, R.M.; Randall, R.E. Virus Replication in Engineered Human Cells That Do Not Respond to Interferons. *J. Virol.* **2003**, *77*, 2174–2181, doi:10.1128/jvi.77.3.2174-2181.2003.

11. Schulze-Horsel, J.; Schulze, M.; Agalaridis, G.; Genzel, Y.; Reichl, U. Infection

dynamics and virus-induced apoptosis in cell culture-based influenza vaccine production-Flow cytometry and mathematical modeling. *Vaccine* **2009**, *27*, 2712–2722, doi:10.1016/j.vaccine.2009.02.027.

12. Majors, B.S.; Betenbaugh, M.J.; Chiang, G.G. Links between metabolism and apoptosis in mammalian cells: Applications for anti-apoptosis engineering. *Metab. Eng.* **2007**, *9*, 317–326, doi:10.1016/j.ymben.2007.05.003.

13. Kim, J.W.; Dang, C. V. Multifaceted roles of glycolytic enzymes. *Trends Biochem. Sci.* **2005**, *30*, 142–150, doi:10.1016/j.tibs.2005.01.005.

14. Pastorino, J.; Hoek, J. Hexokinase II: The Integration of Energy Metabolism and Control of Apoptosis. *Curr. Med. Chem.* **2005**, *10*, 1535–1551, doi:10.2174/0929867033457269.

15. Shaw, M.L.; Stertz, S. Role of Host Genes in Influenza Virus Replication. In *Cellular and Molecular Immunology*; Springer, Cham, 2017; pp. 151–189 ISBN 9783030053697.

16. Fernandes, P.; Santiago, V.M.; Rodrigues, A.F.; Tomás, H.; Kremer, E.J.; Alves, P.M.; Coroadinha, A.S. Impact of E1 and Cre on Adenovirus Vector Amplification: Developing MDCK CAV-2-E1 and E1-Cre Transcomplementing Cell Lines. *PLoS One* **2013**, *8*, e60342, doi:10.1371/journal.pone.0060342.

17. Laske, T.; Bachmann, M.; Dostert, M.; Karlas, A.; Wirth, D.; Frensing, T.; Meyer, T.F.; Hauser, H.; Reichl, U. Model-based analysis of influenza A virus replication in genetically engineered cell lines elucidates the impact of host cell factors on key kinetic parameters of virus growth. *PLOS Comput. Biol.* **2019**, *15*, e1006944, doi:10.1371/journal.pcbi.1006944.

18. Sidorenko, Y.; Reichl, U. Structured model of influenza virus replication in MDCK cells. *Biotechnol. Bioeng.* **2004**, *88*, 1–14, doi:10.1002/bit.20096.

19. Martinez, V.; Gerdtzen, Z.P.; Andrews, B.A.; Asenjo, J.A. Viral vectors for the treatment of alcoholism: Use of metabolic flux analysis for cell cultivation and vector production. *Metab. Eng.* **2010**, *12*, 129–137, doi:10.1016/j.ymben.2009.09.003.

20. Carinhas, N.; Koshkin, A.; Pais, D.A.M.; Alves, P.M.; Teixeira, A.P. 13 C-metabolic flux analysis of human adenovirus infection: Implications for viral vector production. *Biotechnol. Bioeng.* **2017**, *114*, 195–207, doi:10.1002/bit.26063.

21. Carinhas, N.; Pais, D.A.M.; Koshkin, A.; Fernandes, P.; Coroadinha, A.S.; Carrondo, M.J.T.; Alves, P.M.; Teixeira, A.P. Metabolic flux profiling of MDCK cells during growth and canine adenovirus vector production. *Sci. Rep.* **2016**, *6*, 23529, doi:10.1038/srep23529.

22. Ritter, J.B.; Wahl, A.S.; Freund, S.; Genzel, Y.; Reichl, U. Metabolic effects of influenza virus infection in cultured animal cells: Intra- and extracellular metabolite profiling. *BMC Syst. Biol.* **2010**, *4*, 61, doi:10.1186/1752-0509-4-61.

23. Genzel, Y.; Behrendt, I.; König, S.; Sann, H.; Reichl, U. Metabolism of MDCK cells during cell growth and influenza virus production in large-scale microcarrier culture. *Vaccine* **2004**, *22*, 2202–2208, doi:10.1016/j.vaccine.2003.11.041.

24. Silva, A.C.; P. Teixeira, A.; M. Alves, P. Impact of Adenovirus infection in host cell metabolism evaluated by 1H-NMR spectroscopy. *J. Biotechnol.* **2016**, *231*, 16–23, doi:10.1016/j.jbiotec.2016.05.025.

25. Vastag, L.; Koyuncu, E.; Grady, S.L.; Shenk, T.E.; Rabinowitz, J.D. Divergent Effects of Human Cytomegalovirus and Herpes Simplex Virus-1 on Cellular Metabolism. *PLoS Pathog.* **2011**, *7*, e1002124, doi:10.1371/journal.ppat.1002124.

26. Bernal, V.; Monteiro, F.; Carinhas, N.; Ambrósio, R.; Alves, P.M. An integrated analysis of enzyme activities, cofactor pools and metabolic fluxes in baculovirus-infected Spodoptera frugiperda Sf9 cells. *J. Biotechnol.* **2010**, *150*, 332–342, doi:10.1016/j.jbiotec.2010.09.958.

27. Sanchez, E.L.; Lagunoff, M. Viral activation of cellular metabolism. *Virology* **2015**, *479–480*, 609–618, doi:10.1016/j.virol.2015.02.038.

28. Cvijovic, M.; Almquist, J.; Hagmar, J.; Hohmann, S.; Kaltenbach, H.M.; Klipp, E.; Krantz, M.; Mendes, P.; Nelander, S.; Nielsen, J.; et al. Bridging the gaps in systems biology. *Mol. Genet. Genomics* **2014**, *289*, 727–734, doi:10.1007/s00438-014-0843-3.

29. Warburg, O.; Wind, F.; Negelein, E. The metabolism of tumors in the body. *J. Gen. Physiol.* **1927**, *8*, 519–530, doi:10.1085/jgp.8.6.519.

30. Kashiwaya, Y.; Sato, K.; Tsuchiya, N.; Thomas, S.; Fell, D. a; Veech, R.L.; Passonneau, J. V Control of glucose utilization in working perfused rat heart. *J. Biol. Chem.* **1994**, *269*, 25502–14.

31. Suarez, R.K.; Moyes, C.D. Metabolism in the age of 'omes.' *J. Exp. Biol.* **2012**, *215*, 2351–2357, doi:10.1242/jeb.059725.

32. Graham, F.L.; Van Der Eb, A.J. Transformation of rat cells by DNA of human adenovirus 5. *Virology* **1973**, *54*, 536–539, doi:10.1016/0042-6822(73)90163-3.

33. Krougliak, V.; Graham, F.L. Development of Cell Lines Capable of Complementing E1, E4, and Protein IX Defective Adenovirus Type 5 Mutants. *Hum. Gene Ther.* **1995**, *6*, 1575–1586, doi:10.1089/hum.1995.6.12-1575.

34. Blanchard, V.; Liu, X.; Eigel, S.; Kaup, M.; Rieck, S.; Janciauskiene, S.; Sandig, V.; Marx, U.; Walden, P.; Tauber, R.; et al. N-glycosylation and biological activity of recombinant human alpha1-antitrypsin expressed in a novel human neuronal cell line. *Biotechnol. Bioeng.* **2011**, *108*, 2118–2128, doi:10.1002/bit.23158.

35. Gholami, S.; Hamzehloei, T. Hereditary of alpha-1-Antitrypsin deficiency. *Shiraz E Med. J.* **2013**, *14*, 63–75.

36. Kelly, E.; Greene, C.M.; Carroll, T.P.; McElvaney, N.G.; O'Neill, S.J. Alpha-1 antitrypsin deficiency. *Respir. Med.* **2010**, *104*, 763–772, doi:10.1016/j.rmed.2010.01.016.

37. Niklas, J.; Schräder, E.; Sandig, V.; Noll, T.; Heinzle, E. Quantitative characterization of metabolism and metabolic shifts during growth of the new human cell line AGE1.HN using time resolved metabolic flux analysis. *Bioprocess Biosyst. Eng.* **2011**, *34*, 533–545, doi:10.1007/s00449-010-0502-y.

38. Verma, A.; Verma, M.; Singh, A. Animal tissue culture principles and applications. In *Animal Biotechnology*; Elsevier, 2020; pp. 269–293 ISBN 9780128117101.

39. Borchers, S.; Freund, S.; Rath, A.; Streif, S.; Reichl, U.; Findeisen, R. Identification of Growth Phases and Influencing Factors in Cultivations with AGE1.HN Cells Using Set-Based Methods. *PLoS One* **2013**, *8*, e68124, doi:10.1371/journal.pone.0068124.

40. Schräder, E.; Scholz, S.; Niklas, J.; Rath, A.; Barradas, O.P.; Jandt, U.; Sandig, V.; Rose, T.; Pörtner, R.; Reichl, U.; et al. Characterisation of cultivation of the human cell line AGE1.HN.AAT. *BMC Proc.* **2011**, *5*, P87, doi:10.1186/1753-6561-5-S8-P87.

41. Niklas, J.; Priesnitz, C.; Rose, T.; Sandig, V.; Heinzle, E. Metabolism and metabolic burden by α1-antitrypsin production in human AGE1.HN cells. *Metab. Eng.* **2013**, *16*, 103–114, doi:10.1016/j.ymben.2013.01.002.

42. Rath, A. Characterisation of cell growth, metabolism and recombinant protein production during transient and steady state conditions for the human cell line AGE1.HN-AAT, Otto-von-Guericke Universität Magdeburg, 2017.

43. Gaush, C.R.; Hard, W.L.; Smith, T.F. Characterization of an Established Line of Canine Kidney Cells (MDCK). *Exp. Biol. Med.* **1966**, *122*, 931–935, doi:10.3181/00379727-122-31293.

44. Genzel, Y.; Olmer, R.M.; Schäfer, B.; Reichl, U. Wave microcarrier cultivation of MDCK cells for influenza virus production in serum containing and serum-free media. *Vaccine* **2006**, *24*, 6074–6087, doi:10.1016/J.VACCINE.2006.05.023.

45. Hu, A.Y.C.; Weng, T.C.; Tseng, Y.F.; Chen, Y.S.; Wu, C.H.; Hsiao, S.; Chou, A.H.; Chao, H.J.; Gu, A.; Wu, S.C.; et al. Microcarrier-based MDCK cell culture system for the production of influenza H5N1 vaccines. *Vaccine* **2008**, *26*, 5736–5740, doi:10.1016/J.VACCINE.2008.08.015.

46. Bock, A.; Sann, H.; Schulze-Horsel, J.; Genzel, Y.; Reichl, U.; Möhler, L. Growth behavior of number distributed adherent MDCK cells for optimization in microcarrier cultures. *Biotechnol. Prog.* **2009**, *25*, 1717–1731, doi:10.1002/btpr.262.

47. GENZEL, Y.; FISCHER, M.; REICHL, U. Serum-free influenza virus production avoiding washing steps and medium exchange in large-scale microcarrier culture. *Vaccine* **2006**, *24*, 3261–3272, doi:10.1016/j.vaccine.2006.01.019.

48. Simmons, N.L. Cultured monolayers of MDCK cells: a novel model system for the study of epithelial development and function. *Gen. Pharmacol.* **1982**, *13*, 287–291, doi:10.1016/0306-3623(82)90047-7.

49. Pérez Rubio, A.; Eiros, J.M. Cell culture-derived flu vaccine: Present and future. *Hum. Vaccin. Immunother.* **2018**, *14*, 1874–1882, doi:10.1080/21645515.2018.1460297.

50. Zuccotti, G.V.; Fabiano, V. Influvac, a trivalent inactivated subunit influenza vaccine. *Expert Opin. Biol. Ther.* **2011**, *11*, 89–98, doi:10.1517/14712598.2011.541436.

51. Doroshenko, A.; Halperin, S.A. Trivalent MDCK cell culture-derived influenza vaccine Optaflu® (Novartis Vaccines). *Expert Rev. Vaccines* **2009**, *8*, 679–688, doi:10.1586/ERV.09.31.

52. Chu, C.; Lugovtsev, V.; Golding, H.; Betenbaugh, M.; Shiloach, J. Conversion of MDCK cell line to suspension culture by transfecting with human siat7e gene and its application for influenza virus production. *Proc. Natl. Acad. Sci.* **2009**, *106*, 14802–14807, doi:10.1073/PNAS.0905912106.

53. van Wielink, R.; Kant-Eenbergen, H.C.M.; Harmsen, M.M.; Martens, D.E.; Wijffels, R.H.; Coco-Martin, J.M. Adaptation of a Madin–Darby canine kidney cell line to suspension growth in serum-free media and comparison of its ability to produce avian influenza virus to Vero and BHK21 cell lines. *J. Virol. Methods* **2011**, *171*, 53–60, doi:10.1016/J.JVIROMET.2010.09.029.

54. Lohr, V.; Genzel, Y.; Behrendt, I.; Scharfenberg, K.; Reichl, U. A new MDCK suspension line cultivated in a fully defined medium in stirred-tank and wave bioreactor. *Vaccine* **2010**, *28*, 6256–6264, doi:10.1016/j.vaccine.2010.07.004.

55. Huang, D.; Peng, W.J.; Ye, Q.; Liu, X.P.; Zhao, L.; Fan, L.; Xia-Hou, K.; Jia, H.J.; Luo, J.; Zhou, L.T.; et al. Serum-Free Suspension Culture of MDCK Cells for

Production of Influenza H1N1 Vaccines. *PLoS One* **2015**, *10*, e0141686, doi:10.1371/JOURNAL.PONE.0141686.

56. Bissinger, T. Evaluation of MDCK suspension cell lines for influenza A virus production : media , metabolism , and process conditions, Otto-von-Guericke-Universität, Magdeburg, 2020.

57. Mostafa, A.; Abdelwhab, E.; Mettenleiter, T.; Pleschka, S. Zoonotic Potential of Influenza A Viruses: A Comprehensive Overview. *Viruses* **2018**, *10*, 497, doi:10.3390/v10090497.

58. Hause, B.M.; Collin, E.A.; Liu, R.; Huang, B.; Sheng, Z.; Lu, W.; Wang, D.; Nelson, E.A.; Li, F. Characterization of a novel influenza virus in cattle and Swine: proposal for a new genus in the Orthomyxoviridae family. *MBio* **2014**, *5*, doi:10.1128/MBIO.00031-14.

59. Chiapponi, C.; Faccini, S.; De Mattia, A.; Baioni, L.; Barbieri, I.; Rosignoli, C.; Nigrelli, A.; Foni, E. Detection of Influenza D Virus among Swine and Cattle, Italy. *Emerg. Infect. Dis.* **2016**, *22*, 352, doi:10.3201/EID2202.151439.

60. Heldt, F.S.; Frensing, T.; Pflugmacher, A.; Gröpler, R.; Peschel, B.; Reichl, U. Multiscale Modeling of Influenza A Virus Infection Supports the Development of Direct-Acting Antivirals. *PLoS Comput. Biol.* **2013**, *9*, e1003372, doi:10.1371/journal.pcbi.1003372.

61. Krammer, F.; Smith, G.J.D.; Fouchier, R.A.M.; Peiris, M.; Kedzierska, K.; Doherty, P.C.; Palese, P.; Shaw, M.L.; Treanor, J.; Webster, R.G.; et al. Influenza. *Nat. Rev. Dis. Prim. 2018 41* **2018**, *4*, 1–21, doi:10.1038/s41572-018-0002-y.

62. Wua, C.Y.; Lina, C.W.; Tsaia, T.I.; Leea, C.C.D.; Chuanga, H.Y.; Chena, J. Bin; Tsaia, M.H.; Chena, B.R.; Loa, P.W.; Liua, C.P.; et al. Influenza A surface glycosylation and vaccine design. *Proc. Natl. Acad. Sci. U. S. A.* **2017**, *114*, 280–285, doi:10.1073/PNAS.1617174114/SUPPL_FILE/PNAS.201617174SI.PDF.

63. Gao, R.; Gu, M.; Shi, L.; Liu, K.; Li, X.; Wang, X.; Hu, J.; Liu, X.; Hu, S.; Chen, S.; et al. N-linked glycosylation at site 158 of the HA protein of H5N6 highly pathogenic avian influenza virus is important for viral biological properties and host immune responses. *Vet. Res.* **2021**, *52*, 8, doi:10.1186/s13567-020-00879-6.

64. Brunk, E.; Sahoo, S.; Zielinski, D.C.; Altunkaya, A.; Dräger, A.; Mih, N.; Gatto, F.; Nilsson, A.; Preciat Gonzalez, G.A.; Aurich, M.K.; et al. Recon3D enables a three-dimensional view of gene variation in human metabolism. *Nat. Biotechnol.* **2018**, *36*, 272–281, doi:10.1038/nbt.4072.

65. Hefzi, H.; Ang, K.S.; Hanscho, M.; Bordbar, A.; Ruckerbauer, D.; Lakshmanan, M.; Orellana, C.A.; Baycin-Hizal, D.; Huang, Y.; Ley, D.; et al. A Consensus Genome-

scale Reconstruction of Chinese Hamster Ovary Cell Metabolism. *Cell Syst.* **2016**, *3*, 434-443.e8, doi:10.1016/j.cels.2016.10.020.

66. Bertrand, R.L. Lag Phase Is a Dynamic, Organized, Adaptive, and Evolvable Period That Prepares Bacteria for Cell Division. *J. Bacteriol.* **2019**, *201*, 1–21, doi:10.1128/JB.00697-18.

67. Frame, K.K.; Hu, W. Kinetic study of hybridoma cell growth in continuous culture: II. Behavior of producers and comparison to nonproducers. *Biotechnol. Bioeng.* **1991**, *38*, 1020–1028, doi:10.1002/bit.260380910.

68. Rehberg, M. Dynamics in growth and metabolism of adherent MDCK cells unraveled by an integrated modeling approach, Otto-von-Guericke-Universität, Magdeburg, 2015.

69. Ramirez, O.T.; Mutharasan, R. Cell cycle- and growth phase-dependent variations in size distribution, antibody productivity, and oxygen demand in hybridoma cultures. *Biotechnol. Bioeng.* **1990**, *36*, 839–48, doi:10.1002/bit.260360814.

70. BAGGETTO, L. Deviant energetic metabolism of glycolytic cancer cells. *Biochimie* **1992**, *74*, 959–974, doi:10.1016/0300-9084(92)90016-8.

71. Duarte, T.M.; Carinhas, N.; Barreiro, L.C.; Carrondo, M.J.T.; Alves, P.M.; Teixeira, A.P. Metabolic responses of CHO cells to limitation of key amino acids. *Biotechnol. Bioeng.* **2014**, *111*, 2095–2106, doi:10.1002/bit.25266.

72. Glacken, M.W.; Adema, E.; Sinskey, A.J. Mathematical descriptions of hybridoma culture kinetics: I. Initial metabolic rates. *Biotechnol. Bioeng.* **1988**, *32*, 491–506, doi:10.1002/bit.260320412.

73. Butler, M.; Imamura, T.; Thomas, J.; Thilly, W.G. High yields from microcarrier cultures by medium perfusion. *J. Cell Sci.* **1983**, *61*, 351–63, doi:10.1242/jcs.61.1.351.

74. Nirmala, J.G.; Lopus, M. Cell death mechanisms in eukaryotes. *Cell Biol. Toxicol.* **2020**, *36*, 145–164, doi:10.1007/s10565-019-09496-2.

75. Andryukov, B.G.; Somova, L.M.; Timchenko, N.F. Molecular and Genetic Characteristics of Cell Death in Prokaryotes. *Mol. Genet. Microbiol. Virol.* **2018**, *33*, 73–83, doi:10.3103/S0891416818020039.

76. Ferrer-Miralles, N.; Saccardo, P.; Corchero, J.L.; Xu, Z.; García-Fruitós, E. General introduction: recombinant protein production and purification of insoluble proteins. *Methods Mol. Biol.* **2015**, *1258*, 1–24, doi:10.1007/978-1-4939-2205-5_1.

77. Wurm, F.M. Production of recombinant protein therapeutics in cultivated

mammalian cells. *Nat. Biotechnol.* **2004**, *22*, 1393–1398, doi:10.1038/nbt1026.

78. O'Flaherty, R.; Bergin, A.; Flampouri, E.; Mota, L.M.; Obaidi, I.; Quigley, A.; Xie, Y.; Butler, M. Mammalian cell culture for production of recombinant proteins: A review of the critical steps in their biomanufacturing. *Biotechnol. Adv.* **2020**, *43*, 107552, doi:10.1016/j.biotechadv.2020.107552.

79. Pinto, J.; Ramos, J.R.C.; Costa, R.S.; Rossell, S.; Dumas, P.; Oliveira, R. Hybrid deep modeling of a CHO-K1 fed-batch process: combining first-principles with deep neural networks. *Front. Bioeng. Biotechnol.* **2023**, *11*, 1–16, doi:10.3389/fbioe.2023.1237963.

80. Agharafeie, R.; Ramos, J.R.C.; Mendes, J.M.; Oliveira, R. From Shallow to Deep Bioprocess Hybrid Modeling: Advances and Future Perspectives. *Fermentation* **2023**, *9*, 922, doi:10.3390/fermentation9100922.

81. Ramos, J.R.C.; Pinto, J.; Poiares-Oliveira, G.; Peeters, L.; Dumas, P.; Oliveira, R. Deep hybrid modeling of a HEK293 process: Combining long short-term memory networks with first principles equations. *Biotechnol. Bioeng.* **2024**, *121*, 1554–1568, doi:10.1002/bit.28668.

82. Chotteau, V.; Hagrot, E.; Zhang, L.; Mäkinen, M.E.L. Mathematical Modelling of Cell Culture Processes. In; 2021; pp. 431–466.

83. Fredrickson, A.G.; Megee, R.D.; Tsuchiya, H.M. Mathematical Models for Fermentation Processes. In *Advances in Applied Microbiology*; Academic Press, 1970; Vol. 13, pp. 419–465.

84. Shirsat, N.P.; English, N.J.; Glennon, B.; Al-Rubeai, M. Modelling of Mammalian Cell Cultures. In; 2015; pp. 259–326 ISBN 9783319103204.

85. Gatto, F.; Miess, H.; Schulze, A.; Nielsen, J. Flux balance analysis predicts essential genes in clear cell renal cell carcinoma metabolism. *Sci. Rep.* **2015**, *5*, 10738, doi:10.1038/srep10738.

86. Goldrick, S.; Sandner, V.; Cheeks, M.; Turner, R.; Farid, S.S.; McCreath, G.; Glassey, J. Multivariate Data Analysis Methodology to Solve Data Challenges Related to Scale-Up Model Validation and Missing Data on a Micro-Bioreactor System. *Biotechnol. J.* **2020**, *15*, doi:10.1002/biot.201800684.

87. Oliveira, R. Combining first principles modelling and artificial neural networks: a general framework. *Comput. Chem. Eng.* **2004**, *28*, 755–766, doi:10.1016/j.compchemeng.2004.02.014.

88. Teixeira, A.; Cunha, A.E.; Clemente, J.J.; Moreira, J.L.; Cruz, H.J.; Alves, P.M.; Carrondo, M.J.T.; Oliveira, R. Modelling and optimization of a recombinant BHK-21

cultivation process using hybrid grey-box systems. *J. Biotechnol.* **2005**, *118*, 290–303, doi:10.1016/j.jbiotec.2005.04.024.

89. Teixeira, A.P.; Carinhas, N.; Dias, J.M.L.; Cruz, P.; Alves, P.M.; Carrondo, M.J.T.; Oliveira, R. Hybrid semi-parametric mathematical systems: Bridging the gap between systems biology and process engineering. *J. Biotechnol.* **2007**, *132*, 418–425, doi:10.1016/j.jbiotec.2007.08.020.

90. von Stosch, M.; Oliveira, R.; Peres, J.; Feyo de Azevedo, S. Hybrid semi-parametric modeling in process systems engineering: Past, present and future. *Comput. Chem. Eng.* **2014**, *60*, 86–101, doi:10.1016/j.compchemeng.2013.08.008.

91. Psichogios, D.C.; Ungar, L.H. A hybrid neural network-first principles approach to process modeling. *AIChE J.* **1992**, *38*, 1499–1511, doi:10.1002/aic.690381003.

92. Yu, D.; Deng, L. Deep Neural Network-Hidden Markov Model Hybrid Systems. In *Automatic Speech Recognition. Signals and Communication Technology*; 2015; pp. 99–116.

93. Cleland, W.. The kinetics of enzyme-catalyzed reactions with two or more substrates or products: I. Nomenclature and rate equations. *Biochim. Biophys. Acta - Spec. Sect. Enzymol. Subj.* **1963**, *67*, 104–137, doi:10.1016/0926-6569(63)90211-6.

94. Song, H.S.; Morgan, J.A.; Ramkrishna, D. Systematic development of hybrid cybernetic models: Application to recombinant yeast co-consuming glucose and xylose. *Biotechnol. Bioeng.* **2009**, *103*, 984–1002, doi:10.1002/bit.22332.

95. King, E.L.; Altman, C. A Schematic Method of Deriving the Rate Laws for Enzyme-Catalyzed Reactions. *J. Phys. Chem.* **1956**, *60*, 1375–1378, doi:10.1021/j150544a010.

96. A. V., H. The possible effects of the aggregation of the molecules of hemoglobin on its dissociation curves. *J. Physiol.* **1910**, *40*, iv–vii.

97. Monod, J.; Wyman, J.; Changeux, J.P. on the Nature of Allosteric Transitions: a Plausible Model. *J. Mol. Biol.* **1965**, *12*, 88–118, doi:10.1016/S0022-2836(65)80285-6.

98. Moles, C.G. Parameter Estimation in Biochemical Pathways: A Comparison of Global Optimization Methods. *Genome Res.* **2003**, *13*, 2467–2474, doi:10.1101/gr.1262503.

99. Balsa-Canto, E.; Alonso, A.A.; Banga, J.R. Computational procedures for optimal experimental design in biological systems. *IET Syst. Biol.* **2008**, *2*, 163–172, doi:10.1049/IET-SYB:20070069.

100. Efron, B.; Tibshirani, R. Bootstrap Methods for Standard Errors, Confidence Intervals, and Other Measures of Statistical Accuracy. *https://doi.org/10.1214/ss/1177013815* **1986**, *1*, 54–75, doi:10.1214/SS/1177013815.

101. Girolami, M. Bayesian inference for differential equations. *Theor. Comput. Sci.* **2008**, *408*, 4–16, doi:10.1016/J.TCS.2008.07.005.

102. Sontag, E.D. For Differential Equations with r Parameters, 2r+1 Experiments Are Enough for Identification. *J. Nonlinear Sci.* **2003**, *12*, 553–583, doi:10.1007/s00332-002-0506-0.

103. Nolan, R.P.; Lee, K. Dynamic model of CHO cell metabolism. *Metab. Eng.* **2011**, *13*, 108–124, doi:10.1016/j.ymben.2010.09.003.

104. Robitaille, J.; Chen, J.; Jolicoeur, M. A Single Dynamic Metabolic Model Can Describe mAb Producing CHO Cell Batch and Fed-Batch Cultures on Different Culture Media. *PLoS One* **2015**, *10*, e0136815, doi:10.1371/journal.pone.0136815.

105. López-Meza, J.; Araíz-Hernández, D.; Carrillo-Cocom, L.M.; López-Pacheco, F.; Rocha-Pizaña, M. del R.; Alvarez, M.M. Using simple models to describe the kinetics of growth, glucose consumption, and monoclonal antibody formation in naive and infliximab producer CHO cells. *Cytotechnology* **2016**, *68*, 1287–1300, doi:10.1007/s10616-015-9889-2.

106. Fredrickson, A.G.; Mantzaris, N. V. A new set of population balance equations for microbial and cell cultures. *Chem. Eng. Sci.* **2002**, *57*, 2265–2278, doi:10.1016/S0009-2509(02)00116-1.

107. Hashemi, M.; Mousavi, S.M.; Razavi, S.H.; Shojaosadati, S.A. Mathematical modeling of biomass and α-amylase production kinetics by Bacillus sp. in solid-state fermentation based on solid dry weight variation. *Biochem. Eng. J.* **2011**, *53*, 159–164, doi:10.1016/j.bej.2010.09.017.

108. Morgan, J.J.; Surovtsev, I. V.; Lindahl, P.A. A framework for whole-cell mathematical modeling. *J. Theor. Biol.* **2004**, *231*, 581–596, doi:10.1016/j.jtbi.2004.07.014.

109. Rehberg, M.; Ritter, J.B.; Reichl, U. Glycolysis Is Governed by Growth Regime and Simple Enzyme Regulation in Adherent MDCK Cells. *PLoS Comput. Biol.* **2014**, *10*, e1003885, doi:10.1371/journal.pcbi.1003885.

110. Chance, B.; Garfinkel, D.; Higgins, J.; Hess, B.; Chance, E.M. Metabolic Control Mechanisms. *J. Biol. Chem.* **1960**, *235*, 2426–2439, doi:10.1016/S0021-9258(18)64638-1.

111. OTTO, M.; HEINRICH, R.; JACOBASCH, G.; RAPOPORT, S. A Mathematical Model for the Influence of Anionic Effectors on the Phosphofructokinase from Rat Erythrocytes. *Eur. J. Biochem.* **1977**, *74*, 413–420, doi:10.1111/j.1432-1033.1977.tb11406.x.

112. Otto, M.; Heinrich, R.; KUHN, B.; Jacobasch, G. A mathematical model for the influence of fructose 6-phosphate, ATP, potassium, ammonium and magnesium on the phosphofructokinase from rat erythrocytes;. *Eur. J. Biochem.* **1974**, *49*, 169–178.

113. Lambeth, M.J.; Kushmerick, M.J. A Computational Model for Glycogenolysis in Skeletal Muscle. *Ann. Biomed. Eng.* **2002**, *30*, 808–827, doi:10.1114/1.1492813.

114. Choe, M.; Einav, T.; Phillips, R.; Titov, D. V Data-driven model of glycolysis identifies the role of allostery in maintaining ATP homeostasis. *bioRxiv* **2022**, 2022.12.28.522046, doi:10.1101/2022.12.28.522046.

115. Mulukutla, B.C.; Yongky, A.; Daoutidis, P.; Hu, W.-S. Bistability in Glycolysis Pathway as a Physiological Switch in Energy Metabolism. *PLoS One* **2014**, *9*, e98756, doi:10.1371/journal.pone.0098756.

116. Marín-Hernández, A.; Gallardo-Pérez, J.C.; Rodríguez-Enríquez, S.; Encalada, R.; Moreno-Sánchez, R.; Saavedra, E. Modeling cancer glycolysis. *Biochim. Biophys. Acta - Bioenerg.* **2011**, *1807*, 755–767, doi:10.1016/j.bbabio.2010.11.006.

117. Garfinkel, D. Simulation of the Krebs cycle and closely related metabolism in perfused rat liver. I. Construction of a model. *Comput. Biomed. Res.* **1971**, *4*, 1–17, doi:10.1016/0010-4809(71)90044-9.

118. Weiss, R.G.; Gloth, S.T.; Kalil-Filho, R.; Chacko, V.P.; Stern, M.D.; Gerstenblith, G. Indexing tricarboxylic acid cycle flux in intact hearts by carbon-13 nuclear magnetic resonance. *Circ. Res.* **1992**, *70*, 392–408, doi:10.1161/01.RES.70.2.392.

119. Bazil, J.N.; Buzzard, G.T.; Rundell, A.E. Modeling Mitochondrial Bioenergetics with Integrated Volume Dynamics. *PLoS Comput. Biol.* **2010**, *6*, e1000632, doi:10.1371/journal.pcbi.1000632.

120. Wu, F.; Yang, F.; Vinnakota, K.C.; Beard, D.A. Computer Modeling of Mitochondrial Tricarboxylic Acid Cycle, Oxidative Phosphorylation, Metabolite Transport, and Electrophysiology. *J. Biol. Chem.* **2007**, *282*, 24525–24537, doi:10.1074/jbc.M701024200.

121. Nazaret, C.; Heiske, M.; Thurley, K.; Mazat, J.P. Mitochondrial energetic metabolism: A simplified model of TCA cycle with ATP production. *J. Theor. Biol.* **2009**, *258*, 455–464, doi:10.1016/j.jtbi.2008.09.037.

122. Khodayari, A.; Zomorrodi, A.R.; Liao, J.C.; Maranas, C.D. A kinetic model of Escherichia coli core metabolism satisfying multiple sets of mutant flux data. *Metab. Eng.* **2014**, *25*, 50–62, doi:10.1016/j.ymben.2014.05.014.

123. Chassagnole, C.; Noisommit-Rizzi, N.; Schmid, J.W.; Mauch, K.; Reuss, M. Dynamic modeling of the central carbon metabolism of Escherichia coli. *Biotechnol. Bioeng.* **2002**, *79*, 53–73, doi:10.1002/bit.10288.

124. Rizzi, M.; Baltes, M.; Theobald, U.; Reuss, M. In vivo analysis of metabolic dynamics inSaccharomyces cerevisiae: II. Mathematical model. *Biotechnol. Bioeng.* **1997**, *55*, 592–608, doi:10.1002/(SICI)1097-0290(19970820)55:4<592::AID-BIT2>3.0.CO;2-C.

125. Ghorbaniaghdam, A.; Henry, O.; Jolicoeur, M. A kinetic-metabolic model based on cell energetic state: Study of CHO cell behavior under Na-butyrate stimulation. *Bioprocess Biosyst. Eng.* **2013**, *36*, 469–487, doi:10.1007/s00449-012-0804-3.

126. Mulukutla, B.C.; Yongky, A.; Grimm, S.; Daoutidis, P.; Hu, W.-S. Multiplicity of Steady States in Glycolysis and Shift of Metabolic State in Cultured Mammalian Cells. *PLoS One* **2015**, *10*, e0121561, doi:10.1371/journal.pone.0121561.

127. Tripathi, S.; Park, J.H.; Pudakalakatti, S.; Bhattacharya, P.K.; Kaipparettu, B.A.; Levine, H. A mechanistic modeling framework reveals the key principles underlying tumor metabolism. *PLOS Comput. Biol.* **2022**, *18*, e1009841, doi:10.1371/journal.pcbi.1009841.

128. Vicente, T.; Mota, J.P.B.; Peixoto, C.; Alves, P.M.; Carrondo, M.J.T. Rational design and optimization of downstream processes of virus particles for biopharmaceutical applications: Current advances. *Biotechnol. Adv.* **2011**, *29*, 869–878, doi:10.1016/j.biotechadv.2011.07.004.

129. Mandenius, C.-F.; Brundin, A. Review : Biocatalysts and Bioreactor Design. *Biotechnol. Prog.* **2008**, *24*, 1191–1203, doi:10.1021/bp.67.

130. Kreutz, C.; Timmer, J. Systems biology: Experimental design. *FEBS J.* **2009**, *276*, 923–942, doi:10.1111/j.1742-4658.2008.06843.x.

131. Brendel, M.; Marquardt, W. Experimental design for the identification of hybrid reaction models from transient data. *Chem. Eng. J.* **2008**, *141*, 264–277, doi:10.1016/j.cej.2007.12.027.

132. von Stosch, M.; Willis, M.J. Intensified design of experiments for upstream bioreactors. *Eng. Life Sci.* **2017**, *17*, 1173–1184, doi:10.1002/elsc.201600037.

133. Stephanopoulos, G.; Sinskey, A.J. Metabolic engineering - methodologies and future prospects. *Trends Biotechnol.* **1993**, *11*, 392–396, doi:10.1016/0167-

7799(93)90099-U.

134. Stephanopoulos, G.; Stafford, D.E. Metabolic engineering: A new frontier of chemical reaction engineering. *Chem. Eng. Sci.* **2002**, *57*, 2595–2602, doi:10.1016/S0009-2509(02)00088-X.

135. Kyriakopoulos, S.; Ang, K.S.; Lakshmanan, M.; Huang, Z.; Yoon, S.; Gunawan, R.; Lee, D.-Y. Kinetic Modeling of Mammalian Cell Culture Bioprocessing: The Quest to Advance Biomanufacturing. *Biotechnol. J.* **2018**, *13*, 1700229, doi:10.1002/biot.201700229.

136. Stephanopoulos, G. Metabolic Fluxes and Metabolic Engineering. *Metab. Eng.* **1999**, *1*, 1–11, doi:10.1006/mben.1998.0101.

137. Hwang, D.; Stephanopoulos, G.; Chan, C. Inverse modeling using multi-block PLS to determine the environmental conditions that provide optimal cellular function. *Bioinformatics* **2004**, *20*, 487–499, doi:10.1093/bioinformatics/btg433.

138. Orth, J.D.; Thiele, I.; Palsson, B.Ø. What is flux balance analysis? *Nat Biotechnol* **2010**, *28*, 245–248, doi:10.1038/nbt.1614.What.

139. Lee, J.M.; Gianchandani, E.P.; Papin, J. a. Flux balance analysis in the era of metabolomics. *Brief. Bioinform.* **2006**, *7*, 140–150, doi:10.1093/bib/bbl007.

140. Gombert, A.K.; Nielsen, J. Mathematical modelling of metabolism. *Curr. Opin. Biotechnol.* **2000**, *11*, 180–186, doi:10.1016/S0958-1669(00)00079-3.

141. Lee, S.Y.; Park, J.M.; Kim, T.Y. Application of Metabolic Flux Analysis in Metabolic Engineering. In *Methods in Enzymology*; Elsevier Inc., 2011; Vol. 498, pp. 67–93 ISBN 9780123851208.

142. Galleguillos, S.N.; Ruckerbauer, D.; Gerstl, M.P.; Borth, N.; Hanscho, M.; Zanghellini, J. What can mathematical modelling say about CHO metabolism and protein glycosylation? *Comput. Struct. Biotechnol. J.* **2017**, *15*, 212–221, doi:10.1016/j.csbj.2017.01.005.

143. Müller, A.; Bockmayr, A. Thermodynamic Constraints for Metabolic Networks. **2012**, 83.

144. Batt, B.C.; Kompala, D.S. A structured kinetic modeling framework for the dynamics of hybridoma growth and monoclonal antibody production in continuous suspension cultures. *Biotechnol. Bioeng.* **1989**, *34*, 515–531, doi:10.1002/bit.260340412.

145. Bailey, J.E. Mathematical Modeling and Analysis in Biochemical Engineering: Past Accomplishments and Future Opportunities. *Biotechnol. Prog.* **1998**, *14*, 8–20, doi:10.1021/bp9701269.

146. van Riel, N.A.W. Dynamic modelling and analysis of biochemical networks: Mechanism-based models and model-based experiments. *Brief. Bioinform.* **2006**, *7*, 364–374, doi:10.1093/bib/bbl040.

147. Sidoli, F.R.; Mantalaris, A.; Asprey, S.P. Modelling of mammalian cells and cell culture processes. *Cytotechnology* **2004**, *44*, 27–46, doi:10.1023/B:CYTO.0000043397.94527.84.

148. Miskovic, L.; Tokic, M.; Fengos, G.; Hatzimanikatis, V. Rites of passage: Requirements and standards for building kinetic models of metabolic phenotypes. *Curr. Opin. Biotechnol.* **2015**, *36*, 146–153, doi:10.1016/j.copbio.2015.08.019.

149. Jimenez del Val, I.; Nagy, J.M.; Kontoravdi, C. A dynamic mathematical model for monoclonal antibody N-linked glycosylation and nucleotide sugar donor transport within a maturing Golgi apparatus. *Biotechnol. Prog.* **2011**, *27*, 1730–1743, doi:10.1002/btpr.688.

150. Aghamohseni, H.; Ohadi, K.; Spearman, M.; Krahn, N.; Moo-Young, M.; Scharer, J.M.; Butler, M.; Budman, H.M. Effects of nutrient levels and average culture pH on the glycosylation pattern of camelid-humanized monoclonal antibody. *J. Biotechnol.* **2014**, *186*, 98–109, doi:10.1016/j.jbiotec.2014.05.024.

151. Blondeel, E.J.M.; Aucoin, M.G. Supplementing glycosylation: A review of applying nucleotide-sugar precursors to growth medium to affect therapeutic recombinant protein glycoform distributions. *Biotechnol. Adv.* **2018**, *36*, 1505–1523, doi:10.1016/j.biotechadv.2018.06.008.

152. Nielsen, J. Systems Biology of Metabolism. *Annu. Rev. Biochem.* **2017**, *86*, 245–275, doi:10.1146/annurev-biochem-061516-044757.

153. von Stosch, M.; Peres, J.; de Azevedo, S.F.; Oliveira, R. Modelling biochemical networks with intrinsic time delays: A hybrid semi-parametric approach. *BMC Syst. Biol.* **2010**, *4*, 8–12, doi:10.1186/1752-0509-4-131.

154. Chassagnole, C.; Noisommit-Rizzi, N.; Schmid, J.W.; Mauch, K.; Reuss, M. Dynamic modeling of the central carbon metabolism of Escherichia coli. *Biotechnol. Bioeng.* **2002**, *79*, 53–73, doi:10.1002/bit.10288.

155. Heldt, F.S.; Frensing, T.; Reichl, U. Modeling the Intracellular Dynamics of Influenza Virus Replication To Understand the Control of Viral RNA Synthesis. *J. Virol.* **2012**, *86*, 7806–7817, doi:10.1128/JVI.00080-12.

156. Rüdiger, D.; Kupke, S.Y.; Laske, T.; Zmora, P.; Reichl, U. Multiscale modeling of influenza A virus replication in cell cultures predicts infection dynamics for highly different infection conditions. *PLOS Comput. Biol.* **2019**, *15*, e1006819, doi:10.1371/journal.pcbi.1006819.

157. Ramos, J.R.C.; Rath, A.G.; Genzel, Y.; Sandig, V.; Reichl, U. A dynamic model linking cell growth to intracellular metabolism and extracellular by-product accumulation. *Biotechnol. Bioeng.* **2020**, *117*, 1533–1553, doi:10.1002/bit.27288.

158. Ramos, J.R.C.; Bissinger, T.; Genzel, Y.; Reichl, U. Impact of Influenza A Virus Infection on Growth and Metabolism of Suspension MDCK Cells Using a Dynamic Model. *Metabolites* **2022**, *12*, 239, doi:10.3390/metabo12030239.

159. Rehberg, M.; Ritter, J.B.; Genzel, Y.; Flockerzi, D.; Reichl, U. The relation between growth phases, cell volume changes and metabolism of adherent cells during cultivation. *J. Biotechnol.* **2013**, *164*, 489–499, doi:10.1016/j.jbiotec.2013.01.018.

160. Rehberg, M.; Wetzel, M.; Ritter, J.B.; Reichl, U. The regulation of glutaminolysis and citric acid cycle activity during mammalian cell cultivation. *12th IFAC Symp. Comput. Appl. Biotechnol. CAB 2013* **2013**, *12*, 48–53, doi:10.3182/20131216-3-IN-2044.00011.

161. Rath, A.G.; Rehberg, M.; Janke, R.; Genzel, Y.; Scholz, S.; Noll, T.; Rose, T.; Sandig, V.; Reichl, U. The influence of cell growth and enzyme activity changes on intracellular metabolite dynamics in AGE1.HN.AAT cells. *J. Biotechnol.* **2014**, *178*, 43–53, doi:10.1016/j.jbiotec.2014.03.012.

162. Priesnitz, C.; Niklas, J.; Rose, T.; Sandig, V.; Heinzle, E. Metabolic flux rearrangement in the amino acid metabolism reduces ammonia stress in the α1-antitrypsin producing human AGE1.HN cell line. *Metab. Eng.* **2012**, *14*, 128–137, doi:10.1016/j.ymben.2012.01.001.

163. Rehberg, M.; Rath, A.; Ritter, J.B.; Genzel, Y.; Reichl, U. Changes in intracellular metabolite pools during growth of adherent MDCK cells in two different media. *Appl. Microbiol. Biotechnol.* **2014**, *98*, 385–397, doi:10.1007/s00253-013-5329-4.

164. Xie, L.; Wang, D.I.C. Energy metabolism and ATP balance in animal cell cultivation using a stoichiometrically based reaction network. *Biotechnol. Bioeng.* **1996**, *52*, 591–601, doi:10.1002/(SICI)1097-0290(19961205)52:5<591::AID-BIT6>3.0.CO;2-E.

165. Sanderson, C..; Barford, J..; Barton, G.. A structured, dynamic model for animal cell culture systems. *Biochem. Eng. J.* **1999**, *3*, 203–211, doi:10.1016/S1369-703X(99)00021-2.

166. Zhou, F.; Bi, J.X.; Zeng, A.P.; Yuan, J.Q. A macrokinetic and regulator model for myeloma cell culture based on metabolic balance of pathways. *Process Biochem.* **2006**, *41*, 2207–2217, doi:10.1016/j.procbio.2006.08.001.

167. Uldry, M.; Ibberson, M.; Hosokawa, M.; Thorens, B. GLUT2 is a high affinity glucosamine transporter. *FEBS Lett.* **2002**, *524*, 199–203, doi:10.1016/S0014-

5793(02)03058-2.

168. Luni, C.; Marth, J.D.; Doyle, F.J. Computational Modeling of Glucose Transport in Pancreatic ??-Cells Identifies Metabolic Thresholds and Therapeutic Targets in Diabetes. *PLoS One* **2012**, *7*, 1–8, doi:10.1371/journal.pone.0053130.

169. de Tremblay, M.; Perrier, M.; Chavarie, C.; Archambault, J. Optimization of fed-batch culture of hybridoma cells using dynamic programming: single and multi feed cases. *Bioprocess Eng.* **1992**, *7*, 229–234, doi:10.1007/BF00369551.

170. Barford, J.; Phillips, P.; Harbour, C. Simulation of animal cell metabolism. *Math. Comput. Simul.* **1992**, *33*, 397–402, doi:10.1016/0378-4754(92)90128-4.

171. Hyde, R.; Taylor, P.M.; Hundal, H.S. Amino acid transporters: roles in amino acid sensing and signalling in animal cells. *Biochem. J.* **2003**, *373*, 1–18, doi:10.1042/bj20030405.

172. Ozturk, S.S.; Palsson, B.O. Chemical decomposition of glutamine in cell culture media: effect of media type, pH, and serum concentration. *Biotechnol. Prog.* **1990**, *6*, 121–128, doi:10.1021/bp00002a005.

173. J.G.Salway Summary for Policymakers. *Clim. Chang. 2013 - Phys. Sci. Basis* **2004**, *16*, 1–30, doi:10.1017/CBO9781107415324.004.

174. Sauro, H.M. *Enzyme Kinetics for Systems Biology*; Future Skill Software (Ambrosius Publishing), 2011; ISBN 9780982477311.

175. Schmidt, H.; Jirstrand, M. Systems Biology Toolbox for MATLAB: A computational platform for research in systems biology. *Bioinformatics* **2006**, *22*, 514–515, doi:10.1093/bioinformatics/bti799.

176. Cohen, S.D.; Hindmarsh, A.C. CVODE, a stiff/nonstiff ODE solver in C. *Comput. Phys.* **1996**, *10*, 138–143, doi:10.1063/1.4822377.

177. Egea, J.A.; Balsa-Canto, E.; García, M.S.G.; Banga, J.R. Dynamic optimization of nonlinear processes with an enhanced scatter search method. *Ind. Eng. Chem. Res.* **2009**, *48*, 4388–4401, doi:10.1021/ie801717t.

178. Egea, J.A.; Martí, R.; Banga, J.R. An evolutionary method for complex-process optimization. *Comput. Oper. Res.* **2010**, *37*, 315–324, doi:10.1016/j.cor.2009.05.003.

179. Hansen, N.; Kern, S. Evaluating the CMA Evolution Strategy on Multimodal Test Functions. In *Lecture Notes in Computer Science (including subseries Lecture Notes in Artificial Intelligence and Lecture Notes in Bioinformatics)*; Springer Berlin Heidelberg, 2004; pp. 282–291 ISBN 9783540302179.

180. Hansen, N.; Ostermeier, A. Completely Derandomized Self-Adaptation in Evolution Strategies. *Evol. Comput.* **2001**, *9*, 159–195, doi:10.1162/106365601750190398.

181. Rath, A. Characterisation of cell growth, metabolism and recombinant protein production during transient and steady state conditions for the human cell line AGE1.HN-AAT, Otto-von-Guericke Universität Magdeburg, 2017.

182. Nielsen, L.K.; Reid, S.; Greenfield, P.F. Cell cycle model to describe animal cell size variation and lag between cell number and biomass dynamics. *Biotechnol. Bioeng.* **1997**, *56*, 372–379, doi:10.1002/(SICI)1097-0290(19971120)56:4<372::AID-BIT3>3.0.CO;2-L.

183. Brown, A.T.; Wittenberger, C.L. Fructose-1,6-diphosphate-dependent lactate dehydrogenase from a cariogenic streptococcus: purification and regulatory properties. *J. Bacteriol.* **1972**, *110*, 604–615.

184. Coulson, C.J.; Rabin, B.R. Inhibition of lactate dehydrogenase by high concentrations of pyruvate: The nature and removal of the inhibitor. *FEBS Lett.* **1969**, *3*, 333–337, doi:10.1016/0014-5793(69)80171-7.

185. Martínez, V.S.; Dietmair, S.; Quek, L.-E.; Hodson, M.P.; Gray, P.; Nielsen, L.K. Flux balance analysis of CHO cells before and after a metabolic switch from lactate production to consumption. *Biotechnol. Bioeng.* **2013**, *110*, 660–666, doi:10.1002/bit.24728.

186. Xie, J.; Wu, H.; Dai, C.; Pan, Q.; Ding, Z.; Hu, D.; Ji, B.; Luo, Y.; Hu, X. Beyond Warburg effect – dual metabolic nature of cancer cells. *Sci. Rep.* **2015**, *4*, 4927, doi:10.1038/srep04927.

187. Ryll, T.; Valley, U.; Wagner, R. Biochemistry of growth inhibition by ammonium ions in mammalian cells. *Biotechnol. Bioeng.* **1994**, *44*, 184–193, doi:10.1002/bit.260440207.

188. Schmid, G.; Blanch, H.W. Extra- and intracellular metabolite concentrations for murine hybridoma cells. *Appl. Microbiol. Biotechnol.* **1992**, *36*, 621–625, doi:10.1007/BF00183239.

189. Genzel, Y.; Ritter, J.B.; König, S.; Alt, R.; Reichl, U. Substitution of glutamine by pyruvate to reduce ammonia formation and growth inhibition of mammalian cells. *Biotechnol. Prog.* **2005**, *21*, 58–69, doi:10.1021/bp049827d.

190. Hartley, F.; Walker, T.; Chung, V.; Morten, K. Mechanisms driving the lactate switch in Chinese hamster ovary cells. *Biotechnol. Bioeng.* **2018**, *115*, 1890–1903, doi:10.1002/bit.26603.

191. Scholz, S.; Luebbecke, M.; Rath, A.; Schraeder, E.; Rose, T.; Büntemeyer, H.;

Scheper, T.; Reichl, U.; Noll, T. Characterization of the human AGE1.HN cell line: a systems biology approach. *BMC Proc.* **2011**, *5*, P78, doi:10.1186/1753-6561-5-S8-P78.

192. Sonnewald, U. Glutamate synthesis has to be matched by its degradation - where do all the carbons go? *J. Neurochem.* **2014**, *131*, 399–406, doi:10.1111/jnc.12812.

193. Lohr, V.; Hädicke, O.; Genzel, Y.; Jordan, I.; Büntemeyer, H.; Klamt, S.; Reichl, U. The avian cell line AGE1.CR.pIX characterized by metabolic flux analysis. *BMC Biotechnol.* **2014**, *14*, 72, doi:10.1186/1472-6750-14-72.

194. Bröer, S.; Bröer, A. Amino acid homeostasis and signalling in mammalian cells and organisms. *Biochem. J.* **2017**, *474*, 1935–1963, doi:10.1042/BCJ20160822.

195. Tanner, L.B.; Goglia, A.G.; Wei, M.H.; Sehgal, T.; Parsons, L.R.; Park, J.O.; White, E.; Toettcher, J.E.; Rabinowitz, J.D. Four Key Steps Control Glycolytic Flux in Mammalian Cells. *Cell Syst.* **2018**, *7*, 49-62.e8, doi:10.1016/j.cels.2018.06.003.

196. Yalcin, A.; Telang, S.; Clem, B.; Chesney, J. Regulation of glucose metabolism by 6-phosphofructo-2-kinase/fructose-2,6-bisphosphatases in cancer. *Exp. Mol. Pathol.* **2009**, *86*, 174–179, doi:10.1016/j.yexmp.2009.01.003.

197. Sola-Penna, M.; Da Silva, D.; Coelho, W.S.; Marinho-Carvalho, M.M.; Zancan, P. Regulation of mammalian muscle type 6-phosphofructo-1-kinase and its implication for the control of the metabolism. *IUBMB Life* **2010**, *62*, 791–796, doi:10.1002/iub.393.

198. Smolen, P.D.; Baxter, D.A.; Byrne, J.H. Modeling and Analysis of Intracellular Signaling Pathways. In *From Molecules to Networks: An Introduction to Cellular and Molecular Neuroscience: Third Edition*; 2014 ISBN 9780123971791.

199. Westermark, P.O.; Lansner, A. A model of phosphofructokinase and glycolytic oscillations in the pancreatic beta-cell. *Biophys. J.* **2003**, *85*, 126–139, doi:10.1016/S0006-3495(03)74460-9.

200. Mamczur, P.; Gamian, A.; Kolodziej, J.; Dziegiel, P.; Rakus, D. Nuclear localization of aldolase A correlates with cell proliferation. *Biochim. Biophys. Acta - Mol. Cell Res.* **2013**, *1833*, 2812–2822, doi:10.1016/j.bbamcr.2013.07.013.

201. Kim, J.W.; Tchernyshyov, I.; Semenza, G.L.; Dang, C. V. HIF-1-mediated expression of pyruvate dehydrogenase kinase: A metabolic switch required for cellular adaptation to hypoxia. *Cell Metab.* **2006**, *3*, 177–185, doi:10.1016/j.cmet.2006.02.002.

202. Schell, J.C.; Olson, K.A.; Jiang, L.; Hawkins, A.J.; VanVranken, J.G.; Xie, J.; Egnatchik, R.A.; Earl, E.G.; DeBerardinis, R.J.; Rutter, J. A role for the

mitochondrial pyruvate carrier as a repressor of the warburg effect and colon cancer cell growth. *Mol. Cell* **2014**, *56*, 400–413, doi:10.1016/j.molcel.2014.09.026.

203. Sable, H.Z. Biochemistry: The molecular basis of cell structure and function (Lehninger, Albert L.). *J. Chem. Educ.* **2009**, *48*, A288, doi:10.1021/ed048pa288.2.

204. Dean, J.; Reddy, P. Metabolic analysis of antibody producing CHO cells in fed-batch production. *Biotechnol. Bioeng.* **2013**, *110*, 1735–1747, doi:10.1002/bit.24826.

205. Parlo, R.A.; Coleman, P.S. Enhanced rate of citrate export from cholesterol-rich hepatoma mitochondria. The truncated Krebs cycle and other metabolic ramifications of mitochondrial membrane cholesterol. *J. Biol. Chem.* **1984**, *259*, 9997–10003.

206. Filipp, F. V.; Scott, D.A.; Ronai, Z.A.; Osterman, A.L.; Smith, J.W. Reverse TCA cycle flux through isocitrate dehydrogenases 1 and 2 is required for lipogenesis in hypoxic melanoma cells. *Pigment Cell Melanoma Res.* **2012**, *25*, 375–383, doi:10.1111/j.1755-148X.2012.00989.x.

207. Zheng, J. Energy metabolism of cancer: Glycolysis versus oxidative phosphorylation (review). *Oncol. Lett.* **2012**, *4*, 1151–1157, doi:10.3892/ol.2012.928.

208. DeBerardinis, R.J.; Lum, J.J.; Hatzivassiliou, G.; Thompson, C.B. The Biology of Cancer: Metabolic Reprogramming Fuels Cell Growth and Proliferation. *Cell Metab.* **2008**, *7*, 11–20, doi:10.1016/j.cmet.2007.10.002.

209. Zu, X.L.; Guppy, M. Cancer metabolism: facts, fantasy, and fiction. *Biochem. Biophys. Res. Commun.* **2004**, *313*, 459–465, doi:10.1016/j.bbrc.2003.11.136.

210. Wagner, B.A.; Venkataraman, S.; Buettner, G.R. The rate of oxygen utilization by cells. *Free Radic. Biol. Med.* **2011**, *51*, 700–712, doi:10.1016/j.freeradbiomed.2011.05.024.

211. Herst, P.M.; Berridge, M. V. Cell surface oxygen consumption: A major contributor to cellular oxygen consumption in glycolytic cancer cell lines. *Biochim. Biophys. Acta - Bioenerg.* **2007**, *1767*, 170–177, doi:10.1016/j.bbabio.2006.11.018.

212. Barnabé, N.; Butler, M. The effect of glucose and glutamine on the intracellular nucleotide pool and oxygen uptake rate of a murine hybridoma. *Cytotechnology* **2000**, *34*, 47–57, doi:10.1023/A:1008154615643.

213. Warburg, O.; Wind, F.; Negelein, E. I . Killing-Off of Tumor Cells in Vitro . *J. Gen. Physiol.* **1927**, *8*, 519–530.

214. Vander Heiden, M.G.; Cantley, L.C.; Thompson, C.B. Understanding the Warburg effect: the metabolic requirements of cell proliferation. *Science* **2009**, *324*, 1029–33, doi:10.1126/science.1160809.

215. Petch, D.; Butler, M. Profile of energy metabolism in a murine hybridoma: Glucose and glutamine utilization. *J. Cell. Physiol.* **1994**, *161*, 71–76, doi:10.1002/jcp.1041610110.

216. Bonarius, H.P.J.; Özemre, A.; Timmerarends, B.; Skrabal, P.; Tramper, J.; Schmid, G.; Heinzle, E. Metabolic-flux analysis of continuously cultured hybridoma cells using 13CO2 mass spectrometry in combination with 13C-lactate nuclear magnetic resonance spectroscopy and metabolite balancing. *Biotechnol. Bioeng.* **2001**, *74*, 528–538, doi:10.1002/bit.1145.

217. Goudar, C.; Biener, R.; Boisart, C.; Heidemann, R.; Piret, J.; de Graaf, A.; Konstantinov, K. Metabolic flux analysis of CHO cells in perfusion culture by metabolite balancing and 2D [13C, 1H] COSY NMR spectroscopy. *Metab. Eng.* **2010**, *12*, 138–149, doi:10.1016/j.ymben.2009.10.007.

218. Niklas, J.; Sandig, V.; Heinzle, E. Metabolite channeling and compartmentation in the human cell line AGE1.HN determined by 13C labeling experiments and 13C metabolic flux analysis. *J. Biosci. Bioeng.* **2011**, *112*, 616–623, doi:10.1016/j.jbiosc.2011.07.021.

219. Niklas, J.; Priesnitz, C.; Rose, T.; Sandig, V.; Heinzle, E. Primary metabolism in the new human cell line AGE1.HN at various substrate levels: Increased metabolic efficiency and α 1 -antitrypsin production at reduced pyruvate load. *Appl. Microbiol. Biotechnol.* **2012**, *93*, 1637–1650, doi:10.1007/s00253-011-3526-6.

220. Omasa, T.; Furuichi, K.; Iemura, T.; Katakura, Y.; Kishimoto, M.; Suga, K.I. Enhanced antibody production following intermediate addition based on flux analysis in mammalian cell continuous culture. *Bioprocess Biosyst. Eng.* **2010**, *33*, 117–125, doi:10.1007/s00449-009-0351-8.

221. Janke, R.; Genzel, Y.; Händel, N.; Wahl, A.; Reichl, U. Metabolic adaptation of MDCK cells to different growth conditions: Effects on catalytic activities of central metabolic enzymes. *Biotechnol. Bioeng.* **2011**, *108*, 2691–2704, doi:10.1002/bit.23215.

222. Lopez-Lazaro, M. The Warburg Effect: Why and How Do Cancer Cells Activate Glycolysis in the Presence of Oxygen? *Anticancer. Agents Med. Chem.* **2008**, *8*, 305–312, doi:10.2174/187152008783961932.

223. Pelicano, H.; Martin, D.S.; Xu, R.-H.; Huang, P. Glycolysis inhibition for anticancer treatment. *Oncogene* **2006**, *25*, 4633–4646, doi:10.1038/sj.onc.1209597.

224. Im, D.-K.; Cheong, H.; Lee, J.S.; Oh, M.-K.; Yang, K.M. Protein kinase CK2-dependent aerobic glycolysis-induced lactate dehydrogenase A enhances the migration and invasion of cancer cells. *Sci. Rep.* **2019**, *9*, 5337, doi:10.1038/s41598-019-41852-4.

225. Eprintsev, A.T.; Wu, T.L.; Selivanova, N. V.; Khasan Khamad, A. Obtaining homogenous preparations of succinate dehydrogenase isoforms from the D-507 strain of Sphaerotilus natans. *Appl. Biochem. Microbiol.* **2012**, *48*, 541–545, doi:10.1134/S0003683812060038.

226. Manhas, N.; Duong, Q. V; Lee, P.; Richardson, J.D.; Robertson, J.D.; Moxley, M.A.; Bazil, J.N. Computationally modeling mammalian succinate dehydrogenase kinetics identifies the origins and primary determinants of ROS production. *J. Biol. Chem.* **2020**, *295*, 15262–15279, doi:10.1074/jbc.RA120.014483.

227. Cairns, R.A.; Harris, I.S.; Mak, T.W. Regulation of cancer cell metabolism. *Nat. Rev. Cancer* **2011**, *11*, 85–95, doi:10.1038/nrc2981.

228. Cantor, J.R.; Sabatini, D.M. Cancer cell metabolism: One hallmark, many faces. *Cancer Discov.* **2012**, *2*, 881–898, doi:10.1158/2159-8290.CD-12-0345.

229. Grüning, N.M.; Lehrach, H.; Ralser, M. Regulatory crosstalk of the metabolic network. *Trends Biochem. Sci.* **2010**, *35*, 220–227, doi:10.1016/j.tibs.2009.12.001.

230. Yuan, H.-X.; Xiong, Y.; Guan, K.-L. Nutrient Sensing, Metabolism, and Cell Growth Control. *Mol. Cell* **2013**, *49*, 379–387, doi:10.1016/j.molcel.2013.01.019.

231. Barabási, A.L.; Oltvai, Z.N. Network biology: Understanding the cell's functional organization. *Nat. Rev. Genet.* **2004**, *5*, 101–113, doi:10.1038/nrg1272.

232. Batty, M. Digital twins. *Environ. Plan. B Urban Anal. City Sci.* **2018**, *45*, 817–820, doi:10.1177/2399808318796416.

A. Model Kinetics

A.1. AGE1.HN.AAT suspension cell model

Kinetics of the structured of cell growth model

$$r_{Gln^x{}_{trans}} = v_{Gln^x{}_{trans}} \frac{[Gln^x]}{1+\left(\frac{[Gln]}{k_{Gln^x}}\right)^3 + [Gln^x]} V^c \quad \text{A.1.1}$$

$$r_{dGln^x} = k_{dGln^x}[Gln^x] \quad \text{A.1.2}$$

$$r_{Glu^x{}_{trans}} = v_{Glu_{trans}} \frac{\left(\frac{[Glu^x]}{k_{Glu^x}}\right)^2 \left(1-\frac{[Glu]}{[Glu^x]k^{eq}_{Glu^x}}\right)}{1+\left(\frac{[Glu^x]}{k_{Glu^x}}\right)^2 + \left(\frac{[Glu]}{k_{Glu}}\right)^2} V^c \quad \text{A.1.3}$$

$$r_{NH4^x_{trans}} = \left(\omega r_{AAex} + r_{GLNase} + r_{GL\,\mathrm{DH}} - r_{GS}\right)\frac{V^c_s X_v}{V_w} \quad \text{A.1.4}$$

$$r_{Lac^x{}_{trans}} = v_{mLac^x}\left(\frac{\left[Lac^x\right]}{k^m_{mLac^x} + \left[Lac^x\right]}\right)\left(\frac{k^i_{ATPGlc^x}}{k^i_{ATPGlc^x} + k^i_{ATP}[ATP] + k^i_{Glc^x}[Glc^x]}\right)^4 X_v 10^3 \quad \text{A.1.5}$$

$$r_{LDH} = K^{\max}_{LDH} \frac{[Pyr]}{[Pyr] + k^m_{LDH} + \frac{[Pyr]}{k^{iPYR}_{LDH}} + \frac{[ATP]}{k^{iATP}_{LDH}}} \quad \text{A.1.6}$$

$$r_{Pyr^x{}_{trans}} = v_{Pyr^x{}_{trans}} \frac{[Pyr^x]}{1+[Pyr^x]+\left(\frac{[Pyr]}{k_{Pyr}}\right)} V^c \quad \text{A.1.7}$$

Kinetics of alpha-1-antitrypsin formation

$$r_{qAAT} = X_v \mu q_{AAT} E_{Level} \quad \text{A.1.8}$$

Kinetics of the structured model of the intracellular metabolism

Kinetics from glycolysis

$$r_{\mathrm{GLUT}} = \left(r_{X/Glc^x} + r_{m/Glc^x}\right) \frac{V_w}{V_s^c X_v} \quad \text{A.1.9}$$

$$r_{HK} = K_{HK}^{\max} \frac{[Glc][ATP]}{[Glc][ATP]+k_{HK}^m[\mathrm{Glc}]+\mathrm{k}_{ATP_{HK}}^m[Glc]+\mathrm{k}_{ATP_{HK}}^m k_{HK}^m+\frac{[G6P]}{k_{G6P}^i}} \quad \text{A.1.10}$$

$$r_{GPI} = K_{GPI}^{\max} \frac{\left([G6P]-\frac{[F6P]}{k_{GPI}^{eq}}\right)}{k_{GPI}^m+[G6P]+\frac{[F6P]}{k_{GPI}^{eq}}} \quad \text{A.1.11}$$

$$r_{G6PDH} = K_{G6PDH}^{\max} \frac{[G6P]}{[G6P]+k_{G6PFH}^m} \quad \text{A.1.12}$$

$$r_{UT} = K_{UT}^{\max} \frac{[G6P]}{[G6P]+k_{UT}^m} b_{NAD} \quad \text{A.1.13}$$

$$r_{cUGLC} = K_{cUGLC}^{\max} \frac{[UDPGlc]}{[UDPGlc]+k_{cUGLC}^m} \quad \text{A.1.14}$$

$$r_{PFK} = K_{PFK}^{\max} \frac{[F6P]}{k_{PFK}^{m} + [F6P]} \left(\frac{k_{PFK}^{a}}{k_{PFK}^{a} + [ATP]} \right)^{4} \quad \text{A.1.15}$$

$$r_{TATKF6P} = K_{TATKF6P}^{\max} \frac{PPP_{basal}[R5P] - \frac{[F6P]}{k_{TATKF6P}^{eq}}}{\frac{[F6P]}{k_{TATKF6P}^{eq}} + k_{TATKF6P}^{m} + PPP_{basal}[R5P] + [F6P]} \quad \text{A.1.16}$$

$$r_{TATK3PG} = K_{TATK3PG}^{\max} \frac{PPP_{basal}[R5P] - \frac{[3PG]}{k_{TATK3PG}^{eq}}}{\frac{[3PG]}{k_{TATK3PG}^{eq}} + k_{TATK3PG}^{m} + PPP_{basal}[R5P] + [3PG]} \quad \text{A.1.17}$$

$$r_{dR5P} = K_{dR5P}^{\max} \frac{[R5P]}{[R5P] + k_{RDPK}^{m}} \quad \text{A.1.18}$$

$$r_{GLYS} = K_{GLYS}^{\max} \frac{[UDPGlc]}{[UDPGlc] + k_{GLYS}^{m}} \quad \text{A.1.19}$$

$$r_{ENO} = K_{ENO}^{\max} \frac{\left([3PG] - \frac{[PEP]}{k_{ENO_{PEP}}^{eq}} \right)}{1 + \frac{[3PG]}{k_{ENO_{3PG}}^{eq}} + \frac{[PEP]}{k_{ENO_{PEP}}^{eq}}} \quad \text{A.1.20}$$

$$r_{ALD} = K_{ALD}^{\max} \frac{\left([F16P] - \left(\frac{[3PG][ATP]}{k_{ALD}^{eq}} \right) \right)}{1 + [F16P] + \left(\frac{[3PG][ATP]}{k_{ALD}^{eq}} \right) + k_{\mu}^{i}(1 - f)} \quad \text{A.1.21}$$

$$r_{PK} = K_{PK}^{\max} \frac{[PEP] - \frac{[Pyr][ATP]}{k_{PYR}^{PK} k_{ATP}^{PK}}}{\left(([PEP] + 1) + \left(\frac{[ATP]}{k_{ATP}^{PK}} \right) \left(\frac{[Pyr]}{k_{PYR}^{PK}} \right) \right) - 1} \quad \text{A.1.22}$$

$$r_{LDH} = K_{LDH}^{\max} \frac{[Pyr]}{[Pyr] + k_{LDH}^{m} + \frac{[Pyr]}{k_{LDH}^{iPYR}} + \frac{[ATP]}{k_{LDH}^{iATP}}} \quad \text{A.1.23}$$

Kinetics from glycolysis, TCA and other pathways

$$r_{PEPCK} = K_{PEPCK}^{\max} \frac{[OAA]}{[OAA] + k_{PEPCK}^{m}} b_{NAD} \quad \text{A.1.24}$$

$$r_{PDH} = K_{PDH}^{\max} \frac{[Pyr][ATP]}{[Pyr][ATP] + k_{Pyr}^{m}[Pyr] + \mathrm{k}_{ATP_{PDH}}^{m}[Pyr] + \mathrm{k}_{ATP_{PDH}}^{m} k_{Pyr}^{m}} b_{NAD} \quad \text{A.1.25}$$

$$r_{PC} = K_{PC}^{\max} \frac{[Pyr]}{[Pyr] + k_{PC}^{m}} \left(\frac{[AcCoA]}{k_{AcCoA}^{i} + [AcCoA]} \right)^{2} \quad \text{A.1.26}$$

$$r_{ME} = K_{ME}^{\max} \frac{[Mal]}{k_{ME}^{m} \left(1 + \frac{[ATP]}{k_{ATP}^{i}} \right) + [Mal]} \quad \text{A.1.27}$$

Kinetics from TCA

$$r_{AlaTA} = K_{AlaTA}^{\max} \frac{[Pyr]}{k_{AlaTA}^{m} + [Pyr]} \left(\frac{k_{AlaTA}^{i}}{k_{AlaTA}^{i} + [Glc^{x}] k_{Glc_{AlaTA}}^{i} + [ATP] k_{ATP_{AlaTA}}^{i}} \right)^{4} \quad \text{A.1.28}$$

$$r_{CS} = K_{CS}^{\max} \frac{[OAA][AcCoA]}{k_{AcCoA}^{m}[OAA] + k_{OAA}^{m}[AcCoA] + [AcCoA][OAA]} \quad \text{A.1.29}$$

$$r_{ACO} = K_{ACO}^{\max} \left([Cit] - \frac{[cAc]}{k_{ACO}^{eq}} \right) \quad \text{A.1.30}$$

$$r_{ACO2} = K_{ACO}^{\max} \left([cAc] - \frac{[Isocit]}{k_{ACO2}^{eq}} \right) \quad \text{A.1.31}$$

$$r_{CL} = K_{CL}^{\max} \frac{[Cit]}{[Cit] + k_{CL}^{m}} (1 - b_{NAD}) \quad \text{A.1.32}$$

$$r_{ICDH} = K_{ICDH}^{\max} \frac{[Isocit] - \frac{[Keto]}{k_{ICDH}^{eq}}}{k_{ICDH}^{m} + [Isocit] + \frac{[Keto]}{k_{ICDH}^{eq}}} \quad \text{A.1.33}$$

$$r_{GS} = K_{GS}^{\max} \frac{[Glu][ATP]}{[Glu][ATP] + k_{GS}^{m}[\mathrm{Glu}] + \mathrm{k}_{ATP_{GS}}^{m}[Glu] + \mathrm{k}_{ATP_{GS}}^{m} k_{GS}^{m} + \frac{[Gln]}{k_{GS}^{iGln}}} \quad \text{A.1.34}$$

$$r_{Glnase} = K_{Glnase}^{\max} \frac{[Gln]}{[Gln] + k_{G\ln ase}^{m} + \frac{[ATP]}{k_{Glnase}^{iATP}}} \quad \text{A.1.35}$$

$$r_{GLDH} = K_{GLDH}^{\max} \frac{[Glu] - \frac{[Keto]}{k_{GLDH}^{eq}}}{\frac{[Glu]}{k_{GLDH}^{i}} + k_{GLDH}^{m} + [Glu] + \frac{[Keto]}{k_{GLDH}^{eq}}} \quad \text{A.1.36}$$

$$r_{AspTA} = K_{AspTA}^{\max} \frac{\frac{[Keto]}{k_{keto}} - \frac{[OAA][Glu]}{K_{AspTA_{OAA}}^{eq} K_{AspTA_{Glu}}^{eq}}}{k_{AspTA}^{m} + \frac{[OAA][Glu]}{K_{AspTA_{OAA}}^{eq} K_{AspTA_{Glu}}^{eq}} + \frac{[Keto]}{k_{keto}}} \quad \text{A.1.37}$$

$$r_{AAex} = K_{AAex}^{\max} \left(1 - \frac{[Keto]}{k_{AAex}^{eq}}\right) b_{NAD} \quad \text{A.1.38}$$

$$r_{KDH} = K_{KDH}^{\max} \frac{[Keto]}{[Keto] + k_{KDH}^{m}} \quad \text{A.1.39}$$

$$r_{SDH} = K_{KDH}^{\max} \frac{[Suc]}{[Suc] + k_{SDH}^{m} + \frac{[OAA]}{k_{SDH}^{i}}} \quad \text{A.1.40}$$

$$r_{FMA} = K_{FMA}^{\max} \frac{\left([Fum] - \frac{Mal}{k_{FMA}^{eq}} \right)}{k_{FMA}^{m} + [Fum] + \frac{[Mal]}{k_{FMA}^{eq}}} \quad \text{A.1.41}$$

$$r_{MDH} = K_{MDH}^{\max} \frac{[Mal]}{[Mal] + k_{MDH}^{m}} \quad \text{A.1.42}$$

Kinetics from energy production

$$r_{Glycolysis} = r_{PK} + 2r_{ALD} - r_{HK} - r_{PFK} \quad \text{A.1.43}$$

$$r_{TCA} = 2.5 r_{NADH} + 1.5 r_{FADH} \quad \text{A.1.44}$$

$$r_{CCM} = r_{Glycolysis} + r_{TCA} - r_{PDH} - r_{GS} - r_{CL} - r_{PC} \quad \text{A.1.45}$$

$$r_{xATP} = k_{xATP} \mu [ATP] \quad \text{A.1.46}$$

$$r_{mATP} = V_{cs} k_{mATP} [ATP] \quad \text{A.1.47}$$

$$r_{ATPase} = k_{ATPase} \frac{[ATP]}{[ATP] + k_{ATPase}^{m}} \quad \text{A.1.48}$$

$$r_{dATP} = r_{xATP} + r_{mATP} + r_{ATPase} \quad \text{A.1.49}$$

$$r_{NADH} = 2r_{ALD} + r_{MDH} + r_{ICDH} + r_{KDH} + 2r_{AAex} + r_{GLDH} + r_{Lac^{x}_{trans}} \frac{V_w}{V_s^c X_v} - r_{LDH} \quad \text{A.1.50}$$

$$r_{FADH} = r_{SDH} + 2r_{AAex} \quad \text{A.1.51}$$

$$r_{O_2} = 60 \frac{r_{NADH} + r_{FADH}}{2} V_s^c 10^{12} \quad \text{A.1.52}$$

A.2. MDCK.SUS2 suspension cell model

Kinetics of the structured of cell growth model

$$r_{x/\mathrm{Glc}^x} = \mu\left(X_1 f + \sum_{i=2}^{N^c} X_i\right) Y_{x/Glc^x} \qquad \text{A.2.1}$$

$$r_{m/Glc^x} = m_{Glc^x} V^c \Theta\left[Glc^x\right] \qquad \text{A.2.2}$$

$$r_{Gln^x{}_{trans}} = v_{Gln^x{}_{trans}} \frac{[Gln^x]}{1+\left(\frac{[Gln]}{k_{Gln^x}}\right)^3 + [Gln^x]} V^c \qquad \text{A.2.3}$$

$$r_{dGln^x} = k_{dGln^x}[Gln^x] \qquad \text{A.2.4}$$

$$r_{Glu^x{}_{trans}} = v_{Glu^x{}_{trans}} \frac{\left(\frac{[Glu^x]}{k_{Glu^x}}\right)^2 \left(1-\frac{[Glu]}{[Glu^x]k^{eq}_{Glu^x{}_{trans}}}\right)}{1+\left(\frac{[Glu^x]}{k_{Glu^x}}\right)^2 + \left(\frac{[Glu]}{k_{Glu}}\right)^2} V^c \qquad \text{A.2.5}$$

$$r_{\mathrm{NH4}^x_{trans}} = v_{\mathrm{NH4}_{trans}} \frac{\left(\frac{[NH4^x]}{k_{\mathrm{NH4}^x}}\right)^2 \left(1-\frac{[NH4]}{[NH4^x]k^{eq}_{\mathrm{NH4}^x{}_{trans}}}\right)}{1+\left(\frac{[Glu^x]}{k_{\mathrm{NH4}^x}}\right)^2 + \left(\frac{[Glu]}{k_{\mathrm{NH4}}}\right)^2} V^c \qquad \text{A.2.6}$$

$$r_{Lac^x_{trans}} = v_{Lac^x_{trans}} \frac{\left(1-\frac{\left[Lac^x\right]}{[Lac]}{k^{eq}_{Lac^x_{trans}}}\right)\left(\frac{[Lac]}{k_{Lac}} + \frac{[Lacx]}{k_{Lac^x}}\right)^3}{1+\left(\frac{[Lac]}{k_{Lac}} + \frac{[Lacx]}{k_{Lac^x}}\right)^4} V^c \qquad \text{A.2.7}$$

$$r_{Pyr^x{}_{trans}} = v_{Pyr^x{}_{trans}} \frac{[Pyr^x]}{1+[Pyr^x]+k^m_{Pyr^x{}_{trans}}} V^c \quad \text{A.2.8}$$

Kinetics of the structured model of the intracellular metabolism

Kinetics from glycolysis

$$r_{\mathrm{GLUT}} = \left(r_{X/Glc^x} + r_{m/Glc^x}\right)\frac{V_w}{V^c_s X_v} \quad \text{A.2.9}$$

$$r_{HK} = K^{\max}_{HK} \frac{[Glc][ATP]}{[Glc][ATP]+k^m_{HK}[\mathrm{Glc}]+\mathrm{k}^m_{ATP_{HK}}[Glc]+\mathrm{k}^m_{ATP_{HK}}k^m_{HK}} \quad \text{A.2.10}$$

$$r_{GPI} = K^{\max}_{GPI} \frac{\left([G6P]-\frac{[F6P]}{k^{eq}_{GPI}}\right)}{k^m_{GPI}+[G6P]+\frac{[F6P]}{k^{eq}_{GPI}}} \quad \text{A.2.11}$$

$$r_{G6PDH} = K^{\max}_{G6PDH} \frac{[G6P]}{[G6P]+k^m_{G6PFH}} \quad \text{A.2.12}$$

$$r_{UT} = K^{\max}_{UT} \frac{[G6P]}{[G6P]+k^m_{UT}} b_{NAD} \quad \text{A.2.13}$$

$$r_{cUGLC} = K^{\max}_{cUGLC} \frac{[UDPGlc]}{[UDPGlc]+k^m_{cUGLC}} \quad \text{A.2.14}$$

$$r_{PFK} = K^{\max}_{PFK} \frac{[F6P]}{k^m_{PFK}+[F6P]}\left(\frac{k^a_{PFK}}{k^a_{PFK}+[ATP]}\right)^4 \quad \text{A.2.15}$$

$$r_{TATKF6P} = K^{\max}_{TATKF6P} \frac{[R5P] - \frac{[F6P]}{k^{eq}_{TATKF6P}}}{\frac{[F6P]}{k^{eq}_{TATKF6P}} + k^{m}_{TATKF6P} + [R5P]} \quad \text{A.2.16}$$

$$r_{TATK3PG} = K^{\max}_{TATK3PG} \frac{[R5P] - \frac{[3PG]}{k^{eq}_{TATK3PG}}}{\frac{[3PG]}{k^{eq}_{TATK3PG}} + k^{m}_{TATK3PG} + [R5P]} \quad \text{A.2.17}$$

$$r_{dR5P} = K^{\max}_{dR5P} \frac{[R5P]}{[R5P] + k^{m}_{dR5P}} \quad \text{A.2.18}$$

$$r_{GLYS} = K^{\max}_{GLYS} \frac{[UDPGlc]}{[UDPGlc] + k^{m}_{GLYS}} \quad \text{A.2.19}$$

$$r_{ENO} = K^{\max}_{ENO} \frac{\frac{[3PG]}{k_{3PG}}\left(1 - \frac{[PEP]}{[3PG]k^{eq}_{ENO}}\right)}{1 + \frac{[3PG]}{k_{3PG}} + \frac{[PEP]}{k_{PEP}}} \quad \text{A.2.20}$$

$$r_{ALD} = K^{\max}_{ALD} \frac{\frac{[F16P]}{k_{F16P}}\left(1 - \frac{[3PG]}{[F16P]k^{eq}_{ALD}}\right)}{1 + \frac{[F16P]}{k_{F16P}} + \frac{[3PG]}{k_{3PG_{ALD}}} + \frac{[3PG][ATP]}{k_{3PG_{ALD}}k_{ATP_{ALD}}} + \frac{[ATP]}{k_{ATP_{ALD}}} + k^{i}_{\mu}(1-f)} \quad \text{A.2.21}$$

$$r_{PK} = K^{\max}_{PK} \frac{\frac{[PEP]}{k_{PEP_{PK}}} - \frac{[Pyr]}{k_{Pyr_{PK}}}}{1 + \frac{[PEP]}{k_{PEP_{PK}}} + \frac{[Pyr]}{k_{Pyr_{PK}}}} \quad \text{A.2.22}$$

$$r_{LDH} = K_{LDH}^{\max} \frac{\frac{[Pyr]}{k_{Pyr}}\left(1-\frac{[Lac]}{[Pyr]}\right)\left(\frac{[Pyr]}{k_{Pyr_{LDH}}}+\frac{[Lac]}{k_{Lac_{LDH}}}\right)^3}{\left(\frac{[Pyr]}{k_{Pyr_{LDH}}}+\frac{[Lac]}{k_{Lac_{LDH}}}\right)^4 + \left(\frac{1+k^a_{Pyr_{LDH}}\left(\frac{[Pyr]}{k_{cPyr}}\right)^4}{1+[Pyr]^4}\right)\left(\frac{1+k^i_{Glu_{LDH}}\left(\frac{[Glu]}{k_{Glu_{LDH}}}\right)^4}{1+[Glu]^4}\right)} \quad \text{A.2.23}$$

Kinetics from glycolysis, TCA and other pathways

$$r_{PEPCK} = K_{PEPCK}^{\max} \frac{[OAA]}{[OAA]+k^m_{PEPCK}} b_{NAD} \quad \text{A.2.24}$$

$$r_{PDH} = K_{PDH}^{\max} \frac{[Pyr][ATP]}{[Pyr][ATP]+k^m_{Pyr_{PDH}}[Pyr]+\mathrm{k}^m_{ATP_{PDH}}[Pyr]+\mathrm{k}^m_{ATP_{PDH}}k^m_{Pyr_{PDH}}} b_{NAD} \quad \text{A.2.25}$$

$$r_{PC} = K_{PC}^{\max} \frac{[Pyr][ATP]}{[Pyr][ATP]+k^m_{Pyr_{PC}}[Pyr]+\mathrm{k}^m_{ATP_{PC}}[Pyr]+\mathrm{k}^m_{ATP_{PC}}k^m_{Pyr_{PC}}} b_{NAD} \quad \text{A.2.26}$$

$$r_{ME} = K_{ME}^{\max} \frac{[Mal]}{k^m_{ME}\left(1+\frac{[ATP]}{k^i_{ATP_{ME}}}\right)+[Mal]} \quad \text{A.2.27}$$

$$r_{AlaTA} = K_{AlaTA}^{\max} \frac{[Pyr]}{k^m_{AlaTA}+[Pyr]}\left(\frac{[Glu]}{k^a_{Glu_{AlaTA}}+[Glu]}\right)^4 \quad \text{A.2.28}$$

$$r_{d\mathrm{NH4}} = K_{d\mathrm{NH4}}^{\max} \frac{[\mathrm{NH4}]}{k^m_{d\mathrm{NH4}}+[\mathrm{NH4}]}\left(\frac{[ATP]}{k^a_{ATP_{d\mathrm{NH4}}}+[ATP]}\right)^4 \quad \text{A.2.29}$$

Kinetics from TCA

$$r_{CS} = K_{CS}^{\max} \frac{[OAA][AcCoA]}{k_{AcCoA}^{m}[OAA] + k_{OAA}^{m}[AcCoA] + [AcCoA][OAA]} \quad \text{A.2.30}$$

$$r_{ACO} = K_{ACO}^{\max}\left([Cit] - \frac{[cAc]}{k_{ACO}^{eq}}\right) \quad \text{A.2.31}$$

$$r_{ACO2} = K_{ACO}^{\max}\left([cAc] - \frac{[Isocit]}{k_{ACO2}^{eq}}\right) \quad \text{A.2.32}$$

$$r_{CL} = K_{CL}^{\max} \frac{[Cit][ATP]}{[Cit][ATP] + k_{Cit}^{m}[Pyr] + \mathrm{k}_{ATP_{CL}}^{m}[Pyr] + \mathrm{k}_{ATP_{CL}}^{m} k_{Cit}^{m}}(1 - b_{NAD}) \quad \text{A.2.33}$$

$$r_{ICDH} = K_{ICDH}^{\max} \frac{[Isocit] - \frac{[Keto]}{k_{ICDH}^{eq}}}{k_{ICDH}^{m} + [Isocit] + \frac{[Keto]}{k_{ICDH}^{eq}}} b_{NAD} \quad \text{A.2.34}$$

$$r_{GS} = K_{GS}^{\max} \frac{[Glu][ATP]}{[Glu][ATP] + k_{Glu_{GS}}^{m}[ATP] + \mathrm{k}_{ATP_{GS}}^{m}[Glu] + \mathrm{k}_{ATP_{GS}}^{m} k_{Glu_{GS}}^{m}} \quad \text{A.2.35}$$

$$r_{Glnase} = K_{Glnase}^{\max} \frac{[Gln]}{[Gln] + k_{\mathrm{Glnase}}^{m} + \frac{[Glu]}{k_{ATP_{Glnase}}^{i}}} \quad \text{A.2.36}$$

$$r_{GLDH} = K_{GLDH}^{\max} \frac{[Glu] - \frac{[Keto]}{k_{GLDH}^{eq}}}{k_{GLDH}^{m} + [Glu] + \frac{[Keto]}{k_{GLDH}^{eq}} + \frac{[Glu]}{k_{Glu_{GLDH}}^{i}}} \quad \text{A.2.37}$$

$$r_{AspTA} = K_{AspTA}^{\max} \frac{\frac{[Keto]}{k_{keto}} - \frac{[OAA][Glu]}{K_{AspTA_{OAA}}^{eq} K_{AspTA_{Glu}}^{eq}}}{k_{AspTA}^{m} + \frac{[OAA][Glu]}{K_{AspTA_{OAA}}^{eq} K_{AspTA_{Glu}}^{eq}} + \frac{[Keto]}{k_{keto}}} b_{NAD} \quad \text{A.2.38}$$

$$r_{AAex} = K_{AAex}^{\max}\left(1-\frac{[Keto]}{k_{AAex}^{eq}}\right)b_{NAD} \quad \text{A.2.39}$$

$$r_{KDH} = K_{KDH}^{\max}\frac{[Keto]}{[Keto]+k_{KDH}^{m}} \quad \text{A.2.40}$$

$$r_{SDH} = K_{KDH}^{\max}\frac{[Suc]}{[Suc]+k_{SDH}^{m}+\frac{[OAA]}{k_{OAA_{SDH}}^{i}}} \quad \text{A.2.41}$$

$$r_{FMA} = K_{FMA}^{\max}\frac{\left([Fum]-\frac{Mal}{k_{FMA}^{eq}}\right)}{k_{FMA}^{m}+[Fum]+\frac{[Mal]}{k_{FMA}^{eq}}} \quad \text{A.2.42}$$

$$r_{MDH} = K_{MDH}^{\max}\frac{[Mal]}{[Mal]+k_{MDH}^{m}} \quad \text{A.2.43}$$

Kinetics from energy production

$$r_{Glycolysis} = r_{PK} + 2r_{ALD} - r_{HK} - r_{PFK} \quad \text{A.2.44}$$

$$r_{TCA} = 2.5r_{NADH} + 1.5r_{FADH} \quad \text{A.2.45}$$

$$r_{CCM} = r_{Glycolysis} + r_{TCA} - r_{GS} - r_{CL} - r_{PC} \quad \text{A.2.46}$$

$$r_{xATP} = k_{xATP}\mu[ATP] \quad \text{A.2.47}$$

$$r_{mATP} = V_{cs}k_{mATP}[ATP] \quad \text{A.2.48}$$

$$r_{ATPase} = k_{ATPase}\frac{[ATP]}{[ATP]+k_{ATPase}^{m}} \quad \text{A.2.49}$$

$$r_{dATP} = r_{xATP} + r_{mATP} + r_{ATPase} \quad \text{A.2.50}$$

$$r_{NADH} = 2r_{ALD} + r_{MDH} + r_{ICDH} + r_{KDH} + 2r_{AAex} + r_{GLDH} + r_{PDH} - r_{LDH} \quad \text{A.2.51}$$

$$r_{FADH} = r_{SDH} + 2r_{AAex} \quad \text{A.2.52}$$

$$r_{O_2} = 60\frac{r_{NADH} + r_{FADH}}{2} V_s^c 10^{12} \quad \text{A.2.53}$$

B. Local and global parameters

B1. AGE1.HN.AAT suspension cell model

Table B1.1.: Estimated global parameters of AGE1.HN.AAT structured intracellular model with confidence intervals between 0.025-quantile and 0.972-quantile ($Q_{0.025}$ – $Q_{0.975}$), calculated via bootstrap method with 2000 repetitions.

Parameter	Value	$Q_{0.025}$–$Q_{0.975}$	Unit	Parameter	Value	$Q_{0.025}$–$Q_{0.975}$	Unit
$v_{HK}^{\max}$	3.45e-12	2.82e-12–5.47e-11	L/cell/min	$v_{ENO}^{\max}$	8.39e-11	6.10e-11–9.89e-11	L/cell/min
$v_{GPI}^{\max}$	3.48e-10	3.00e-10–7.00e-10	L/cell/min	$v_{PK}^{\max}$	4.66e-10	3.37e-10–5.16e-10	L/cell/min
$v_{G6PDH}^{\max}$	1.13e-11	9.91e-12–1.31e-11	L/cell/min	$v_{LDH}^{\max}$	3.75e-10	3.20e-10–3.95e-10	L/cell/min
$v_{dR5P}^{\max}$	3.30e-08	2.77e-08–5.42e-08	L/cell/min	$v_{PDH}^{\max}$	1.82e-13	8.73e-14–3.67e-13	L/cell/min
$v_{UT}^{\max}$	7.64e-15	5.91e-15–8.40e-15	L/cell/min	$v_{ACO}^{\max}$	3.88e-10	3.45e-10–1.59e-04	L/cell/min
$v_{GLYS}^{\max}$	2.43e-15	1.81e-15–3.58e-15	L/cell/min	$v_{CL}^{\max}$	3.86e-13	2.66e-13–5.40e-13	L/cell/min
$v_{PFK}^{\max}$	3.88e-12	2.94e-12–4.55e-12	L/cell/min	$v_{ICDH}^{\max}$	9.14e-10	6.67e-10–1.30e-09	L/cell/min
$v_{TATKF6P}^{\max}$	3.01e-11	2.56e-11–7.97e-10	L/cell/min	$v_{GS}^{\max}$	7.52e-12	5.15e-12–9.47e-12	L/cell/min
$v_{TATK3PG}^{\max}$	1.07e-11	9.73e-12–1.79e-11	L/cell/min	$v_{KDH}^{\max}$	7.43e-11	7.06e-11–9.41e-11	L/cell/min
$v_{ALD}^{\max}$	7.26e-11	6.21e-11–8.62e-11	L/cell/min	$v_{SDH}^{\max}$	1.71e-10	1.58e-10–2.06e-10	L/cell/min
$v_{FMA}^{\max}$	2.95e-10	1.31e-10–3.63e-10	L/cell/min	$v_{AspTA}^{\max}$	1.10e-10	6.33e-14–1.21e-10	L/cell/min
$v_{MDH}^{\max}$	4.12e-10	3.13e-10–6.84e-10	L/cell/min	$v_{GLDH}^{\max}$	1.97e-12	1.08e-16–2.25e-12	L/cell/min
$v_{ATPase}^{\max}$	5.88e-12	1.72e-13–6.33e-12	L/cell/min	$v_{GLNase}^{\max}$	1.08e-12	2.74e-13–1.40e-12	L/cell/min
$v_{AAex}^{\max}$	2.79e-13	2.48e-13–1.05e+00	L/cell/min	k_{HK}^{m}	1.44e-02	9.86e-13–1.60e-02	mmol/L
$v_{cUGLC}^{\max}$	9.17e-13	8.19e-13–6.30e-12	L/cell/min	k_{GPI}^{m}	3.31	2.24–3.72	mmol/L
$v_{CS}^{\max}$	4.46e-12	2.53e-13–5.08e-12	L/cell/min	k_{GPI}^{eq}	0.23	1.94e-01–1.46e+01	–

Table B1.1.: Estimated global parameters of AGE1.HN.AAT structured intracellular model with confidence intervals between 0.025-quantile and 0.972-quantile ($Q_{0.025}$ – $Q_{0.975}$), calculated via bootstrap method with 2000 repetitions (continued).

Parameter	Value	$Q_{0.025}$–$Q_{0.975}$	Unit	Parameter	Value	$Q_{0.025}$–$Q_{0.975}$	Unit
$v_{ME}^{\max}$	3.59e-13	2.82e-13–1.15e-12	L/cell/min	k_{G6PDH}^{m}	1.31e+01	1.00e-01–1.36e+01	mmol/L
$v_{PEPCK}^{\max}$	7.05e-14	5.45e-14–6.87e-12	L/cell/min	k_{UT}^{m}	1.76e-02	1.34e-02–2.15e-02	mmol/L
$v_{PC}^{\max}$	2.98e-13	2.56e-13–4.53e-13	L/cell/min	$k_{TATKF6P}^{eq}$	1.44e+01	2.89e+00–1.72e+01	mmol/L
$v_{AlaTA}^{\max}$	1.48e-11	1.75e-14–1.57e-11	L/cell/min	$k_{TATK3PG}^{eq}$	4.00	0.19–5.09	mmol/L
k_{PFK}^{m}	2.66e-03	2.36e-03–1.96e+01	mmol/L	k_{ICDH}^{m}	3.07	2.36e+00–1.21e+02	mmol/L
k_{ALD}^{m}	1.10e+01	1.58e-02–1.35e+01	mmol/L	k_{ICDH}^{eq}	5.04	9.10e-03–5.64e+00	mmol/L
k_{ENO}^{eq}	0.49	4.69e-01–2.02e+01	–	k_{AAex}^{eq}	0.26	0.21–4.54	–
k_{PK}^{m}	1.13	0.92–5.56	mmol/L	k_{SDH}^{eq}	5.98e+01	1.36e-01–7.59e+01	mmol/L
k_{LDH}^{m}	2.70	1.77e+00–1.14e+01	mmol/L	k_{FMA}^{eq}	7.69	2.91–8.91	mmol/L
k_{LDH}^{iPYR}	1.21e-02	1.21e-02–1.31e+00	$mmol^2/L^2$	k_{FMA}^{m}	4.12	4.08–5.87	mmol/L
k_{Pyr}^{m}	7.95e+01	1.08e+00–9.68e+01	mmol/L	k_{MDH}^{m}	4.19e+02	2.14e-01–4.44e+02	mmol/L
k_{ACO}^{eq}	1.12e-02	9.95e-03–7.57e-01	–	k_{xATP}	2.63e+03	5.81e+01–3.22e+03	cell/L/min
k_{ACO2}^{eq}	3.73	2.18–4.20	–	k_{mATP}	2.65e+10	2.42e10–2.65e11	cell/L/min
k_{m}^{CL}	0.14	1.15e-02–1.89e-01	mmol/L	NAD_{basal}	0.58	0.58–8.90	mmol/L
k_{cUGLC}^{m}	9.01e+01	7.48e+01–6.32e+02	mmol/L	k_{RDPK}^{m}	1.19e+02	1.60e-03–1.25e+02	mmol/L
k_{CS}^{m}	2.73	2.36e+00–3.52e+03	mmol/L	k_{SDH}^{m}	7.21e+02	4.44e+01–9.81e+02	mmol/L
k_{ME}^{m}	2.64e+01	7.80e-01–2.96e+01	mmol/L	k_{PEPCK}^{m}	3.26e+01	3.13e+01–1.82e+02	mmol/L
k_{ATP}^{i}	6.59e+01	5.36e-01–8.15e+01	$mmol^2/L^2$	PPP_{basal}	1.42	1.00e+00–1.93e+01	mmol/L

Table B1.1.: Estimated global parameters of AGE1.HN.AAT structured intracellular model with confidence intervals between 0.025-quantile and 0.972-quantile ($Q_{0.025}$ – $Q_{0.975}$), calculated via bootstrap method with 2000 repetitions (continued).

Parameter	Value	$Q_{0.025}$–$Q_{0.975}$	Unit	Parameter	Value	$Q_{0.025}$–$Q_{0.975}$	Unit
k_{UT}^{eq}	5.78	5.21e+00–1.52e+02	mmol/L	$k_{TATK3PG}^{m}$	1.45e+01	4.88e-05–1.60e+01	mmol/L
k_{μ}^{i}	1.12e+02	2.58e+00–1.33e+02	mmol/L	$k_{TATKF6P}^{m}$	0.53	4.26e-01–8.38e+02	mmol/L
k_{PFK}^{eq}	3.91e+01	2.47e+01–3.98e+01	–	$k_{ENO_{PEP}}^{eq}$	1.47	1.90e-02–1.80e+00	–
k_{GS}^{m}	5.68	3.73e+00–1.14e+02	mmol/L	$k_{ENO_{3PG}}^{eq}$	0.79	2.16e-03–8.79e-01	–
k_{ICDH}^{m}	3.07	2.36e+00–1.21e+02	mmol/L	k_{G6P}^{i}	3.10	1.44e-02–3.21e+00	$mmol^2/L^2$
k_{ICDH}^{eq}	5.04	9.10e-03–5.64e+00	–	k_{PC}^{m}	8.00e-07	6.40e-07–3.92e+01	mmol/L
k_{AlaTA}^{m}	1.62	1.08–2.24	mmol/L	k_{ATPase}^{m}	2.29	1.07e-02–2.60e+00	mmol/L
k_{KDH}^{m}	3.12e+01	2.57e+01–2.88e+03	mmol/L	k_{GLDH}^{m}	1.60e+02	4.40e+00–1.77e+02	mmol/L
$k_{AspTA_{OAA}}^{eq}$	1.82e-02	1.41e-02–4.50e+00	mmol/L	$k_{ATP_{HK}}^{m}$	0.95	0.83–2.04	mmol/L
$k_{AspTA_{Glu}}^{eq}$	7.53	7.20e-07–1.02e+01	mmol/L	k_{ALD}^{eq}	1.75	1.12–2.15	–
k_{keto}	9.60	1.56e+00–1.04e+01	mmol/L	k_{PYR}^{PK}	6.83e+02	1.13e-01–8.62e+02	mmol/L
k_{AspTA}^{m}	4.17	2.08e+00–3.33e+01	mmol/L	k_{ATP}^{PK}	0.84	4.73e-02–1.23e+00	mmol/L
k_{GLDH}^{i}	4.34e-02	3.86e-02–2.25e-01	mmol/L	$v_{GLU_{trans}}$	2.37e-03	1.49e-03–1.90e+00	mmol/ mmol/L/µL/ min
k_{Glnase}^{m}	3.48e-04	2.67e-04–9.56e-02	mmol/L	k_{Glu^x}	1.47e-02	1.22e-02–9.07e+01	mmol/L
k_{Glnase}^{iGln}	1.84e-02	1.72e-02–3.44e+01	$mmol^2/L^2$	k_{Glu}	1.00	9.40e-01–4.72e+01	mmol/L
k_{GLDH}^{eq}	7.23e-03	6.55e-03–1.22e+01	–	$k_{Glu^x}^{eq}$	0.19	1.49e-01–1.85e+02	mmol/L
$v_{Gln^x_{trans}}$	0.17	0.11–1.25	mmol/L/µL/ min	k_{GLYS}^{m}	1.49e-03	1.14e-03–2.17e+00	mmol/L
k_{Gln^x}	0.75	0.49–2.75	mmol/L	k_{AlaTA}^{m}	2.90e-11	2.24e-11–3.93e-04	mmol/L

Table B1.1.: Estimated global parameters of AGE1.HN.AAT structured intracellular model with confidence intervals between 0.025-quantile and 0.972-quantile ($Q_{0.025}$ – $Q_{0.975}$), calculated via bootstrap method with 2000 repetitions (continued).

Parameter	Value	$Q_{0.025}$–$Q_{0.975}$	Unit	Parameter	Value	$Q_{0.025}$–$Q_{0.975}$	Unit
$v_{Pyr^x_{trans}}$	3.38e-04	2.85e-04–6.28e+04	mmol/L/µL/min	k^m_{OAA}	9.73e+03	9.53e+01–9.73e+03	mmol/L
k_{pyr}	3.88	3.12–5.71	mmol/L	k^m_{AcCoA}	4.73e+01	3.75e+01–5.45e+01	mmol/L
ω	1.45	3.35e-02–1.59e+00	–	k^a_{PFK}	4.43	3.88e+00–1.02e+04	mmol/L
k^m_{AspTA}	7.22	1.68e-03–8.94e+00	mmol/L	$v^{\max}_{mLac^x}$	1.75e-08	1.51e-08–6.72e-03	mmol/L/cell/min
$k^m_{ATP_{GS}}$	1.23e+01	1.50e-01–1.30e+01	mmol/L	$k^m_{ATP_{PDH}}$	3.52	1.81e+00–1.26e+01	mmol/L
k^{iATP}_{Glnase}	2.64	5.83e-02–3.21e+00	mmol²/L²	k^i_{AlaTA}	0.12	1.54e-02–1.75e-01	mmol/L
k^i_{SDH}	9.95e-02	7.59e-02–7.58e-01	mmol/L	$k^i_{Glc_{AlaTA}}$	8.07	3.97e-03–1.01e+01	mmol/L
k^{iATP}_{LDH}	8.01e+03	1.20e+00–9.50e+03	mmol²/L²	$k^i_{ATP_{AlaTA}}$	4.79e-02	6.50e-03–7.57e-02	mmol/L
$k^m_{mLac^x}$	8.6	2.81e-04–9.31e+00	mmol/L	k^i_{AcCoA}	0.44	3.98e-02–5.57e-01	mmol/L

Table B1.2.: Estimated global parameters of AGE1.HN.AAT segregated cell growth model with confidence intervals between 0.025-quantile and 0.972-quantile ($Q_{0.025}$ – $Q_{0.975}$), calculated via bootstrap method with 2000 repetitions.

Parameter	Value	$Q_{0.025}$–$Q_{0.975}$	Unit	Parameter	Value	$Q_{0.025}$–$Q_{0.975}$	Unit
$k^m_{Glc^x}$	2.71	1.17–6.01	mmol/L	α	6.90e+05	3.353e+03–9.77e+05	–
$\mu_{\max}$	1.80e-02	1.72e-02–2.25e-02	1/h	$k^{\min}_d$	1.99e-06	2.11e-07–7.98e-06	1/min
k_{dGln^x}	2.5e-05	3.07e-06–6.39e-05	1/min	$k^{\max}_d$	3.41e-05	2.22e-05–6.38e-05	1/min
Y_{x/Glc^x}	3.0e-05	3.15e-07–6.25e-06	mmol/L/cell	β	4.64e-05	2.01e-05–5.04e-04	1/min
m_{Glc^x}	5.0e-04	1.61e-04–8.18e-04	mmol/L/µL/min	q_{AAT}	3.41e-05	2.46e-05–3.60e-05	mg/cell

Table B1.3.: Initial conditions used for the simulation of the four AGE1.HN.AAT batch cultivations.

Local parameter	Cult1	Cult2	Cult3	Cult4	Unit
$\left[Glc^x\right]\ (t=0)$	30.52	31.53	30.00	33.96	mmol/L
$\left[G\ln^x\right]\ (t=0)$	3.27	3.40	3.41	3.80	mmol/L
$\left[Glu^x\right]\ (t=0)$	0.62	0.58	0.74	0.88	mmol/L
$\left[Lac^x\right]\ (t=0)$	0.00	0.00	0.49	0.50	mmol/L
$\left[NH4^x\right]\ (t=0)$	0.49	0.60	0.40	0.40	mmol/L
$\left[Pyr^x\right]\ (t=0)$	2.44	2.5	2.09	2.03	mmol/L
$X_1(t=0)$	2.62e+05	2.24e+05	2.41e+05	3.06e+05	cells/mL
$X_2(t=0)$	1.18e+05	1.01e+05	1.08e+05	1.38e+05	cells/mL
$X_3(t=0)$	1.31e+05	1.12e+05	1.21e+05	1.53e+05	cells/mL
$X_4(t=0)$	0.66e+05	0.56e+05	0.60e+05	0.76e+05	cells/mL
$X_5(t=0)$	0.66e+05	0.56+e05	0.60e+05	0.76e+05	cells/mL
$AAT(t=0)$	0.00	0.00	0.00	0.00	mg/L
d_c	21.50	22.81	19.70	19.00	µm
d_m	13.50	12.50	14.5	14.50	µm
E_{Level}	1.00	1.01	0.98	0.9283	–
V_w	1.00e-03	1.00e-03	1.00e-03	1.00e-03	–

Table B1.4.: Initial conditions of intracellular metabolites used for simulation of the AGE1.HN.AAT pre-culture of cultivations.

B. Local and global parameters

Local parameter	Pre-culture	Unit	Local parameter	Pre-culture	Unit
$[G6P]\ (t=0)$	0.12	mmol/L	$[Glu]\ (t=0)$	0.41	mmol/L
$[F6P]\ (t=0)$	0.03	mmol/L	$[Suc]\ (t=0)$	1.80	mmol/L
$[R5P]\ (t=0)$	4.43e-04	mmol/L	$[Mal]\ (t=0)$	0.43	mmol/L
$[UDPGlc]\ (t=0)$	0.38	mmol/L	$[Keto]\ (t=0)$	0.18	mmol/L
$[F16P]\ (t=0)$	0.21	mmol/L	$[Fum]\ (t=0)$	0.06	mmol/L
$[3PG]\ (t=0)$	0.07	mmol/L	$[OAA]\ (t=0)$	0.02	mmol/L
$[PEP]\ (t=0)$	0.05	mmol/L	$[ATP]\ (t=0)$	4.21	mmol/L
$[Pyr]\ (t=0)$	0.19	mmol/L	$[AcCoA]\ (t=0)$	1.08	mmol/L
$[Gln]\ (t=0)$	1.21	mmol/L	$[IsoCit]\ (t=0)$	0.04	mmol/L
$[Glc]\ (t=0)$	0.06	mmol/L			

B2. MDCK.SUS2 suspension cell model

Table B2.1.: Estimated global parameters of MDCK.SUS2 structured intracellular model with confidence intervals between 0.025–quantile and 0.972–quantile ($Q_{0.025}$ – $Q_{0.975}$) calculated via bootstrap method with 2500 runs.

Parameter	Value	$Q_{0.025}$–$Q_{0.975}$	Unit	Parameter	Value	$Q_{0.025}$–$Q_{0.975}$	Unit
$v_{HK}^{\max}$	6.25e-13	6.15e-13–1.21e-12	L/cell/min	$v_{PK}^{\max}$	1.44e-12	1.25e-12–1.48e-12	L/cell/min
$v_{GPI}^{\max}$	1.29e-12	8.43e-13–4.99e-12	L/cell/min	$v_{LDH}^{\max}$	3.79e-09	1.73e-09–1.20e-08	L/cell/min
$v_{G6PDH}^{\max}$	1.06e-14	1.03e-14–3.50e-14	L/cell/min	$v_{PDH}^{\max}$	5.82e-13	1.30e-13–1.14e-12	L/cell/min
$v_{UT}^{\max}$	9.86e-16	6.16e-16–1.70e-15	L/cell/min	$v_{ACO}^{\max}$	3.10e-08	1.02e-08–4.99e-08	L/cell/min
$v_{GLYS}^{\max}$	2.44e-17	6.32e-18–8.96e-17	L/cell/min	$v_{CL}^{\max}$	1.79e-16	2.43e-17–9.12e-16	L/cell/min
$v_{PFK}^{\max}$	7.88e-13	6.67e-13–9.96e-13	L/cell/min	$v_{ICDH}^{\max}$	6.47e-15	2.66e-15–1.39e-14	L/cell/min
$v_{TATKF6P}^{\max}$	3.45e-14	1.56e-14–6.17e-14	L/cell/min	$v_{GS}^{\max}$	7.61e-13	1.05e-14–1.44e-12	L/cell/min
$v_{TATK3PG}^{\max}$	7.50e-14	3.72e-14–1.18e-13	L/cell/min	$v_{KDH}^{\max}$	7.90e-13	6.62e-13–9.68e-13	L/cell/min
$v_{ALD}^{\max}$	3.34e-10	1.77e-10–8.27e-10	L/cell/min	$v_{SDH}^{\max}$	1.48e-10	8.11e-11–3.35e-10	L/cell/min
$v_{ENO}^{\max}$	2.17e-11	1.17e-11–4.00e-11	L/cell/min	$v_{FMA}^{\max}$	8.45e-08	3.07e-08–1.00e-07	L/cell/min
$v_{MDH}^{\max}$	1.97e-13	2.87e-14–3.93e-13	L/cell/min	$v_{GLDH}^{\max}$	9.44e-09	5.96e-09–2.01e-08	L/cell/min
v_{dR5P}	2.90e-12	1.28e-12–4.85e-12	L/cell/min	$v_{GLNase}^{\max}$	1.23e-11	4.99e-12–7.20e-11	L/cell/min
$v_{ATPase}^{\max}$	4.52e-11	3.18e-11–7.64e-11	L/cell/min	$v_{AlaTA}^{\max}$	4.69e-12	2.26e-12–1.12e-11	L/cell/min
$v_{AAex}^{\max}$	4.34e-13	3.28e-13–5.80e-13	L/cell/min	$v_{d\mathrm{NH4}}$	8.58e-11	4.17e-11–2.24e-10	L/cell/min
$v_{cUGLC}^{\max}$	1.19e-14	7.01e-15–2.29e-14	L/cell/min	$v_{Lac_{trans}^{x}}$	1.92e+03	4.05e+02–7.6e+03	mmol/L/µL/min
$v_{CS}^{\max}$	4.32e-10	2.05e-10–9.39e-10	L/cell/min	$v_{\mathrm{Gln}_{trans}^{x}}$	2.35e-04	1.95e-04–2.72e-04	mmol/L/µL/min
$v_{ME}^{\max}$	7.05e-13	5.53e-13–9.30e-13	L/cell/min	$v_{Pyr_{trans}^{x}}$	4.31e-04	3.90e-04–5.12e-04	mmol/L/µL/min
$v_{PEPCK}^{\max}$	2.84e-13	1.12e-13–3.36e-13	L/cell/min	$v_{\mathrm{NH4}_{trans}^{x}}$	4.25e-04	1.09e-04–2.99e-03	mmol/L/µL/min
$v_{PC}^{\max}$	1.55e-12	5.36e-13–2.40e-12	L/cell/min	$v_{Glu_{trans}^{x}}$	4.70e-05	2.15e-05–1.01e-04	mmol/L/µL/min

Table B2.1.: Estimated global parameters of MDCK.SUS2 structured intracellular model with confidence intervals between 0.025–quantile and 0.972–quantile (Q0.025 – Q0.975) calculated via bootstrap method with 2500 runs (continued).

Parameter	Value	$Q_{0.025}$–$Q_{0.975}$	Unit	Parameter	Value	$Q_{0.025}$–$Q_{0.975}$	Unit
$v_{AspTA}^{\max}$	9.54e-09	3.44e-09–3.11e-08	L/cell/min	k_{HK}^{m}	5.01e-04	2.00e-04–3.26e-03	mmol/L
k_{GPI}^{m}	7.97e-02	1.37e-02–3.25e-01	mmol/L	$k_{Pyr_{PK}}$	3.21e+03	8.00e+02–8.29e+03	mmol/L
k_{GPI}^{eq}	1.55e+00	5.63e-01–6.12e+02	–	$k_{Pyr_{PDH}}$	4.97e-07	1.56e-07–1.31e-06	mmol/L
k_{G6PDH}^{m}	3.39e-03	9.91e-04–9.19e-03	mmol/L	k_{ACO}^{eq}	1.46e-02	1.28e-02–1.61e-02	–
k_{UT}^{m}	7.23e-02	1.33e-02–1.82e-01	mmol/L	k_{ACO2}^{eq}	2.14e+00	1.90e+00–2.38e+00	–
$k_{TATKF6P}^{eq}$	7.01e-01	2.03e-01–1.73e+00	–	k_{Cit}^{m}	7.83e+01	1.32e+01–2.75e+02	mmol/L
$k_{TATK3PG}^{eq}$	6.63e-06	1.09e-06–4.82e-05	–	k_{ICDH}^{eq}	2.33e+01	1.21e+01–3.30e+01	–
k_{PFK}^{m}	5.67e-03	3.12e-03–1.13e-02	mmol/L	k_{AAex}^{eq}	6.72e+05	1.64e+05–9.00e+05	–
k_{F16P}	1.55e-02	4.99e-03–3.12e-02	mmol/L	k_{FMA}^{eq}	7.71e+00	5.63e+00–3.66e+03	–
k_{ENO}^{eq}	4.17e+02	1.20e+02–3.66e+03	–	k_{FMA}^{m}	5.54e+03	1.49e+03–1.72e+04	mmol/L
$k_{PEP_{PK}}$	1.64e-03	8.58e-04–2.36e-03	mmol/L	k_{MDH}^{m}	3.25e+00	6.91e-01–7.79e+00	mmol/L
k_{xATP}	3.00e+02	2.00e+02–4.79e+02	cell/L/min	k_{OAA}^{m}	2.31e-04	1.92e-05–6.18e-04	mmol/L
k_{mATP}	1.33e+07	1.00e+07–8.81e+07	cell/L/min	k_{AcCoA}^{m}	1.10e+05	4.29e+04–3.05e+05	mmol/L
NAD_{basal}	2.33e+00	1.26e+00–3.55e+00	mmol/L	k_{SDH}^{m}	4.07e+00	2.78e-03–6.39e+00	mmol/L
k_{cUGLC}^{m}	4.07e+00	1.97e+00–6.39e+00	mmol/L	k_{dR5P}^{m}	5.25e-01	1.96e-01–	mmol/L
k_{ME}^{m}	2.27e-01	1.53e-01–4.49e-01	mmol/L	k_{PEPCK}^{m}	3.93e-09	8.42e-10–1.26e-08	mmol/L
$k_{ATP_{ME}}^{i}$	6.89e+04	1.90e+04–1.99e+05	$mmol^2/L^2$	$k_{Pyr_{PC}}^{m}$	7.62e-02	9.36e-03–1.24e-01	mmol/L
k_{μ}^{i}	1.31e+03	3.87e+02–2.75e+03	mmol/L	k_{ME}^{eq}	1.84e+04	4.28e+02–6.93e+04	–
$k_{Glu_{AlaTA}}^{i}$	1.89e-01	9.75e-02–3.61e-01	$mmol^2/L^2$	k_{KDH}^{m}	1.14e-01	7.42e-02–2.06e-01	mmol/L
$k_{Glu_{GS}}^{m}$	2.33e-03	8.16e-04–2.51e-02	mmol/L	$k_{OAA_{AspTA}}$	1.15e+03	2.89e+02–3.05e+03	mmol/L

Table B2.1.: Estimated global parameters of MDCK.SUS2 structured intracellular model with confidence intervals between 0.025–quantile and 0.972–quantile (Q0.025 – Q0.975) calculated via bootstrap method with 2500 runs (continued).

Parameter	Value	$Q_{0.025}$–$Q_{0.975}$	Unit	Parameter	Value	$Q_{0.025}$–$Q_{0.975}$	Unit
k^m_{ICDH}	1.52e-07	5.07e-08–5.63e-07	mmol/L	$k_{Glu_{AspTA}}$	2.70e-03	7.99e-04–8.22e-03	mmol/L
$k_{Keto_{AspTA}}$	1.93e+00	4.91e-01–4.57e+05	mmol/L	$k^m_{TATKF6P}$	4.41e-07	1.10e-07–1.60e-06	mmol/L
$k_{Glu_{GLDH}}$	6.27e-05	2.57e-05–9.71e-05	mmol/L	k^m_{GLDH}	3.32e+04	1.44e+04–6.37e+04	mmol/L
k^m_{Glnase}	1.69e-04	2.99e-05–2.59e-02	mmol/L	$k^m_{ATP_{HK}}$	2.36e-06	7.20e-07–7.32e-06	mmol/L
k^{eq}_{GLDH}	4.51e-01	1.25e-01–1.71e+00	–	$k^m_{ATP_{ALD}}$	7.40e+04	1.93e+04–2.31e+05	mmol/L
k^{eq}_{ALD}	8.95e+03	2.59e+03–4.02e+04	–	$k^m_{3PG_{ALD}}$	1.47e-04	4.57e-05–2.99e-04	mmol/L
k^a_{PFK}	3.39e+00	2.88e+00–4.28e+00	mmol/L	$k^m_{ATP_{PC}}$	4.06e-09	4.39e-10–1.16e-08	mmol/L
k^m_{ATPase}	1.37e+01	8.79e+00–2.24e+01	mmol/L	$k^m_{ATP_{PDH}}$	3.94e+02	2.16e+02–7.31e+02	mmol/L
k_{3PG}	1.35e+00	6.39e-01–2.94e+00	mmol/L	k_{Glu^x}	2.47e+01	1.46e+01–4.57e+01	mmol/L
$k_{PEP_{ENO}}$	1.01e-02	3.53e-03–1.90e-02	mmol/L	k_{Glu}	2.00e+03	4.71e+02–1.03e+04	mmol/L
$k^m_{TATK3PG}$	6.59e-09	5.14e-10–2.77e-08	mmol/L	$k^{eq}_{Glu^x_{trans}}$	3.56e-05	4.05e-06–9.25e-05	–
k_{Gln^x}	1.05e+01	4.63e+00–4.86e+01	mmol/L	$k_{Lac_{trans}}$	2.73e+00	1.46e+00–7.52e+00	mmol/L
$k^m_{Pyr^x_{trans}}$	2.55e-04	3.24e-05–1.07e-03	mmol/L	$k_{Lac^x_{trans}}$	7.97e+01	2.68e+01–1.42e+02	mmol/L
ω	8.57e-06	2.66e-06–2.20e-05	–	$k_{Pyr_{LDH}}$	6.37e-02	3.21e-02–1.24e-01	mmol/L
k^m_{AspTA}	4.25e+03	2.81e+02–1.14e+04	mmol/L	$k_{Lac_{LDH}}$	4.39e-02	2.71e-02–1.01e-01	mmol/L
$k^m_{ATP_{GS}}$	1.88e+01	1.05e+01–1.17e+02	mmol/L	k_{cPyr}	9.10e-06	1.48e-06–5.27e-05	$mmol^2/L^2$
$k^i_{ATP_{Glnase}}$	2.81e-02	1.16e-02–7.50e-02	$mmol^2/L^2$	$k^a_{Pyr_{LDH}}$	3.07e-05	1.07e-05–9.84e-05	–
$k^i_{OAA_{SDH}}$	1.56e-01	6.11e-02–2.85e-01	$mmol^2/L^2$	$k_{Glu_{LDH}}$	2.08e+01	8.97e+00–6.08e+01	$mmol^2/L^2$
k^m_{GLYS}	8.96e+05	1.95e+05–9.00e+05	mmol/L	$k^i_{Glu_{LDH}}$	1.73e+01	6.41e+00–9.50e+01	–
$k^m_{ATP_{CL}}$	3.08e+04	3.47e+03–9.44e+04	mmol/L	k^{eq}_{LDH}	1.01e+01	5.26e+00–1.84e+01	–

Table B2.1.: Estimated global parameters of MDCK.SUS2 structured intracellular model with confidence intervals between 0.025–quantile and 0.972–quantile (Q0.025 – Q0.975) calculated via bootstrap method with 2500 runs (continued).

Parameter	Value	$Q_{0.025}$–$Q_{0.975}$	Unit	Parameter	Value	$Q_{0.025}$–$Q_{0.975}$	Unit
$k^{eq}_{Lac^x_{trans}}$	3.73e+01	1.88e+01–5.88e+01	–	k^{m}_{dNH4}	8.12e+02	2.48e+02–1.65e+03	mmol/L
$k^{a}_{ATP_{dNH4}}$	5.27e-03	1.35e-03–3.66e-02	mmol/L	k_{NH4}	1.92e-02	7.14e-03–3.36e-02	mmol/L
k_{NH4^x}	2.45e+00	1.22e+00–7.33e+00	mmol/L	k^{m}_{AlaTA}	1.68e-01	7.59e-02–4.91e-01	mmol/L
$k^{eq}_{NH4^x_{trans}}$	7.46e-06	3.51e-06–2.28e-05	–				

Table B2.2.: Estimated global parameters of MDCK.SUS2 segregated cell growth model with confidence intervals between 0.025-quantile and 0.975-quantile ($Q_{0.025}$ – $Q_{0.975}$) calculated via a bootstrap method with 2500 runs.

Parameter	Value	$Q_{0.025}$–$Q_{0.975}$	Unit	Parameter	Value	$Q_{0.025}$–$Q_{0.975}$	Unit
$k^{m}_{Glc^x}$	9.78e+00	4.52e+00-1.25e+01	mmol/L	α	3.66e+05	3.08e+05 -	-
μ_{max}	4.20e-04	3.46e-04- 4.73e-04	1/min	k_d^{min}	1.93e-12	1.93e-14-3.27e-05	1/min
Y_{x/Glc^x}	6.02e-09	4.96e-09- 1.32e-06	mmol/L/cell	k_d^{max}	9.48e-05	6.66e-05-1.02e-04	1/min
m_{Glc^x}	4.28e-04	1.70e-04- 4.49e-04	mmol/L/µL/min	β	1.46e-19	1.46e-21-1.02e-05	1/min

Table B2.3.: Initial conditions of substrates and metabolic by-products with local parameters used for the simulation of Cultivation 1 (Cult1) and Cultivation 2 (Cult2) of MDCK.SUS2.

Local parameter	Cult1	Cult2	Unit		Cult1	Cult2	Unit
$\left[Glc^x\right]\ (t=0)$	19.50	19.50	mmol/L	E_{Level}	1.00	1.00	-
$\left[G\ln^x\right]\ (t=0)$	4.65	4.56	mmol/L	V_w	1e-3	1e-3	-
$\left[Glu^x\right]\ (t=0)$	1.50	1.50	mmol/L	$X_1(t=0)$	2.19e+05	2.35e+05	cells/mL
$\left[Lac^x\right]\ (t=0)$	0.00	0.00	mmol/L	$X_2(t=0)$	1.49+05	1.57+05	cells/mL

$\left[NH4^x\right]\ (t=0)$	0.25	0.25	mmol/L	$X_3(t=0)$	1.50+05	1.58+05	cells/mL
$\left[Pyr^x\right]\ (t=0)$	7.66	7.86	mmol/L	$X_4(t=0)$	1.30+05	1.30+05	cells/mL
d_c	19.58	19.58	µm	$X_5(t=0)$	1.12+05	1.12+05	cells/mL
d_m	9.76	9.96	µm	$\left[V_t\right]\ (t=48.1)$	-	1.71e08	Virions/mL
k_{dGln^x}	8.8e-05	8.8e-05	1/min	$\rho 1$	-	4.85	-
$\rho 2$	-	15.61	-	$\rho 3$	-	6.00	-
$k_d^{\min\inf}$	-	4.9e-08	1/min	$k_d^{\max\inf}$	-	2.9e-04	1/min
v_p	-	6.45e+00	virions/cell/min				

Table B2.4.: Initial conditions of intracellular metabolites used for simulation of the MDCK.SUS2 pre-culture of cultivations.

Local parameter	Pre-culture	Unit	Local parameter	Pre-culture	Unit
$\left[G6P\right]\ (t=0)$	0.12	mmol/L	$\left[Glu\right]\ (t=0)$	1.89	mmol/L
$\left[F6P\right]\ (t=0)$	0.036	mmol/L	$\left[Suc\right]\ (t=0)$	0.019	mmol/L
$\left[R5P\right]\ (t=0)$	0.016	mmol/L	$\left[Mal\right]\ (t=0)$	0.42	mmol/L
$\left[UDPGlc\right]\ (t=0)$	0.19	mmol/L	$\left[Keto\right]\ (t=0)$	0.17	mmol/L
$\left[F16P\right]\ (t=0)$	0.035	mmol/L	$\left[Fum\right]\ (t=0)$	0.09	mmol/L
$\left[3PG\right]\ (t=0)$	0.15	mmol/L	$\left[OAA\right]\ (t=0)$	0.24	mmol/L
$\left[PEP\right]\ (t=0)$	0.013	mmol/L	$\left[ATP\right]\ (t=0)$	2.53	mmol/L
$\left[Pyr\right]\ (t=0)$	0.036	mmol/L	$\left[AcCoA\right]\ (t=0)$	0.99	mmol/L
$\left[Gln\right]\ (t=0)$	1.49	mmol/L	$\left[IsoCit\right]\ (t=0)$	0.023	mmol/L
$\left[Glc\right]\ (t=0)$	0.019	mmol/L	$\left[NH4\right]\ (t=0)$	5.98	mmol/L
$\left[Lac\right]\ (t=0)$	0.00	mmol/L			

C. Supplementary studies

C.1 Impact of number of cell class on cell volume and enzymes

Five cell classes were used, analogous to the models used to describe cell growth of suspension AGE1.HN.AAT and adherent MDCK cells [1,2]. In the following, *in silico* studies were performed to compare the effects varying the number of cell classes on the model fitness (Fig. C.1.1, Table C.1.1).

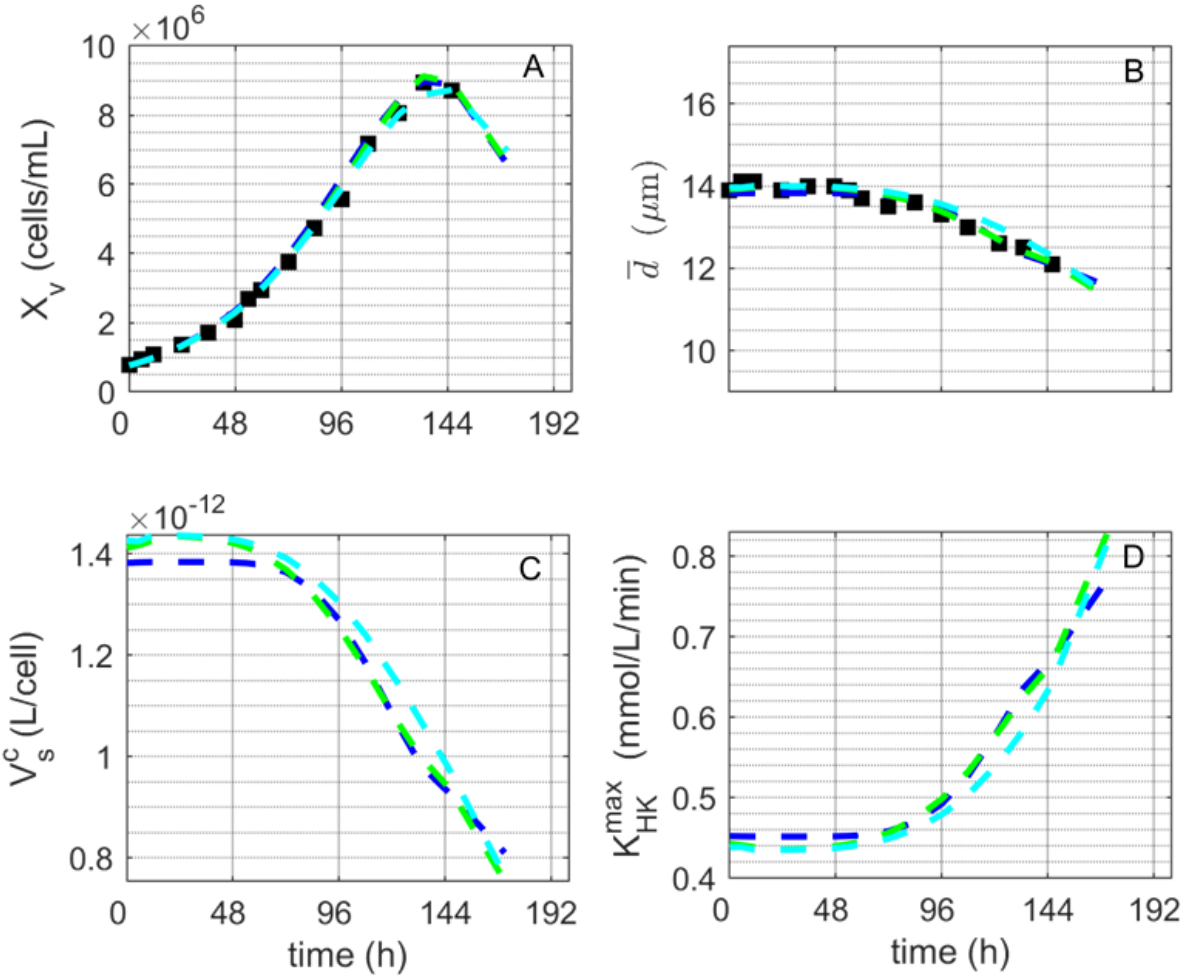

Figure C.1.1.: Model simulations considering a different number of cell classes. (A) Viable cell concentration, (B) mean cell diameter, (C) cell-specific volume and (D) cell-specific hexokinase activity. N^c: number of cell classes (Blue: N^C=2, Green: N^C=5 and Cyan: N^C= 7). Black squares: experimental data of Cultivation 1.

Table C.1.1.: Model fitness for the viable cell concentration and the mean cell diameter for different cell classes.

	Model Fitness*		
Number of cell Classes	Viable cell concentration (X_v)	Mean cell diameter ($\bar{d}$)	Overall
N^c=2	0.0102	0.0026	0.0128
N^c=5	0.0067	0.0011	0.0078
N^c=7	0.0043	0.0034	0.0077

*Model fitness was calculated using Eq. 3.1.86 (Models and methods section).

These findings indicate that reducing the number of cell classes results in a worse fit of the viable cell concentration (X_v, Table C.1.1) and the mean cell diameter ($\bar{d}$, Table C.1.1). For example, when two cell classes were used, the cell-specific volume ranges between 0.71–1.38 × 10^{-12} L/cell, whereas when five classes were used, the range was 0.63–1.44 × 10^{-12} L/cell (V_s^c, Fig C.1.1C). Consequently, these differences in the cell-specific volume also had a noticeable impact on cell-specific enzyme activities (e.g., for hexokinase, Fig. C.1.1D), which had a significant impact on metabolism prediction over the course of 200 h. The relationship between the cell-specific volume and maximum volumetric enzyme activities was introduced in Eq. 3.1.85). Increasing the number of cell classes, specifically to seven classes in this case, did not improve model fitness significantly. Given these results, five cell classes were chosen, which is also similar to previous studies and limits the model complexity [1–4].

C.2 Impact of growth-related time step function after virus infection

Cell growth is halted within a few hours after viral infection, virions are released and the cells die. Cell staining can be used to monitor the transition of a cell between its growth and apoptotic state, which is also indicated by a decline in viable cell concentration and mean cell diameter. In theory, after complete cell growth arrest, most cells will remain in

the first cell class (X_1) containing the smallest cells rather than transitioning to the last cell class (X_5) that contains the largest cells. This implies that cells would only grow in size during the cell growth phase to produce two daughter cells. In theory, this also implies that the mean cell diameter will tend to decrease to the smallest possible value as cell growth decreases over time. For this reason, a step function that accurately describes the transition from cell growth to cell death following viral infection is required to accurately describe the viable cell concentration, mean cell diameter, and the viable cell volume. In the following, an *in silico* study compares the use of a smooth step-function and the absence of a step function (cell growth assumed to be zero immediately) after infection (results shown in Fig. C.2.1 and Table C.2.1).

Overall, a better fit of the viable cell concentration (X_v, Fig. C.2.1A and Table C.2.1) and the mean cell diameter ($\bar{d}$, Fig. C.2.1B and Table C.2.1) is obtained using the smooth step function (Φ_1, introduced in Eq. 3.1.44). This step function allows a better description of the decrease in the cell growth rate observed after virus infection. The decision to use a step function was also influenced by the accuracy of metabolic model predictions. For example, mean cell diameter affects the cell-specific volume (V_s^c, Fig. C.2.1C), which in turn has an impact on cell-specific enzyme activities (e.g., the cell-specific hexokinase activity, Fig. C.2.1D). The correlation between the cell-specific volume and the maximum volumetric enzyme activities is described by Eq. 3.1.85. In this instance, without a step function, the cell-specific hexokinase activity ranges between 0.43–94 mmol/L/min, while with a step function it ranges between 0.43–1.07 mmol/L/min. These small differences have a significant effect on the model's prediction after virus infection, demonstrating the importance of using a step function.

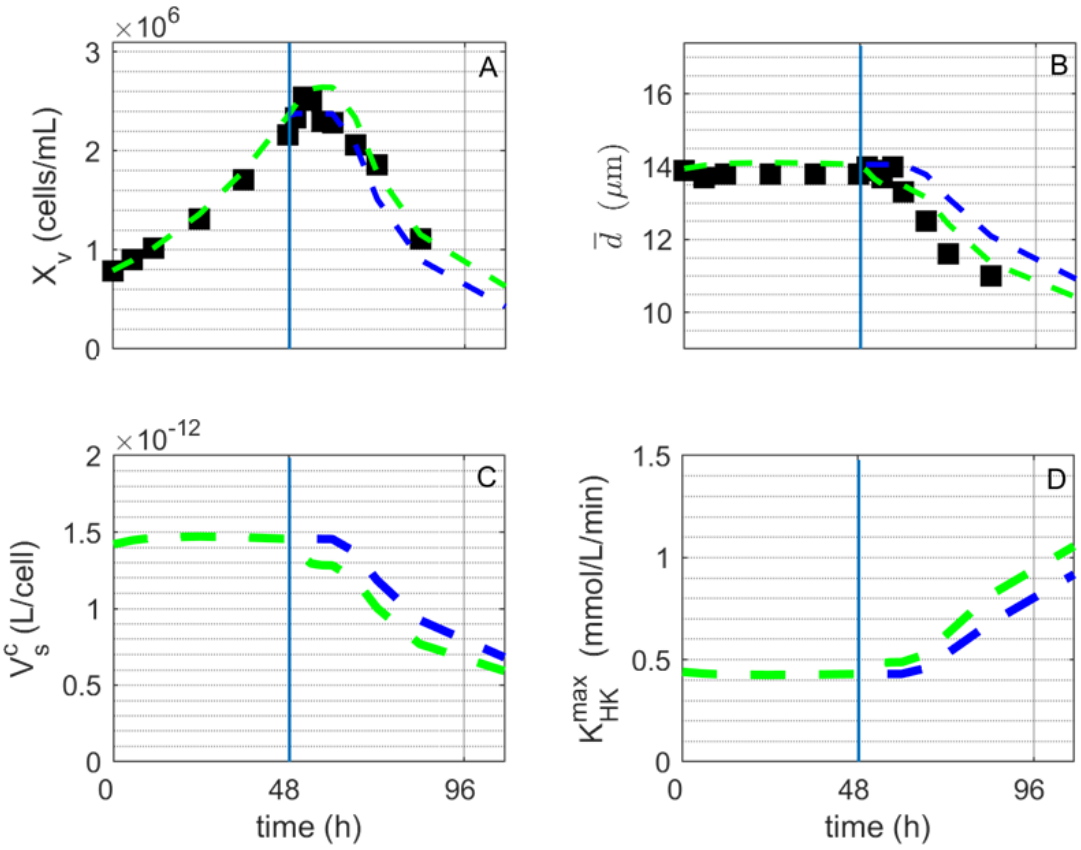

Figure C.2.1. Model simulations considering a step function for the decrease in the cell transition rate after virus infection. (A) Viable cell concentration, (B) mean cell diameter, (C) cell-specific volume and (D) cell-specific hexokinase activity. Blue line: cell growth without a step function. Green: cell growth with a step function. Black squares: experimental data of Cultivation 2. Vertical blue line: time of infection (48 h).

Table C.2.1. Model fitness for viable cell concentration and mean cell diameter with and without step function for the cell growth rate.

	Model Fitness*		
Step function	Viable cell concentration (X_v)	Mean cell diameter ($\bar{d}$)	Overall
without	0.0621	0.0333	0.0954
with	0.0670	0.0107	0.0776

*Model fitness was calculated using Eq. 3.1.86 (Models and methods section).

C.3 Impact of cell lysis on model prediction

C.3.1 Impact of intracellular metabolites leaking into the supernatant

The following section describes an *in silico* study regarding the impact of intracellular metabolite release on the extracellular metabolite concentration after cell lysis. To investigate the impact of intracellular metabolite (glucose, lactate, pyruvate, glutamate, glutamine and ammonia) release on their concentration in the supernatant after cell lysis, it was assumed that cell death occurs concomitantly with cell lysis. To begin, new model variables were introduced for each cell class's dead cells (X_{di},cells/ L, Eq. C.3.1). The total number of dead cells per class is derived from multiplication of the cell death rate with the cell concentration of each cell class. The total number of dead cells (X_d, dead cells/ L, Eq. C.3.2) is the sum of dead cells from all cell classes.

$$X_{di} = k_d X_i \quad i = 1,\ldots,N^c \qquad \text{C.3.1}$$

$$X_d = \sum_{i=1}^{N^c} X_{di} \qquad \text{C.3.2}$$

Similar to the average cell diameter of a viable cell, the average cell diameter of a dead cell ($\overline{d_d}$) was calculated using Eq. C.3.3).

$$\overline{d_d} = \sum_{i=1}^{N^c} \left(d_m + \frac{d_c - d_m}{N^c - 1}(i-1) \right) \frac{X_{id}}{X_d} \qquad \text{C.3.3}$$

Like the viable cell volume, the dead cell volume (V^{dc}, Eq. C.3.4) was calculated using the average diameter of dead cells and the total number of dead cells.

$$V^{dc} = \pi \frac{\overline{d_d}^3}{6} X_d 10^{-9} \qquad \text{C.3.4}$$

Finally, the dead cell-specific volume (V_s^{dc}) was estimated using Eq. C.3.5.

$$V_s^{dc} = \frac{V_d^c}{X_d} 10^{-6} \qquad \text{C.3.5}$$

Taking into account the conversion required to link the microscopic scale (cell volume) to the macroscopic scale (working volume) (introduced in Eq. 3.1.84), the total number of moles of any intracellular metabolite (C) that can potentially be released into to the supernatant can be calculated by the multiplication of its intracellular concentration by the total volume of lysed cells ($V_s^{dc} X_d$). The corresponding increase of this metabolite on the supernatant or the macroscopic scale (C^x) was estimated taking into account the conversion of the total number of intracellular metabolite C into bioreactor level using the working volume (V_w), as shown in Eq. C.3.6. In Eq. C.3.6 the term φ refers to the other variables previously used to describe extracellular metabolites consumption/ secretion, as shown in Eqs. 3.1.16–3.1.21 and 3.1.54–3.1.59. Note that certain substrates and metabolic by-products are present both in the supernatant and intracellularly, thus making it possible to estimate the impact of their release from intracellular to the bioreactor level. For example, intracellular glucose was designated Glc and the extracellular glucose as Glc^x.

$$\frac{d\left[C^x\right]}{dt} = \varphi + \frac{[C] V_s^{dc} X_d}{V_w} \qquad \text{C.3.6}$$

The results of intracellular metabolites leaking into the bioreactor based on the dead cells volume are presented in Tables C.3.1A and C.3.1B.

Table C.3.1A.: Concentration of extracellular metabolites after virus infection with (+) and without (-) leakage of intracellular metabolites due to cell lysis. (Glc^x) extracellular glucose, (Lac^x) extracellular lactate and (Glu^x) extracellular glutamate; diff (%): percentage difference between both scenarios.

	Glc^x			**Lac^x**			**Glu^x**		
Time (h)	(-)	(+)	diff (%)	(-)	(+)	diff (%)	(-)	(+)	diff (%)
49.90	16.72	16.72	2.67E-06	6.36	6.36	4.46E-05	1.928	1.928	1.43E-05
51.90	16.54	16.54	4.27E-06	6.769	6.769	4.25E-05	1.956	1.956	4.14E-05
54.10	16.34	16.34	4.28E-06	7.195	7.195	3.85E-05	1.985	1.985	7.17E-05
57.00	16.09	16.09	4.39E-06	7.739	7.739	3.41E-05	2.021	2.021	0.00017
59.90	15.84	15.84	5.58E-06	8.271	8.271	9.33E-06	2.055	2.055	0.00133
66.10	15.33	15.33	1.77E-05	9.306	9.306	0.001687	2.117	2.119	0.1108
72.10	14.98	14.98	6.47E-06	9.939	9.94	0.004518	2.143	2.148	0.2672
83.80	14.6	14.6	3.42E-05	10.5	10.5	0.007366	2.155	2.163	0.37
107.00	14.26	14.26	**5.41E-05**	10.78	10.79	**0.009126**	2.158	2.167	**0.4062**

Table C.3.1B.: Concentration of extracellular metabolites after virus infection with (+) and without (-) leakage of intracellular metabolites due to cell lysis. (Pyr^x) extracellular pyruvate, (Gln^x) extracellular glutamine and ($NH4^x$) extracellular ammonium; diff (%): percentage difference between both scenarios.

	Pyr^x			**Gln^x**			**$NH4^x$**		
Time (h)	(-)	(+)	diff (%)	(-)	(+)	diff (%)	(-)	(+)	diff (%)
49.90	5.447	5.447	2.42E-06	2.611	2.611	2.55E-05	1.137	1.137	8.12E-05
51.90	5.297	5.297	2.30E-06	2.518	2.518	4.49E-05	1.163	1.163	1.68E-04
54.10	5.134	5.134	2.25E-06	2.417	2.417	6.72E-05	1.19	1.19	2.68E-04
57.00	4.922	4.922	2.63E-06	2.288	2.288	1.43E-04	1.224	1.224	0.0006158
59.90	4.711	4.711	8.89E-06	2.161	2.161	1.08E-03	1.256	1.256	0.004894
66.10	4.291	4.291	4.22E-04	1.913	1.915	0.0978	1.319	1.325	0.4282
72.10	4.011	4.011	1.13E-03	1.738	1.742	0.2403	1.373	1.388	1.049
83.80	3.708	3.708	1.80E-03	1.517	1.523	0.3384	1.466	1.487	1.47
107.00	3.441	3.441	**2.30E-03**	1.254	1.259	**0.3824**	1.621	1.646	**1.561**

Tables C.3.1A and C.3.1B clearly show that the leakage of intracellular metabolites into the supernatant after cell lysis has only a minor impact on their corresponding extracellular concentrations. The smallest difference was found for glucose and pyruvate, followed by lactate (below 0.1 %, at 107 h). The highest difference between these two scenarios was found for glutamine, glutamate and ammonium (0.38–1.56 %, at 107 h). Overall, these results suggest that a leakage of intracellular metabolites into the extracellular environment can be neglected, especially as in this case only relatively low cell concentrations (2.1×10^6 cells/mL) was infected. Nevertheless, high cell density cultivations [5–8] like 20×10^6 cells/mL could result in more than 15% of the accumulated ammonium in the cultivation vessel being due to cell lysis.

C.3.2 Impact of intracellular enzymes leaking into the supernatant

The following section describes an *in silico* study of the possibility of intracellular enzymes leaking into the supernatant after cell lysis remains active. More specifically, the possibility of amino acid degradation or conversion to glutamate and production of ammonium occurring on the supernatant. This essentially means converting the enzyme's activity on the viable cell volume scale (microscale) to the volume scale of the bioreactor (macroscale). The conversion between these scales was introduced in Eq. 3.1.84. To begin evaluation of the impact of the activity of intracellular enzymes released into the supernatant on the extracellular concentration of glutamate and ammonium, it was assumed that cell death occurs concomitantly with cell lysis. New model variables were introduced to describe the concentration of dead cells for each cell class (X_{di} , cells/ mL) as described in Eq. C.3.1 and the total concentration of dead cells (X_d , cells/mL) using Eq. C.3.2. The average diameter of a dead cell ($\overline{d_d}$) was calculated using Eq. C.3.3 and the dead cell-specific volume (V_s^{dc}) was calculated using Eq. C.3.5, introduced in the preceding section.

Next, the volumetric enzyme activity related to the dead cell volume ($K_e^{\max dc}$, mmol/L/min) was estimated based on the dead cell-specific volume (V_s^{dc}).

$$K_e^{\max dc} = \frac{v_e E_{level}}{V_s^{dc}} \qquad \text{C.3.7}$$

The corresponding volumetric enzyme activity after cell lysis on the macroscopic scale ($K_e^{\max macro}$) was estimated taking into account the working volume (V_w, 10^{-3}) and the total dead cell volume ($V_s^{dc} X_d$) as shown in Eq. C.3.8 (similar to the conversion of the micro- to the macroscale described in Eqs. 3.1.84 and 3.1.85)

$$K_e^{\max macro} = K_e^{\max dc} \frac{V_s^{dc} X_d}{V_w} \qquad \text{C.3.8}$$

To evaluate the impact of the amino acid metabolism on the production of glutamate and ammonium, the estimated amino acid degradation rate (r_{AAex}, Eq. A.2.39) was modified as shown in Eq. C.3.9.

$$r_{AAex}^{x} = K_{AAex}^{\max\, macro} b_{NAD} \Theta \qquad \text{C.3.9}$$

Here, r_{AAex}^{x} describes the amino acid degradation rate on the supernatant after cell lysis, $K_{AAex}^{\max\, macro}$ is the macroscopic volumetric amino acid degradation rate, b_{NAD} is the relative NADH level, Θ is a step function which is zero for non-infected cells and one for infected cells.

The model simulations of this *in silico* study are shown in Fig. C.3.1.

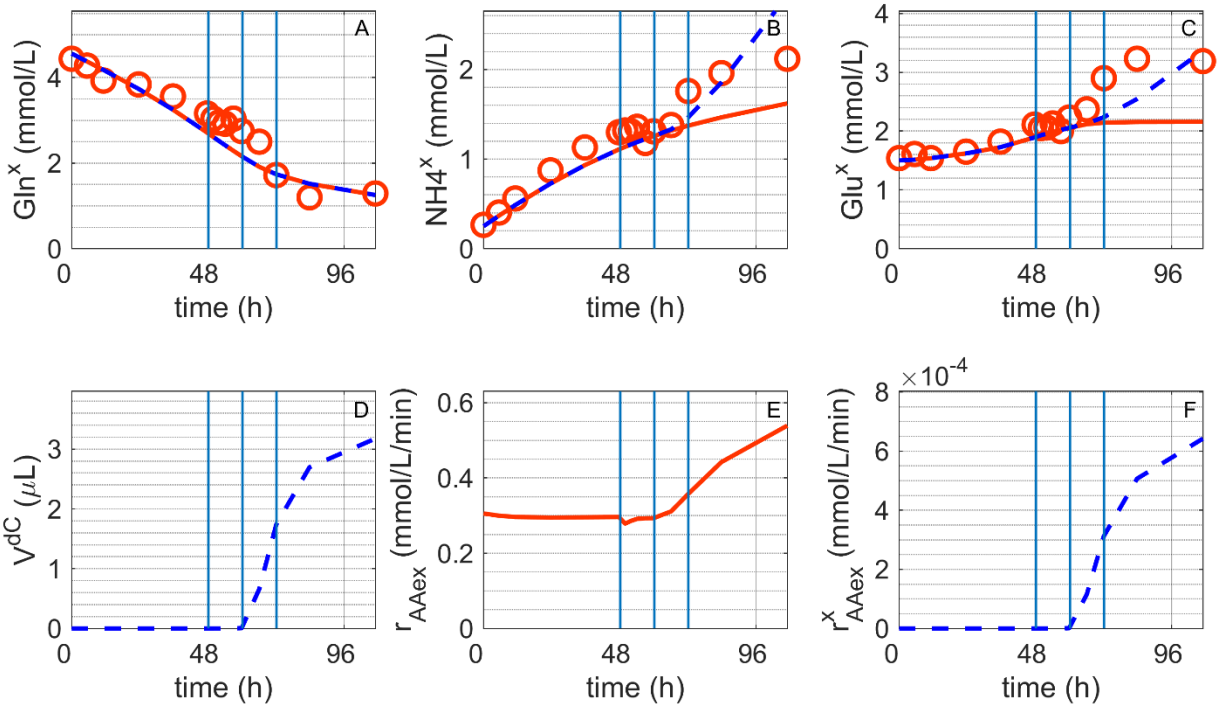

Figure C.3.1.: Concentration of extracellular metabolites before and after virus infection with (- -) and without (—) leakage of enzymes related to amino acid degradation into the supernatant. (A) extracellular glutamine, (B) extracellular ammonium, (C) extracellular glutamate, (D) volume of dead cells, (E) intracellular amino acid degradation rate and (F) extracellular amino acid degradation rate. Blue vertical lines: 0, 12 and 24 hours post infection. Experimental data of Cultivation 2. Blue line: enzyme leakage (+). Red line: enzyme leakage (-). Red circles: experimental data of Cultivation 2.

These results demonstrate that accounting for extracellular amino acid degradation caused by the intracellular enzyme leakage (r^{x}_{AAex}, Fig. C.3.1F) has no impact on the concentration of glutamine in the supernatant (Fig. C.3.1A). On the other hand, this results in a significant increase in the concentration of ammonium and glutamate in the extracellular environment (Figs. C.3.1B and C.3.1C). This is true even when the rate of extracellular amino acid degradation (Fig. 3F) is significantly lower than the rate of intracellular amino acid degradation (r^{x}_{AAex}, Fig. C.3.1E). As can be seen, the rate of extracellular amino acid degradation is proportional to the increase in the volume of dead cells volume (V^{dC}, Fig. C.3.1D) which would be proportional to the amount of intracellular enzyme leaked.
Overall, these results indicate that if enzymes leak into the supernatant after cell lysis and remain active, they can have a significant impact on the concentration of extracellular metabolites. Additional experiments should be performed to support this finding.

C.4 References of Supplementary Studies

1. Rehberg, M.; Ritter, J.B.; Genzel, Y.; Flockerzi, D.; Reichl, U. The relation between growth phases, cell volume changes and metabolism of adherent cells during cultivation. J. Biotechnol. 2013, 164, 489–499, doi:10.1016/j.jbiotec.2013.01.018.

2. Rehberg, M.; Ritter, J.B.; Reichl, U. Glycolysis Is Governed by Growth Regime and Simple Enzyme Regulation in Adherent MDCK Cells. PLoS Comput. Biol. 2014, 10, e1003885, doi:10.1371/journal.pcbi.1003885.

3. Rehberg, M.; Wetzel, M.; Ritter, J.B.; Reichl, U. The regulation of glutaminolysis and citric acid cycle activity during mammalian cell cultivation. 12th IFAC Symp. Comput. Appl. Biotechnol. CAB 2013 2013, 12, 48–53, doi:10.3182/20131216-3-IN-2044.00011.

4. Ramos, J.R.C.; Rath, A.G.; Genzel, Y.; Sandig, V.; Reichl, U. A dynamic model linking cell growth to intracellular metabolism and extracellular by-product accumulation. Biotechnol. Bioeng. 2020, 117, 1533–1553, doi:10.1002/bit.27288.

5. Genzel, Y.; Vogel, T.; Buck, J.; Behrendt, I.; Ramirez, D.V.; Schiedner, G.; Jordan, I.; Reichl, U. High cell density cultivations by alternating tangential flow (ATF) perfusion for influenza A virus production using suspension cells. Vaccine 2014, 32, 2770–2781, doi:10.1016/j.vaccine.2014.02.016.

6. Gränicher, G.; Babakhani, M.; Göbel, S.; Jordan, I.; Marichal-Gallardo, P.; Genzel, Y.; Reichl, U. A high cell density perfusion process for Modified Vaccinia virus Ankara production: Process integration with inline DNA digestion and cost analysis. Biotechnol. Bioeng. 2021, 118, 4720–4734, doi:10.1002/bit.27937.

7. Nikolay, A.; Léon, A.; Schwamborn, K.; Genzel, Y.; Reichl, U. Process intensification of EB66® cell cultivations leads to high-yield yellow fever and Zika virus production. Appl. Microbiol. Biotechnol. 2018, 102, doi:10.1007/s00253-018-9275-z.

8. Bissinger, T.; Fritsch, J.; Mihut, A.; Wu, Y.; Liu, X.; Genzel, Y.; Tan, W.-S.; Reichl, U. Semi-perfusion cultures of suspension MDCK cells enable high cell concentrations and efficient influenza A virus production. Vaccine 2019, 37, 7003–7010, doi:10.1016/j.vaccine.2019.04.054.